UNIVERSITY OF CALIFORNIA

Los Angeles

Towards actively mode-locked terahertz quantum-cascade VECSELs

A dissertation submitted in partial satisfaction

of the requirements for the degree

Doctor of Philosophy in Electrical and Computer Engineering

by

Yu Wu

2023

ABSTRACT OF THE DISSERTATION

Towards actively mode-locked terahertz quantum-cascade VECSELs

by

Yu Wu

Doctor of Philosophy in Electrical and Computer Engineering

University of California, Los Angeles, 2023

Professor Benjamin S. Williams, Chair

The invention of optical frequency combs generated by mode-locked lasers revolutionized time and frequency metrology in the late 1990s. This concept has been explored in several laser systems; the quantum cascade laser (QCL) is one such system that operates in the terahertz (THz) frequency range. THz QCL was first invented in 2001 as a reliable semiconductor source for compact, high-power THz radiation. The inherently strong third-order nonlinearity in its QC-gain medium allows for spontaneous frequency comb formation as a result of spatial hole burning induced by Fabry-Perot cavities and four-wave mixing, which synchronizes the dispersed cavity modes. It was noticed that the self-generated combs are naturally frequency-modulated with quasi-continuous power output, whereas amplitude-modulated combs, i.e., mode-locking, are considered challenging in THz QCLs because of the inherent fast gain recovery time. One effective method to trigger active mode-locking is RF injection locking. It involves injecting RF current modulation into the QC-device at a frequency that is close to the cavity round-trip frequency. This locks the spacing between adjacent lasing modes, and pulses with a duration of 4–5 ps have been reported. In recent

years, the study of frequency comb/mode-locking in THz QCLs has raised increasing interest because of its potential for a number of applications, including astronomy, biomedicine, fast spectroscopy, non-invasive imaging, and non-destructive evaluation. So far, research has concentrated on ridge-waveguide and ring QCLs.

On the other hand, THz quantum-cascade vertical-external-cavity surface-emitting-laser (QC-VECSEL) was introduced in 2015 as a novel external cavity configuration of THz QCLs. The key concept of THz QC-VECSEL is to engineer its gain chip into a millimeter-scale reflectarray metasurface for free-space THz radiation and further incorporation into a resonant laser cavity as an active reflector. This enables watt-level output power with near-Gaussian distributed beam quality; versatile functionality may be incorporated into the amplifying metasurface; and broadband frequency tunability is provided by the VECSEL architecture. Despite the fact that VECSELs are widely used for mode-locking at near-infrared and optical frequencies, THz QC-VECSELs have not yet been exploited in frequency comb and mode-locking applications.

In this thesis, we report for the first time the techniques utilized to achieve frequency comb/mode-locking operations in THz QC-VECSELs. Both the metasurface design and VECSEL cavity geometry are optimized for this purpose. The double-patch metasurface design is considered optimal for broadband frequency response and low dispersion, and a well-designed RF package is needed for efficient RF signal injection and extraction. On the other hand, an off-axis parabolic (OAP) mirror is introduced to build a V-shaped intra-cryostat focusing VECSEL cavity. This OAP-focusing cavity design eliminates most of the intra-cavity diffraction losses and, therefore, enables lasing in an ultra-long external cavity using a small-sized metasurface that supports continuous wave (CW) biasing. It is highly suited for frequency comb/mode-locking applications as the cavity round-trip frequency is lowered to a typical value of 3–5 GHz.

In contrast to ridge-waveguide or ring QCLs, self-generated frequency combs have not

been observed in THz QC-VECSELs — in fact, they prefer to lase in a single-mode regime primarily due to a lack of spatial hole burning. To promote multimode operation in THz QC-VECSELs, we present a technique based on a specific combination of output coupler thickness and external cavity length. Through Vernier selection and reflectance compensation in a cascaded Fabry-Perot cavity, we are able to perform simultaneous nine modes lasing with a free-spectral range (FSR) of ∼21 GHz. The number of lasing modes that can be generated using this method is limited by the maximum available output coupler thickness.

A more effective way to promote multimoding, as well as possible frequency comb or even mode-locking operations, is through RF injection locking. The successful demonstration of RF injection locking in THz QC-VECSELs for the first time is the main focus of this thesis. Lasing spectral broadening has been observed under strong RF modulation, with a maximum bandwidth of around 100–300 GHz. An intermodal beat-note is produced as a result of beating between each of the two lasing modes. It is locked to the RF injection signal as the injection frequency is tuned around the cavity round-trip frequency. This suggests that the lasing modes are equally spaced, which is a prerequisite of frequency comb/mode-locking. Several impacting factors, including metasurface design, external cavity length, and optical feedback, are experimentally investigated in the RF-injection locked QC-VECSELs, which may help control and tune the laser states. THz QC-VECSEL is consequently considered to be a superior platform that enables a more thorough investigation of the fundamental physics of mode-locking/frequency comb operation in QCL systems. Our research on mode-locked THz QC-VECSELs opens the way for future development of semiconductor lasers operating in the 2–5 THz region that produce picosecond-scale pulses.

The dissertation of Yu Wu is approved.

Aydin Babakhani

Chee Wei Wong

Mona Jarrahi

Benjamin S. Williams, Committee Chair

University of California, Los Angeles

2023

Contents

List of Figures

ACKNOWLEDGEMENTS

This Ph.D. thesis represents not only an academic accomplishment but also a personal journey of growth, challenges, and learning made possible by the unwavering support and encouragement of many.

First and foremost, I want to express my deepest thanks to my adviser, Prof. Benjamin Williams, for his constant guidance and support throughout my Ph.D. journey. His knowledge and insights have been extremely helpful in shaping my research, and his mentorship extends beyond academic guidance; it has been a guiding light in my personal and professional development. I made the best decision in sending that self-introduction email to Ben five years ago, and I am eternally grateful for the opportunities Ben has provided me.

Next, I am immensely grateful to all of my labmates and collaborators over the years. Special thanks to Dr. Chris Curwen and Dr. Luyao Xu for their pioneering contributions to our field and for the early training and mentorship I received from them. I am also thankful for my labmates, Yue Shen, Anthony Kim, Eilam Morag, Mohammad Shahili, Jordane Bloomfield, Daniel Mcgovern, and Alexander Song. I am profoundly grateful to each one for their contributions to my academic journey and for the memorable experiences we have shared.

I must express my gratitude to my thesis committee, Prof. Mona Jarrahi, Prof. Chee Wei Wong, and Prof. Aydin Babakhani. Their perspectives and rigorous evaluations have significantly contributed to my scholarly development. I am also grateful to Prof. David Burghoff, Prof. Benedikt Schwarz, Prof. Lukasz Sterczewski, Dr. Andres Forrer, Dr. Urban Senica, and Dr. Dmitry Kazakov for their valuable suggestions and guidance for our research. Additionally, we thank the National Science Foundation (2041165) and National Aeronautics and Space Administration (80NSSC19K0700) for funding support throughout this work.

Finally, words cannot express how grateful I am to my family. My mother has always been a source of love and support for me. My father, a distinguished physics professor, has always been a role model in my life. I've tried to follow in his footsteps, and now I have finally begun to catch up to his pace. I'd also like to thank Fangyao, my husband. We met on our first day at UCLA, and he has always been there to love, understand, and support me throughout my time at UCLA. Even when I doubted myself, he believed in me. My last thanks go to my little furry friend, Mocha. He has a significant impact on both this thesis and my life.

CURRICULUM VITAE

2013–2017 B.S. in Physics, Nanjing University

2017–2020 M.S. in Electrical Engineering, University of California, Los Angeles (UCLA)

2020–present Ph.D. Candidate in Electrical Engineering, University of California, Los Angeles (UCLA)

PUBLICATIONS

Yu Wu, Christopher A. Curwen, Mohammad Shahili, John L. Reno, and Benjamin S. Williams, RF Injection Locking of THz Metasurface Quantum-Cascade VECSEL. Laser & Photonics Reviews, 2023, 2300007 (2023).

Yu Wu, Christopher A. Curwen, Darren J. Hayton, John L. Reno, and Benjamin S. Williams, Continuous wave operation of terahertz metasurface quantum-cascade VECSEL with a long intra-cryostat cavity. Appl. Phys. Lett, 121, 191106 (2022).

Yu Wu, Sadhvikas Addamane, John L. Reno, and Benjamin S. Williams, Multi-mode lasing in terahertz metasurface quantum-cascade VECSELs. Applied Physics Letter, 119, 111103 (2021).

Yu Wu, Yue Shen, Sadhvikas Addamane, John L. Reno, and Benjamin S. Williams, Tunable quantum-cascade VECSEL operating at 1.9 THz. Optics Express, 29, 34695 (2021).

Anthony D. Kim, Christopher A. Curwen, **Yu Wu**, John L. Reno, Sadhvikas J. Addamane,

and Benjamin S. Williams, Wavelength Scaling of Widely-Tunable Terahertz Quantum-Cascade Metasurface Lasers. in IEEE Journal of Microwaves, 3, 305–318, (2023).

Sidharth Thomas, Sam Razavian, Wei Sun, Benyamin Fallahi Motlagh, Anthony D. Kim, **Yu Wu**, Benjamin S. Williams, and Aydin Babakhani, A 0.4–4 THz p-i-n Diode Frequency Multiplier in 90-nm SiGe BiCMOS. IEEE J. Solid-state Circuits, 58, 2407–2420, (2023).

Yu Wu, Christopher A. Curwen, John L. Reno, and Benjamin S. Williams, RF Injection Locking of THz Metasurface Quantum-Cascade VECSEL: Effect of Cavity Length Variation. MIOMD 2023, Aug 6–10 2023, Norman, Oklahoma. (Best Student Presentation Award)

Yu Wu, Christopher A. Curwen, John L. Reno, and Benjamin S. Williams, RF Injection Locking of THz Metasurface Quantum-Cascade VECSEL. SPIE. Photonics West 2023, Jan 28–Feb 02 2023, San Francisco, California.

Yu Wu, Christopher A. Curwen, John L. Reno, and Benjamin S. Williams, Continuous wave operation of terahertz metasurface quantum-cascade VECSEL with a long intra-cryostat cavity. CLEO 2022, May 15–20 2022, San Jose, California.

Yu Wu, Sadhvikas Addamane, John L. Reno, and Benjamin S. Williams, Multi-mode lasing in terahertz metasurface quantum-cascade VECSELs. SPIE. Photonics West 2022, Jan 22–27 2022, San Francisco, California.

Chapter 1

Introduction

1.1 THz technology

Terahertz (THz) radiation bridges the gap between microwave and infrared regions as its frequency ranges from 0.1–10 THz [1]. THz light shows unique properties that find broad applications in spectroscopy, imaging, astrophysics, security, and communication [2]. Historically, THz is the least explored region in the electromagnetic spectrum band due to the difficulty in developing efficient, compact, and economical THz sources. To be more specific, traditional electronic sources used in microwaves, i.e., oscillators and amplifiers, are limited by the transit time and resistance-capacitance effects that cause high-frequency output power roll-off. On the other hand, photonic sources have difficulties extending to THz frequencies because there exists no natural material with such narrow energy gaps. Furthermore, the energy of THz photons approaches that of lattice phonons in III-V semiconductors, which serve as both a source of loss and a fast non-radiative scattering channel for electrons. Although cryogenic cooling can help with this issue, it makes the construction of THz lasers with sustainable population inversion more difficult.

So far, many attempts have been made to build THz sources with milliwatt output powers.

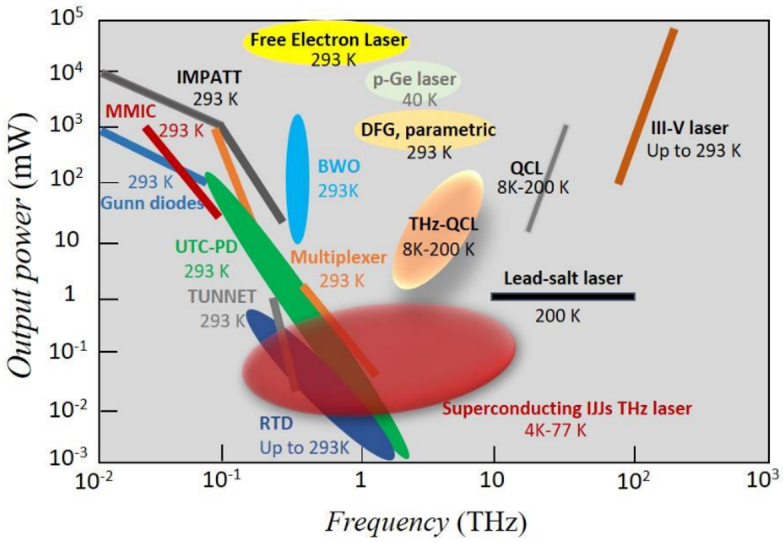

Figure 1.1.1: THz output power as a function of frequency for existing THz sources reported up to 2020. Solid lines represent conventional THz sources; Ovals denote recent THz sources. Figure taken from Ref. [3].

An overview of present-day THz sources is presented in Figure 1.1.1. Room temperature, solid-state electronics devices are already well established at the low-frequency end of the THz regime. Among the examples are the resonant tunneling diodes (RTDs), which were utilized to successfully demonstrate emission over 1 THz [4], and the uni-travelling-carrier photodiodes (UTC-PDs), which use photomixing to produce high-quality sub-THz waves [2]. Radio-frequency (RF) sources like Gunn diodes [5] and heterojunction bipolar transistors (HBTs) [6] typically generate fundamental oscillations between 100–500 GHz. Following chains of nonlinear frequency multiplication and power amplification, such as those based on Schottky diode techniques, higher harmonics of these fundamental oscillations have been reported approaching the THz regime over 2 THz [7]–[9]. Nevertheless, the radiated power decreases noticeably above 1 THz for each of these sources.

Frequency down-conversion is another strategy to generate THz radiation. By pumping a mode-locked femtosecond optical laser onto a nonlinear crystal or photoconductive antenna (PCA), THz pulses are generated through optical rectification in the nonlinear crystal or fast electron oscillations and relaxation induced in the PCA. This is part of the THz time-domain

spectroscopy (TDS), which is suitable for phase-resolved measurement with a typical THz averaged power of a few to hundreds of μW range and a bandwidth of 0.1–6 THz, depending on the exact THz emitter/receiver system used [10].

Some examples of THz lasers include optically-pumped molecular gas lasers, where electronic transitions between rotational states in gas molecules generate THz radiation up to 10 THz [11], [12]; free electron lasers (FEL), which enable high-power THz radiation but are restricted to a few laboratories due to the extremely bulky and expensive systems [13]; p-type germanium (p-Ge) lasers, which rely on cryogenic temperatures around 40 K and magnetic fields [14].

Among all the THz sources, electrically pumped THz quantum-cascade lasers (QCLs) are perhaps the best candidates for compact, high-power THz sources that cover roughly the range between 1 and 6 THz. The first THz QCL was introduced in 2002 by Köhler *et al.* with the demonstration of THz radiation at 4.4 THz using a chirped superlattice (CSL) active region and a semi-insulating surface-plasmon (SI-SP) waveguide [15]. Since then, THz QCLs have been developed rapidly, with a power record of 138 mW in continuous-wave (CW) mode [16] and 2.4 W in pulsed mode [17]. A spectral coverage of 1.2–5.6 THz [18], [19] has been demonstrated, while the upper-frequency end originates from the existence of the Reststrahlen band in the QC material, and the lower frequency end is limited by sufficient injection selectivity and waveguide confinement [20]–[23]. Most THz QCLs operate at cryogenic temperatures, but significant progress has been achieved; the maximum temperature of a pulsed QCL has reached 261 K as a promising step towards futureroom-temperature operation [24].

1.2 THz quantum cascade lasers

1.2.1 Active region designs

QCLs are electrically pumped, unipolar semiconductor lasers that give out THz or mid-IR radiation through electronic intersubband transitions. This contrasts with traditional semiconductor lasers, where optical amplification is based on interband transition across the material bandgap, typically operating in near-IR and visible regions. The active material of QCLs is made of a periodic stack of semiconductor heterostructures grown layer by layer by molecular beam epitaxy (MBE) to a total thickness of 5–10 μm; GaAs and $Al_xGa_{(1-x)}As$ are the most commonly used, lattice-matched well and barrier materials. The thicknesses of the layers are on the order of a DeBroglie wavelength, so the edges of the conduction and valence bands form cascaded quantum wells to restrict electronic motion in the MBE growth direction and quantize the continuous energy into discrete subbands. The electronic transitions between energy subbands are therefore named intersubband transitions, which enable smaller energy separations falling into the mid-IR and THz frequency ranges. The energy separation as well as radiative and nonradiative intersubband transition rates are engineerable by varying layer composition, thicknesses, and doping.

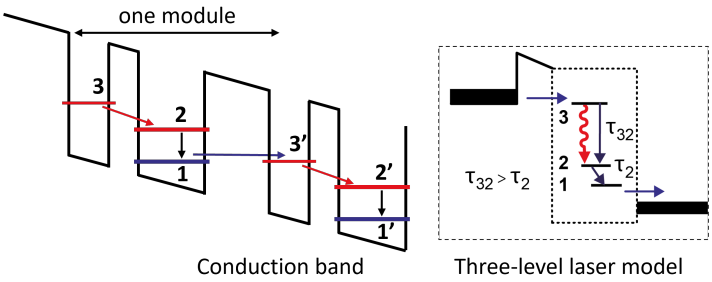

Figure 1.2.1: Schematic of the basic operation principle of a QCL and depiction of the three-level laser model.

As illustrated in Figure 1.2.1, QCL can be described as a three-level laser where the electronic transition occurs between states 2 and 3. The electrons then quickly relax to the ground state 1. At an appropriate bias, the ground state 1 in the former module aligns with

the upper lasing state 3' in the next module, which enables electron transportation between modules through resonant tunneling. Efficient electron injection from states 1 to 3', along with fast electron depopulation from 2 to 1, helps build up sufficient population inversion. The initial active region design is based on radiative transitions between the edges of two minibands formed in chirped superlattice (CSL) structure, where intra-miniband scattering quickly depopulates electrons to the bottom of the lower miniband [15]. Besides that, two major classes of design methods are bound-to-continuum (BTC) [26], and resonant-phonon (RP) [27], depending on the depopulation mechanisms used as shown in Figure 1.2.2. In BTC designs, radiative transitions happen between the bound "defect" state and the minibands, while depopulation occurs through electronic intra-miniband scattering. In RP designs, depopulation is facilitated through rapid resonant tunneling and LO-phonon scattering. As

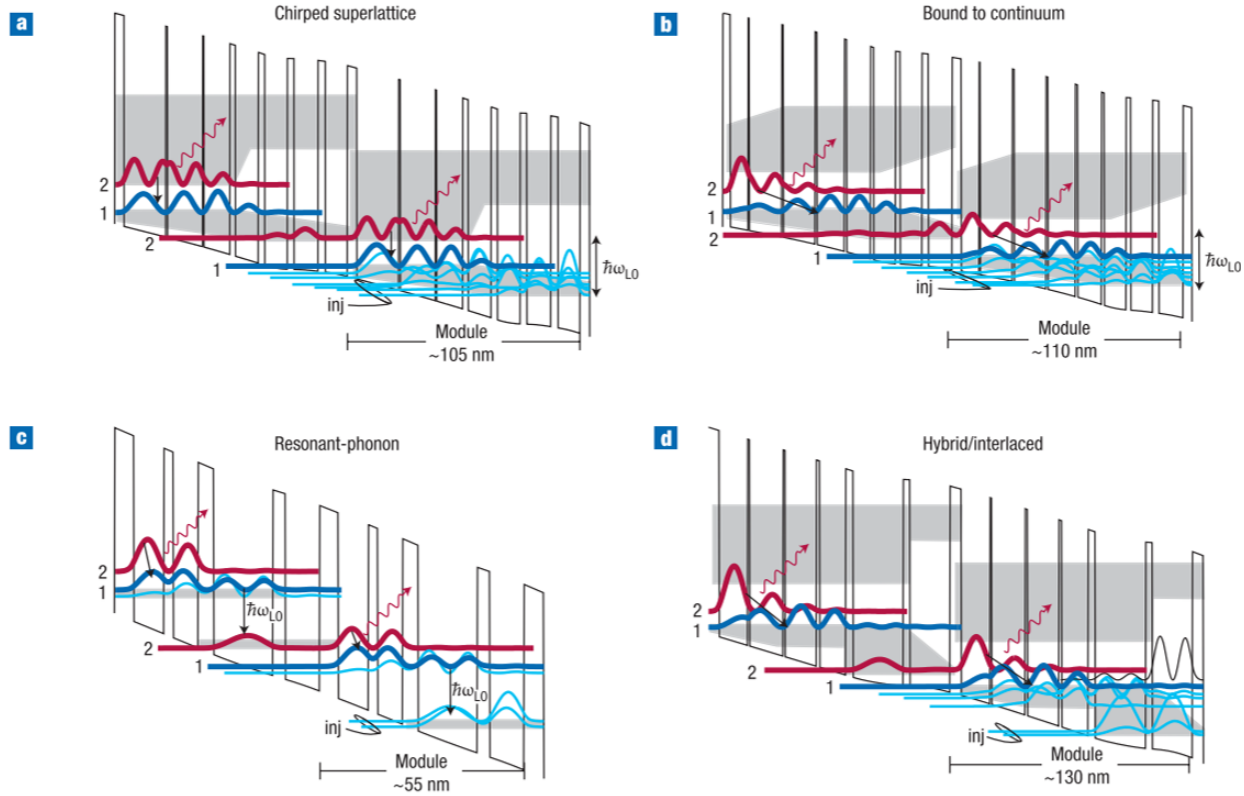

Figure 1.2.2: Band diagrams for major THz QC-active region design schemes: (a) chirped superlattice (CSL), (b) bound-to-continuum (BTC), (c) resonant-phonon (RP), (d) hybrid BTC and RP design. Figure taken from Ref. [25]

the energy of the THz photon is comparable to that of the LO phonon in the GaAs/AlGaAs material system, efficient electron-LO phonon scattering reduces the electron lifetime in the lower lasing state to sub-ps scale to maintain sufficient population inversion and optical gain, as well as the electron lifetime in the upper lasing state to 1–10 ps, which we will discuss in the following sections, prohibiting mode-locking operation in QCLs.

1.2.2 Waveguide designs

Conventional dielectric waveguides used for mid-IR QCLs are not suitable for THz QCLs mainly due to two reasons: 1) the thicknesses of active region and cladding layers should be proportional to the lasing wavelength and become too thick to be feasible for MBE growth at THz frequencies; 2) the free carrier absorption loss in doped semiconductor layers scales with wavelength as λ^2. Two solutions have now become commonplace for THz QCLs: semi-insulating surface-plasmon (SI-SP) waveguides [15] and metal-metal (MM) waveguides [28] as shown in Figure 1.2.3.

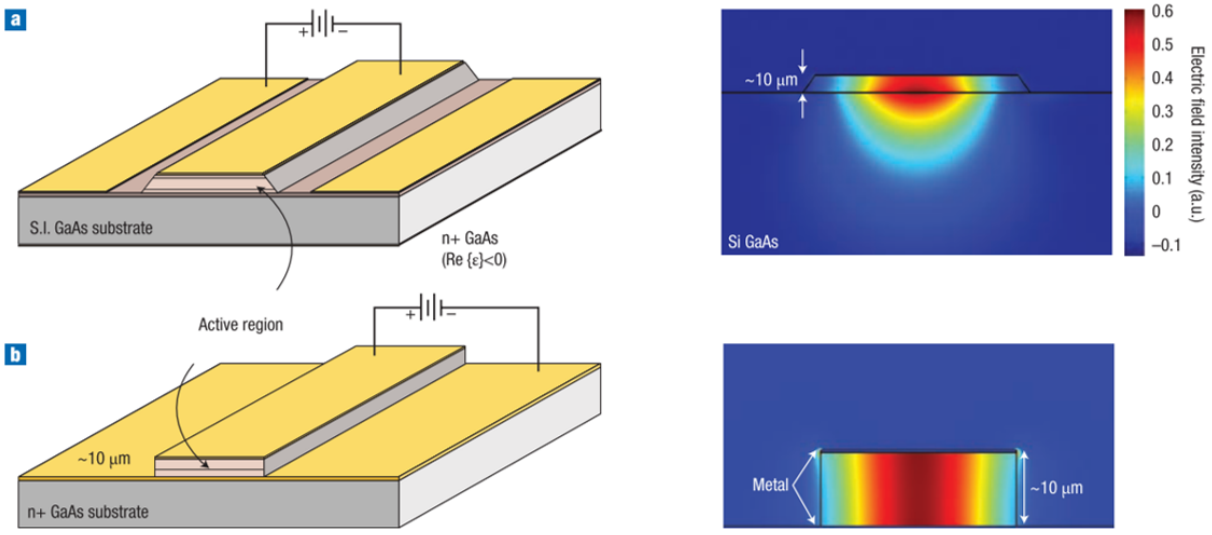

Figure 1.2.3: Schematic diagram of SI-SP (a) and MM waveguides (b) with mode profiles. Figure taken from Ref. [25]

In SI-SP waveguide design, the active region is sandwiched between a thin heavily doped

layer and top metallic cladding to support a surface-plasmon mode. The highly doped layer is made super thin to reduce its spatial overlap with the THz beam and thus the free-carrier loss, which produces a loose confinement of THz radiation — there are still substantial evanescent THz fields leaking into the semi-insulating GaAs substrate as the doped layer is thinner than the skin depth. This offers higher output power and beam quality, but higher threshold gain and worse temperature performance compared to MM waveguides. The MM waveguides, instead, provide nearly unity confinement factor and low waveguide losses by placing metal claddings on both the top and bottom of the active region. Better temperature performances have been demonstrated [24], [29], however, the subwavelength radiating apertures (i.e., the waveguide facets) result in severally diffractive beam patterns [30].

To satisfy simultaneous high output power and good beam quality, the concept of vertical-external-cavity surface-emitting-laser (VECSEL) has been borrowed from the solid-state community to THz QCLs, and a new architecture of QCL, named QC-VECSEL, has been introduced in Ref. [31] and developed in the recent years, which will be discussed in detail in Section 1.6.

1.3 Frequency comb formation in QCLs

1.3.1 Concept of frequency combs

A frequency comb is a spectrum of phase-coherent, evenly spaced, narrow laser lines. It has a very simple mathematical expression in the frequency domain, where each tooth of a frequency comb f_n is defined in the following way:

$$f_n = f_{cep} + n \times f_{rep}. \tag{1.3.1}$$

The frequency of n-th mode is fully defined by two frequencies: the carrier envelope offset frequency f_{ceo} and the repetition frequency f_{rep}. As f_{ceo} and f_{rep} are located in the RF domain where hyperfine reference clocks (cesium atomic clocks) are available, f_{ceo} and f_{rep} can be stabilized to a reference frequency to obtain an easy stabilization of the entire comb. In this way, frequency combs provide absolute rulers in the optical domain that can directly link and compare optical frequencies to microwave frequencies phase coherently in a single step. Its invention revolutionized time and frequency metrology in the late 1990s and led to the Nobel Prize in 2005 in Physics for John Hall and Theodor W. Hänsch [32]–[34].

After the concept of frequency comb was first demonstrated in mode-locked Ti: sapphire lasers in near-IR spectral region [32], it quickly extended to other laser systems, including QCLs. The first attempt was made in mid-IR QCL by Paiella *et al.* in 2000 [35]. The author modulated the laser current at the cavity round-trip frequency and saw the proliferation of lasing modes. The laser output was sent into a fast quantum well infrared photodetector (QWIP) to extract the beat-note generated by optical coupling between adjacent lasing modes, and the large spectral width of the pedestal in the beat-note spectrum in fact indicates incoherent locking. In the same year, the same group reported on spontaneously generated "mode-locking" of a mid-IR QCL while an optical beat-note with a full-width half maximum (FWHM) below 100 kHz at the round-trip frequency of 13 GHz was collected. The authors falsely interpret the generation of narrow beat-note to come from pulses. In fact, we need to clarify that although mode-locked lasers are the most straightforward and initially used method to generate frequency combs, frequency combs do not necessarily originate from mode-locked lasers.

If we have a look at the electric field of a frequency comb in the time domain, it can be expressed as:

$$E(t) = \sum_n A_n e^{i\phi_n} e^{-i\omega_n t}, \tag{1.3.2}$$

with A_n and ϕ_n being the amplitude and phase of each mode. For a frequency comb to be

phase-coherent, it means that the phase of each mode is temporally constant (ϕ_n is not a function of time). If all the modes have equal phases, the temporal field shows pulses with an exact repetition frequency of f_{rep}. This is a conventional picture of mode-locking, which produces a so-called amplitude-modulated (AM) comb. Phase-coherence includes another case where all the modes in a frequency comb have a random but fixed phase relationship. In this case, instead of high-peak intensity pulses, a quasi-CW output will be produced whose temporal field envelope is still perfectly periodic in time, reflecting its comb nature. This situation is often referred to as a frequency-modulated (FM) comb. As we will later see, QCLs generally tend to operate naturally close to an FM comb state.

1.3.2 Spontaneous FM combs in ridge-waveguide QCLs

QCLs have fundamental difficulty in mode-locking. In interband transition-based diode lasers, the lifetime of electrons on the upper lasing state is determined by electron-hole recombination on the order of ∼1 ns. However, the electron lifetime in QCLs is dominated by fast electron-optical phonon scattering, which leads to ps-scale gain recovery time τ_g — typical values are around 1 ps for mid-IR QCLs [36] and 5–10 ps for THz QCLs [37]. On the other hand, the typical value of cavity round-trip time τ_{rt} is around 50–100 ps in a Fabry-Pérot (FP) ridge-waveguide QCL of several millimeters' length. The condition of $\tau_g < \tau_{rt}$ violates the requirement of mode-locking — energy cannot be efficiently stored in the gain medium between the pulses and then released in short powerful bursts (as in a normal mode-locked laser); QCLs favor constant power output as a result of short gain recovery time.

The most obvious way to maintain constant power output is to operate in a single-mode regime. However, the broadband gain along with spatial and spectral hole burning in QCLs in fact promotes multimode lasing. Spatial hole burning (SHB) originates from the standing wave pattern in the FP cavity due to the interference of forward and backward propagating

electric fields. This leads to a static population grating with a period of half the wavelength, which effectively increases the gain for the side modes with different spatial profiles and thus induces multimode operation. While SHB in standard semiconductor lasers is eliminated by carrier diffusion, it is a dominant effect in QCLs as the gain recovery process is faster than carrier diffusion.

Considering both the requirements of constant power and multimode operation, QCLs end up showing FM waveform. Benefited by the inherently strong third-order optical nonlinearity in the QC-gain medium (i.e., Kerr nonlinearity), four-wave mixing (FWM) locks the phase and frequency of each comb tooth through degenerate and non-degenerate FWM processes. This is very similar to frequency comb generation in micro-cavity resonators where a strong CW laser with a frequency close to one of its resonance frequencies is coupled into the high-Q micro-resonator and triggers the parametric FWM processes [38].

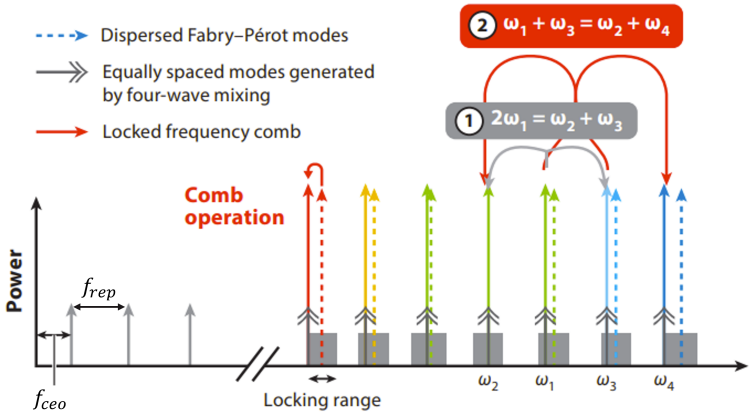

Figure 1.3.1: Schematic of frequency comb generated by a QCL. ① and ② are degenerate and non-degenerate FWM processes. The FWM process locks the frequencies of resonator longitudinal modes and generates a frequency comb if the mismatch between equidistant FWM modes and non-equidistant resonator modes is small. Figure taken from Ref. [39]

The ability of FWM processes to lock longitudinal modes is limited by the overall group velocity dispersion (GVD) in the laser cavity. In a dispersion-free cavity, the equally spaced modes generated by FWM overlap with resonator longitudinal modes, such FWM processes will be enhanced. While in a dispersive cavity, the longitudinal modes are no longer equidis-

tant, and the comb generation suffers according to the mismatch between FWM modes (solid lines in Figure 1.3.1) and resonator modes (dashed lines in Figure 1.3.1).

Different from mid-IR QCLs, THz light strongly couples with optical phonons, therefore III-V semiconductors are extremely dispersive in the THz regime. To overcome this problem, several dispersion compensation strategies have been applied. For example, as illustrated in Figure 1.3.2(a), a chirped corrugation was etched into the facet of the QCL whose period tapers from short to long as its amplitude increases [40]. This structure enables long-wavelength waves, which have larger group velocities, to travel longer distances, while short-wavelength waves reflect earlier, thereby compensating dispersion. Another example of dispersion compensation scheme is based on a Gires-Tournois interferometer (GTI), which is first introduced in mid-IR QCLs [41] and then applied to THz QCLs [42]. The GTI mirror is made of dielectric coating terminated with a gold layer and is directly deposited on the back facet of the device. Dispersion is introduced as the phase of light reflected at the GTI mirror becomes frequency-dependent due to resonance in the equivalent FP cavity.

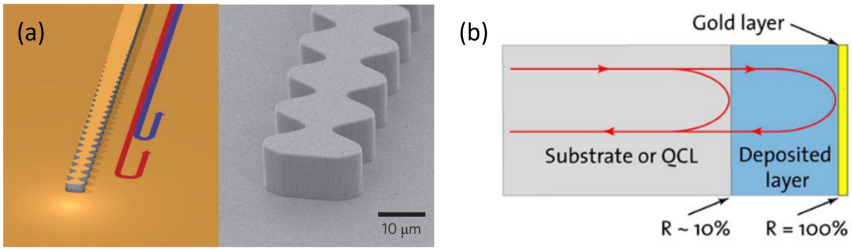

Figure 1.3.2: Schematic of integrated dispersion compensation schemes. (a) Chirped laser facet [40]. (b) Gires-Tournois interferometer (GTI) mirror [41]

Spontaneous FM comb generation was first demonstrated in a mid-IR QCL with sufficiently low GVD and broadband heterogeneous gain medium by Hugi *et al.* in 2012 [43]. Only a few years later, demonstrations were extended into the THz frequency range [40], [44], [45]. Initially, the FM nature of spontaneous frequency combs was predicted in numerical models [46], [47], suggesting a near-constant temporal envelope, while firm experimental demonstrations were performed after Burghoff introduced an effective and phase-sensitive characteri-

zation method: Shifted Wave Interference Fourier Transform Spectroscopy (SWIFTS) [40]. SWIFTS has a similar setup as a Fourier-Transform Infrared (FTIR) Spectroscopy, where the interference light from an interferometer is captured by a fast detector with bandwidth over comb repetition frequency. SWIFTS therefore provides the information of intermodal phase and can be used to tell the coherence of an optical spectrum. With the help of SWIFTS, a better understanding of spontaneous FM combs was performed in Ref. [48], [49]: the phase differences between adjacent modes were found linearly sweeping from $-\pi$ to π, which leads to a linear chirp of the instantaneous frequency; quasi-CW output power indicates the nature of FM combs (Figure 1.3.3). It is also concluded that the spanning of linear frequency chirp, i.e., spectrum width, is determined by the combined effects of SHB, GVD, and Kerr nonlinearity [49]. A nonzero Kerr nonlinearity strongly shifts the range of GVD required for FM comb operation which explains why QCL frequency combs have been found close to zero GVD — the optimum FM comb operation may not happen at exactly zero GVD.

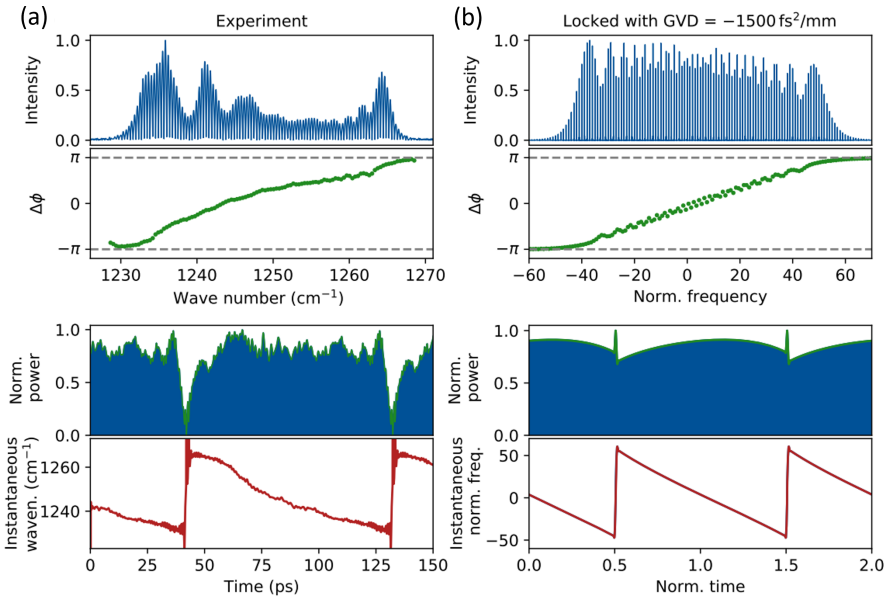

Figure 1.3.3: Analysis of spontaneous FM comb in a QCL. Top: normalized intensity spectrum with chirped intermodal phases that cover 2π over the spectral span. Bottom: quasi-continuous normalized output intensity and linearly chirped instantaneous frequency in the time domain. (a) and (b) are experimental results and simulated reproduction. Figures taken from Ref. [49]

1.3.3 Harmonic frequency combs

More recently, a novel laser state has been discovered in ridge-waveguide QCLs, named harmonic frequency combs [50]–[52]. As illustrated in Figure 1.3.4, self-generated harmonic frequency combs have been demonstrated in mid-IR and THz QCLs at certain bias currents. Their lasing spectra are characterized by phase-coherent modes that are separated by multiple cavity round-trip frequencies. This essentially differs from fundamental dense QCL frequency combs covered in the section above, which are populated with adjacent cavity modes. As the bias current is adjusted, transitions between these two frequency comb states were observed.

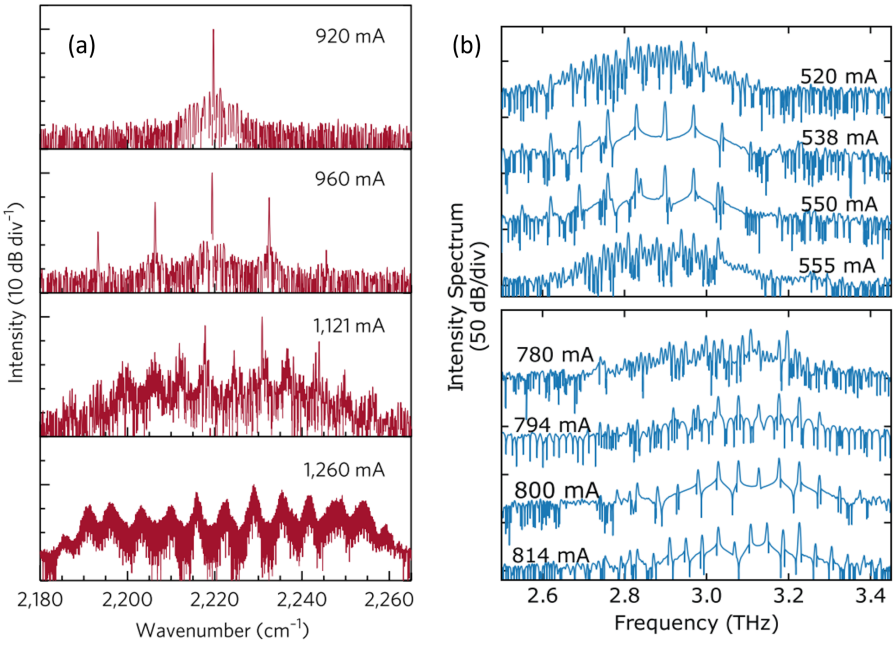

Figure 1.3.4: Observation of self-generated harmonic frequency combs in (a) mid-IR and (b) THz QCLs. (a) A harmonic comb with mode separation of 400 GHz is obtained at a bias current of 960 mA; it was converted to a fundamental comb with a round-trip frequency of 7.7 GHz as the bias current was increased to 1121 mA. Figure taken from [50]. (b) Transition from a dense state to a harmonic comb state and back at various bias currents. The harmonic comb exhibits mode spacing of 5 times the round-trip frequency. Figure taken from [52].

According to Refs. [53]–[55], the origin of harmonic comb state is the mutual interaction between population pulsation and population grating inside the laser cavity. Population

grating is caused by SHB, which produces a spatially nonuniform distribution of population inversion. Population pulsation, on the other hand, results from beating between two frequencies (e.g., the primary lasing frequency and spontaneous emission at a different frequency) that creates an amplitude modulation of the field intensity. The AM field temporally modulates population inversion, which then acts back on the light fields and affects their gain in a nonlinear way. Consequently, population pulsation provides an additional source of gain known as parametric gain — in addition to the saturated gain — and can initiate lasing of sidemodes that are spectrally apart from the primary lasing modes. Stronger population pulsation (weaker population grating) can therefore promote the generation of harmonic comb states.

According to the harmonic comb generation theory, laser dynamics and cavity geometry control the frequency spacing between harmonic comb teeth. For example, thermal tuning has been demonstrated in mid-IR QCLs to tune the spacing of a harmonic comb up to 17% [53]. This is because the electron diffusivity is reduced with temperature, which prevents the population grating from smoothing out and results in a stronger population grating contrast. Besides that, optical seeding and RF injection have been demonstrated as effective methods to induce QCL harmonic combs and tune the comb spacing [56], [57].

Harmonic frequency combs produce coherent modes with broader frequency spacing than dense combs and are considered advantageous when access to individual comb lines is required. It may be used for optical and microwave arbitrary waveform synthesis and for producing low-noise, spectrally pure microwave and THz waves for wireless networking technologies. Thanks to the intrinsic ultrashort gain recovery time of laser dynamics, they are able to generate the THz and microwave waves directly inside the gain medium via beating between comb teeth, eliminating the requirement for an external optical-to-electrical converter. Moreover, the harmonic comb state is considered attractive in terms of the study of mode-locking. As it allows more than one pulse to circulate per round-trip in the laser

cavity, the effective round-trip time can be reduced to a number smaller than the gain recovery time. This may contradict the concept of FM combs discussed in the previous section and trigger possible AM operation in a QCL harmonic comb [54]. Some initial demonstrations of harmonic mode-locking have been discussed in Ref. [57]. As shown in Figure 1.3.5, the author observed free-running high-harmonic emission with multi-pulse behavior in the time domain. Despite the fact that the harmonic state is not pure and no clean pulses are observed—rather, it is more like slight amplitude modulation—the author highlights the possibility of self-starting harmonic mode-locking in THz QCLs.

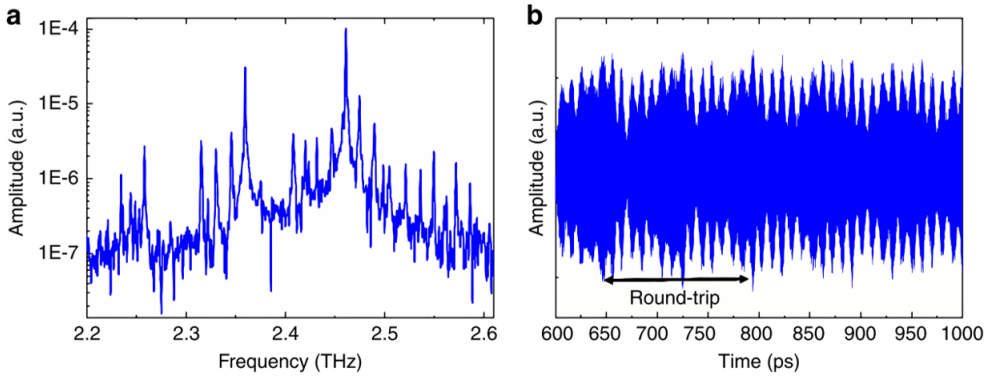

Figure 1.3.5: (a) Self-starting high-harmonic emission showing several frequency bands separated by the 15th harmonic of the round-trip frequency, and each frequency band has a mode spacing of the 2nd harmonic of the round-trip frequency. (b) Electric field profile in the time domain with 15 pulses per round trip and a large modulation at half the round-trip time. Figure taken from [57].

1.3.4 Frequency combs in ring QCLs

We have clarified that SHB plays an important role in promoting multimode operation and frequency comb generation in ridge-waveguide QCLs [49], [58]. However, SHB is not expected to occur in a ring resonator, as the clockwise and counterclockwise modes are not naturally coupled. It was previously thought that multimode operation can only be achieved in ring QCLs at large pumping levels from 8 to 14 times above the laser threshold by Risken-Nummedal-Graham-Haken instability [59], [60]. However, in 2020 Piccardo *et al.* demonstrated that ring QCLs can undergo multimode instability at a pumping level

only fractionally higher than the lasing threshold owing to a phenomenon known as phase turbulence [61]. In this theory, amplitude fluctuation of a lasing mode is associated with phase fluctuation via the inherent linewidth enhancement factor (LEF) of the gain material. LEF is defined as $\alpha = (\frac{dn'}{dN})/(\frac{dn''}{dN})$, where n' and n'' are the real and imaginary parts of the material refractive index, and N is its carrier density. LEF couples the real and imaginary parts of material permittivity based on the Kramers-Kronig relationship. In QCLs, the non-zero LEF value is enabled by the asymmetric Bloch gain coming from the superlattice QC-gain structure with fast dynamic [62] — this produces the phase-amplitude coupling needed for the phase turbulence. Starting from spontaneous emission, the laser field undergoes discontinuous changes which produce fluctuations of n' in the QC-active region. This leads to fluctuations in the spacing between the lasing modes and shifts the side mode with respect to the gain peak, which eventually leads to multimode lasing, despite the absence of SHB.

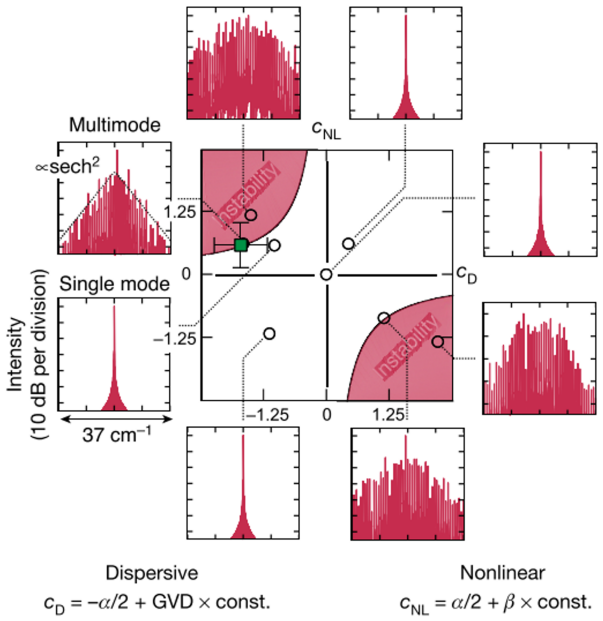

Figure 1.3.6: Behavior of ring QCL plotted in (c_D,c_{NL}) parameter space solving from CGLE. GVD is the group velocity dispersion, α is the linewidth enhancement factor and β is the Kerr nonlinearity. Figure taken from Ref. [61]

The behavior of ring QCL frequency combs can be theoretically explained using the complex Ginzburg-Landau equation (CGLE), where the multimode instability is controlled by

two parameters c_D and c_{NL}, related to GVD and Kerr coefficient respectively. Figure 1.3.6 shows the simulated spectra plotted in the (c_D,c_{NL}) parameter space obtained by solving the laser master equation. Different stability regions are defined by $1 + c_D c_{NL} = 0$, where the inner region confined by the lines (white) has stable, purely single-mode solutions; the solutions lying in the two outer regions (red) exhibit multimode instability.

Spontaneous frequency comb generation has been demonstrated in ring QCLs at mid-IR [63] and THz [64] frequencies. Different from FM combs demonstrated in ridge-waveguide QCLs, in the frequency domain, ring QCL frequency combs show a bell-shaped envelope that fits well to a sech^2 function, while time traces of the laser intensity show high-contrast amplitude modulations. If defects with sufficient reflectivity are introduced into the ring cavity, the temporal power output will result in a nearly flat intensity waveform, as a ridge-waveguide QCL FM comb [61].

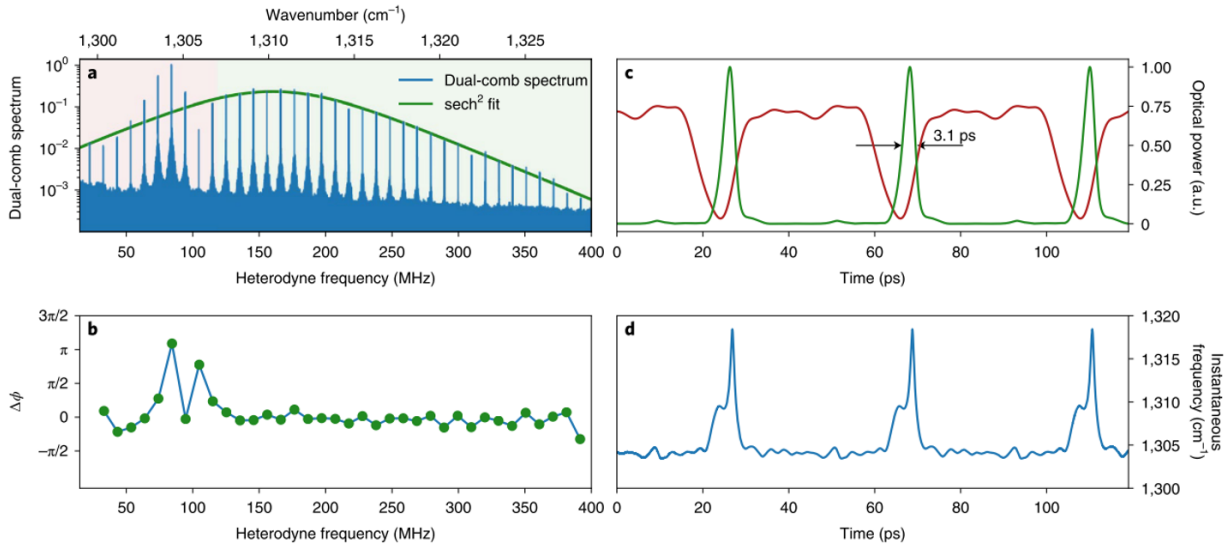

Figure 1.3.7: Spectral phases and waveform of QCL solitons. (a) Dual-comb spectrum, where the red- and green-shaded regions denote normal and anomalous dispersions, respectively. Spectrum in anomalous dispersion region shows sech^2-shape, and (b) In-phase synchronization, as expected for a soliton. (c) Reconstructed waveform of the sech^2-shaped part (green) and the normal dispersive part (red) of the spectrum. Anomalous dispersion is necessary for soliton generation, with a temporal width of ~3 ps. (d) Instantaneous wavenumber of the waveform in (c). Figures taken from Ref. [65]

Ring QCL frequency combs can be directly linked to Kerr combs generated in micro-resonators based on a generalized LLE equation [66]. In optical micro-resonators, a special state named dissipative Kerr soliton was found whose waveform could preserve its shape while propagating through dispersive, nonlinear, and lossy mediums [67], [68]. These solitons rely on a double balance between 1) anomalous cavity dispersion and Kerr nonlinearity, and 2) cavity loss and parametric frequency conversion of the pump light (i.e., parametric gain). The observation of dissipative Kerr soliton in micro-resonators yields a merging of soliton physics and has found great applications in dual-comb spectroscopy [69], parallel coherent optical communication [70], chip-scale light detection and ranging (LIDAR) [71], [72], integrated optical frequency synthesizer [73]. Recently, dissipative Kerr soliton generation has been demonstrated by Meng *et al.* in mid-IR ring QCLs [65]. The QCL ring cavities were fabricated into buried heterostructure waveguides whose top cladding is capped with a highly doped InP layer. The resulting plasmon mode introduces the anomalous GVD which balances the Kerr effect and is essential for soliton formation. As a result, soliton generation is demonstrated with a reconstructed temporal width of ~3 ps by SWIFTS (Figure 1.3.7). Kerr soliton was later demonstrated in THz ring QCLs by the same group [74]. The ring cavity is based on coupled double-ring MM waveguides to compensate for the large positive GVD caused by optical phonon resonance and to reach the anomalous dispersion condition, where self-starting 12-ps-long pulses were observed.

1.4 Mode-locked THz QCLs

While FM combs generate constant power output, AM combs are more favored to concentrate energy into ultrashort pulses with high peak intensity. In order to generate ultrashort pulses specifically in the THz region, mode-locking mechanisms are needed. It is categorized into two varieties: active mode-locking where the laser gain is modulated by external sources around its repetition rate, e.g., based on the approach of RF injection locking and

THz injection seeding, and passive mode-locking where the cavity loss is modulated by a fast saturable absorber.

1.4.1 RF injection locking

RF current modulation was initially applied to mid-IR QCLs in 2000 for lasing mode proliferation [35], while more detailed studies were later performed in THz QCLs [75]–[78]. A low-power RF signal at cavity round-trip frequency is injected into the electrical bias of the laser to modulate the bias current. The current flowing through the QCL directly contributes to the population inversion which is related to the intensity of light field through stimulated emission: $\Delta I \propto \Delta n \propto E_1^2 + E_2^2 + E_1 E_2^* e^{i\Delta\omega t}$. The beating between two lasing modes will modulate the population inversion and thus the bias current at their difference frequency $\Delta\omega$, i.e., cavity round-trip frequency. Accordingly, a direct modulation of the device bias current will help lock the spacing of adjacent free-running lasing modes or seed new ones. When the detuning between the modulation frequency and the cavity round-trip frequency is large, the emission spectrum shows a single lasing mode with sideband generation spaced by the modulation frequency. As the detuning is decreased, more and more modes will be brought above the lasing threshold by their neighbors' sidebands. Demonstration of spectrum broadening has been reported in Refs. [78]–[81] under relative weak RF injection.

Whereas a weak electrical modulation can be used to lock and stabilize the beat-note of FM combs, a strong modulation could enforce in-phase coupling of intermodal beat-notes produced by each pair of neighboring comb lines and generate AM combs along with ultrashort pulses in the same device [82], [83]. Strong RF modulation has been applied to generate actively mode-locked THz QCLs first performed in 2011 by Barbieri *et al.* using single-plasmon waveguides [84]. The authors were able to drive 10 longitudinal modes above the threshold, producing mode-locked pulses with a duration of ∼10 ps, where the temporal intensity was reconstructed based on electro-optical sampling using a femtosecond laser.

The pulse width was later narrowed to 5 ps using MM waveguide with a broader spectral bandwidth [85], and to 4.4 ps using a new planarized MM waveguides embedded in low-loss polymer [86].

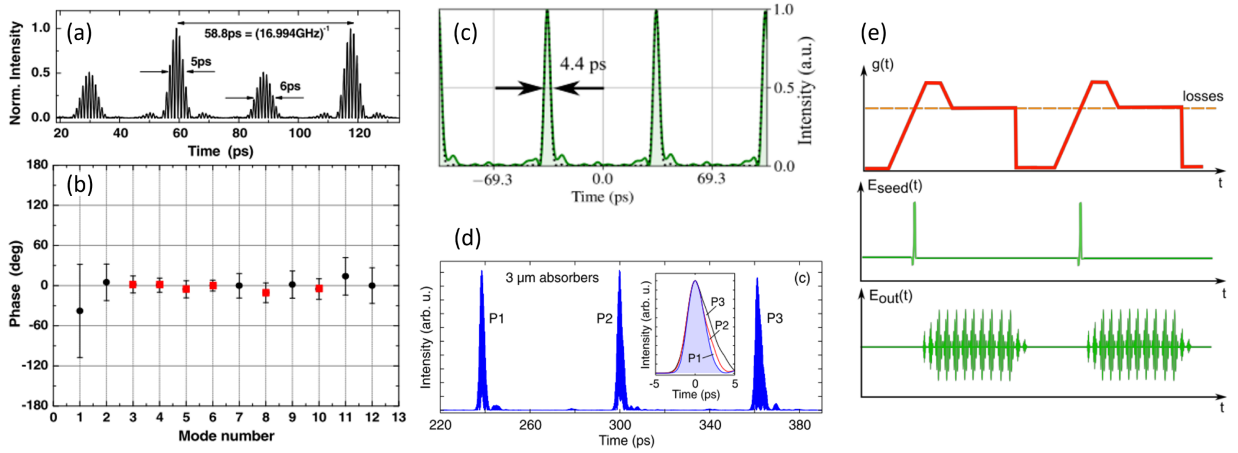

Figure 1.4.1: Active mode-locking demonstrated in THz QCLs. (a) 5-ps pulses generated through RF modulation, the lasing modes are in-phase as required for mode-locking (b) [85]. (c) 4.4-ps pulses generated through RF modulation in BCB-planarized MM waveguide [86]. (d) 2.5-ps pulses generated in injection-seeded THz QCL with side-absorbers to suppress high-order modes [87]. (e) Schematic of injection seeding in a THz QCL [88].

1.4.2 Injection seeding

Another method used for active mode-locking is called injection seeding. External phase-locked THz seed pulses — typically generated from a femtosecond laser by optical rectification or photomixing — are seeded into the QCL device and initiate lasing at a fixed phase rather than set randomly by the inherent spontaneous emission [89]. As illustrated in Figure 1.4.1(e), the QCL is periodically switched on and off (red curve). If no injected THz pulse is present, every time the QCL is switched on, the phase of the spontaneous emission determines the carrier phase of the QCL pulses, which will be random. Here, whenever the QCL is on, a THz seed pulse (green curve, middle panel) is injected into the laser cavity synchronously. The THz pulse has an electric field greater than the spontaneous emission; it is amplified by the unclamped gain and finally saturates the gain triggering steady-state lasing. The carrier phase of the QCL output pulse is therefore set by the phase of the coherent

THz pulse (green curve in the bottom panel). This method requires more complicated laser drive electronics than RF injection locking, while narrower THz pulses were obtained: the first demonstration was performed in Ref. [88], where THz pulses with 9 ps duration were generated; later in Ref. [87], heterogeneous active regions with improved coupled cavity device geometry were applied to obtain a pulse width as narrow as 2.5 ps.

1.4.3 Passive mode-locking

Passive mode-locking in QCLs has long been thought to be inherently hindered due to the ultrashort gain recovery time versus cavity round-trip time. However recently, researchers found that the gain recovery time in THz QCLs may be larger than expected. Unlike mid-IR QCLs, THz photon energy is lower compared with LO-phonon energy, and the LO-phonon scattering is suppressed at low temperatures. According to experimental data, the gain recovery time has been measured as 18 ps [37] and 50 ps [90], using BTC active region designs; 34–50 ps using hybrid BTC/RP active region design [91]. Moreover, Tzenov *et al.* have predicted that passive mode-locking is in fact possible in THz QCLs with the help of fast saturable absorbers [92]. The THz QCL discussed in their theory is designed with multi-section cavity geometry consisting of alternating gain and absorber sections. Provided that its upper state lifetime is 40 ps, the round-trip time in the FP waveguide is 28 ps, and a fast saturable absorber is used with recovery time $T_{1g} \leq 5$ ps, stable single pulse train is predicted to be achievable according to Maxwell-Bloch equations and the pulse width is linearly related to T_{1g} (Figure 1.4.2(b)).

In 2023, Riccardi *et al.* demonstrated the first passively mode-locked THz QCL [93]. Graphene was used as a saturable absorber thanks to its high transparency modulation and fast recovery times (2–3 ps, faster than the gain recovery time in THz QCLs). The multilayer graphene was shaped as a couple of stripes and integrated on the top surface of the MM QCL cavity (distributed along the entirety length of the cavity as shown in Figure 1.4.2(c-d)).

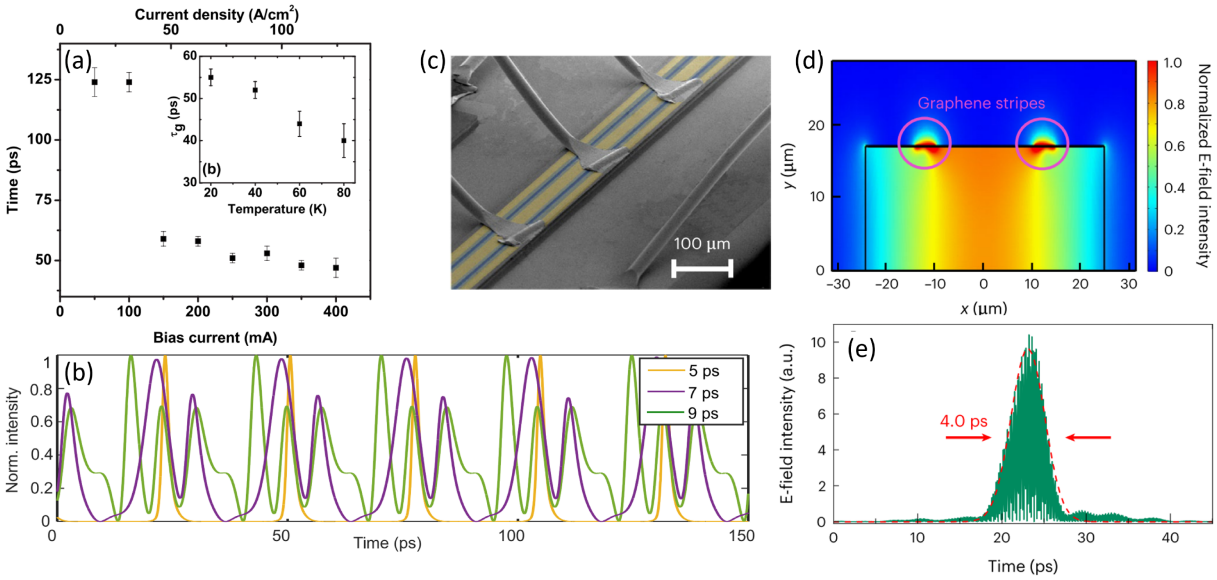

Figure 1.4.2: Passive mode-locking studies in THz QCLs. (a) Gain recovery time measured as a function of bias current and temperature [90]. (b) Simulated normalized optical intensity at various saturable absorber lifetimes. With a short lifetime of 5 ps, a single pulse train is produced in [92]. (c) MM waveguide QCL with distributed graphene saturable absorber on top, and its simulated E-field distribution (d). THz pulses with a FWHM of 4.0 ps has been observed as a demonstration of passive mode-locking [93].

While the intra-cavity THz radiation experiences saturable losses from the graphene, QCL favors pulsed emission over naturally occurring CW emission. As shown in Figure 1.4.2(e), self-starting pulse emission with 4.0-ps duration was observed using a coherent measurement based on injection seeding (the one introduced in Ref. [89]).

1.5 Applications of THz QCL frequency combs

1.5.1 Spectroscopy

THz is well-known as the so-called molecule fingerprint area, where many molecules have rotational and vibrational features in this frequency range. For this reason, one of the most promising applications of THz QCL frequency combs lies in spectroscopy. THz spectroscopy has been applied in greenhouse gas sensing and environmental monitoring [94], [95], detection and identification of explosive and bio-chemical materials [96]–[98] and in astrophysics to

trace star formation and galactic evolution [99].

As mentioned previously, the entire frequency comb can be stabilized simply by locking two frequencies f_{ceo} and f_{rep}, the great frequency resolution, frequency accuracy, as well as broad bandwidth, and high output power of frequency combs then enable an ultrahigh-resolution, high-sensitivity broadband spectroscopy technique, which is named as dual-comb spectroscopy [100]. As sketched in Figure 1.5.1, dual-comb spectroscopy utilizes two coherent frequency combs with slightly different repetition rates, i.e., f_r and $f_r + \Delta f_r$. Their output lights are co-collimating and focusing onto a fast photodiode. Distinguishable heterodyne beat-notes between each pair of optical comb teeth make up an RF comb. This RF comb then becomes easily accessible with commercial RF electronics and contains the relative spectral information in the optical comb spectra. To perform spectroscopy, a sample is introduced into either one optical beam path to extract its phase and amplitude response, or into both optical beam paths, which is analogous to the typical FTIR configuration and measures only the sample's absorption. The sample's response is encoded on the comb light and can be recovered through heterodyne detection later.

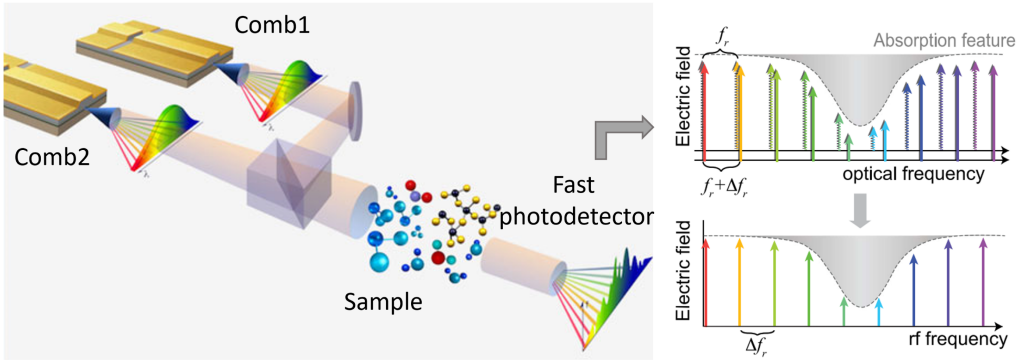

Figure 1.5.1: Concept of dual-comb spectroscopy. Figure modified from Ref. [100].

Dual-comb spectroscopy surpasses traditional Fourier-transform spectroscopy in better resolution, higher signal-to-noise ratio, and faster speed, as no moving component is required; Its frequency accuracies are ensured by the fully stabilized optical frequency combs which are traceability to the underlying frequency reference. The exploitation of dual-comb spec-

troscopy relies on the development of frequency combs in the desired spectral range, while frequency combs based on QCLs provide exciting possibilities toward chip-scale, electrically-pumped systems for dual-comb spectroscopy at mid-IR [101], [102] and THz regions [103]–[105]. Active stabilization of QCL frequency combs used in dual-comb spectroscopy has been achieved through phase-locking [106] and RF injection [107].

1.5.2 Non-destructive evaluation

THz technology is considered a promising alternative method in non-destructive evaluation in industry and biomedical applications and becomes competitive in certain aspects compared with other spectral regions [108]–[111]. Unlike X-ray scanners, THz radiation has very low photon energy and is considered biologically innocuous. Thus, it will not cause harmful ionization in biological tissues and save costs entailed in extensive radiation protection. Compared to microwaves, THz waves achieve higher spatial resolution, so that submillimeter-sized features can be imaged, or micrometer-thin coatings can be analyzed.

Non-destructive thickness measurements have been applied in industry for cost management, quality control, and process monitoring particularly related to the fact that many opaque non-polar materials such as plastics, papers, coatings, paint, etc., are relatively transparent in the THz regime. For example, in automotive manufacturing, the paint and coating thicknesses must be carefully monitored to ensure that the layers remain functional in resisting UV radiation damage and corrosion throughout the lifetime of the product and to minimize expenditure of the coating materials [111], [112]. In polymer extrusion, precise thickness measurements can reduce material usage and wastage while ensuring uncompromised product quality. Other than that, THz systems are particularly suitable for the inspection of plastic components and the detection of defects [113]. In the pharmaceutical industry, THz technique has focused on two main areas: inspection of tablet and capsule coatings and monitoring of tablet porosity and pore size, which helps to preserve drug func-

tionality while in storage, and to facilitate timely drug dissolution inside human bodies [114], [115].

THz techniques are very suitable for medical applications as diagnostic methods thanks to the low photon energy of THz radiation and sensitivity to polar substances, such as water and hydration state [116]. For example, THz pulsed imaging was introduced in 1997 to demonstrate a contrast between muscle and fats in porcine tissue [117]. This initial study promoted later research on the application of THz imaging to other biological samples and now enables 3D imaging of layered structures based on the depth information of the internal dielectric profiles [118]. One potential application of THz imaging is the diagnosis of skin cancer, i.e., to determine regions of skin cancer non-invasively using a reflection geometry imaging system [119]. It can also be applied in finding dental caries, as caries lead to a change in refractive index within the enamel which can be detected [120]. Burn depth diagnosis is another promising application as the waveforms and optical parameters of the burn wounds have shown a contrast between burn-damaged tissue and healthy tissue with the information of burnt depth [121].

At this time, these applications are mostly performed by time-of-flight measurements using THz time-domain systems, where sub-ps THz pulses are generated based on the downconversion of ultrafast lasers from the optical regime using photoconductive antennas or nonlinear crystals. Compared with the THz time-domain system, THz mode-locked QCLs can be an alternative source of THz pulses for the abovementioned applications with the following benefits. First, the average power output from the time-domain system is typically μW level, while THz QCLs have significantly higher THz output powers on the order of tens of mW. Second, THz QCLs have the possibility of operating at higher frequencies (2–5 THz) and with higher repetition rates ($\sim$10s of GHz) for faster acquisition times. Third, THz time-domain systems need complicated optical setup and femtosecond laser which is bulky and expensive, while THz QCLs are compact and lead to the possibility of on-chip products.

1.6 The THz QC-VECSEL

1.6.1 Introduction

The THz quantum-cascade vertical-external-cavity surface emitting laser (QC-VECSEL) was introduced by Prof. Benjamin Williams' lab in 2015 as a novel approach for designing THz QCLs [31]. Different from conventional VECSEL concept in solid-state and diode laser communities, the gain chip is further engineered into a large-area reflective metasurface which provides multiple functions: 1) couple with free-space THz radiation; 2) rotate the incident polarization to be perpendicular to the MBE growth direction to satisfy the "intersubband selection rule"; 3) provide THz amplification under external electrical bias; 4) act as a reflector and form a resonating FP cavity when it is paired with another reflector, i.e., an output coupler. Figure 1.6.1(a) depicts a typical QC-VECSEL design.

The amplifying metasurface is made of a subwavelength array of MM ridge waveguide antennas that is loaded with QC-gain material (Figure 1.6.1(b)). Instead of supporting guided waveguide modes, each element acts in the same way as an elongated microwave patch-antenna that couples to the free-space radiation through TM_{01} mode at a resonance frequency of $\nu_0 \approx c/(2nw)$, where w is the width of the ridges and n is the refractive index of the QC-material filling the ridges. The ridge width is designed to be half-wavelength or its odd multiples, so the odd symmetry of electric fields on the two sidewalls of the ridge results in free-space radiation that constructively interferes (the radiating apertures are the sidewalls). The constructive interference will not be averaged out as the waveguides are operating at cutoff frequency so there is no propagation or phase variation along the length of the ridges. Furthermore, the spacing between the ridges is designed to be subwavelength ($\Lambda < \lambda$) to suppress Bragg diffraction. Bragg diffraction results in light bounded to in-plane surface propagation with less free-space radiation loss. Therefore, the adjustment of the ridge period can be used to tune the radiative quality factor of the metasurface by affecting the hybridization between the radiating TM_{01} resonance and the bounded surface wave.

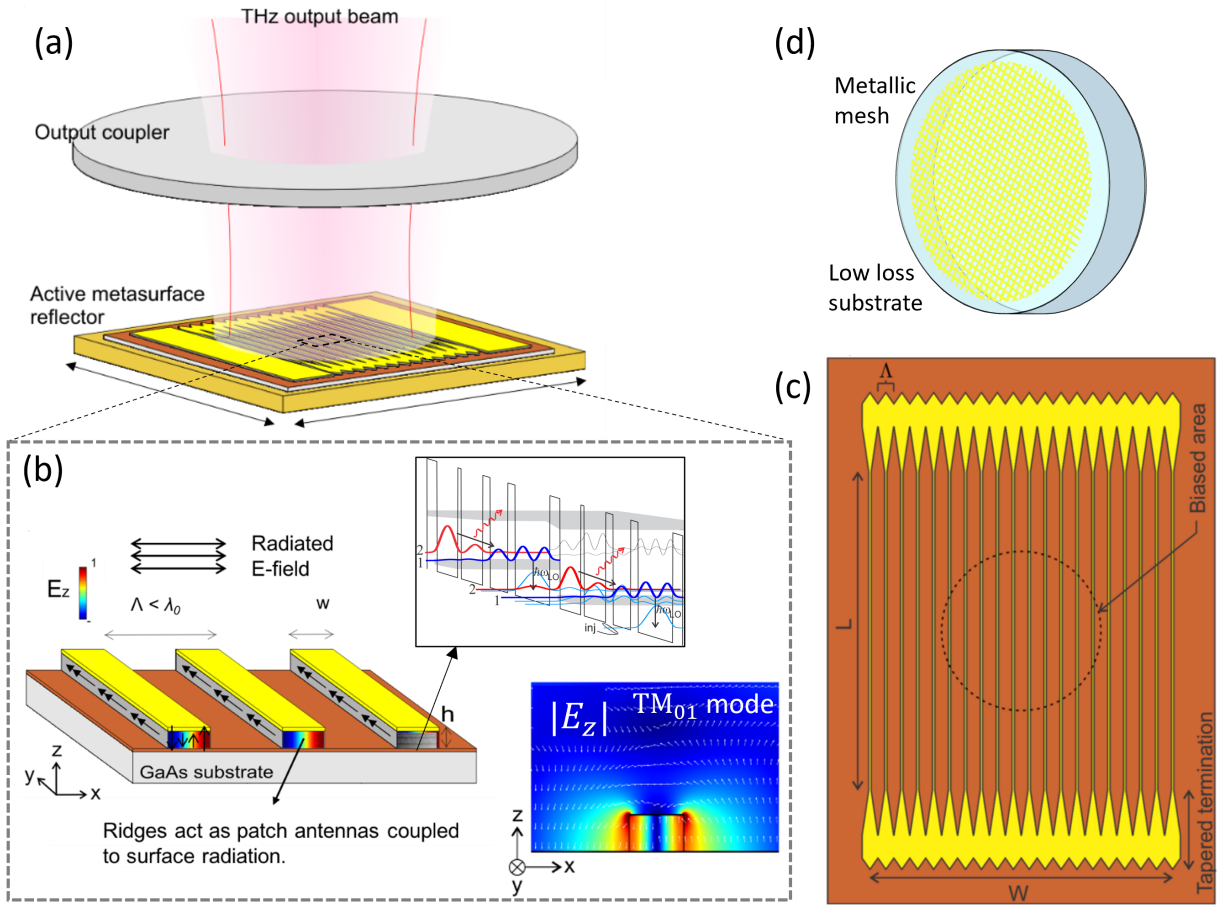

Figure 1.6.1: (a) Illustration of the THz QC-VECSEL which is made of an amplifying metasurface (c) and an output coupler (d). (b) The amplifying metasurface is made of a subwavelength array of MM ridge waveguide antennas that is loaded with QC-gain material. The inset shows the simulated E-field distribution of TM_{01} mode.

If we zoom out and look at the entire metasurface (Figure 1.6.1(c)), the MM ridges are terminated by lossy taper areas, which introduce extra loss to prevent self-lasing in guided TM_{00} waveguide mode and also provide a large wire-bonding area for electrical bias. Moreover, significant free-space radiation limits the value of radiative quality factor associated with the TM_{01} metasurface resonant mode (typically ~5–15), which ensures that lasing only occurs in the external VECSEL cavity when the amplifying metasurface is paired with an output coupler. We should point out that, to pump the fundamental Gaussian mode in the VECSEL cavity, only a central circular area on the metasurface is biased.

The other necessary component of a QC-VECSEL is the output coupler. It is typically made of an inductive metallic mesh evaporated on low THz loss, double-side-polished substrate, e.g., high-resistivity silicon or quartz, while the mesh pattern determines the overall transmittance magnitude [122]. The detailed spectral response of the metasurfaces and output couplers used in specific experiments will be covered in the following chapters.

1.6.2 Significance of QC-VECSELs

By increasing the radiating aperture from the sub-wavelength ridge waveguide facet to the millimeter-scale metasurface, we are now able to achieve scalable high output power and near-Gaussian distributed beam quality at the same time. What's more, other than the baseline metasurface design, the amplifying metasurface can be engineered with versatile functionalities for various applications. For example, 2π phase shift is associated with the metasurface resonance and by varying the ridge width spatially, parabolic phase shift is realized across the metasurface, mimicking reflection from a spherical mirror and enabling focusing of THz radiation [123]; by designing two interdigitated sets of patch resonators which are oriented 90°from each other, the metasurface can be electrically switched between two orthogonal polarizations [124]; MM waveguide array designed at higher odd-order transverse resonant mode (TM_{03}) results in a metasurface with a higher spatial density of gain material, leading to watt-level output power [125]; coupled-resonator metasurface was introduced by gathering two ridge elements into a single period with slightly different ridge widths or spacings, which enables broadband frequency response [126]; patch-based metasurface reduces the fill factor of active elements and therefore promote CW operation by reducing the injection current and heat dissipation [127]; metasurface with randomly distributed ridge elements was proposed to produce radiation with low spatial coherence [128].

Another significant benefit of THz QC-VECSELs is the easy tunability of its operation frequency compared with traditional ridge-waveguide QCLs. In ridge-waveguide QCLs with

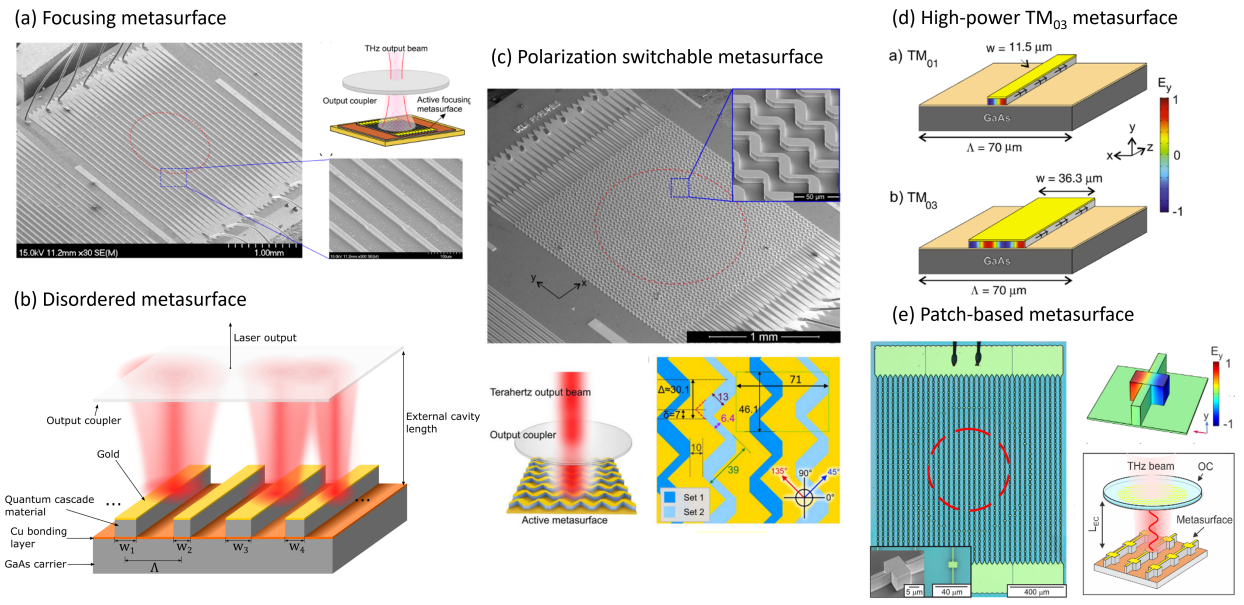

Figure 1.6.2: Versatile metasurface designs demonstrated in THz QC-VECSELs. (a) Focusing metasurface [123]. (b) Disordered metasurface [128]. (c) Polarization-switchable metasurface [124]. (d) High-power TM_{03} metasurface [125]. (e) Patch-based metasurface [127].

well-defined cavity lengths, small frequency tuning is typically achieved by temperature or electrical current-induced refractive index change. The usage of monolithic sampled-grating or coupled-cavity approaches can further broaden the tuning range by stitching together several mode-hop free continuous tuning regimes [129]–[131]. Continuous fractional tuning up to 8.6% has been achieved by mechanically moving a MEMS plunger near a THz QC-wire laser to manipulate its transverse optical mode. However, the subwavelength waveguide facets of the laser lead to extremely divergent beams and low outcoupling efficiency [132]. This is also the reason why applying external cavity approaches (e.g., Littrow configurations) into THz QCLs for broadband tuning becomes challenging.

Alternatively, the external-cavity nature of THz QC-VECSELs allows for easy tunability of the operation frequency, as the cavity length can be adjusted simply by moving the output coupler using a piezoelectric stage (see Figure 1.6.3(c)). By mechanically reducing the cavity length to wavelength or sub-wavelength scale, in combination with broadband metasurface

designs, continuous frequency tuning with more than 20% fractional bandwidth has been demonstrated in Ref. [133], while its high power and good beam quality are maintained across the tuning range (Figure 1.6.3(a-b)). Figure 1.6.3(d) summarizes the single-mode continuous frequency tuning demonstrated at various center frequencies in THz QC-VECSELs [134].

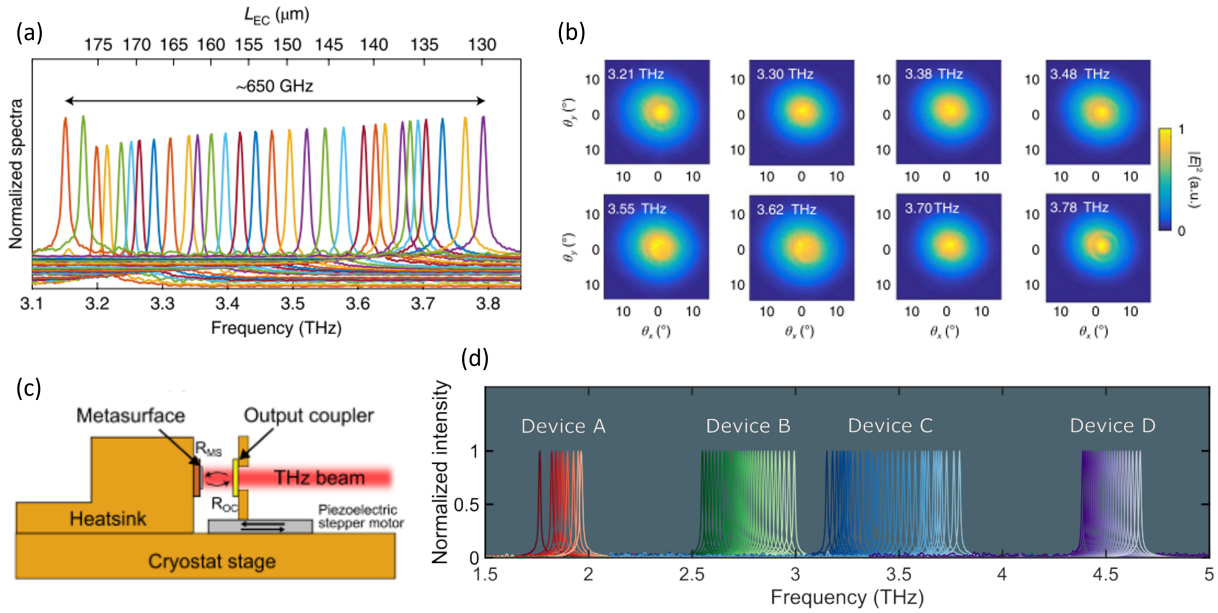

Figure 1.6.3: (a) Continuous frequency tuning in a THz QC-VECSEL with good beam quality across the tuning range (b) [133]. (c) Schematic of the tunable VECSEL architecture. (d) Broadband tuning achieved in four representative QC-VECSELs at various frequency ranges [134].

1.6.3 Towards frequency comb/mode-locking

Compared with traditional ridge-waveguide or ring QCLs, QC-VECSELs are considered better platforms for exploiting frequency comb and mode-locking operation in QC-systems. The main benefits are summarized as follows:

(1) The great flexibility in metasurface design enables a broadband gain and low dispersion, which is favorable for broadband (e.g., octave-spanning) frequency comb and transform-limited ultrashort THz pulses generation. In QC-VECSELs, gain bandwidth is typically limited to QC-metasurface amplification bandwidth instead of

the active material, as ultrabroad gain bandwidth can be achieved in heterogeneous QC-active region designs by stacking multiple QC-structures centering at different frequencies together [135]. To broaden the spectral response of the metasurface, a coupled-resonator metasurface design has been introduced which enables broadband lasing over 1 THz (31% fractional bandwidth) and low values of group delay dispersion (GDD) over hundreds of GHz frequencies [126]. This method, however, applies a relatively dense fill factor of active material and requires the device to operate only under pulsed bias, which is not favorable for mode-locking as there is extra noise and fluctuations from the pulsing instruments. To reduce the fill factor and thus promote CW operation, patches are used in the replacement of ridges. The metasurface combining the coupled-resonator concept and patch elements is considered the best option for mode-locking applications, which is named a double-patch design. Figure 1.6.4 shows the spectral response of an example double-patch design centering at 3.8 THz with a simulated gain bandwidth $\approx$ 1 THz and GDD $\leq$ 0.4 ps^2.

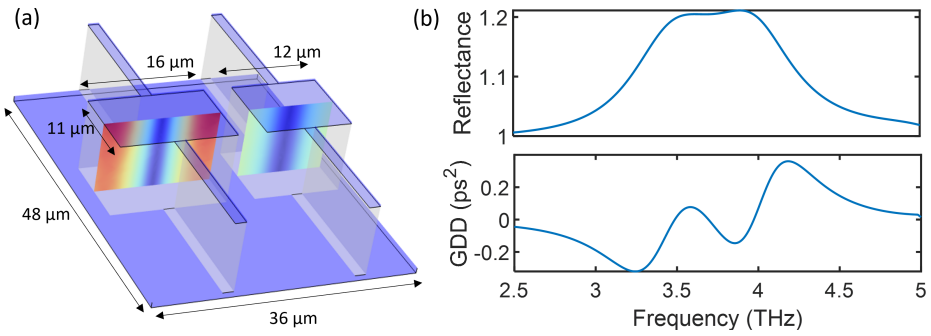

Figure 1.6.4: (a) A single periodic unit cell of the double-patch metasurface. (b) Corresponding simulated amplification bandwidth and GDD.

(2) The easily adjustable external cavity length of a QC-VECSEL is beneficial for mode-locking operation. Since the gain is present on a "per-reflection" basis from the amplifying metasurface, and not on a "per-unit-length" basis as in a ridge waveguide, the external cavity can be made extremely short with no penalty in gain, or extremely long with no penalty in dispersion. This will provide flexibility in adjusting the round-trip time τ_{RT} to be shorter or longer than the gain recovery time τ_g. For example, if the cavity length

is adjusted in a range between 150 μm to 20 mm, the corresponding round-trip time is tuned in a wide range from 1 ps to 133 ps. This makes QC-VECSELs good platforms to study the underline physics, e.g., the laser dynamics and temporal profile, of mode-locked QCLs under different conditions of $\frac{\tau_{RT}}{\tau_g}$. Also, the tunable cavity length is beneficial for spectroscopy applications, as the spacing of comb teeth could be continuously tuned for full spectral coverage.

(3) The long external cavity configuration of QC-VECSELs makes it easy for the integration of external optic elements. For example, we are proposing to insert a metasurface saturable absorber mirror (metaSAM) into the external cavity to exploit possible passive mode-locking in QC-VECSELs. The novel metaSAM has a similar structure as the amplifying QC-metasurfaces, where quantum-well structures are loaded into reflective metasurfaces while broadband and fast saturable absorption is realized through intersubband transitions. This special saturable absorber enables a saturation intensity at the level comparable to the circulating intensity of our THz QC-VECSELs.

While VECSELs are commonly employed for mode-locking at optical and near-infrared frequencies, no frequency comb or mode-locking application has yet made use of QC-VECSELs. Different from ridge-waveguide or ring QCLs, where frequency combs are generated spontaneously, QC-VECSELs "prefer" to lase in only one or two modes at a time. As is reported in previous demonstrations, as the cavity length is tuned, the lasing mode shifts and hops to the next longitudinal modes, but only one or two lasing modes were observed at the same time [122]. The primary reason is that QC-VECSELs experience SHB in a fundamentally different way than waveguide-based QC-lasers. The longitudinal modes primarily reside within the external cavity, and each interacts with the gain material through the same metasurface resonance with nearly the same spatial overlap. This leads to effective gain clamping at the lasing threshold, and typically only a single mode that is spectrally closest to the gain peak lases. As the cavity length is changed, two-mode operation is briefly seen as the main mode

is detuned from the gain peak and a new mode begins to lase. On the other hand, ring QCLs also do not experience SHB but self-generated frequency combs are demonstrated at a certain combination of dispersion and nonlinearity. However, similar phenomena haven't been observed in any QC-VESCELs yet.

This thesis focuses on my efforts — in collaboration with the Williams research group and others — to achieve frequency comb or mode-locking in THz QC-VECSELs. This covers techniques such as metasurface engineering, external cavity design, methods to promote multimode instabilities, characterization, etc. In Chapter 2, we will discuss an effective method to promote multimode operation in a QC-VESCEL using a specially engineered output coupler and precisely controlled cavity length. In Chapter 3, a novel intra-cryostat focusing VECSEL design is introduced for CW lasing in ultralong cavity lengths ($\geq 30\,\mathrm{mm}$). This is the cavity configuration used for the demonstration of RF injection locking, which is described in detail in Chapter 4, as an initial realization of QC-VECSEL combs. Chapter 5 includes some preliminary discussion on a home-build FTIR and certain data treatment. Finally, a comprehensive summary is provided in Chapter 6, where we will highlight the accomplishments made thus far and suggest avenues for future research.

Chapter 2

Reflectance compensation induced multimode operation

As we discussed in the previous chapter, the lack of SHB is considered the fundamental reason that prevents QC-VECSELs from multimode operation. The material gain is clamped at the lowest value needed for a longitudinal mode to lase, resulting in only one or two lasing modes at the same time. Additionally, the partially transmitting output couplers used in the intra-cryostat QC-VECSEL cavities exhibit frequency-dependent reflectance characteristics; this adds to the differential gain needed for additional modes to reach the lasing threshold.

In this chapter, we demonstrate that multimode operation can in fact be achieved in a well-designed QC-VECSEL. Reflectance compensation between the amplifying metasurface and the output coupler guarantees the presence of numerous longitudinal modes with similar lasing thresholds, which allows them to potentially lase at the same time. Using this method, we successfully demonstrated up to nine lasing modes with a free-spectral range (FSR) as small as 21 GHz [136].

2.1 Working principle

As depicted in Figure 2.1.1(a), a typical QC-VECSEL consists of an active metasurface and a slab output coupler. It can be viewed as an equivalent three-mirror cascaded cavity, where the output coupler itself forms an FP cavity that couples to the external laser cavity. Each FP cavity generates a series of longitudinal modes, where the alignment between these modes determines actual lasing modes, i.e., Vernier selection. The output coupler is typically made of an inductive Ti/Au mesh evaporated on one side of a 100 μm-thick quartz substrate. Its mesh pattern enables high reflectivity, while the substrate thickness determines FP oscillation in the reflectance spectrum — this frequency-dependent feedback results in different gain needed for different longitudinal modes to lase, and finally only the one with the lowest threshold could lase. This idea is plotted conceptually in Figure 2.1.1(b), where the output coupler reflectance R_{OC} at different cavity resonance frequencies ν_m shows different values (blue dots); the mode with the lowest R_{OC} is supposed to lase if we neglect the frequency dependence coming from the metasurface and gain material. As the cavity length is tuned,

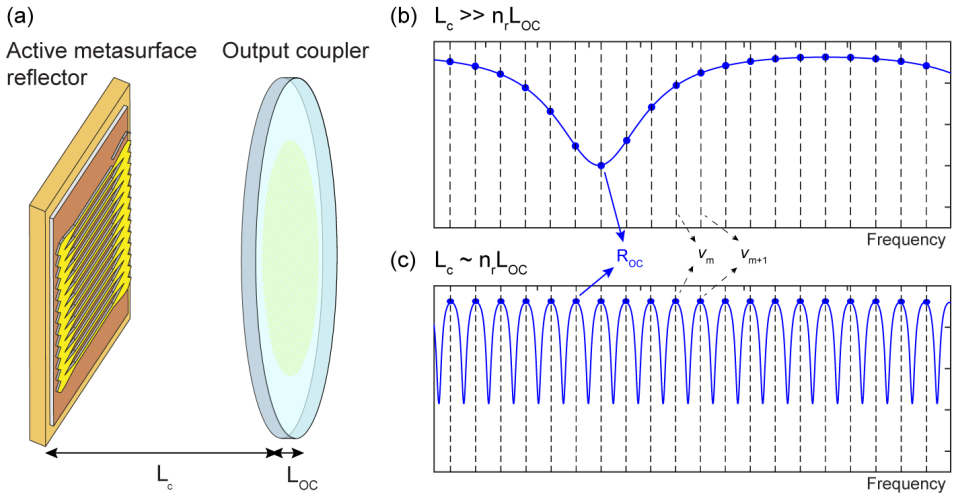

Figure 2.1.1: (a) Illustration of the QC-VECSEL made of an active metasurface and a slab output coupler. (b-c) The conceptual idea of Vernier frequency selection in a compound cavity. Blue curves represent the output coupler reflectance; black dashed lines label the frequencies of longitudinal modes supported in the cascaded cavity. At a specific condition of $L_c \sim n_r L_{OC}$, each longitudinal mode "sees" a similar output coupler reflectance and therefore has a similar lasing threshold.

all the longitudinal modes (black dashed lines) will be shifted with respect to the output coupler reflectance, resulting in the shifting and hopping of the lasing mode.

Alternatively, if a thick output coupler is used in combination with a certain external cavity length, where $L_c \sim n_r L_{OC}$, the FSR of the cavity longitudinal modes (black dashed lines) nearly matches the periodic output coupler spectrum (blue curve). In this case, each mode experiences similar output coupler reflectance and requires similar values of gain to lase as shown in Figure 2.1.1(c). Though gain still clamps at the lowest threshold value due to a lack of SHB, now there are multiple longitudinal modes that obtain sufficient gain and are able to lase at the same time. In real experiments, the frequency dependence coming from metasurface reflectance should also be taken into consideration, as well as the diffraction loss. This leads to the shift of external cavity length L_c with respect to $n_r L_{OC}$ to reach a condition where compensation between the output coupler reflectance and active metasurface reflectance seen by each longitudinal mode is achieved; this enables multiple modes with similar lasing threshold to lase simultaneously. A more detailed analytical model will be developed in Section 2.3.

2.2 Experimental demonstration

In order to promote more lasing modes through Vernier selection and reflectance compensation, a long external lasing cavity is desired in combination with thick substrate output couplers. The metasurface used in the following experiments is labeled VA1035-TM_{03}. It is based on a TM_{03} resonance design for high output power [125], where the width of each ridge antenna (32.5 μm) is approximately three half-wavelengths at resonance, while the ridge period is 65 μm. The metasurface was designed to be resonant at 3.75 THz, which is close to the peak gain frequency of the QC-active material (wafer number is VA1035). The size of the metasurface was deliberately made larger than previous demonstrations — 5 $\times$ 5 mm^2 in overall area where electrical bias is applied to a central circular area of 2.4 mm

in diameter. This large dimension is needed to reduce the diffraction loss in a plano-plano cavity and allows long external cavity lengths up to 12 mm. However, it comes at the cost of large power dissipation, and the device can only operate in pulsed mode with 0.5% duty cycle (1 μs pulses at 5 kHz repetition rate).

Modeling of the metasurface reflectance and reflection phase spectra was performed using full-wave 2D finite-element (FEM) electromagnetic simulations (Ansys HFSS) and is plotted in Figure 2.2.1(a). In FEM simulation, the metasurface is assumed to be infinite in extent, where a single metasurface period is simulated with periodic boundary conditions. Simulated losses in the metal thin films are estimated using the Drude model ($n_{Au} = 5.9 \times 10^{22}\,\mathrm{cm}^{-3}$, $\tau_{Au,77\,K} = 39\,\mathrm{fs}$ [137]), while a constant $30\,\mathrm{cm}^{-1}$ of frequency-independent material gain is loaded in the semiconductor layer for simplicity.

2.2.1 Reference experiment using a thin output coupler

For comparison, the metasurface was first paired with a typical thin quartz output coupler — inductive Ti/Au mesh (10 μm period and 4 μm wide lines, labeled as P10-A4) is evaporated on a 100 μm-thick double-side-polished quartz substrate. Its experimental and FEM-simulated transmittance is plotted in Figure 2.2.1(b), where at 3.75 THz transmittance around 2% is measured. The output coupler was mounted inside the cryostat on a single-axis piezoelectric stepping stage (Attocube ANPx311) that can be used to adjust the cavity length. The light and voltage vs. current ($L-I-V$) curves are plotted in Figure 2.2.1(c), where the power was collected with a pyroelectric detector (Gentec), and the absolute power levels were measured using a calibrated thermopile. The threshold current density is J_{th} = 448 A/cm^2, and the linear slope efficiency (dP/dI) is 192 mW/A (calculated by considering the 67% transmittance through the 3 mm-thick polyethylene cryostat window). The observed dynamic range was limited by the current limit (14 A) of the pulse generator; as a result, larger powers could in principle be obtained. The lasing spectra were measured

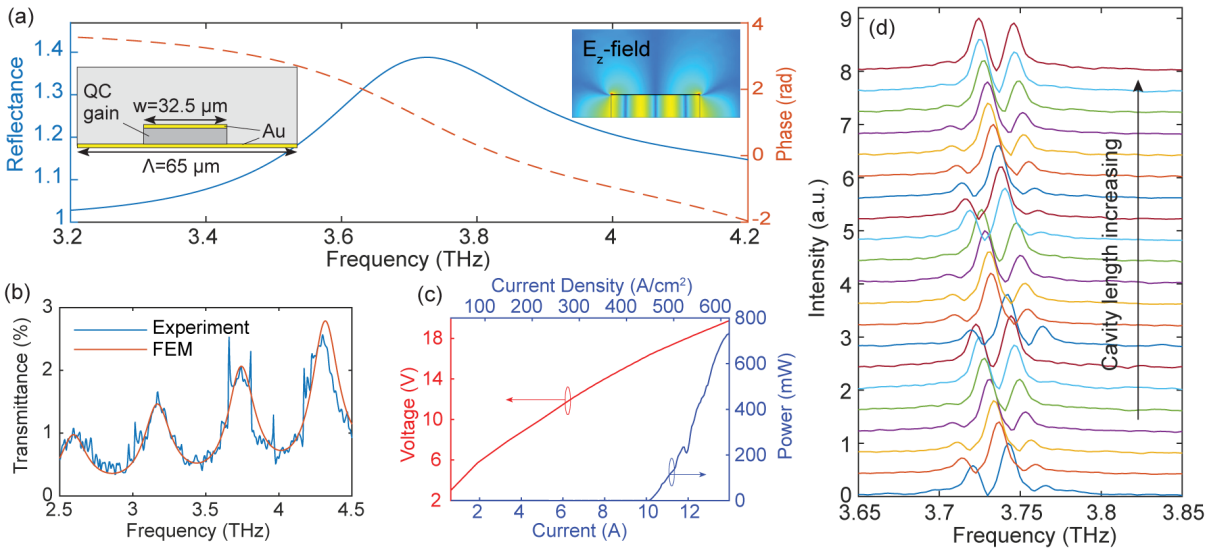

Figure 2.2.1: (a) FEM simulated reflectance (blue) and reflection phase (red dashed) spectra of the amplifying TM_{03} metasurface, where constant $30\,\mathrm{cm}^{-1}$ of material gain is applied. (b) Experimental transmittance spectrum (blue) and analytical fitting (red) of the thin quartz output coupler (P10-A4). (c) Pulsed L–I–V characteristics. (d) Normalized FTIR spectra at different cavity lengths, tuned by an intra-cryostat piezoelectric stage (offset for clarity). The device was biased at 12.6 A at 77 K.

using a commercial FTIR (Nicolet 8700) with a resolution of $0.25\,\mathrm{cm}^{-1}$, as shown in Figure 2.2.1(d). By stepping the piezoelectric stage, the lasing spectra were tuned between 3.71 THz and 3.76 THz with an FSR of 21 GHz, which indicates a cavity length of $L_c \approx 7$ mm. Despite such a long cavity length, only two or three lasing modes were observed, spanning at most ∼50 GHz — much narrower than the bandwidth of the metasurface (FWHM ≈ 300 GHz) and underlying gain material (∼1 THz).

2.2.2 Multimode operation promoted by Vernier selection

In order to promote multimode lasing, we replaced the thin quartz mesh output coupler with an output coupler using a thick high-resistivity silicon substrate ($L_{OC} = 2.07$ mm) and a lower-reflectance metallic pattern (13 μm period and 3 μm wide lines, labeled as P13-A3). The external cavity length was adjusted to satisfy the condition $L_c \approx n_r L_{OC}$, at which point the longitudinal modes of the cavity are approximately spectrally aligned with the reflectance

peaks of the output coupler.

The experiment lasing spectra at different output coupler positions, i.e., external cavity lengths, are plotted in Figure 2.2.2(a-b), where we can see that at a specific external cavity length, the system suddenly shifts from two-mode lasing to multimode lasing, with dense lasing modes shifting towards higher frequencies and covering over 170 GHz frequency range. This phenomenon is sensitive to the external cavity length and disappeared as L_c was changed by only a few microns. It is also repeatable: the lasing modes will hop back to their original frequencies, displaying dense multimode spectrum, once the cavity length was adjusted by around half-wavelength distances. The lasing spectrum with the most lasing modes is plotted in Figure 2.2.2(c) in log scale. We can distinguish at least nine lasing modes ranging from 3.77 THz to 3.94 THz, with an FSR around 21 GHz. The frequency spacing between adjacent modes does not appear to be exactly equidistant due to the extra frequency-dependent phase

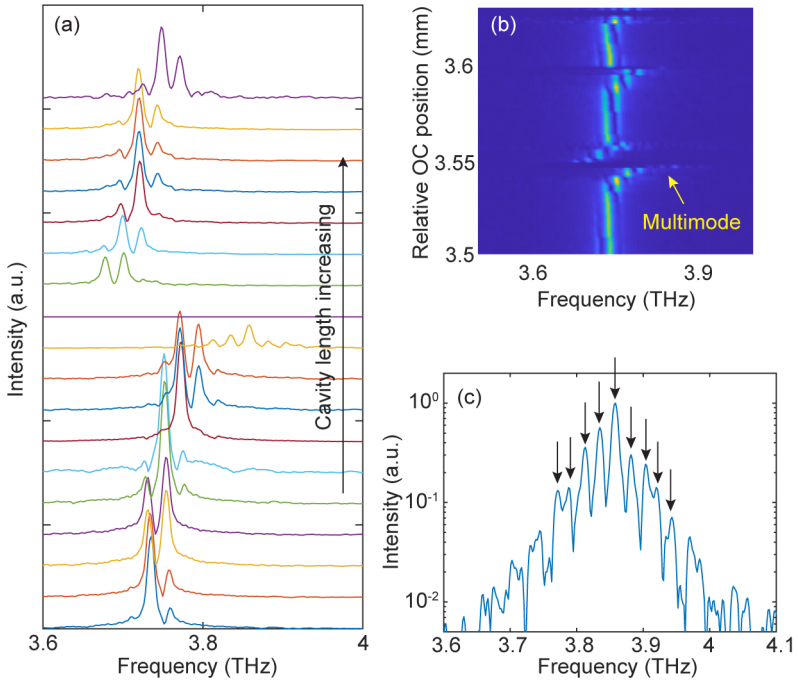

Figure 2.2.2: (a-b) Color plot and normalized lasing spectra (offset for clarity) measured at different cavity lengths. The device was biased at 12.6 A. The yellow arrow in (a) points out the cavity length where a sudden emergence of multiple lasing modes was observed. (c) Log scale lasing spectra with up to nine lasing modes.

shift provided by the QC-metasurface, while the exact values are not measurable due to the limited resolution of 7.5 GHz of the Nicolet FTIR. This is the first demonstration of dense multimode operation in a free-running QC-VECSEL.

This multimoding phenomenon is repeatable using different output couplers, both of different thicknesses and of different reflectances. For example, we consider a 2.07 mm-thick silicon output coupler with a much more reflective mesh (P10-A4). Figure 2.2.3(a) plots the lasing spectra at varying applied bias currents, ranging from a value slightly above the lasing threshold ($I_{th} = 10.7$ A) to almost the maximum bias provided by the 14 A pulse generator (13.5 A). At lower biases, the amplification factor provided by the QC-metasurface

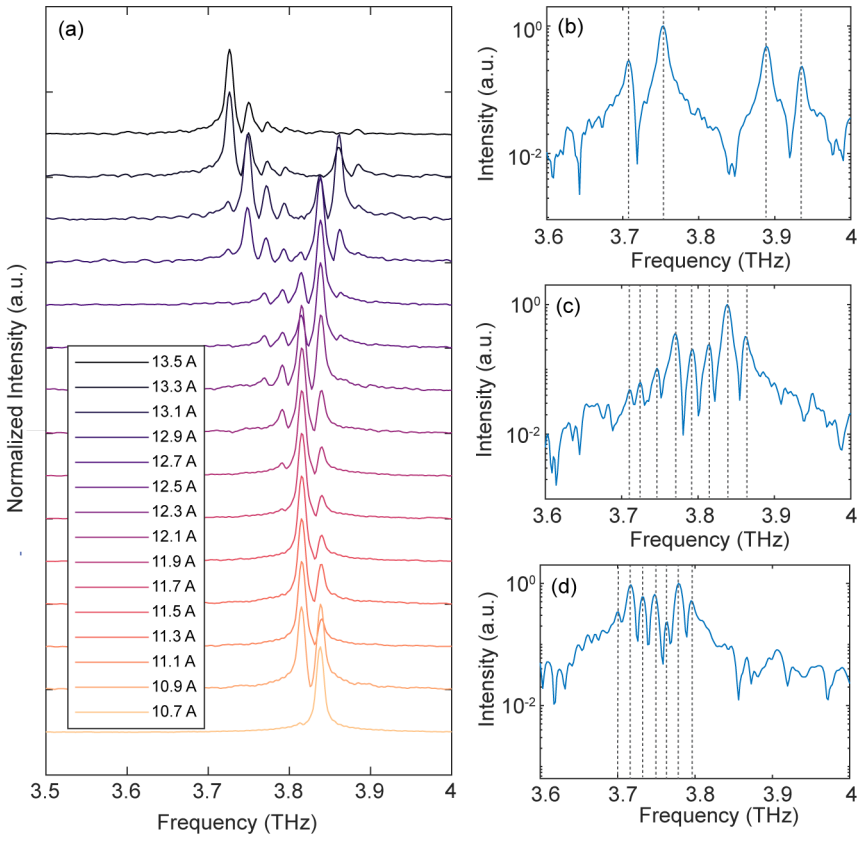

Figure 2.2.3: (a) Normalized lasing spectra at the cavity length supporting multiple lasing modes measured under different bias currents (offset for clarity). A more reflective output coupler was used with the metallic pattern P10-A4 and a 2.07 mm-thick silicon substrate. (b-d) Log scale lasing spectra with multiple lasing modes using silicon output couplers with thicknesses of 1 mm, 2 mm, and 3 mm, respectively.

is smaller and can only support lasing mode around metasurface resonance, resulting in single-mode operation. As the applied bias increases, more lasing modes are observed, and the multimode regime appears to split into two in the spectra — a phenomenon similar to the Risken-Nummedal-Graham-Haken (RNGH) instability that has been observed in mid-IR QC-laser [138].

On the other hand, Figure 2.2.3(b-d) compares the experimental spectra measured using silicon output couplers with three different thicknesses: 1 mm, 2 mm, and 3 mm. The same inductive metallic mesh (P10-A4) was applied to all three output couplers, among which the one with a thickness of 2 mm is the same one as used in Figure 2.2.3(a). In each case, a specific cavity length is chosen to maximize the number of lasing modes; the cavity lengths are 3.2 mm, 6.9 mm and 9.2 mm, respectively, estimated from the FSRs shown in the spectra: 47.0 GHz, 21.7 GHz and 16.3 GHz. It is noteworthy that when we use a thicker output coupler, the number of lasing modes does not increase correspondingly; the reason will be discussed in Section 2.4.1.

2.3 Analytical multi-section cavity model

To analyze how lasing modes develop as the relative position of the thick output coupler is tuned, we develop a simple multi-section cavity model that self-consistently calculates cavity resonant frequencies ν_m and their threshold gain coefficients $g_{th,m}$ at various external cavity lengths L_c, based upon the complex reflection coefficients of both the metasurface and output coupler. The effective reflectance of the output coupler seen by the intra-cavity circulating field is modeled using transmission line theory as:

$$R_{OC} = \Gamma_{OC}^2 = \left| \frac{Z_{OC} - Z_0}{Z_{OC} + Z_0} \right|^2 . \tag{2.3.1}$$

where Z_0 and Z_{OC} are the impedances of free space and output coupler, respectively; considering FP oscillations in its thick substrate, Z_{OC} has an expression of:

$$Z_{OC} = \frac{1}{\frac{1}{Z_{in}} + \frac{1}{Z_{mesh}}}, Z_{in} = \frac{Z_0 + jZ_r \tan(n_r k_0 L_{OC})}{Z_r + jZ_0 \tan(n_r k_0 L_{OC})} \tag{2.3.2}$$

where $Z_r = Z_0/n_r$ is the intrinsic impedance of the output coupler substrate, for which we use a refractive index of $n_r = 3.418$ for high-resistivity silicon at THz frequencies [139]. L_{OC} is the thickness of the output coupler and is measured at 2.07 mm using a micrometer caliper. The sheet impedance of the inductive mesh is chosen to be $Z_{mesh} = j60\,\Omega$ for pattern P13-A3, to fit the experimental output coupler transmittance (Figure 2.2.1(b)).

On the other hand, the spectral response of the metasurfaces is commonly characterized by FEM simulation, as plotted in Figure 2.2.1(a) under a constant intersubband gain. The metasurface reflectance changes from absorbing to amplifying as the gain coefficient loaded in the semiconductor layer increases. It can be described by an analytical model as [122]:

$$R_{MS} = e^{\xi(\nu)(g - g_{tr})}, \tag{2.3.3}$$

where g_{tr} is the transparency gain coefficient needed to balance material losses (from the metal and semiconductor) so that $R_{MS} = 1$, and $\xi(\nu)$ is an effective interaction length that contains the metasurface spectral response. Here, the values of these parameters are chosen to match the results from FEM simulations: $g_{tr} = 7\,\mathrm{cm}^{-1}$; $Q = 9.35$; $\omega_0 = 2\pi \times 3.73\,\mathrm{THz}$ and at metasurface resonance frequency $\xi_0 = 0.013\,\mathrm{cm}$.

In the compound laser cavity, the lasing threshold of each longitudinal mode $g_{th,m}$ can be easily determined based on the condition:

$$R_{MS}(g_{th,m}) R_{OC} T_{diff} = 1. \tag{2.3.4}$$

T_{diff} is the intra-cavity transmittance factor that accounts for the round-trip diffraction loss and is neglected here, i.e., $T_{diff} = 1$. The threshold gain coefficients $g_{th,m}$ are the material gain needed for the QC-metasurface to obtain an amplification large enough to compensate for the output coupler reflection loss for the longitudinal mode of index m. They can therefore be obtained according to Eqs. 2.3.1, 2.3.2, 2.3.3, 2.3.4, where the frequencies of longitudinal modes supported in the cascaded cavity are given by the following resonance condition:

$$2k_0L_c - \phi_{MS} - \phi_{OC} = 2m\pi. \tag{2.3.5}$$

ϕ_{MS} and ϕ_{OC} represent the phase shifts provided by the metasurface and the output coupler, respectively. k_0 is the free-space wavenumber, L_c is the length of the external cavity, and m is the integer mode index. This multi-section cavity model determines the lasing threshold of each longitudinal mode. To incorporate the effects of gain clamping phenomenologically, we assume that at least one mode with the lowest lasing threshold $g_{th,min}$ always lases, at which point the QC-gain clamps at $g_{cutoff} = g_{th,min} + \delta g$. The hypothesis is made that all the modes with calculated threshold gain coefficients lower than g_{cutoff} will lase due to gain clamping, while a higher offset value δg indicates a lower degree of gain clamping.

The simulated lasing spectra are plotted in Figure 2.3.1(a) with respect to various cavity lengths from 6.4 mm to 7.4 mm, where lasing modes are determined by a Vernier selection mechanism between two sets of modes generated in the external laser cavity and by the thick output coupler itself. If the two sets of modes have widely different frequency spacings (Case 1 shown in Figure 2.3.1(a)), only one cavity mode at a time sees the high effective reflectance from the output coupler, and mostly single-mode behavior is predicted. As the cavity length is varied, lasing spectra are predicted to exhibit a combination of continuous frequency tuning punctuated by mode-hopping over one FSR as well as a larger-scale mode-hopping over the metasurface bandwidth (between 3.65 THz and 3.9 THz). If the two sets of modes have nearly the same frequency spacing (Case 2), multiple longitudinal cavity modes

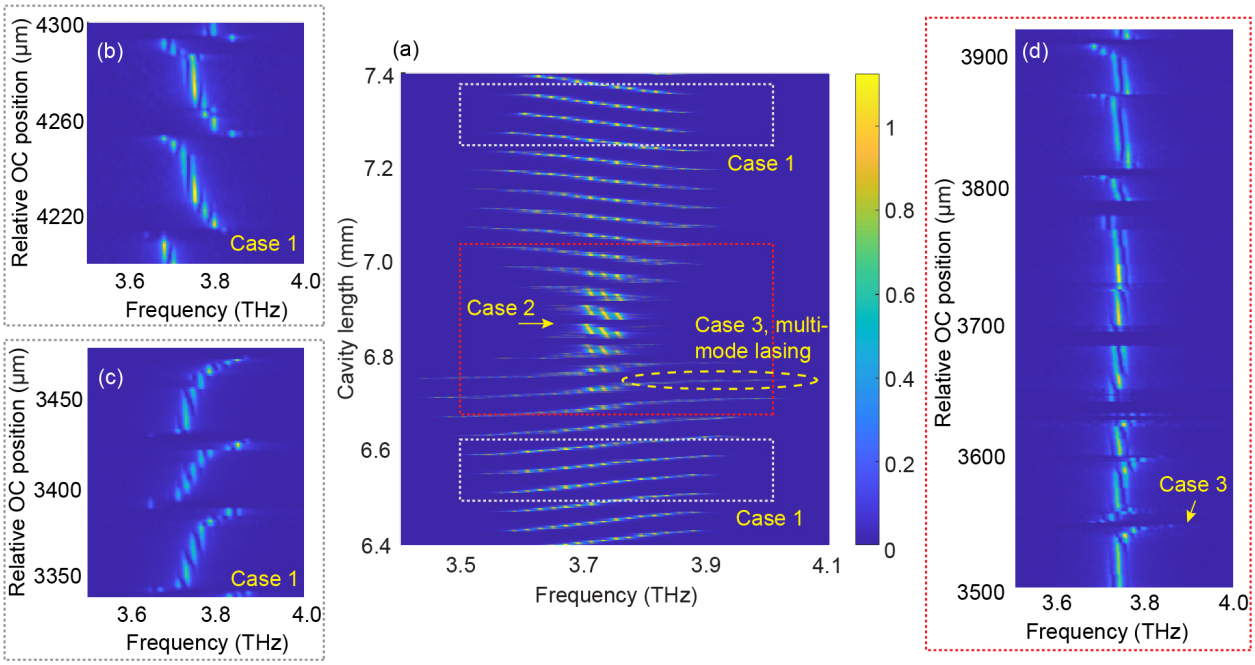

Figure 2.3.1: (a) Simulated lasing spectra of QC-VECSELs using the 2.07 mm-thick silicon output coupler at different cavity lengths. δg is assumed to be 0.15 cm^{-1}. Three cases are highlighted: gray dotted boxes represent lasing spectra in Case 1 with corresponding experimental data plotted in (b) and (c) (biased at 12.6 A); red dotted box represents lasing spectra in Case 2 with high likelihood of multimode lasing highlighted by a yellow dashed circle (Case 3) — the corresponding experimental demonstration is plotted in (d)

see similar effective output coupler reflectance, the lasing thresholds are now determined by the frequency-dependent metasurface reflectance, and those modes closest to the gain peak will lase. It should be noted that perfect matching across the entire bandwidth is impossible, as the phase dispersion of the metasurface reflection reduces the cavity FSR near the metasurface resonance. Additionally, there exist certain positions (Case 3) where the cavity lengths are slightly smaller than in Case 2, and the combination of FP modes alignment and reflectance compensation leads to a large number of modes with similar lasing thresholds. These are visualized as the multimode lasing "tails", as shown in Figure 2.3.1(a) (yellow circle). The equivalent experiment lasing spectra at different output coupler positions, i.e., cavity lengths, are plotted in dotted boxes in Figure 2.3.1(b-d). Good qualitative agreement is observed with the simulated prediction, which confirms the Vernier tuning characteristics.

Case 3 is the desired condition for multimode operation; Figure 2.3.2 shows the reflectance compensation condition in this case. In Figure 2.3.2, blue and red curves represent the analytical reflectance of the output coupler and the TM_{03} metasurface, respectively. The theoretical lasing thresholds of each longitudinal mode calculated using the multi-section cavity model are labeled as black and magenta asterisks. A cavity length of $L_c = 6.776\,\text{mm}$ is chosen to match the longitudinal resonances (vertical dashed lines) with the experimental lasing spectrum (black solid line). Magenta lines and asterisks denote those lasing modes with thresholds $g_{th} < g_{cutoff}$, while black color represents those modes with $g_{th} > g_{cutoff}$ that could not lase. It is obvious that at this specific cavity length, the output coupler reflectance seen by each longitudinal mode (blue dots) compensates for the frequency-dependent active reflectance of the QC-metasurface (red curve), which enables multiple modes with a similar lasing threshold to lase simultaneously, as experimentally demonstrated.

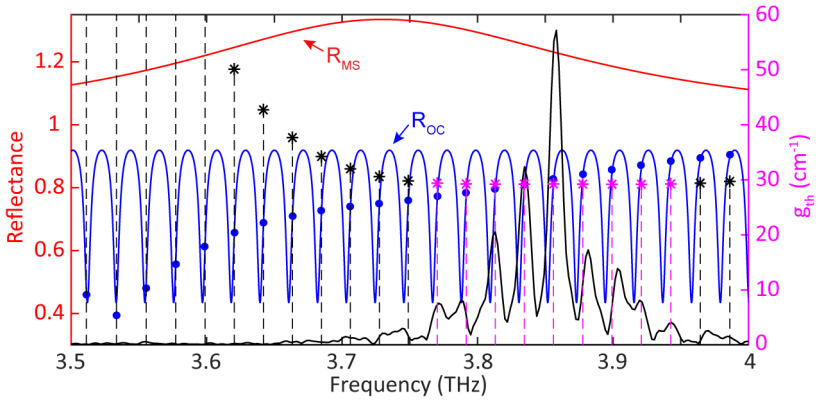

Figure 2.3.2: Comparison of experimental nine-mode lasing spectrum with analytic multi-section cavity model prediction.

2.4 Discussion

2.4.1 Effect of diffraction loss

Considering our multimode lasing spectra obtained with output couplers of different thicknesses, the multimode lasing spectrum using the 3 mm-thick silicon output coupler shows a

smaller FSR. The lasing modes, however, span over a narrower spectral range, which prevents us from obtaining a larger number of lasing modes compared with the case of using the 2 mm-thick output coupler (Figure 2.2.3 (c-d)). Our explanation is that the thicker output coupler and corresponding longer cavity length will introduce more diffraction loss, which increases the required material gain for the device to reach the lasing threshold according to Eq. 2.3.4. At the particular cavity lengths that promote multimoding, the reflectance of the output coupler and the active metasurface are both frequency dependent and they compensate to generate nearly frequency-independent lasing thresholds for several longitudinal modes. However, if the required material gain is larger and therefore R_{MS} becomes more frequency dependent (according to Eq. 2.3.3), it becomes more difficult for the R_{OC} to

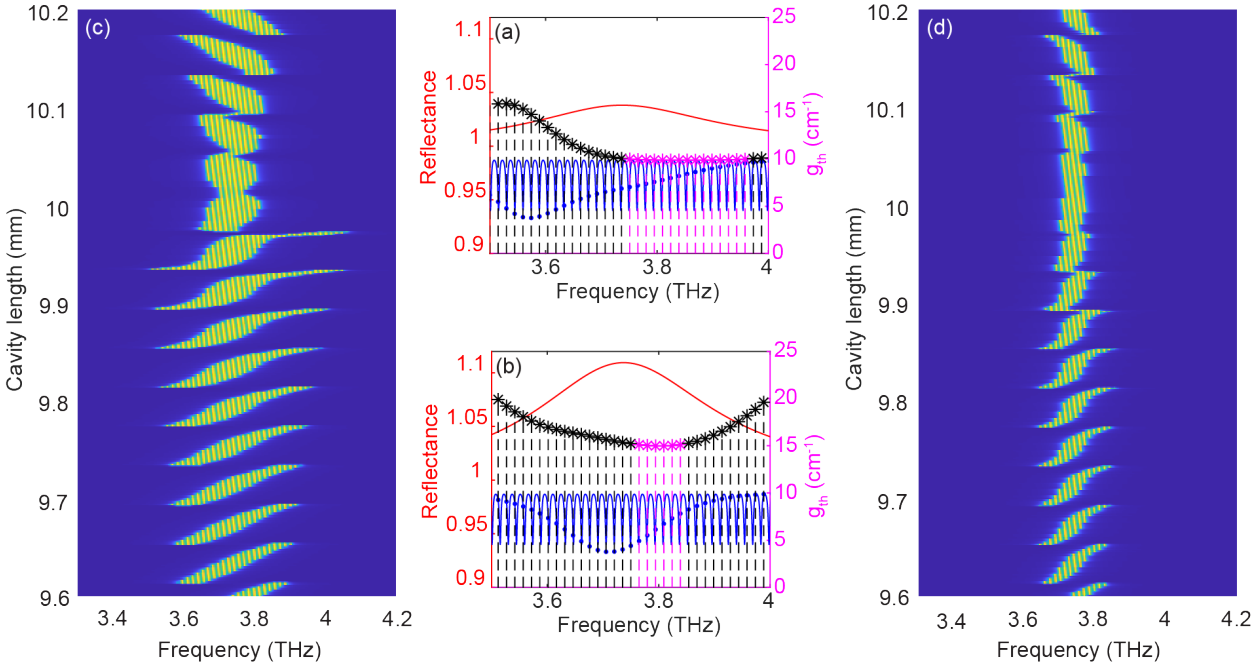

Figure 2.4.1: (a-b) Theoretical lasing thresholds of longitudinal modes supported in the QC-VECSEL assuming there is (a) no diffraction loss and (b) 5% diffraction loss per round trip. The output coupler is set to have a thickness of 3 mm and metallic mesh P10-A4. The external cavity length is chosen as 9.970 mm in (a) and 9.892 mm in (b) to maximize the number of lasing modes. Blue and red curves represent the analytical reflectance of the output coupler and that of the metasurface at the lowest lasing threshold. The values of g_{th} in magenta are those assumed to meet the lasing condition. (c-d) Simulated lasing spectra with respect to cavity length in the case of (c) no diffraction loss and (d) 5% diffraction loss per round trip.

compensate for R_{MS}. In this way, larger diffraction loss leads to more frequency-dependent $g_{th,m}$ and a smaller number of lasing modes.

This phenomenon is illustrated in Figure 2.4.1 using the same multi-section cavity model. Figure 2.4.1(a-b) plots the calculated lasing thresholds of each longitudinal mode at cavity lengths $L_c = 9.970\,\text{mm}$ and $9.892\,\text{mm}$ which are chosen to maximize the number of lasing modes; (c-d) plots the analytical lasing spectra with respect to cavity length, assuming gain offset $\delta g = 0.15\,\text{cm}^{-1}$. The output coupler is assumed with a 3 mm-thick high-resistivity silicon substrate and a high-reflectance metallic mesh (P10-A4). In Figure 2.4.1 (a) and (c), no diffraction loss is added, and in (b) and (d), diffraction loss is estimated as 5% per round trip, i.e., $T_{diff} = 0.95$. A clear decrease in the number of lasing modes is observed with the extra diffraction loss added to the model.

2.4.2 Dispersion compensation

We attribute the observation of multimode lasing to reflectance compensation between the output coupler and the active metasurface. In this section, we will discuss whether dispersion or phase compensation exists in this system. As dispersion leads to non-equidistant spacing of cavity longitudinal modes, dispersion compensation has been considered an important mechanism for frequency comb generation. According to Eq. 2.3.5, the frequency of longitudinal mode with a mode index of m is expressed as:

$$\nu_m = \frac{c}{2L}(m - \frac{\phi_{MS}(\nu_m)}{2\pi} - \frac{\phi_{OC}(\nu_m)}{2\pi}). \tag{2.4.1}$$

To obtain constant FSRs between each longitudinal mode, the total reflection phase of the metasurface and output coupler $\phi_{MS} + \phi_{OC}$ should be constant at various ν_m or a linear function of ν_m (i.e., zero GDD). Figure 2.4.2(a) plots the reflection phases of the metasurface (blue) and two output couplers (red), respectively. It is notable that the metasurface reflection phase is orders of magnitude higher than that of the output coupler. The summa-

tion of their reflection phases $\phi_{MS} + \phi_{OC}$ is plotted in Figure 2.4.2(b), which is dominated by the contribution from the metasurface and does not satisfy the condition of dispersion compensation.

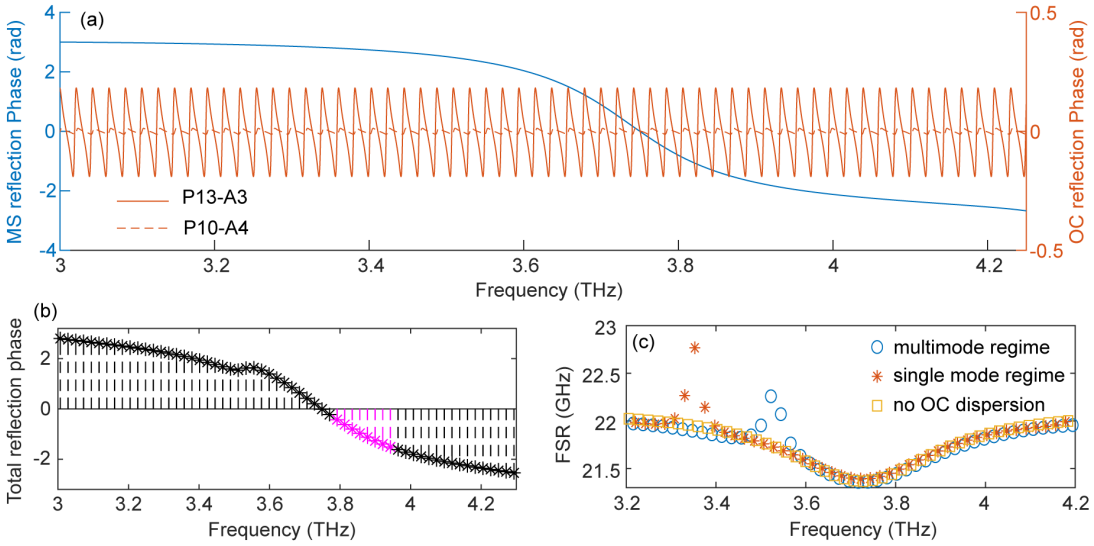

Figure 2.4.2: (a) Analytical reflection phases of the metasurface (blue) and the output couplers (red solid curve for P13-A3, red dashed curve for P10-A4). (b) Total reflection phase (in the case of P13-A3 output coupler). Black and magenta asterisks point out the cases of non-lasing modes and lasing modes. (c) Simulated frequency spacing between each two modes. Blue circles and red asterisks represent the FSRs of a QC-VECSEL when the output coupler (P13-A3) is put at the position promoting multiple and single lasing modes, respectively. Yellow squares represent the FSRs calculated in the case of no output coupler dispersion.

The dispersion of QC-metasurface leads to nonuniform frequency spacing between each two cavity modes in the multimode spectrum. The frequency spacing is plotted in Figure 2.4.2(c) with the same parameters discussed in Section 2.3. Three different cases are taken into consideration: 1) The output coupler is put at the position promoting multimode lasing ($L_c = 6.776\,\text{mm}$); 2) the output coupler is put where only one or two modes are expected to lase ($L_c = 6.765\,\text{mm}$); 3) there is no dispersion from the output coupler. In all three cases, a very similar cavity-pulling effect is observed, while the sudden increase of FSR around 3.35 THz (red asterisks) and 3.5 THz (blue circles) can be explained by adjacent cavity modes aligning with the minimum and maximum of the output coupler reflectance, which leads to

a relatively large shift in phase. This further confirms that the output coupler has little contribution to the overall cavity dispersion, and no significant dispersion compensation is achieved using this QC-VECSEL architecture.

2.4.3 Summary and limitations

In this chapter, we introduce a useful approach to promote multimode operation in QC-VECSELs by obtaining similar values of the lasing threshold for multiple longitudinal modes through Vernier frequency selection and reflectance compensation. The dense multimode operation is a promising first step for the eventual purpose of mode-locking and frequency combs; moreover, the FSR is reduced to a range readily accessible for RF beat-note measurement and RF injection locking using modest instrumentations.

However, the full potential of applying this method in frequency comb research has not been fully explored, limited by the plano-plano cavity architecture. First, large-sized metasurfaces are required for acceptable diffraction loss in a plano-plano cavity, which, however, precludes CW operation in such metasurfaces. Second, the maximum available output coupler thickness sets a limit on the number of lasing modes. However, because of increased diffraction loss in a correspondingly longer plano-plano cavity, a thicker silicon output coupler may not produce more lasing modes; additionally, there is a good chance that the diverging beam will go off the edge of a thicker silicon substrate and introduce additional loss into the VECSEL cavity. Thus, in Chapter 3, we will present a novel focusing cavity architecture of QC-VECSELs. It gets rid of the limitations of plano-plano cavities and will serve as the dominant platform for future frequency comb/mode-locking applications. The feasibility of adapting this method to focusing QC-VECSELs will be discussed in Chapter 4, along with some preliminary experimental results.

Chapter 3

Intra-cryostat focusing cavity design

3.1 Introduction

So far, the demonstrations of QC-VECSELs have been limited to simple plano-plano cavities using flat optics. This is the most straightforward method since spherical output coupler mirrors are not readily available in the THz frequency range. Furthermore, since THz QCLs do not operate at room temperature, the external cavity should be built entirely within the cryostat to avoid excess atmospheric losses and etalon effects from a cryostat window. However, due to increasing diffraction loss, the maximum plano-plano cavity lengths have been limited to ∼10 mm [136]. This was only achieved by using a metasurface with a large central circular bias area of diameter 2.4 mm, as discussed in the previous chapter, where CW operation is not allowed due to excess current draw and heat dissipation. An alternative method is using a planar focusing QC-metasurface; such an approach results in a large spot on the metasurface and a small spot on the output coupler, still requiring a large metasurface device. Also, such designs are based upon resonant metasurface elements and thus are not suitable for broadband applications [123].

Here, encouraged by versatile cavity architectures of VECSELs in solid-state communities

[140], a similar V-cavity QC-VECSEL has been introduced by inserting an off-axis paraboloid (OAP) mirror into the VECSEL cavity. The illustration of the cavity is shown in Figure 3.1.1, in which a planar thin output coupler is positioned perpendicular to the optical axis of the OAP mirror and an active QC-metasurface is placed at the focal point of the mirror to generate a resonant laser cavity. In this case, the intra-cavity diffraction loss has been significantly reduced or canceled, CW lasing using small-sized metasurfaces in an external cavity length over 30 mm has been demonstrated, while the tunability of the external cavity is preserved, and excellent performance has been reported, such as high output power, low current consumption, low divergence beam patterns, and narrow free-running linewidth [141].

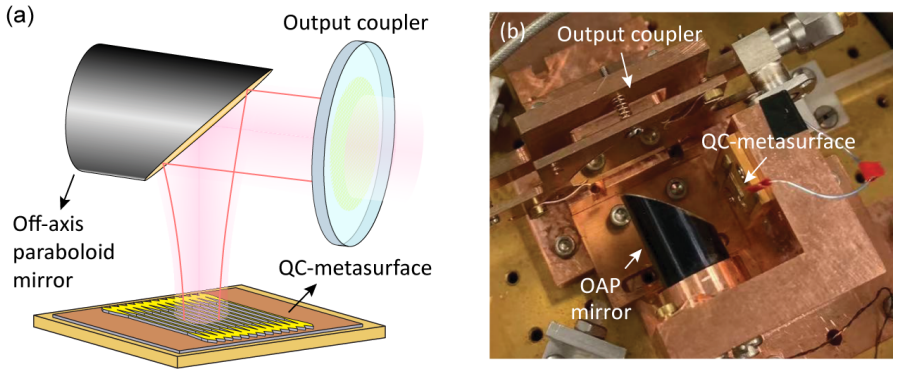

Figure 3.1.1: (a) Schematic of the QC-VECSEL based on an intra-cryostat OAP-focusing cavity design. (b) Top view of the cavity in the cryostat.

In terms of frequency comb realization, the benefits of this OAP-focusing QC-VECSEL design are twofold: 1) The long external cavity allows more modes to be accommodated in a given gain bandwidth with an FSR accessible using modern RF instrumentations; 2) CW operation gets rid of the noise and fluctuation coming from pulsing equipment.

3.2 Theoretical analysis

3.2.1 Comparison between plano-plano and OAP-focusing cavities

To quantify the intra-cavity diffraction loss in VECSEL cavities and make comparisons between traditional plano-plano cavities versus OAP-focusing cavities, we constructed a 2D full-wave electromagnetic external cavity eigenmode simulation using COMSOL Multiphysics (Figure 3.2.1). The metasurface we used in the simulation model and also in the following experiments is labeled VB0739-SR. It is loaded with 10 μm-thick QC-wafer that was grown at Sandia National Labs with wafer number VB0739. The metasurface is spatially uniform across the $1.5 \times 1.5\,\mathrm{mm}^2$ area, while electrical bias is selectively applied to a small central circular area of diameter $d = 0.4\,\mathrm{mm}$ for reduced injection current. The array of MM ridge antennas is designed with a ridge width of 12.2 μm and a period of 41.7 μm for a resonance around 3.3 THz. Its amplification factor is characterized using regular FEM reflectance simulation (Ansys HFSS) as described in Section 2.2, where Drude loss and constant intersubband gain are assigned to the metal and semiconductor layers, respectively. By numerically fitting the simulated R_{MS} with respect to the intersubband gain coefficient g according to Eq. 2.3.3, a transparency gain coefficient of $g_{tr} = 5.2\,\mathrm{cm}^{-1}$ is obtained, which characterizes the value of material loss in the metasurface. This value will also be used as a benchmark for comparing the threshold gain needed for lasing in different external cavities.

The cross-section of the above-mentioned metasurface is modeled in the 2D external cavity eigenmode simulation, which accounts for the finite dimension of the metasurface along one axis and assumes infinite length along the ridges. The metasurface contains 35 periods of ridge antennas, where only the central 9 antennas are selectively biased and loaded with uniform QC-gain. The same metal losses are applied as in the reflectance simulation. The threshold QC-gain coefficient g_{th} is defined as that needed to make the cavity eigenfrequency fully real (i.e., no net loss or gain). For simplicity, the output coupler is modeled as a perfect electric conductor (PEC) boundary to form an external cavity with adjustable cavity

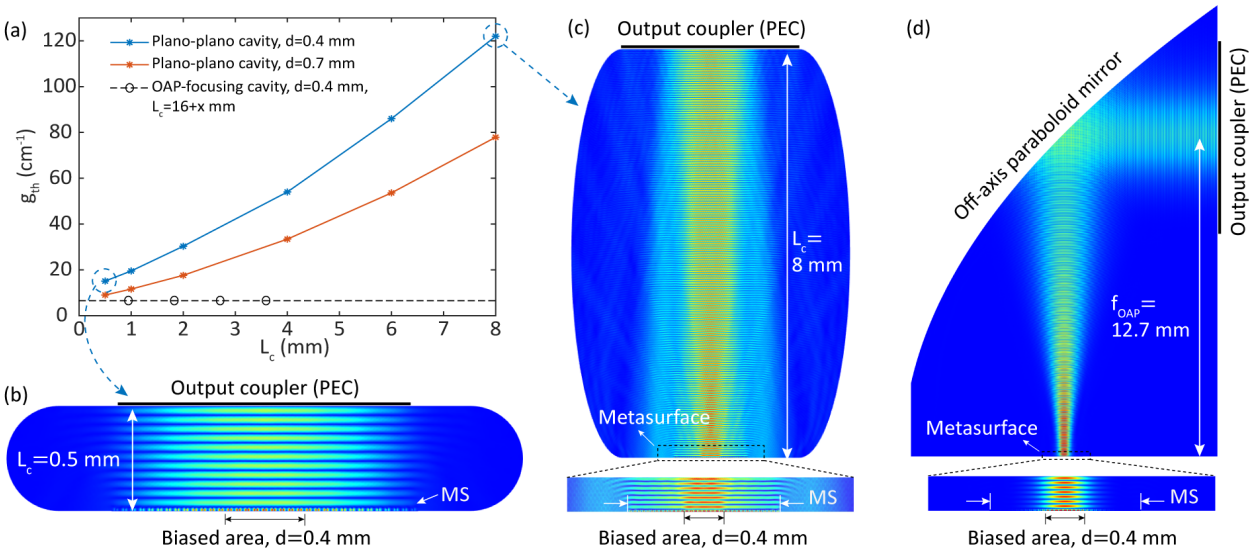

Figure 3.2.1: (a) Simulated threshold gain coefficients with respect to external cavity lengths in plano-plano cavities. In the FEM simulation, 35 ridge antennas are modeled with a total length of around 1.5 mm, while only the central 9 (blue curve) or 17 (red curve) antennas are selectively biased, corresponding to a bias diameter of 0.4 mm or 0.7 mm. (b-c) E-field plots of FEM-simulated plano-plano cavities with cavity lengths of 0.5 mm and 8 mm, in the case of using a 0.4 mm bias diameter metasurface. The absorbing boundaries will collect the diffracted light, which contributes to the intra-cavity diffraction loss. (d) E-field plot of FEM-simulated OAP-focusing cavity with a cavity length of 18.7 mm and bias diameter of 0.4 mm, which clearly shows the improvement in light diffraction. The value of g_{th} simulated with a cavity length of $16+x$ mm is pointed out by the black circles in (a) for better comparison.

lengths. As a result, this simulated g_{th} does not include losses from realistic output couplers; instead, it only includes metasurface and diffraction losses. In Figure 3.2.1(a), the QC-gain coefficients needed to compensate for overall losses in plano-plano cavities are plotted as a function of external cavity length ranging from 0.5 mm to 8 mm. As expected, g_{th} increases dramatically with respect to L_c and exceeds 100 cm^{-1} for a cavity length of 8 mm, indicating that lasing is prohibited in such a VECSEL cavity (blue curve). This trend actually describes two entangled "diffractive" effects: (1) the general increase in the cavity eigenmode spot size that increases its overlap with the unbiased area of the metasurface, and (2) the increase of scattering losses out of the cavity eigenmode. By enlarging the bias diameter to $d = 0.7$ mm, i.e., selectively adding gain to the central 17 antennas, g_{th} as well as round-trip losses are

reduced, showing a slower increase with respect to L_c (red curve). However, the dissipated heat would increase by a factor of three as a tradeoff because of the quadratic dependence of the current draw on the bias diameter

As a comparison, we introduce a curved PEC facet mimicking an OAP mirror into the simulation model and center the biased area at its focal point (Figure 3.2.1(d)). The threshold gain coefficient is then reduced to a reasonable value of $g_{th} = 6.5\,\mathrm{cm}^{-1}$ for a cavity length over 16 mm and stays constant at longer cavities. This is a value smaller than any plano-plano cavity results and only slightly higher than the transparency gain of the active metasurface ($g_{tr} = 5.2\,\mathrm{cm}^{-1}$). It is equivalent to an excess loss of 1% per round trip in this 2D model — an actual 3D cavity would exhibit approximately twice that. Furthermore, it is worth noting that these values are highly dependent on the absorbance in the unbiased region of the metasurface. For example, in our FEM simulations, we assume only metal losses are loaded in the unbiased antennas (to be active region "agnostic"). However, in a real case, there may exist strong absorption losses coming from intersubband resonance within the active material [142], which will exacerbate the round-trip losses in a plano-plano cavity [142], [143].

3.2.2 Alignment tolerance of the OAP-focusing cavity

For the best performance of the OAP-focusing cavity in reducing diffraction loss as well as lasing threshold, both the QC-metasurface and the output coupler should be perfectly aligned with respect to the OAP mirror, i.e., the center of the bias circle should be placed at the focus point of the OAP mirror, and the output coupler should be perpendicular to the optical axis of the OAP mirror. Any misalignment will result in degradation in the lasing performance. Here, we assume that an increase of $5\,\mathrm{cm}^{-1}$ in the lasing threshold will result in the cessation of lasing, i.e., when g_{th} rises from $6.5\,\mathrm{cm}^{-1}$ to $11.5\,\mathrm{cm}^{-1}$, the metasurface amplification will not be enough to compensate for the overall losses. In this

case, we simulated how much the cavity could tolerate against output coupler rotation and metasurface displacement in both horizontal and vertical directions. 2D full-wave eigenmode simulation (COMSOL Multiphysics) shows that with a QC-gain of 11.5 cm^{-1} the maximum allowable displacement of the metasurface is $\pm 150\,\mu$m in the horizontal direction, and ± 1 mm in the vertical direction; the maximum rotation angle of the output coupler is $\pm 0.5\,^{\circ}$ (Figure 3.2.2(a-c)). The corresponding beam profile collected at the plane above the metasurface in each case is plotted in Figure 3.2.2(d-f). It is noted that bad alignment causes the beam profile to overlap more with the unbiased region and metasurface edge, which adds up to the intra-cavity overall losses. If there exists significant intersubband absorption loaded in the

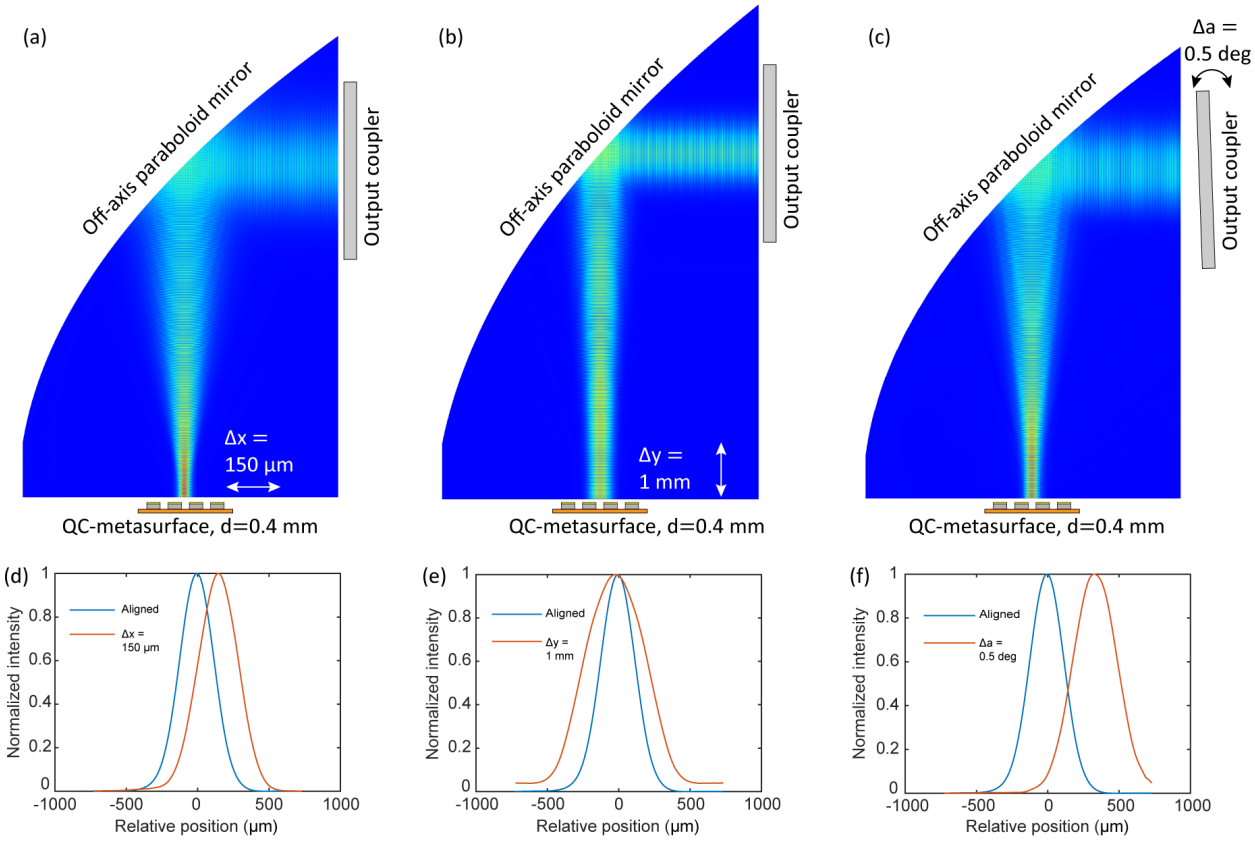

Figure 3.2.2: (a-c) E-field plots of the FEM-simulated OAP-focusing cavity and (d-e) corresponding 1D intensity distribution at the plane above the metasurface. The central 9 out of 35 antennas are loaded with QC-gain of 11.5 cm^{-1}. (a,d) The maximum displacement of the metasurface in the horizontal (x) direction is 150 μm to obtain a fully real eigenfrequency. (b,e) The maximum displacement in the vertical (y) direction is 1 mm. (c,f) The maximum rotation angle of the output coupler is $0.5\,^{\circ}$.

unbiased region, the alignment tolerance will be worse [142]. It will help if the biased area has a larger dimension.

3.3 Experimental demonstration of laser performances

3.3.1 $L-I-V$ and temperature performance

The metasurface VB0739-SR was positioned in the OAP-focusing cavity with a cavity length of ∼30 mm for experimental characterization. The output coupler used has a reflectance of $R_{OC} \approx 95\%$ (P13-A3), and the OAP mirror has a focal length of 12.7 mm. Alignment of the output coupler takes place at room temperature with the aid of a He-Ne laser; alignment is preserved following cooldown within a liquid-nitrogen cooled vacuum cryostat (see Appendix for alignment details). The resulting QC-VECSEL has been experimentally characterized in both CW mode and pulsed mode with 0.5% duty cycle (500 ns pulses at 10 kHz repetition rate). The $L-I-V$ curves are plotted in Figure 3.3.1 at various temperatures.

The output power was collected using a pyroelectric detector (GentecEO) and is measured as 20 mW and 11.5 mW at 77 K, with a peak wall-plug efficiency of 0.8% and 0.5%, a slope efficiency of 313 mW/A and 272 mW/A in pulsed and CW mode, respectively. The reported power has been corrected based on the 65% transmittance of the 3 mm-thick polyethylene cryostat window. $L-I$ characteristics as a function of varying heat-sink temperatures (T) demonstrate that the device lases up to a maximum temperature of 132 K in pulsed mode and 105 K in CW mode. The insets of Figure 3.3.1 show the phenomenological fit to the expression $J_{th} = J_0 \exp(T/T_0)$, which results in values of $T_{0,pulsed} = 145$ K and $T_{0,CW} = 88$ K. By using a more reflective output coupler ($R_{OC} > 99\%$, P10-A4), the maximum operation temperatures increase to 145 K in pulsed mode and 111 K in CW mode, at a sacrifice of over three times smaller output powers. As a comparison, the maximum pulsed-mode operating

temperature demonstrated using the same QC-wafer (VB0739) has been measured to be 170 K in a MM ridge waveguide and 129 K for a focusing metasurface VECSEL with L_c = 2.1 mm [123]. The improved temperature performance of a QC-VECSEL designed with an OAP-focusing cavity is a clear indication that, although it still shows a larger overall loss compared with ridge waveguides, the OAP-focusing cavity enables reduced loss and better beam spot confinement in the biased area when compared to plano-plano VECSELs with more than 10× shorter cavities.

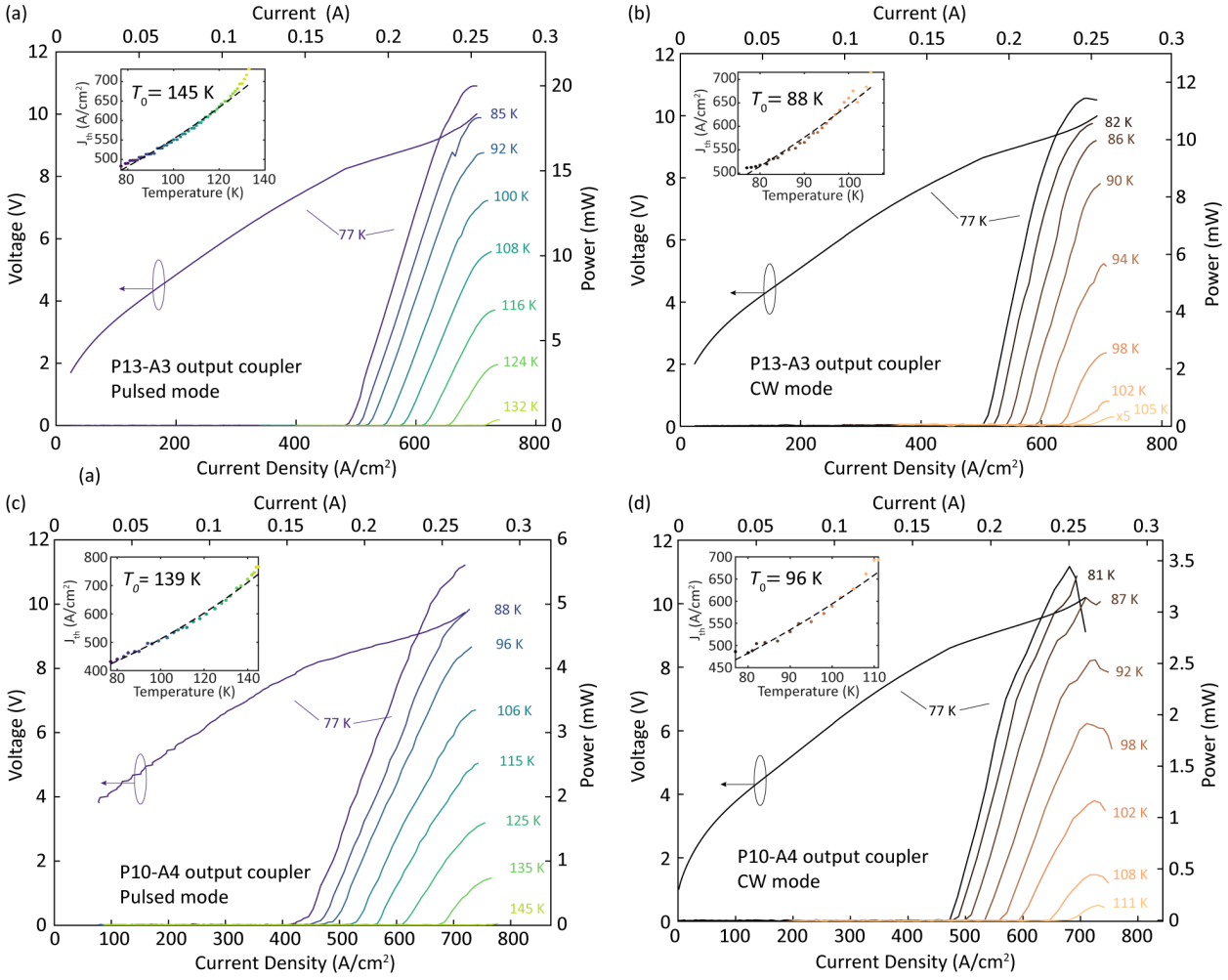

Figure 3.3.1: (a) Pulsed and (b) CW $L-I-V$ characteristics of the QC-VECSEL using an output coupler with $R_{OC} \approx 95\%$ (P13-A3). $I-V$ curves are measured at 77 K, while $L-I$ curves are collected as a function of varying heat-sink temperature T. Insets show plots of threshold current density vs. heat-sink temperature. (c) Pulsed and (d) CW $L-I-V$ characteristics of the QC-VECSEL using an output coupler with $R_{OC} \approx 99\%$ (P10-A4).

3.3.2 Lasing spectra and free-running linewidths

The emission spectra were collected using a commercial Nicolet FTIR first in pulsed mode. As shown in Figure 3.3.2, the FTIR spectra at various bias currents show FWHM bandwidth around 58 GHz. Though we are not able to spectrally resolve individual lasing modes due to the limited FTIR resolution of 7.5 GHz, it clearly indicates multimode lasing operation occurring under pulsed biasing. This multimode lasing is still present for pulse widths of at least up to 60 μs (60% duty cycle) as shown in Figure 3.3.2(c).

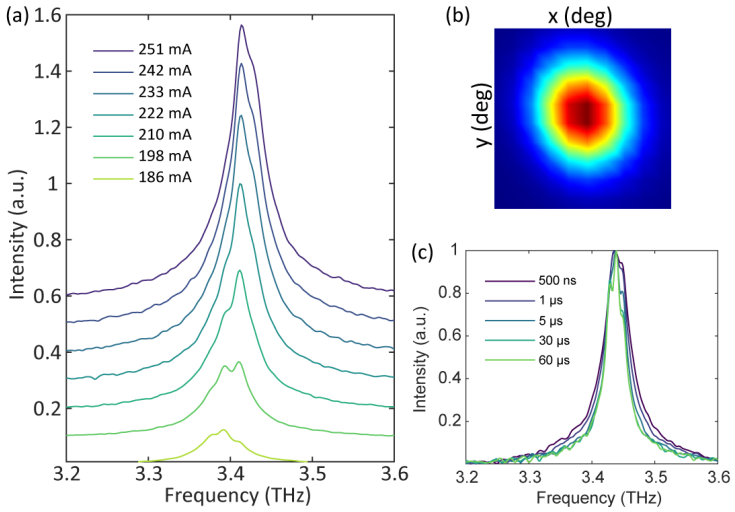

Figure 3.3.2: (a) Pulsed lasing spectra measured as a function of applied bias current at 77 K. (b) A high-quality far-field beam pattern measured in pulsed mode. It was collected using a two-axis scanning pyroelectric detector with a 2 mm-diameter aperture rotating at a constant distance of ~15 cm from the device. (c) Pulsed lasing spectra measured at a fixed repetition rate of 10 kHz and increasing pulse widths from 500 ns to 60 μs.

However, collapse to single-mode operation was observed as we switched to CW biasing. This indicates that the collapse process may take place on relatively long tens- or hundreds-μs timescales. In Figure 3.3.3(a), a single lasing peak is observed around 3.37 THz despite the fact that the gain bandwidth of the metasurface is at least 100 times larger than the FSR (5 GHz), re-emphasizing the preference of QC-VECSELs to operation in the single-mode regime. Moreover, a circular, Gaussian far-field beam profile has been demonstrated in Figure 3.3.2(b), which ensures that lasing occurs in a single transverse mode in the OAP-

focusing VECSELs.

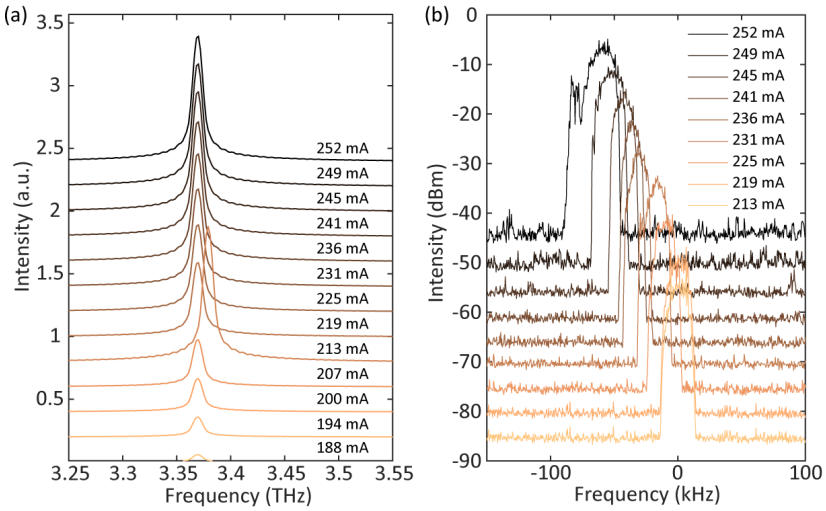

Figure 3.3.3: (a) CW lasing spectra and (b) free-running beat-notes measured as a function of applied bias current at 77 K. The beat-notes were obtained by operating the spectrum analyzer (Keysight N9020a) in the Max. Hold mode over 10 seconds with a resolution bandwidth as small as 180 Hz.

Next, we performed high-resolution spectral measurements at NASA Jet Propulsion Laboratory (JPL) with the help of Christopher Curwen. We downconverted the CW QC-VECSEL emission into the RF using a sub-harmonic Schottky-diode mixer. The mixer is a modified version of that used in Ref. [144] and is pumped by the 35_{th} harmonic of a 100 GHz local oscillator (LO). A beat-note signal was generated through frequency downconversion as $f_{BN} = mf_{LO} - f_{THz}$, where $m = 35$. It was measured using a spectrum analyzer (Keysight N9020a) with a resolution bandwidth of 180 Hz, which allowed for precise characterization of the free-running linewidth and electrical tuning of the laser emission. In Figure 3.3.3(b), the collected beat-notes are plotted at various applied bias currents whose center frequencies are subtracted for clarity. As we increased the LO frequency, f_{BN} increased accordingly, which indicates that the lasing frequency is smaller than the LO frequency. Based on accurate knowledge of the beat-note frequency, we obtain the exact lasing frequency at 3.3823347 THz with the device biased at 213 mA at 77 K. Free-running linewidths are obtained by operating the spectrum analyzer in the Max. Hold mode for over 10 seconds; the measured values

are in the range of 20–50 kHz. This value is considerably smaller than the free-running linewidths of ridge-waveguide based THz QCLs, which are typically on the order of a few MHz when measured over times of more than a few seconds and are primarily limited by temperature and current fluctuations [145]–[147]. This is expected since the QC-VECSEL is less sensitive to refractive index fluctuations of the semiconductor because the majority of its cavity mode resides within the vacuum rather than the QC-active material. This is also consistent with the fact that its electrical tuning coefficient is measured to be 1.7 kHz/mA, which is 3–4 orders of magnitude smaller than that reported for waveguide-based QCLs, or even short-cavity VECSELs.

Instead, we expect that the primary source of frequency instability lies in mechanical noise in the external cavity, e.g., mechanical vibrations of the output coupler. The experimentally observed frequency fluctuations of $\delta\nu \sim 20$–50 kHz correspond to cavity length fluctuations on the order of $\delta L \sim 1$ nm, assuming $\delta\nu/\nu = \delta L/L$. Experimental results from Ref. [148] show that a phase-locked short-cavity VECSEL exhibits many peaks in the phase noise spectrum that primarily lie between 10 Hz to 10 kHz. These noise peaks were attributed to mechanical noise in the system by the author. Although similar phase noise measurement is not possible in the OAP-focusing QC-VECSEL discussed in this chapter because it is not stabilized, its frequencies of fluctuations are generally consistent with those of mechanical noise in Ref. [148] as similar mechanical mounts of output couplers were applied. Additionally, we noted that even single spectrum analyzer scans with a 12 ms sweep time show evidence of a narrower line fluctuating over the same 20–50 kHz range. This implies the Max. Hold linewidths in Figure 3.3.3(b) are not a result of a slow drift of a narrower line over the 10-second time scale but likely originate from fluctuations at millisecond timescales or faster.

3.4 Other experimental results using different metasurfaces or output couplers

3.4.1 Double-ridge metasurface

A coupled-cavity metasurface made of two ridges with slightly different ridge widths was used in replacement of the single-ridge metasurface. The double-ridge metasurface was designed with a period of 41.7 μm and two ridge widths of 13.65 μm and 9.45 μm, the same design as reported in Ref. [126]. Compared with single-ridge metasurfaces, it exhibits a broader metasurface reflectance with FWHM over 1 THz, while providing a high amplification factor. GDD of the metasurface is kept lower than 0.2 ps^2 over a wide spectral range, as plotted in Figure 3.4.1(a). Such types of metasurfaces with three different bias diameters, i.e., d_{bias} = 1 mm, 0.4 mm, 0.3 mm, were inserted into the OAP-focusing cavity paired with a high reflectivity output coupler (P10-A4). They were tested only in pulsed mode with a 0.5% duty cycle (500 ns pulses at 10 kHz repetition rate), considering excess heat dissipation in such metasurfaces with a large fill factor of active elements. The collected pulsed $L-I-Vs$ in three cases are plotted in Figure 3.4.1(a). It is noticed that the metasurface with a smaller bias area requires a higher lasing threshold and generates lower THz power. This is expected as a result of increasing alignment difficulty or lower alignment tolerance for a smaller bias area.

Lasing spectra of the QC-VECSEL with a metasurface bias diameter of 0.4 mm are plotted in Figure 3.4.1(c-d), which indicates a broad spectral coverage benefited by the coupled-cavity design. There exist two clusters of lasing modes around 3.2 THz, and 3.7 THz, respectively. They are consistent with the non-flat spectral response of the amplifying metasurface which produces a dip around 3.6 THz in the lasing spectrum. Although we were not able to spectrally resolve all the lasing modes limited by the Nicolet FTIR resolution of 7.5 GHz, we estimate that hundreds of modes exist in the system, considering a lasing bandwidth over

500 GHz and FSR around 5 GHz. This system, i.e., an OAP-focusing cavity in combination with a broadband coupled-cavity metasurface, is considered a good platform for frequency comb operation and will be further discussed in Section 4.4.2.

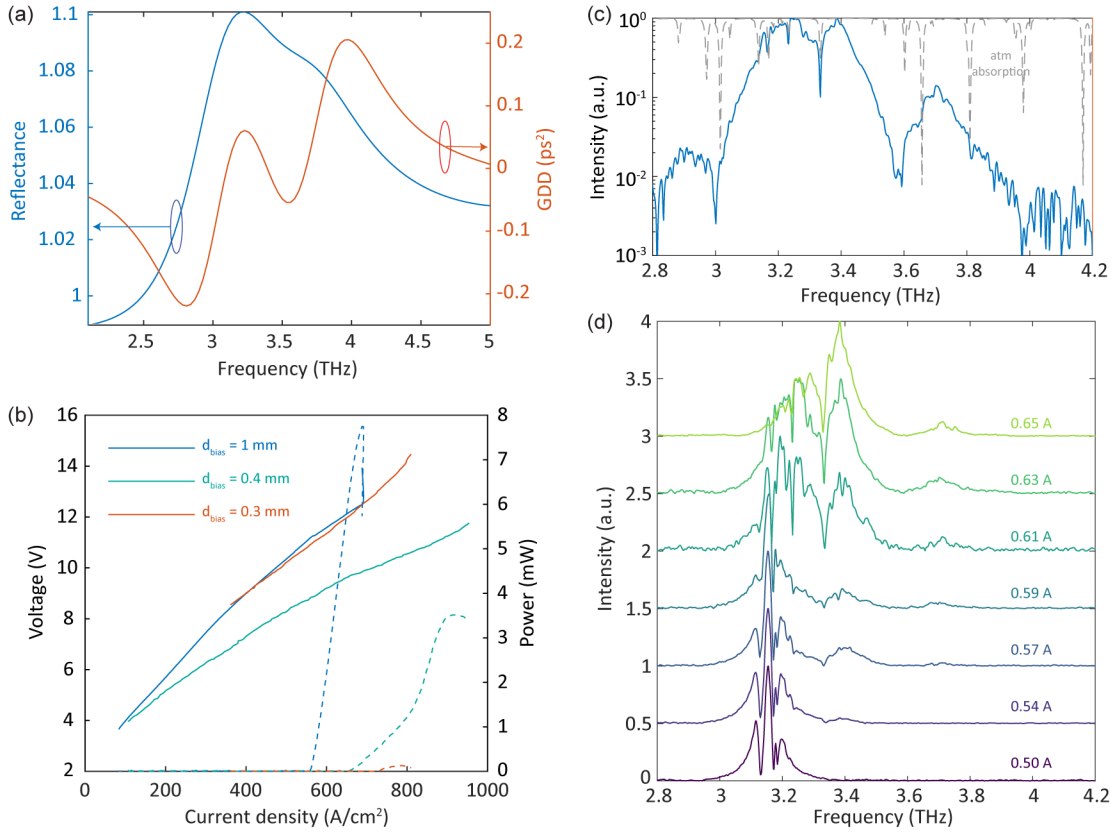

Figure 3.4.1: (a) FEM-simulated metasurface reflectance (blue) and GDD (red) of the double-ridge design. A constant gain coefficient of 30 cm^{-1} was loaded to the semiconductor layer. (b) Pulsed $L-I-V$s of the OAP-focusing QC-VECSELs made of double-ridge metasurfaces with bias diameters of 1 mm, 0.4 mm, 0.3 mm and a high reflectivity output coupler (P10-A4). (c-d) Lasing spectra of OAP-focusing QC-VECSEL with a metasurface bias diameter of 0.4 mm. (c) Log scale lasing spectrum at a bias current of 0.61 A. The grey dashed line represents atmospheric absorption. (d) Linear scale spectra at various bias currents ranging from threshold to near NDR.

3.4.2 Ultrathin parylene film output coupler

The typical QC-VECSEL output coupler is made of a metallic mesh deposited on a 100 μm-thick quartz substrate. Despite the deliberate selection of a thin substrate to mitigate FP oscillations in its reflectance spectrum, a notable dispersion stays — the FP fringe period is

approximately 700 GHz, which is still less than the lasing bandwidth of certain broadband devices (e.g., coupled-cavity metasurfaces display gain bandwidths exceeding 1 THz). To further minimize GDD coming from the output coupler for frequency comb generation, we exploit the feasibility of ultrathin output couplers using free-standing thin-film substrates. The idea originally came from flexible electronics, where electronic devices are mounted on flexible plastic substrates [149]. Some of the commonly used materials are parylene [150], PDMS [151]–[154] and polyimide [155]–[157]. These materials are transparent at THz frequencies and are therefore suitable for THz flexible metamaterials, where large optical frequency tunability has been demonstrated due to their mechanical stretchability [152]–[154].

Here, we chose parylene as the free-standing output coupler material. Around 7 μm-thick Parylene-C was coated onto silicon substrates through SCS Parylene Coater, followed by standard photolithography and metal lift-off. The parylene film with a metallic pattern (15 μm period and 2.5 μm wide lines, P15-A2.5) deposited was peeled off from the silicon substrate and fixed to an output coupler mount as pictured in Figure 3.4.2(a). This parylene output coupler was inserted into the OAP-focusing QC-VECSEL, paired with the metasurface VB0739-SR. Its $L-I-V$ was collected in pulsed mode at 0.5% duty cycle first and is compared with that of a QC-VECSEL using a standard 100 μm-thick quartz substrate output coupler with the same metallic mesh (P15-A2.5). In Figure 3.4.2(b), QC-VECSEL with the parylene output coupler exhibits a higher lasing threshold and lower output power. The possible reason is that the non-flat surface of the parylene thin film acts as an imperfect reflector and adds additional scattering losses. Its lasing spectra are plotted in Figure 3.4.2(c-e). The spectra clearly show multimode operation while at some bias currents, multiple lasing modes are separated by ~44 GHz (Figure 3.4.2(d,e)); the spectra resemble harmonic frequency combs, which have been demonstrated in ridge-waveguide QCLs, while the repetition rate is multiple times of the cavity round-trip frequency [50], [52]–[54].

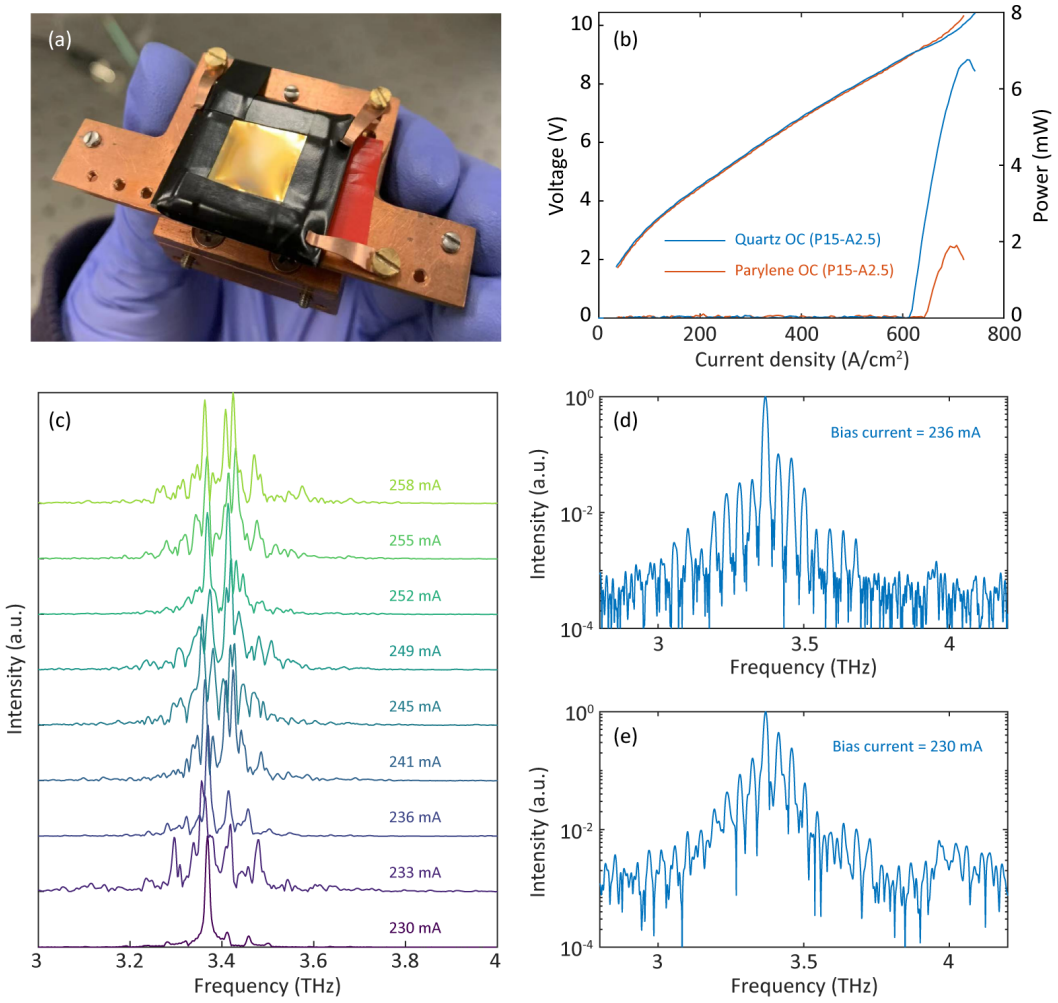

Figure 3.4.2: (a) Picture of a parylene output coupler. (b) Pulsed $L-I-Vs$ of the OAP-focusing QC-VECSELs using 7 μm-thick parylene (red) and 100 μm-thick quartz (blue) output couplers with the same metallic pattern (P15-A2.5) and the same metasurface. (c-e) Pulsed lasing spectra of OAP-focusing QC-VECSEL using the parylene output coupler. (c) Linear scale spectra at various bias currents ranging from threshold to near NDR. (d-e) Log scale lasing spectra at bias currents of 236 mA and 230 mA, which exhibit harmonic features.

Furthermore, the same QC-VECSEL was tested in CW mode, and the lasing spectra are plotted in Figure 3.4.3. In previous experiments, though multimode lasing was observed in pulsed mode, it collapsed to a single lasing mode when the device was biased continuously. On the contrary, using an ultrathin film output coupler, the multimode operation was maintained when we switched to CW biasing. Similar harmonic spectra were observed at specific bias currents ($f_{rep} \approx 9\, f_{rt}$ in Figure 3.4.3(b); $f_{rep} \approx 11\, f_{rt}$ in Figure 3.4.3(d)). Though the exact

reason leading to this phenomenon is unknown, one hypothesis is that the ultrathin film output coupler shows negligible FP oscillation and minimizes the overall dispersion in the laser cavity, which may trigger spontaneous frequency combs; further characterization will be needed to determine whether these spectra are associated with self-generated harmonic frequency combs through, e.g., beat-note extraction, higher resolution spectroscopy, and phase-sensitive measurement.

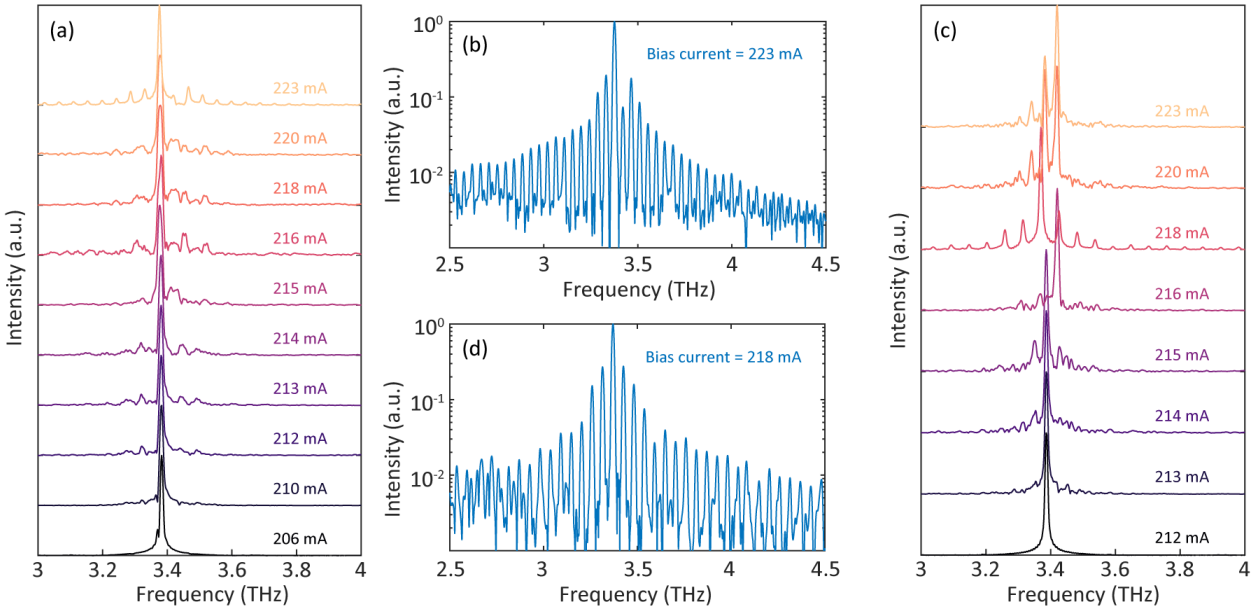

Figure 3.4.3: CW lasing spectra of OAP-focusing QC-VECSEL using parylene output coupler. (a,c) Two consecutive sweeps of device bias currents, the collected spectra are plotted in linear scale. (b) Log scale lasing spectra with observed harmonic behavior in bias sweep (a) with frequency spacing ∼44 GHz. (d) Log scale lasing spectra with similar harmonic behavior in bias sweep (c) with frequency spacing ∼54 GHz

Ultrathin film output couplers show promising potential in terms of the study of QC-VECSEL frequency combs. However, the difficulty resides in fabrication, where uneven stress from the metallic side of the parylene crinkles the film when it is released from the silicon substrate. The wrinkles on the film lead to optical scattering (this can be found during QC-VCESEL alignment, where the He-Ne alignment beam was scattered at the output coupler and generated a blurry beam pattern) and make the QC-VECSEL hard to lase. Moreover, the mechanical vibration of the drum-like film output coupler adds extra phase noise; it was

discussed in Section 3.3.2 that phase noise at frequencies 10 Hz–10 kHz is associated with the mechanical noise of a QC-VECSEL, as the output coupler is mounted separately from the lasing chip and has adjustable alignment screws and springs [148]. The use of a film output coupler will exacerbate this problem and may be a possible reason for multimode instability as the cavity FSR keeps fluctuating. The mechanical instability of the device is indicated in Figure 3.4.3(a,c), while in separate two sweeps of bias current, the collected lasing spectra are not consistent at the same bias. As the device needs to be cooled down to cryogenic temperatures, the sustainability of the film material should also be taken into consideration. Based on the author's experience, after leaving the device at cryogenic temperature overnight, the parylene film was mechanically broken.

Chapter 4

RF injection locking in THz QC-VECSELs

RF current modulation of QCLs has been demonstrated as a successful method for the control and stabilization of QCL frequency comb states; by injecting an RF signal near the cavity round-trip frequency, the generated side modes will lock the existing adjacent free-running lasing modes or seed new ones, which allows for the generation of broadband frequency combs [76], [77], [81], [158]. RF injection locking is also an important mechanism for achieving active mode-locking in THz QCLs; pulses as narrow as 4–5 ps have been reported [85], [86]. So far, all the demonstrations of RF injection locking are focused on ridge-waveguide or ring QCLs, while in this chapter, we applied this method to THz QC-VECSELs for the first time. Although previous chapters have discussed the preference of THz QC-VECSELs for single-mode lasing, we believe that RF modulation is an effective method to encourage multimode operation and the formation of frequency combs or even mode-locked lasers in THz QC-VECSELs.

In this chapter, we demonstrate the emergence of spectral broadening and multimoding in THz QC-VECSEL as we inject strong RF current modulation to its electrical bias at a

frequency close to the cavity round-trip frequency; at the same time, round-trip frequency pulling and locking to the injected RF signal is observed [159]. This system is considered a good platform to study the underlying physics of frequency comb/mode-locking in QCL systems as it provides a great degree of freedom in controlling and tuning the RF injection-locked laser state; some of the impacting factors, e.g., RF injection frequencies and powers, metasurface designs, cavity lengths (round-trip time), and optical feedback conditions, will be discussed in detail. We also report on novel experimental phenomena of harmonic and sub-harmonic injection, where the RF injection frequency is set around an integral multiple or submultiple of the round-trip frequency, and some preliminary results adopting the technique introduced in Chapter 2.

4.1 Baseline experimental results

The QC-VECSELs used in all the following measurements are based on the intra-cryostat OAP-focusing cavity design discussed in Chapter 3, which allows for CW operation and long lasing cavities at the same time. Long lasing cavities over ∼30 mm enable small cavity mode spacing, i.e., round-trip frequency ∼5 GHz, which can then be efficiently modulated and detected using commercial RF instrumentations. The QC-metasurface used in the initial experiment is the same one as discussed in Chapter 3 (VB0739-SR), which has a small bias area of diameter $d = 0.4$ mm for reduced injection current. It is designed to be resonant at 3.3 THz and consists of an array of ridges of width 12.2 μm repeated with a period of 41.7 μm (Figure 4.1.1(a)). An output coupler with $R_{OC} \approx 95\%$ is used in pair with the metasurface to form a laser cavity. Both two components are dispersive and contribute to the GDD over one round trip — it exhibits a maximum value exceeding 0.35 ps^2 in the frequency range where lasing occurs. The simulated spectral response of the metasurface and the output coupler are plotted in Figure 4.1.1(b) based on full-wave 2D FEM electromagnetic reflectance simulation (Ansys HFSS). The metasurface is modeled with Drude loss in the metal thin films and a

constant 30 cm^{-1} of frequency-independent material gain in the semiconductor, while the output coupler is made of 100 μm-thin quartz deposited with metallic mesh (P13-A3).

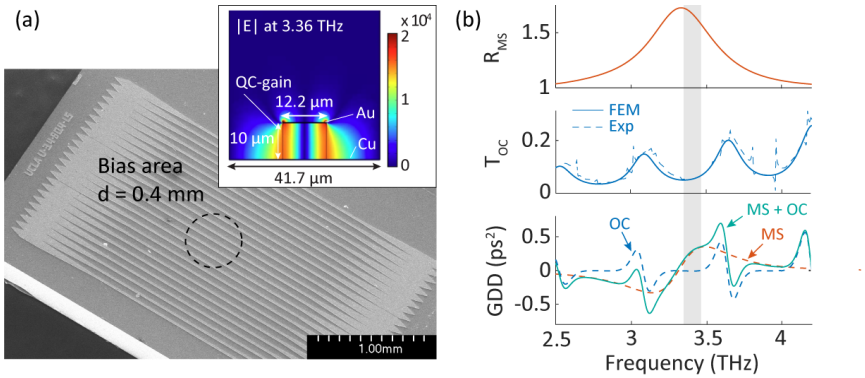

Figure 4.1.1: (a) Scanning electron microscopy (SEM) image of the fabricated QC-metasurface with a bias diameter of 0.4 mm. The inset shows the dimension and E-field distribution in a single ridge antenna. (c) FEM simulated active metasurface reflectance, output coupler transmittance, and GDD contributed by the two components. The shaded area indicates the frequency range where lasing is observed.

The experimental setup for RF injection locking is depicted in Figure 4.1.2. All the measurements were performed in vacuum at a temperature of 77 K. For better RF injection efficiency, we used formable semi-rigid coaxial cable within the cryostat up to the chip carrier package. The device is connected to a bias-T for simultaneous DC bias and RF modulation: electrical bias is applied to the DC port of the bias-T while its AC port is connected to an RF synthesizer (Hewlett-Packard 83650B) through a constant-20 dBm microwave amplifier (Hewlett-Packard 8349B). Multiple lasing modes generated by the device will produce a beat-note signal that is electrically detected by a spectrum analyzer (Agilent N9020a). A directional coupler is used enabling the extraction of beat-note signal to the spectrum analyzer while minimizing the pick up of RF signal from the synthesizer. Due to impedance mismatch between the 50 Ω SMA port of the semi-rigid coaxial cable and the electrical package of the QC-device, the spectrum analyzer collects not only the generated beat-note from the QC-device (labeled as f_{BN}) but also the RF injection signal reflected at the interface of SMA/QC-device (labeled as f_{RF}).

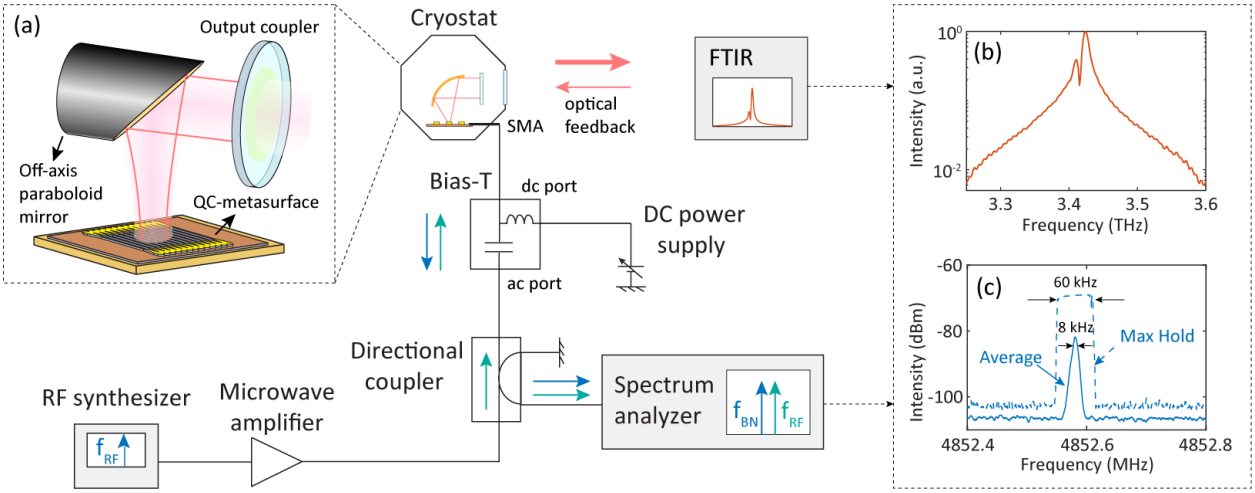

Figure 4.1.2: (a) Schematic of the experimental setup for RF injection locking. THz lasing spectrum (b) and beat-note spectrum (c) of the free-running QC-device in the existence of optical feedback are collected at a DC bias of 0.235 mA, where optical feedback is provided by the moving FTIR mirrors. The beat-note spectrum is measured with an RBW of 20 kHz.

The device is first tested in the free-running case (i.e., without RF modulation). Although only single-mode lasing was observed using the same QC-device as discussed in Section 3.3.2 (Figure 3.3.3), we note that the existence of optical feedback can in fact induce multimode operation [160], [161]. Due to the temporally varying small feedback from the scanning FTIR (Nicolet 8700) mirrors, we observed at least two lasing modes separated by ~14 GHz in the emission spectrum as plotted in Figure 4.1.2(b). Additional low-intensity sidemodes may also exist but cannot be resolved by the limited FTIR resolution of 7.5 GHz. This phenomenon is similar to that observed in Ref. [161], where additional lasing modes are observed in a mid-IR QC-laser under tilted optical feedback. Through nonlinear mixing of the free-running lasing modes, a narrow and single-peak electrical beat-note signal is observed, with a signal-to-noise ratio (S/N) of 26 dB. It is collected using the spectrum analyzer with a resolution bandwidth (RBW) of 20 kHz, which indicates a round-trip frequency $f_{BN} \approx 4852.7$ MHz and an equivalent cavity length around 31 mm (Figure 4.1.2(c)). It should be highlighted that the beat-note frequency as well as the lasing spectrum is highly dependent on the exact condition of optical feedback; we experimentally demonstrate that optical feedback plays an important role in determining not only the free-running beat-note frequency but also the

injection locking range, which will be discussed in detail in Section 4.3.

With the knowledge of an accurate value of cavity round-trip frequency, we are able to systematically study the modulation-dependent behavior of this QC-device. We swept the RF modulation frequency around the round-trip frequency at various modulation powers from -20 dBm to 20 dBm. All RF powers indicated in this chapter refer to the nominal output level of the RF synthesizer or after a 20 dBm amplifier, while the RF attenuation from the synthesizer to the SMA connector and injection efficiency from the SMA connector into QC-device will be considered separately in Section 4.2. The applied DC bias is fixed at a current of 0.235 mA ($\approx 1.17 \times I_{th}$). In Figure 4.1.3, we recorded the THz emission spectra and the intermodal beat-note locking bandwidth at different RF powers. Here, we analyze the experimental results with respect to RF power injection level:

1. At the lowest power level of -20 dBm, the beat-note spectral map in Figure 4.1.3(a) clearly shows that the beat-note is pulled toward the injection signal and finally locked. A locking range of 30 kHz is demonstrated which increases with respect to the RF injection power as shown in Figure 4.1.3(c). In Figure 4.1.3(c), the experimental locking ranges collected at various RF injection powers are recorded as blue asterisks. To analyze the phenomenon of RF injection locking, Adler's equation is commonly used with a locking bandwidth given by [162], [163]:

$$\Delta\nu = \frac{2\nu_0}{Q}\sqrt{\frac{P_{inj}}{P_0}}, \tag{4.1.1}$$

where Q is the cold-cavity quality factor, ν_0 and P_0 are the frequency and power of a free-running longitudinal mode, while P_{inj} is the power of the injected sideband induced by RF modulation. Adler's equation indicates a square root dependence of the locking bandwidth on the RF power and fits our experimental results well at low RF powers (red dashed line).

2. Starting from an RF power of -2.5 dBm, injection locking occurs before the beat-note is fully pulled to meet the injected signal f_{RF} (Figure 4.1.3(b)); at the same time, lasing

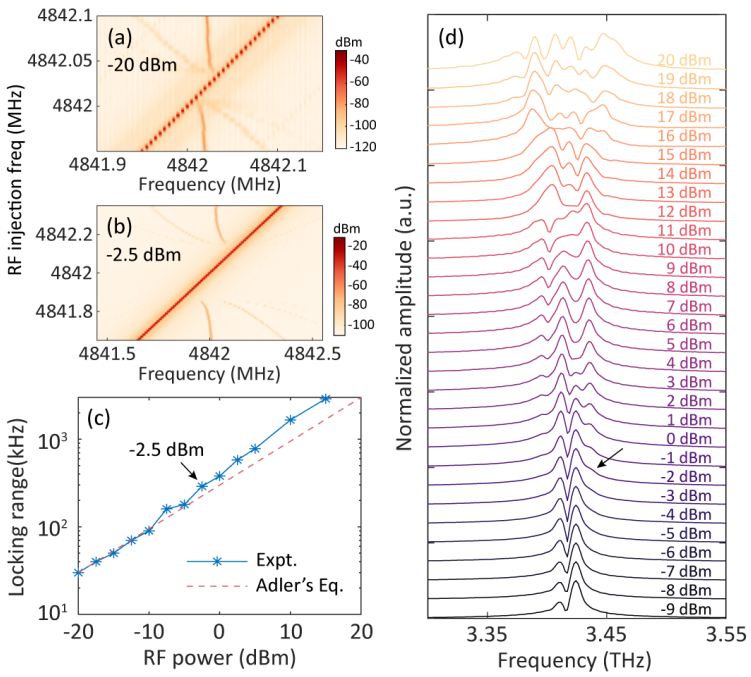

Figure 4.1.3: Beat-note spectral map under constant RF injection power of -20 dBm (a) and -2.5 dBm (b) with RF modulation frequency sweeping around the round-trip frequency. It should be pointed out that the beat-note frequency at detuned RF injection is shifted compared to the free-running value in Figure 4.1.2, this is due to the movement of cryostat which changes the amount of optical feedback (see detailed discussion in Section 4.3). (c) The experimental injection locking range is plotted at different RF injection powers as blue asterisks, following a $\frac{1}{2}$-slope dependence in the log-log scale (red dashed line). (d) Normalized THz lasing spectra (linear scale) are plotted at increasing RF power when f_{RF} is fixed at 4852.7 MHz.

bandwidth broadening is observed in the THz emission spectra as pointed out in Figure 4.1.3(d) — there is an extra lasing mode being excited at RF power between -2 dBm and -3 dBm (pointed out by a black arrow). This spectral broadening also shows an increasing trend with respect to RF power. It is noticed from Figure 4.1.3(c) that at an RF powers $>$ -2.5 dBm, the experimental locking range starts to deviate from Adler's equation towards higher values. This may indicate the limitation of Adler's equation in explaining RF injection locking in the case when multiple new lasing modes are excited under relatively strong RF modulation, since Adler's equation assumes a weak injection signal where amplitude perturbation induced by the injection signal is not considered.

3. The maximum RF injection power used in this measurement is 20 dBm limited by the max allowable power of the bias-T. THz emission and RF beat-note spectral maps in this case are plotted in Figure 4.1.4(a-b). In Figure 4.1.4(a), the symmetry of the lasing spectrum is highest at $f_{RF} = 4852.7$ MHz, where the maximum bandwidth is observed; at injection frequencies above/below this value, the lasing modes concentrate toward lower/higher portion of the spectrum. This phenomenon is similar to that reported in Ref. [164] and a possible explanation can be found in Ref. [165] due to phase mismatch between the mod-

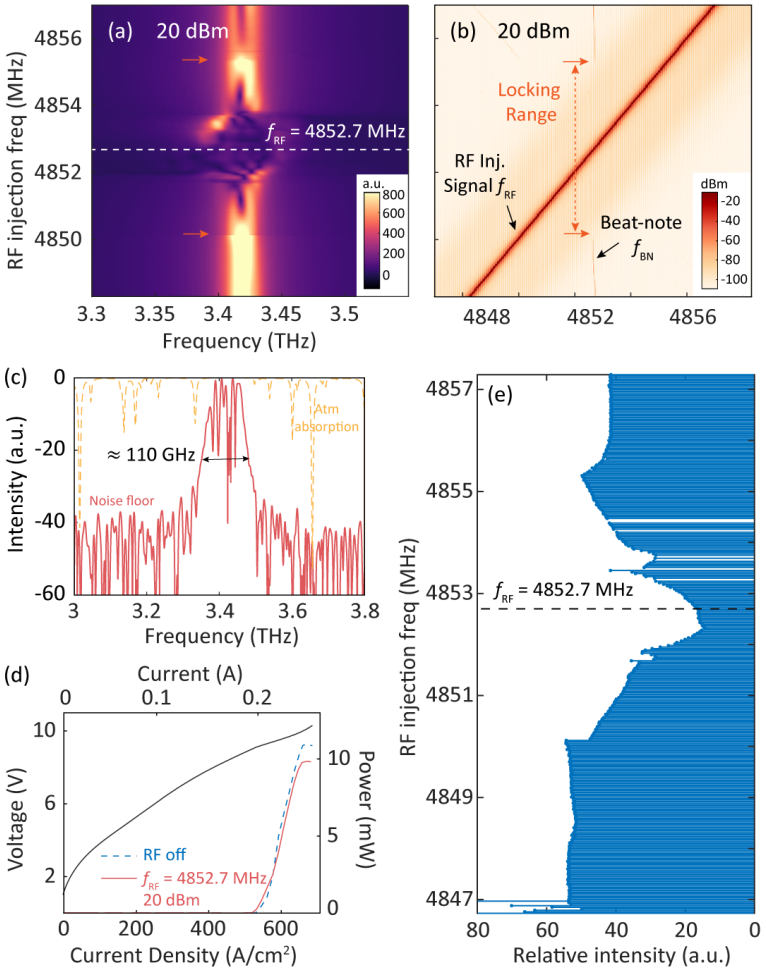

Figure 4.1.4: (a) THz lasing spectral and (b) electrical beat-note maps of the device under constant RF injection power of 20 dBm. The estimated locking range is pointed out by the red arrows. The maximum spectral broadening occurs at $f_{RF} = 4852.7$ MHz (white dashed line), the THz lasing spectrum and corresponding $L - I - V$ curves in this case are plotted in (c-d). (e) Relative intensity is obtained by integrating the FTIR spectrum over frequency and is plotted with respect to RF injection frequency.

ulation period and group round-trip time. The maximum spectral broadening collected at $f_{RF} = 4852.7\,\text{MHz}$ is plotted in Figure 4.1.4(c) with lasing modes spanning around a max. observable bandwidth of 110 GHz. However, due to the limited FTIR resolution of 7.5 GHz, we were not able to spectrally resolve individual lasing modes; phase correction and certain apodization have been applied to better resolve the spectrum, which will be discussed in detail in Chapter 5. The corresponding power and voltage vs. current ($L-I-V$) curves in this case are plotted in Figure 4.1.4(d) (solid curve). A maximum output power of ~10 mW was collected using a pyroelectric detector (GentecEO). Compared with the $L-I$ characteristic collected in the free-running case (dashed curve), the output power, as well as the lasing threshold, is slightly lower. To better analyze how the lasing power varies under RF modulation, we integrate the amplitude of the FTIR spectrum over frequency to get a qualitative idea of THz output power. The relative intensity is plotted with respect to RF injection frequencies in Figure 4.1.4(e), which indicates a lower output power is observed when more lasing modes are excited as f_{RF} is tuned closer to f_{BN}; the lowest output power is observed at $f_{RF} = 4852.7\,\text{MHz}$ where maximum spectral broadening is obtained (black dashed line).

On the other hand, RF beat-note collection becomes difficult under strong RF modulation as the pick-up RF signal from the synthesizer becomes strong and attenuation has to be applied on the spectrum analyzer, which also attenuates the collected beat-note. For this reason, there is no significant beat-note pulling observed in Figure 4.1.4(b), and the locking bandwidth is estimated as 5.3 GHz. It should be noticed that the emission spectrum undergoes distinct changes as the beat-note disappears (pointed out by red arrows) — it is believed that this is a signature of injection locking and occurs in our measurements under different RF powers. The injection locking range obtained in our QC-VECSEL device is considerably smaller compared with those demonstrated in RF injection-locked ridge-waveguide QCLs at the same level of RF power (e.g., 70 MHz at -20 dBm RF power in Ref. [162]; ~500 kHz at -10 dBm RF power in Ref. [78]). One of the reasons is that QC-VECSELs have higher quality factors compared with ridge-waveguide QCLs. Our QC-VECSEL has a 31 mm-long external

cavity and low loss from the ∼95% reflectance output coupler; using a coupled-cavity model, we estimate a cold-cavity linewidth of $\nu_0/Q \approx 70\,\mathrm{MHz}$. This is around 300 times smaller than a value of 25 GHz estimated in Ref. [162]. In addition, intrinsic and technical issues with our QC-VECSEL setup result in a low efficiency of RF power transfer at ∼4.8 GHz from the synthesizer to the QC-metasurface bias terminal; this will be discussed in detail in the next section.

4.2 Electrical package and RF injection efficiency

RF attenuation and impedance mismatch severely limit the modulation efficiency. Strong RF reflection at the interface of the 50 Ω SMA port and the QC-device impedes the detection of the electrical beat-note signal using the spectrum analyzer. The reasons for low RF injection efficiency at the cavity round-trip frequency, which is typically 3–5 GHz in an OAP-focusing cavity, are mainly:

1. Compared with ridge-waveguide QCLs which typically have impedances of 20 Ω [162], [166], QC-metasurface is equivalent to multiple cascaded ridge waveguides, which exhibits smaller impedance and exaggerates the impedance mismatch. Moreover, it exhibits a large RC time constant due to a large parasitic capacitance.

2. The electrical packaging has not been optimized for RF operation. The wire bonds and wire bonding pads contribute parasitic inductance and capacitance, respectively, and reduce the RF modulation efficiency as we go to higher RF frequencies.

3. An additional ∼8 dB RF attenuation has been characterized, which accounts for losses through cables and directional coupler from the synthesizer to the SMA connector.

In this section, we will characterize the RF injection efficiency of the device used in the above experiment, and provide suggestions for improvement.

4.2.1 Simulated transmission loss in the QC-device

To estimate the transmission loss in the QC-device due to impedance mismatch, a FEM simulation is used, accounting for the finite dimension of the metasurface, including its electrical packaging. Figure 4.2.1(a) shows the QC-device mounted in the OAP-focusing cavity that is modelled using Ansys HFSS in Figure 4.2.1(b). Only the electrically biased ridges are modeled with metal layers loaded with Drude loss; the circular biased area is assumed to be loaded with GaAs with a shunt conductivity derived from the experimental dI/dV curve, while the unbiased area is defined as bulk GaAs. Two 1-mil bond wires of approximately 2 mm length electrically connect the metasurface to a "gold pad": a 2.5 mm × 4.5 mm × 0.254 mm thick Al_2O_3 pad coated with Au above and below. The pad is soldered to the center pin of an SMA connector on the other side. The E-field distribution along one of the biased ridges is simulated at 5 GHz which indicates the injected RF signal propagating

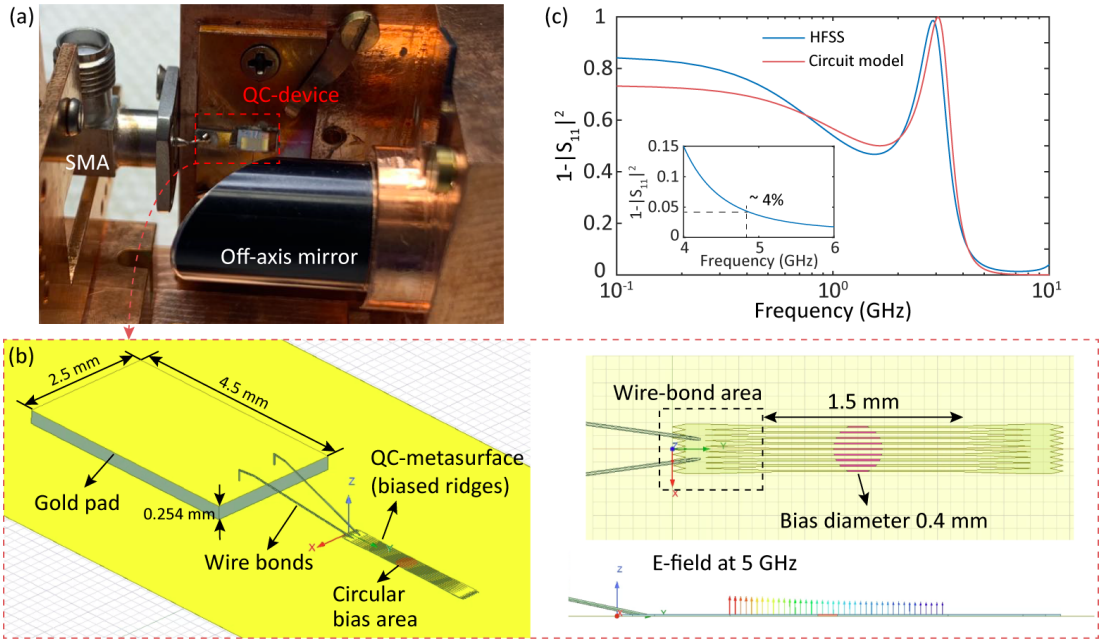

Figure 4.2.1: (a) Image of QC-device mounted in the focusing cavity. (b) The electrical packaging structure that is modeled in Ansys HFSS including the gold pad and bond wires. Their dimensions are labeled, and the simulated E-field distribution along one of the biased ridges at 5 GHz is plotted. (c) The transmission coefficient simulated within HFSS assumes an excitation port of 50 Ω (blue) and is calculated using the lumped element circuit model (red).

along the QC-metasurface has an effective wavelength much longer than its dimension. The simulated power dissipation with a 50 Ω excitation port is plotted in Figure 4.2.1(c), the resulting transmittance of RF signal through the SMA/QC-package boundary is simulated to be ∼4% at a target frequency of 4.8 GHz which shows good agreement with the circuit model result (see Section 4.2.2) except at lower frequencies. This indicates that only a small portion of the RF signal can be injected into the QC-metasurface due to severe impedance mismatch, while only part of it will be applied to modulate the gain material.

4.2.2 Lumped-element circuit model

Based on the electrical package displayed in Figure 4.2.1, an equivalent lumped-element circuit is introduced to model the RF injection efficiency of the QC-device as plotted in Figure 4.2.2. Since the QC-metasurface has a dimension much smaller than the RF operation wavelength, which is usually the case, it is represented as a parallel plate capacitor in parallel with a resistor coming from the effect of QC-active material. Its capacitance C_{MS} is calculated based on the dimension and thickness of the metasurface assuming a permittivity of 12.5 for the GaAs/AlGaAs active region. The differential shunt resistance R_{AR} from the active material is obtained based on the experimental slope of the $I-V$ curve at the bias point. L_{wire} is the inductance of the two wire bonds connected in series with the RC circuit and is estimated based upon the rule of thumb of ∼1 nH/mm/wire. $C_{goldpad}$ is the capaci-

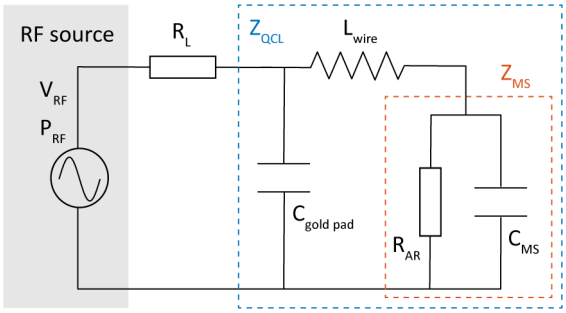

Figure 4.2.2: Equivalent lumped element circuit model. Blue and red dashed boxes point out the impedances of the QC-device and metasurface.

tance of the gold pad whose value is estimated based on its dimension and the permittivity of Al_2O_3. The gold pad is connected to the RF source with a 50 Ω generator impedance R_g, which provides an RF power of P_{RF} and an equivalent RF voltage of $V_{RF} = 2\sqrt{R_g P_{RF}}$.

The rectification voltage of the QC-device can be calculated according to Ref. [167]:

$$V_{rect} = \frac{1}{2}|V''|_{I_0} I_{RF,QCL}^2, \tag{4.2.1}$$

where V'' is the second derivative of the $I-V$ curve at DC bias current I_0. $I_{RF,QCL}$ is the RF modulation current injected into the QC-active material:

$$I_{RF,QCL} = V_{RF} \frac{R_L}{R_{AR}(Z_{QCL} + R_L)} \frac{Z_{MS}}{(j\omega L + Z_{MS})}, \tag{4.2.2}$$

where the impedance of the QC-device Z_{QCL} and the metasurface Z_{MS} are pointed out in blue and red dashed boxes in Figure 4.2.2. For the device used in the baseline experiment (VB0739-SR), the parameters are chosen as $C_{MS} = 6.1\,\text{pF}$, $R_{AR} = 16\,\Omega$, $C_{goldpad} = 3.8\,\text{pF}$, $L_{wire} = 1\,\text{nH}$, which gives an analytical RF transmittance as plotted in Figure 4.2.1(c).

4.2.3 Microwave rectification measurement

To experimentally characterize the response of QC-device to the injected RF signal, microwave rectification technique has been applied as described in Ref. [80], [166], [167]. The RF signal generated from the synthesizer is amplitude modulated and injected into the QC-device through the AC port of bias-T, while the latter is biased at a constant current. Due to the inherent nonlinear IV characteristics of QC-device itself, the change in DC voltage is measured as a characterization of its response to the RF signal. The experimental setup is sketched in Figure 4.2.3(a). A function generator is connected to the RF synthesizer to provide external amplitude modulation at 10 kHz, while the variation in DC rectification voltage is measured using a lock-in amplifier triggered at the same frequency of the ampli-

tude modulation. The injected RF power is kept constant at -10 dBm with frequency swept from 0.5 GHz to 8 GHz. The collected rectification voltage is normalized with respect to its low RF frequency value and is plotted in 4.2.3(b) at a bias current of 0.235 mA (roughly the bias we applied in RF injection locking measurements in Section 4.1). This result is well described by the lumped-element circuit model (dashed curve). Notably, an electrical resonance is present at 3 GHz which is associated with the LC parasitics — its frequency is determined by the dimensions of the gold pad, bond wires, as well as the QC-metasurface. The rectification voltage shows a 3-dB cutoff frequency at 3.7 GHz and a 10-dB cutoff frequency at 4.4 GHz, followed by a rapid roll-off towards higher frequencies. Consequently, the response of the QC-device to RF signal, i.e., RF injection efficiency at the experimental $f_{RF} \approx 4.8$ GHz is reduced to ~5% of that at lower frequencies.

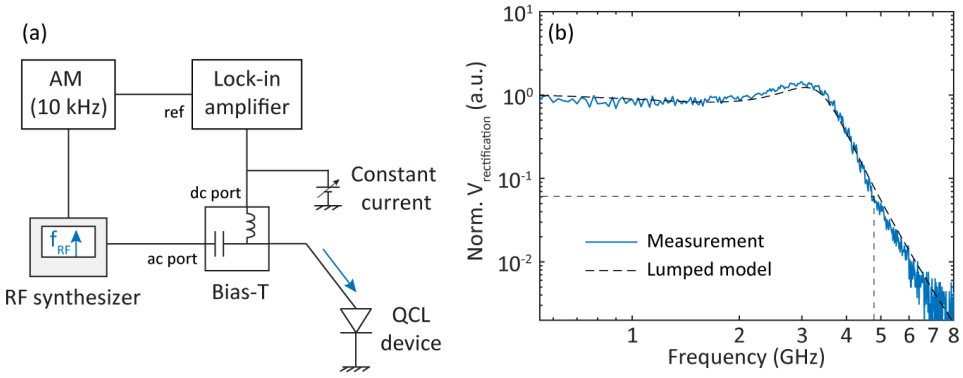

Figure 4.2.3: (a) Schematic of the experimental setup for microwave rectification technique. (b) Normalized rectification voltage (solid curve) measured at a bias current of 0.235 mA, together with the theoretical fits (dashed curve) obtained based on an analytical lumped element circuit model.

4.2.4 Improving RF injection efficiency

Here, the author provides several suggestions for optimizing the electrical package of the QC-device, i.e., reducing the capacitance and inductance portions of the equivalent circuit, and alleviating the impedance mismatch problem. Following these methods, a better RF injection efficiency has been demonstrated and will be further discussed in Section 4.5.1.

1. Redesigning the QC-metasurface with reduced unbiased area and taper area. In previous QC-metasurface designs, the dimension of the whole metasurface was twice as big as the bias diameter, considering light diffraction, which generated a larger beam size than the bias area. However, thanks to the OAP-focusing cavity design, spatial overlap between the THz beam and the unbiased region is minimized, and the overall size of the metasurface can be largely reduced for smaller capacitance. At the same time, the taper area is reduced while maintaining the function of self-lasing suppression (should make sure enough space is left for wire bonding). This also points out one of the benefits of patch-design over ridge-design — there is no self-lasing in TM_{00} mode.

2. Referring to previous demonstrations of ridge-waveguide QCLs that use well-designed RF feed structures, e.g., RF coplanar probes [162], [167], RF launchers[80], or custom high-frequency printed circuit board (PCB) mounts[86], modulation of QCLs up to 35 GHz has been successfully demonstrated. Here, we replaced the electrical ceramic gold pad with a 50 Ω coplanar waveguide designed on a PCB that feeds up to the edge of the metasurface chip for impedance matching (Figure 4.2.4).

3. By adding multiple flat and parallel wire bonds and minimizing their length, RF losses

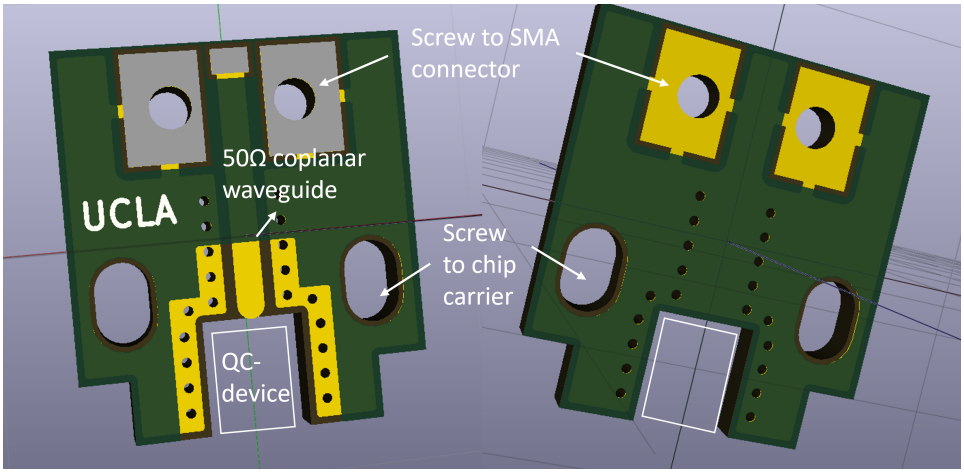

Figure 4.2.4: Sketch of the PCB design. The QC-device is wire bonded to a 50 Ω coplanar waveguide for impedance matching.

due to the parasitic inductance of the wire bonds can be reduced (further discussion can be found in Ref. [168] Chapter 2). The finite size of the metasurface taper area should be taken into consideration, while too many wire bonds may increase the risk of an electrical short.

4. Low RF loss adapters and cables (e.g., semi-rigid SMA cables instead of BNC cables) will help reduce the RF attenuation. Especially, a low-loss cable with minimized length connecting the device to the spectrum analyzer will help extract and display a weak beat-note signal.

4.3 Effects of optical feedback on RF injection-locked QC-VECSELs

The behavior of RF injection-locked QC-VECSELs is influenced by a number of parameters. These impacting factors cause some uncertainty and non-repeatability in the experimental observation, but they also offer options for controlling RF injection-locked laser states and conducting a systematical investigation of frequency comb/mode-locking behavior in QCL systems. In Section 4.1, we experimentally found that optical feedback, even weak feedback originating from the FTIR mirrors, induces extra lasing modes in a free-running QC-VECSEL. This can be useful, as it provides exact information of the cavity round-trip frequency from an observed beat-note — without feedback, the device lases in a single-mode regime with no beat-note detected. In this section, we will focus on how the performances of the laser (e.g., free-running beat-note, spectral characteristics, injection locking range) are affected by the strength, length (i.e., phase of feedback light), and tilted angle of the optical feedback. We will review previous demonstrations on the effect of optical feedback on QCLs/QCL frequency combs and provide a theoretical hypothesis to analyze the experimental phenomenon. We will talk about additional impacting factors, such as external cavity

length and metasurface design, in the next section.

4.3.1 Effects of optical feedback in free-running case

We did a series of experiments to qualitatively demonstrate the effects of optical feedback on free-running beat-note frequency as well as the RF injection locking range. First, we fixed a flat mirror on a translation stage and put it in front of the cryostat window (approximately

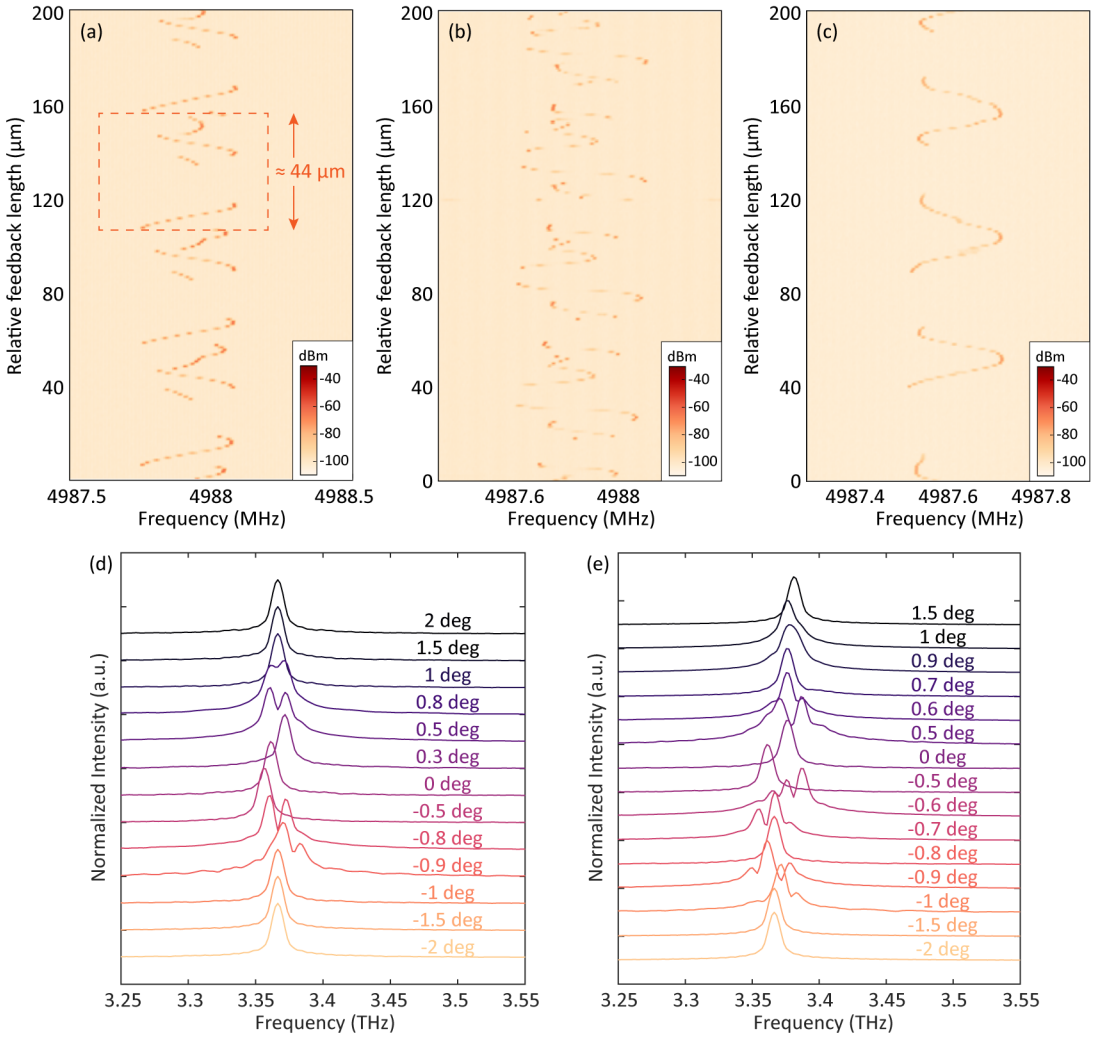

Figure 4.3.1: (a-c) The free-running beat-note spectral maps show periodic behavior with optical feedback length. Multiple measurements are collected under different optical feedback angles and distances between the feedback mirror and cryostat window. (d-e) The free-running lasing spectra were collected at different optical feedback angles. Multimode operation is observed only under tilted optical feedback.

15 cm from the device). As we stepped the translation stage, the optical feedback length was tuned and the free-running beat-note shows periodic behavior with a period of half wavelength $\Lambda \approx 44\,\mu m$ as plotted in Figure 4.3.1(a-c); multiple beat-note spectral maps show different feedback length dependent behavior as we adjusted the optical feedback angle or distance between the feedback mirror and the cryostat window. The same half-wavelength periodicity was demonstrated in ridge-waveguide QCL frequency combs in Refs. [45], [169], [170]; it is believed that the comb operation stability is unaffected by the change in optical feedback length under moderate feedback strength. It is important to note that multiple lasing modes are induced and an electrical beat-note is observed only at specific feedback positions; at other positions, no beat-note is collected, indicating single-mode lasing — this indicates that multimode instability requires a specific optical feedback condition. This is also revealed in the free-running spectra collected at various optical feedback angles. In this experiment, a flat mirror is positioned on a rotating platform with an angle readout, and a silicon beam splitter is used to provide optical feedback from the flat mirror and simultaneous FTIR spectrum collection. The collected free-running spectra indicate that multimode operation is only triggered when the optical feedback is tilted at an angle between $\pm 0.5^\circ$ to $\pm 1^\circ$, i.e., under the condition of tilted optical feedback (Figure 4.3.1(d-e)).

4.3.2 Effects of optical feedback in RF injection-locked case

The effect of optical feedback on injection locking bandwidth is discussed with respect to different feedback lengths, feedback strengths, as well as bias currents. A low RF injection power of -15 dBm was applied for all the measurements.

A. Injection locking bandwidth under various optical feedback lengths and strengths

Figure 4.3.2(a-c) plots the recorded injection locking bandwidth at different feedback lengths, it is supposed to show the same half-wavelength periodicity as the free-running beat-note. To control the optical feedback strength, a rotatable wire-grid polarizer was

added between the cryostat window and the flat feedback mirror. THz radiation coming from the QC-VECSEL has a polarization perpendicular to the ridge antennas and the QC-metasurface only interacts with light at that polarization. We label it "90°" for the case when 100% of the THz radiation passes through the polarizer. As the polarizer was rotated from "90°" to "70°", the amount of light reflected back into the QC-device was reduced. The collected beat-note spectral maps are plotted in Figure 4.3.2(d-f) which indicate an increasing locking range with respect to the reduced optical feedback strength. Moreover, the free-running beat-notes were also collected in Figure 4.3.2(g) showing frequency shift as the optical feedback strength was changed.

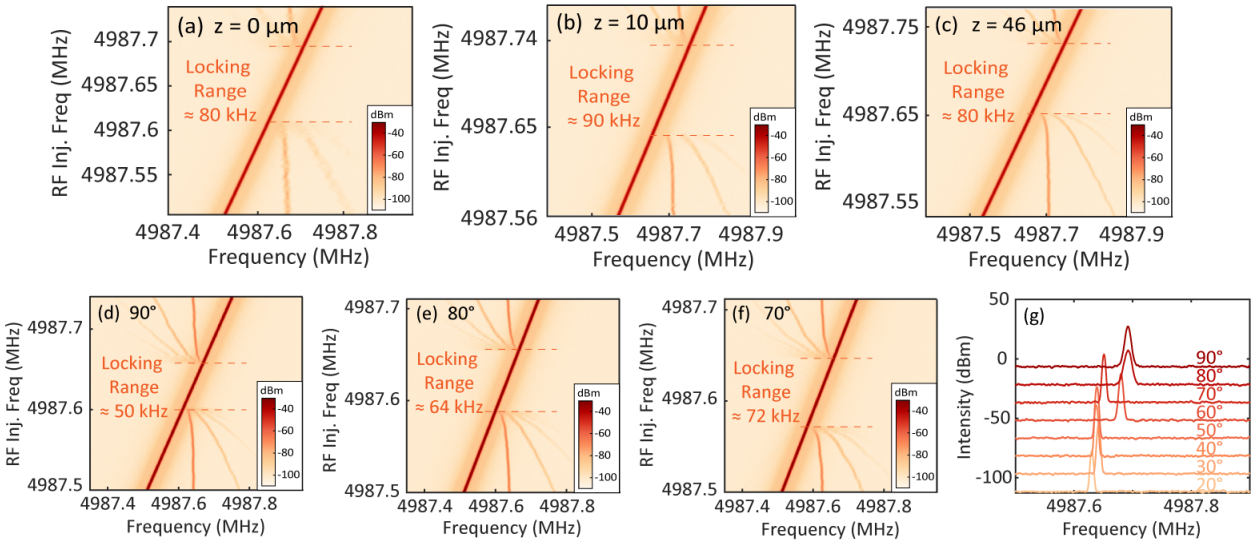

Figure 4.3.2: (a-c) Beat-note spectral maps under constant RF injection power of -15 dBm at different relative feedback lengths of z=0, 10, 46 μm respectively. (d-e) Beat-note spectral maps under constant RF injection power of -15 dBm in the case when the strength of optical feedback is reduced by reducing the rotational angle from "90°" to "70°". The locking bandwidths are labeled in the figures. (g) The free-running beat-note frequency is shifted with reduced optical feedback strength.

B. Bias-dependent behavior under the influence of optical feedback

The behavior of this QC-device at various DC biases ranging from the lasing threshold to near the NDR point was also studied and plotted in Figure 4.3.3. Figure 4.3.3(a) shows the lasing spectra under 20 dBm RF injection at a frequency of f_{RF} = 4852.7 MHz. Significant

spectral broadening is observed at all the applied biases, and the lasing bandwidth increases only slightly with respect to the bias current as more modes are brought above the lasing threshold.

The effects of device bias on the injection locking bandwidth were discussed in Ref. [162], which points out that the RF power injected into the device to modulation its gain material, i.e., P_{inj} in Adler's equation (Eq. 4.1.1), can be expressed as the product of RF modulation current injected into the device multiplied by dP/dI obtained from the experimental $L-I$ characteristic according to small signal approximation. The RF modulation current is the same as that derived in Eq. 4.2.2, which stays nearly constant at various biases (assuming fixed RF power and neglecting the change in device impedance). In this case, the injection locking bandwidth decreases as the bias current increases — the slope of the $L-I$ curve becomes smaller at a bias current closer to the NDR point. However, a similar phenomenon was not observed in our QC-VECSEL system.

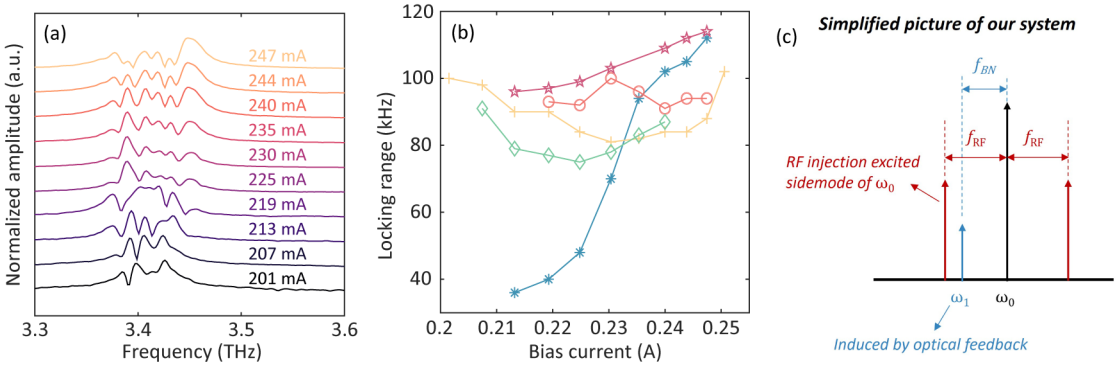

Figure 4.3.3: (a) Normalized THz lasing spectra (linear scale) at various biases when RF signal at 4852.7 MHz is injected into the QC device, the RF power used is 20 dBm for significant spectral broadening. (b) Injection locking range as a function of bias current under 15 dBm RF power in the cases of different lengths/strengths/angles of optical feedback. (c) A simple theoretical picture assuming two free-running modes: mode ω_1 is induced by optical feedback and is locked by the RF-excited sideband of the main lasing peak ω_0.

To investigate the effects of applied bias on our system, we swept the RF modulation frequency around the round-trip frequency at a fixed injection power of -15 dBm and measured the injection locking bandwidth at various biases. A small injection power was used so the

locking range could be more clearly observed. Additionally, we repeated such bias sweeps while providing different magnitudes, phases, and angles of feedback light from the external feedback mirror, the corresponding locking ranges are indicated by different colored curves in Figure 4.3.3(b). Our experimental observation reveals that the relationship between locking range and device bias is related to the condition of optical feedback, and is significantly different from previous demonstrations using ridge-waveguide QCLs in Ref. [162]. Here, the author introduces a simple theoretical picture to analyze what's happening in the system. We could make a simple assumption that there are two free-running modes, where mode ω_1 is induced by optical feedback around the main lasing peak ω_0 and is locked by the RF-excited sideband of the latter. The ratio of P_{inj}/P_0 in Adler's equation can be estimated as the ratio of the free-running power of mode ω_0 and that of mode ω_1 as the injected RF power is fixed, which determines the injection locking range. Thus, how the locking range varies is determined by the evolution of the relative strength of two lasing modes with regard to bias. Regretfully, our FTIR's resolution prevents us from experimentally observing this. In theory, the spectral characteristics of the device versus applied bias are expected to be affected by the changes in threshold gain induced by optical feedback and the alignment of compound-cavity modes formed in the external cavity with respect to gain, which is related to not only the length and strength of optical feedback but also the tilt angle of external mirror [171].

4.3.3 Theoretical analysis of optical feedback

Based on our experimental results, optical feedback will trigger the generation of extra lasing modes as well as an electrical beat-note at cavity round-trip frequency. It seems that this phenomenon is more likely to be observed under tilted optical feedback. Compared with common optical feedback, where the external mirror is well aligned with the optical path, tilted optical feedback will lead to the degeneration of the odd-order round-trip reflections in the external feedback cavity and the even-order round-trip reflections. While light passing

through even-order reflections still couples efficiently into the internal laser cavity, light passing through odd-order reflections can only couple into the laser's active region by the diffraction effect — this is because the reflected light is tilted and shifted in position with respect to the active region — and is therefore very sensitive to the tilted angle of the external mirror. Under tilted optical feedback, unusual phenomena have been reported; examples include multiple types of nonlinear dynamics in QCLs [172]–[174]; frequency splitting of the required lasing threshold gain is predicted [175]; in Ref. [172], a mid-IR QCL under tilted feedback is observed to have an additional lasing mode separated by ∼2.5 times the FSR, and the relative strength of the two lasing modes is related to the tilted angle.

Here, we attempted to use an analytical multi-section cavity model to qualitatively analyze the multimode instability of a free-running QC-VECSEL under optical feedback. The model is similar to that described in Section 2.3, while the internal laser cavity is coupled to the external feedback cavity as depicted in Figure 4.3.4(a). To degenerate the odd-order and even-order reflections, the effective reflection coefficient of the external cavity is multiplied by an extra factor as:

$$f_{odd}(\theta_{tilt}) = C_{eff}\frac{sin(\pi\theta_{tilt})}{\pi\theta_{tilt}}, \tag{4.3.1}$$

$$f_{even} = C_{eff}, \tag{4.3.2}$$

where C_{eff} accounts for the coupling efficiency between the internal and external cavities and θ_{tilt} is the tilted angle of the external feedback mirror normalized with respect to the first zero of the diffraction pattern. Detailed mathematics can be found in Refs. [171], [175]. Similarly, we defined that the QC-gain clamps at a gain coefficient of $g_{cutoff} = g_{th,min} + \delta g$ and all the modes with calculated threshold gain coefficients lower than g_{cutoff} will lase. In our simulation, the output coupler is assumed to have a constant reflectance of $R_{OC} = 0.95$ without taking substrate thickness into consideration, and the feedback mirror is assumed to have a unity reflectance of $R_{mirror} = 1$. In Figure 4.3.4(b), a single-mode operation is predicted in the case of no external feedback cavity. A gain offset value of $\delta g = 0.004\,\mathrm{cm}^{-1}$

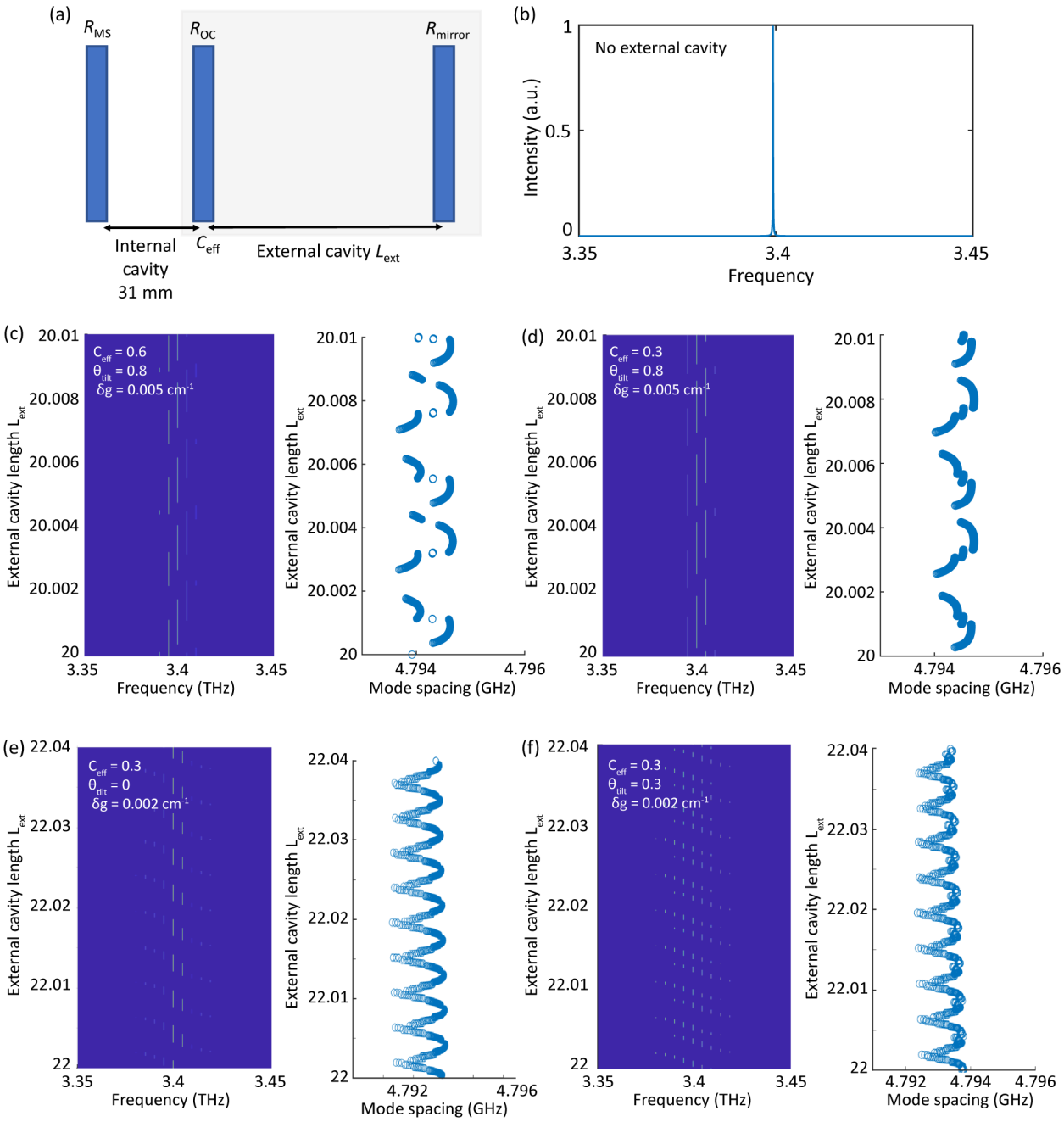

Figure 4.3.4: (a) Sketch of the multi-section cavity model made of an internal VECSEL cavity coupling with the external feedback cavity. (b) Single-mode operation is predicted when there is no external feedback cavity. (c-f) Simulated lasing spectra and averaged mode spacing as a function of external cavity lengths. The simulation variables are labeled in each plot.

is applied, above which multiple lasing modes are excited. In (c-f), we plotted the simulated lasing spectra with respect to the stepping external cavity length L_{ext}. The mean spacing

between each two lasing modes is calculated in order to simulate the beat-note spectrum. Different simulation variables, i.e., C_{eff}, θ_{tilt}, δg are applied, and their values are labeled for each plot. It was noticed that the simulated mode spacing (i.e., beat-note) exhibits a periodicity of half-wavelength, and its external cavity-dependent behavior is related to the exact optical feedback condition. For normal feedback, the beat-note shows a sine-wave dependence with L_{ext}, whereas for tilted feedback, the dependence is no longer a perfect sine-wave but is disturbed. This simulation model partially reproduces some of the experimental results shown in Figure 4.3.1.

To fully understand the complicated behavior of optical feedback in our QC-VECSEL system, more theoretical study of laser dynamics and instabilities will be needed. For example, in Ref. [176], a full set of effective semiconductor Maxwell-Bloch equations has been applied to a ridge-waveguide QCL, and four regimes: single-mode, frequency comb, mixed state, and self-pulsations have been demonstrated in free-running QCLs under different strengths and lengths of optical feedback. On the other hand, systematic measurements of the RF-injected system with well-controlled, adjustable optical feedback will be needed for a full experimental characterization of the effects of optical feedback and should be considered in the future.

4.4 Other impacting factors of RF injection-locked QC-VECSELs

4.4.1 External cavity length

A. Fixed cavity length at ~47 mm

According to the microwave rectification results in Figure 4.2.3, the RF injection efficiency of the QC-device at 4.8 GHz is only 5% of that at lower RF frequencies, and it peaks at a frequency of 3 GHz, which corresponds to an equivalent external cavity length around

50 mm. Thanks to the OAP-focusing VECSEL cavity design, THz radiation reflected by the OAP mirror towards the output coupler is in principle a collimated beam, which enables us to increase the cavity length without significant degradation of output power or dynamic range. Using the same device in Section 4.1, we increased the cavity length to ∼47 mm. As a result, the round-trip frequency decreased to around 3.2 GHz, where the QC-device exhibits maximum modulation response. In Figure 4.4.1(a), $L-I-V$s of the device are plotted with an external cavity length of ∼31 mm (blue) and ∼47 mm, respectively. The lasing threshold is increased from 508 A/cm^2 to 550 A/cm^2, while the output power is decreased from ∼10 mW to ∼4.4 mW; a better alignment will help alleviate the degradation.

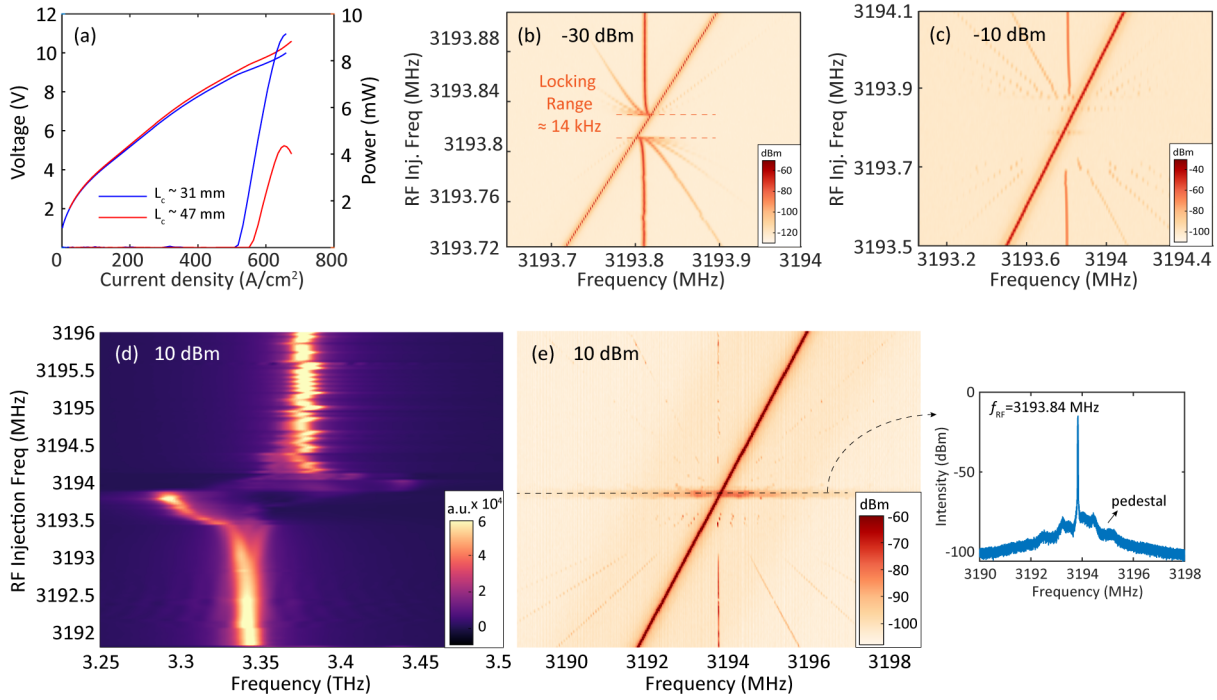

Figure 4.4.1: (a) CW $L-I-V$ characteristics of the device used in Section 4.1 with different external cavity lengths L_c ∼31 mm (blue)/47 mm (red). Beat-note spectral maps under an RF modulation power of -30 dBm (b) and -10 dBm (c). (d-e) THz lasing spectra as well as corresponding beat-notes under 10 dBm RF power. The inset indicates the beat-note spectrum where pedestals were observed.

Similarly, we performed a systematic RF sweeping around the round-trip frequency at various RF powers from -30 dBm to 10 dBm and recorded the THz emission and beat-note spectral maps. At weak RF injection powers, similar pulling and locking of the beat-note is

observed and plotted in Figure 4.4.1(b). While a higher RF injection power (e.g., -10 dBm in Figure 4.4.1(c)) induces side peaks in the beat-note spectra which indicates a non-comb behavior. At an RF injection power of 10 dBm, complicated behavior is observed in the beat-note spectra along with lasing modes spanning over 200 GHz (Figure 4.4.1(d-e)). Within the locking range where spectral broadening occurs, regions with pedestal or side peaks around the injected RF signal are observed and pointed out in the inset of Figure 4.4.1(e). This phenomenon is similar to that described in Ref. [83], where the authors pointed out that a weak electrical modulation can be used to lock and stabilize the intermodal beat-note in an anti-phase state, while a strong modulation enforces in-phase coupling of beat-note and generates AM comb. When the beat-note was not phase-locked at certain modulation frequencies, they observed a similar beat-note spectrum (Figure 3(c-d) in [83]). To fully understand and characterize the AM/FM frequency comb state in this case, techniques such as SWIFTS or dual-comb spectroscopy are needed to obtain phase coherence or recover the temporal waveform.

B. Tunable cavity length from ~30 mm to ~50 mm

In this experiment, we fixed the output coupler on a piezoelectric stage to tune the cavity length and recorded the maximum lasing bandwidth at the appropriate RF injection fre-

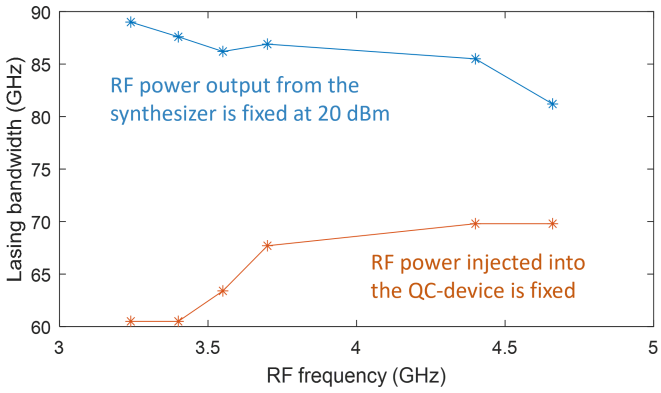

Figure 4.4.2: Maximum lasing bandwidth under fixed 20 dBm RF power (blue) and under scaled RF power (red). It is plotted with respect to various beat-note frequencies as the external cavity length is tuned using an intra-cryostat piezoelectric stage.

quency. The results are plotted in Figure 4.4.2. The blue curve records the maximum lasing bandwidth at varying external cavity lengths from ∼30 mm to ∼50 mm, i.e., beat-note ranging from 3.2 GHz to 4.8 GHz, when the RF power output from the synthesizer was fixed at 20 dBm. Lasing bandwidth shows a decreasing trend as the RF injection efficiency decreases in this RF frequency range (see Figure 4.2.3). In order to ensure that the power injected into the QC-device is the same, the RF power was then scaled in accordance with the RF injection efficiency. The red curve records the maximal lasing bandwidth for various external cavity lengths in this case. There appears to be a rising tendency in the lasing bandwidth, which may be associated with the decreasing ratio of cavity round-trip time versus gain recovery time $\frac{\tau_{rt}}{\tau_g}$. However, we are unable to eliminate the impact of optical feedback because, as the cavity length was adjusted, the optical feedback's condition changed, potentially affecting the lasing bandwidth under strong modulation.

4.4.2 Metasurface design

Theoretically, we expect the QC-metasurface to possess a broader gain bandwidth as well as a smaller GDD, which is favorable for the generation of a broadband frequency comb or shorter THz pulses. For this reason, we switched to a different QC-metasurface with a double-patch design (labeled as VA1035-DP) and paired it with a high reflective output coupler (P10-A4) to make a QC-VECSEL with an external cavity length of ∼31 mm. The double-patch metasurface is sketched in Figure 4.4.3(b) that in a periodic unit cell of 36 μm by 48 μm, two patches have the same length of 11 μm but slightly different widths of 16 μm and 12 μm. The FEM-simulated metasurface reflectance and GDD are plotted in Figure 4.4.3(a), indicating a simulated gain bandwidth $\approx$ 1 THz and GDD $\leq$ 0.4 ps^2.

As discussed in Section 1.6.3, coupled non-degenerate unit cells in a double-patch metasurface design enable a broad spectral response, while the patch-based unit cells allow for a relatively low heat dissipation for CW biasing. This metasurface is injected with 20 dBm RF

power at appropriate frequency $f_{RF} \approx f_{BN}$. The maximum lasing bandwidth is recorded in Figure 4.4.3(c) with an estimated value of ~250 GHz, which is substantially broader than prior results using a single-ridge metasurface. This suggests that double-patch metasurfaces are preferred in the investigation of QCL frequency comb/mode-locking.

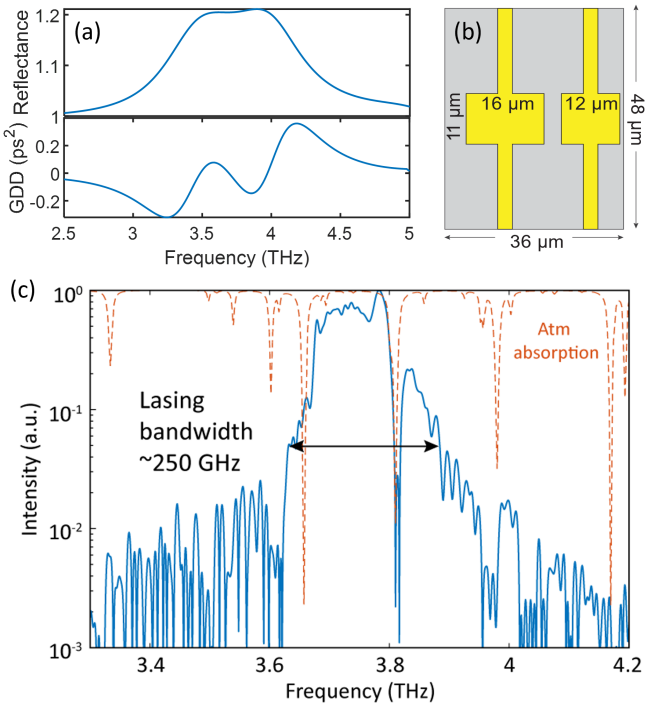

Figure 4.4.3: Double-patch metasurface provides broader gain bandwidth and lower GDD compared with single-ridge designs. Its dimension is sketched in (b) with corresponding FEM-simulated reflectance and GDD plotted in (a). Under 20 dBm RF power at $f_{RF} \approx f_{BN}$, the maximum lasing bandwidth reaches ~250 GHz.

4.5 Harmonic and sub-harmonic RF injection

4.5.1 Improved RF injection efficiency

We optimized the RF package of the QC-device in accordance with the discussion in Section 4.2, and under harmonic and sub-harmonic RF injection, we saw unique experimental phenomena. To lower its parasitic capacitance, the QC-metasurface was first modified with a reduced size. In Figure 4.5.1(a), it is illustrated in comparison to the metasurface used in the

baseline experiment. Thanks to the OAP-focusing cavity design, the circulating THz beam is effectively confined within the central circular biased area with minimal spatial overlap with the lossy unbiased region. This is demonstrated by the 2D FEM full-wave eigenmode simulation shown in Figure 4.5.1(b-c), where the simulated threshold gain loaded in biased ridges — which is necessary to balance the overall losses — shows no increase for metasurfaces designed with a fixed bias diameter of 500 μm but reduced unbiased regions, i.e., the metasurface length is reduced from 1.5 mm (blue) to 0.8 mm (red) to 0.6 mm (yellow). The beam patterns are primarily confined within the biased ridges. This provides the feasibility of reducing the length of the ridges with no sacrifice of lasing performances. Additionally,

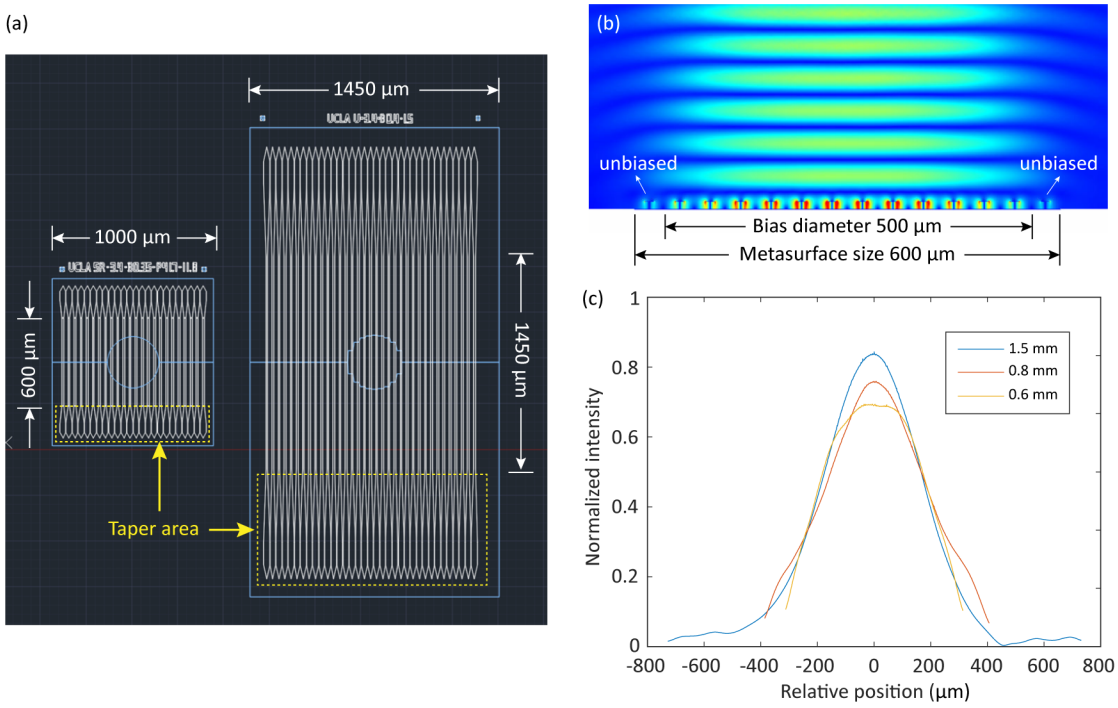

Figure 4.5.1: (a) Comparison of the metasurface designs of the RF-improved metasurface (left) and the one used in previous experiments (right). The new metasurface is designed with the ridge length shortened from 1450 μm to 600 μm and reduced taper area. (b-c) 2D FEM full-wave eigenmode simulation of the OAP-focusing cavity. The bias diameter of the metasurface is fixed at 500 μm, while its overall length is reduced from 1.5 mm (blue) to 0.8 mm (red) to 0.6 mm (yellow, where only one more ridge at each edge of the metasurface is unbiased as indicated in the E-field plot (b)). Simulation results indicate no increase in the threshold gain loaded in biased ridges that are required to balance the overall losses, and the beam patterns are mostly confined among the biased ridges (c).

the tapers at two ends of the ridges are deliberately made small in size. Considering that longer tapers could provide more reflection losses, the right taper dimension is selected to preserve the function of self-lasing suppression at the same time guaranteeing sufficient room for wire bonding.

Second, a well-designed PCB with 50 Ω coplanar waveguide (CPW) is used in replacement of the gold pad for electrical connection to the QC-metasurface to improve RF impedance matching (Figure 4.2.4). For this purpose, the ground metal of the metasurface is selected as gold instead of copper so that it may be exposed without oxidation after dry etching for wire bonding directly to the ground plane. For this reason, this metasurface was fabricated using Au-Au thermocompression bonding instead of Cu-Cu bonding. It, as well as the top metal

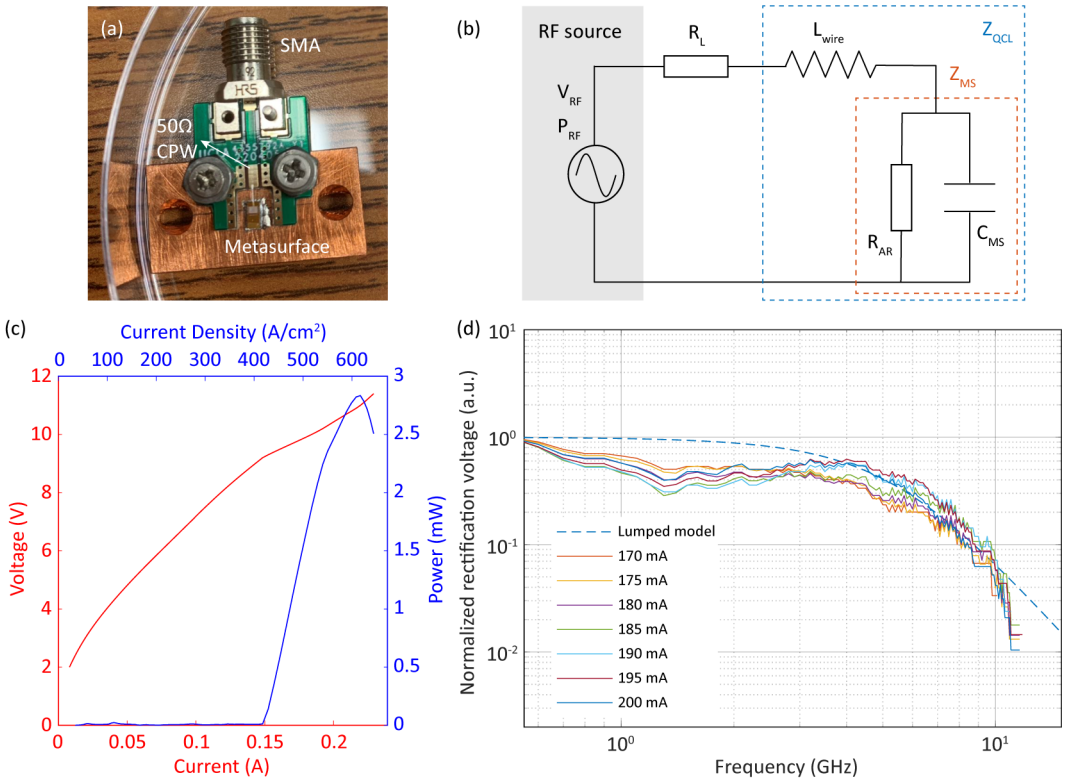

Figure 4.5.2: (a) A picture of the QC-metasurface with improved RF package, its equivalent lumped circuit model is sketched in (b). (c) The experimental CW $L-I-V$ of the device using a ∼99%-reflectance output coupler (P10-A4). (d) Measured rectification voltages as a function of RF modulation frequency are plotted at various bias currents and fit well with the lumped circuit model in (b).

layer, is wire bonded to the ground and signal ports of the CPW respectively, while the CPW is directly fed into a 50 Ω SMA connector that is screwed at the edge of the PCB. A picture of the QC-metasurface with the improved RF package is shown in Figure 4.5.2(a), labeled as VA1204-SR. It is paired with a ∼99%-reflectance output coupler (P10-A4) to make a QC-VECSEL, and its experimental $L-I-V$ measured in CW mode is plotted in Figure 4.5.2(c). To characterize the response of this QC-device to injected RF signal, microwave rectification measurement was performed, and the normalized rectification voltages measured at various bias currents are plotted in Figure 4.5.2(d) in solid curves. Compared with previous results in Figure 4.2.3, the RF injection efficiency of the new device is greatly improved with a 3-dB cutoff frequency increased to 4.5 GHz and 10-dB cutoff frequency increased to 8.4 GHz; no significant electrical resonance is observed. The experimental rectification voltage fits the lumped circuit model nicely, as seen by the blue dashed curve. The lumped circuit model is sketched in Figure 4.5.2(b) with the parallel capacitor coming from the gold pad removed.

4.5.2 RF injection locking phenomenon

The RF-improved device, VA1204-SR, was applied in a series of RF injection locking experiments. We maintained the DC bias current at 0.22 mA ($\approx 1.44 \times I_{th}$) and the RF power at 18 dBm (nominal output level from the RF synthesizer) as we swept the RF modulation frequency. THz emission spectra and the corresponding intermodal beat-note are recorded at the same time. The experimental findings obtained with various RF injection strategies are explained in detail below.

Fundamental injection

As the frequency of the RF injection signal f_{RF} is swept around the cavity round-trip frequency $f_{rt} \sim 3.89$ GHz, lasing bandwidth broadening and intermodal beat-note locking are observed, as plotted in Figure 4.5.3. The experimental phenomena are similar to the baseline experiments discussed in Section 4.1; the higher RF injection efficiency is most

likely the cause of the increased maximum lasing bandwidth and locking range. The locking range is estimated at ∼6.7 MHz. It is noted that within the locking range, there exist regions with pedestal or side peaks that suggest an unlocked beat-note; Figure 4.4.1 likewise shows a similar phenomenon.

In Figure 4.5.3(a), the lasing spectra are collected using Nicolet FTIR with a limited resolution of 7.5 GHz, which is not able to provide precise lasing bandwidths and FSRs. For this reason, we also present the high-resolution lasing spectra collected using a home-built FTIR with a nominal resolution of 0.75 GHz (discussed in detail in Section 5.3). Figure 4.5.4 plots the high-resolution FTIR spectra collected at different RF injection frequencies and clearly shows that the spacing between each two lasing modes is fixed at $1 f_{rt}$. At $f_{RF} = 3890.1$ MHz, a maximum lasing bandwidth of about ∼330 GHz is estimated; this is much larger than the ∼110 GHz achieved in the previous device VB0739-SR in Section 4.1. The dips in the spectra may be caused by water vapor absorption in the optical path.

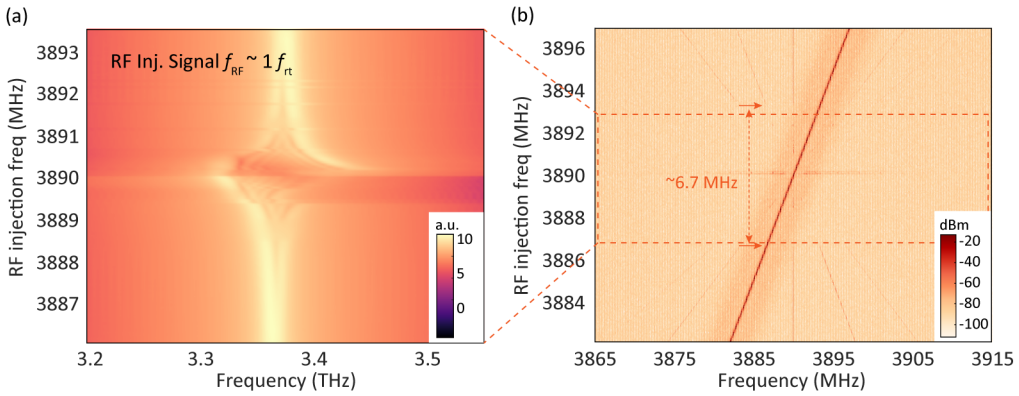

Figure 4.5.3: (a) Log scale lasing spectra and (b) corresponding beat-note collected as the RF injection frequency is swept around the cavity round-trip frequency $f_{RF} \approx 1 f_{rt}$. The red dashed box indicates the beat-notes collected in the same RF injection frequency range as the lasing spectra in (a). An injection locking bandwidth of ∼ 6.7 MHz is estimated and labeled in (b).

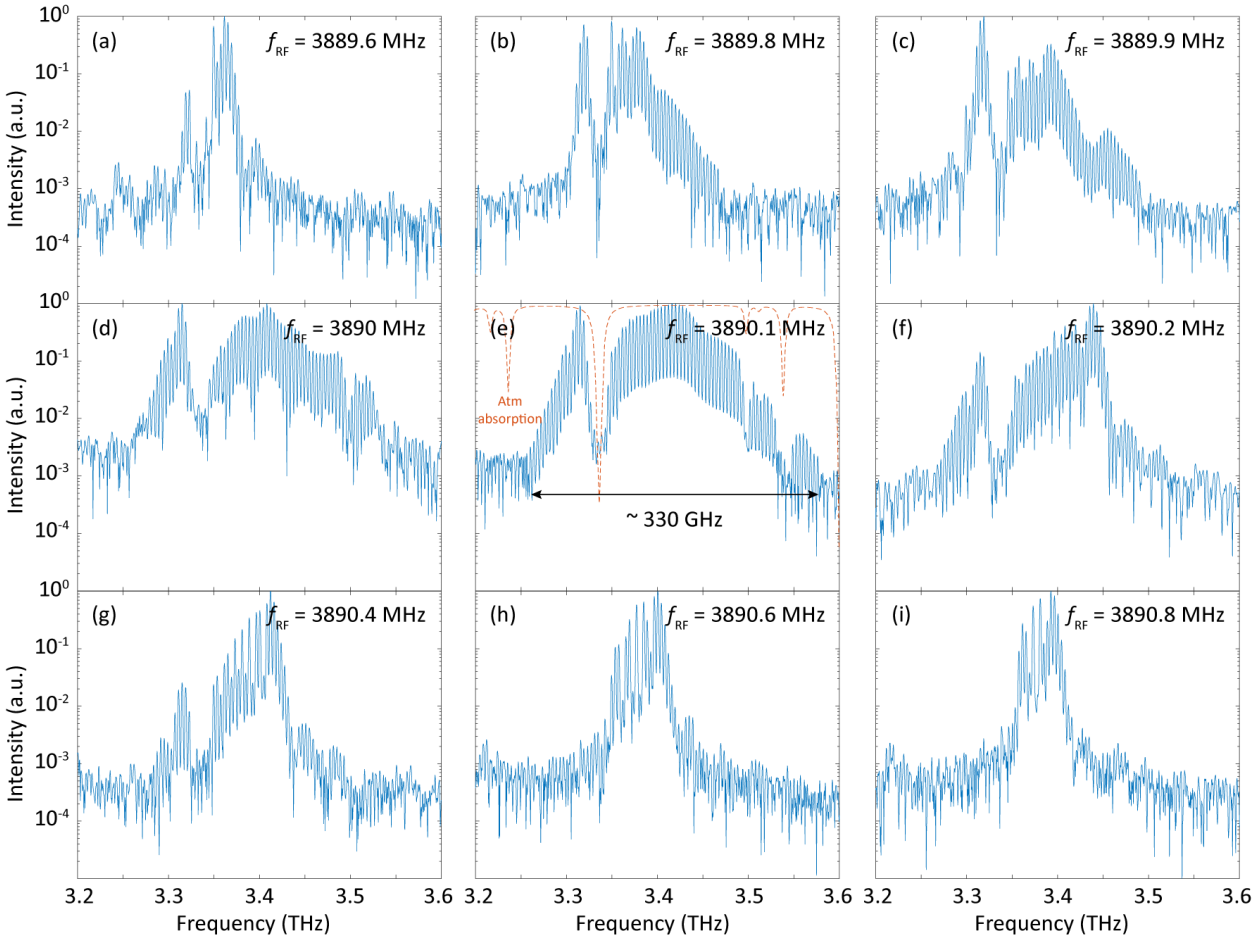

Figure 4.5.4: Fundamental injection. (a-e) High-resolution FTIR spectra collected at various RF injection frequencies. (e) The maximum lasing bandwidth around 330 GHz is observed at $f_{RF} = 3890.1$ MHz.

Harmonic injection

Thanks to the improved RF package, free-running beat-notes up to third-order harmonic frequency become detectable (Figure 4.5.5). This allows us to do what we call harmonic injection — injecting an RF modulation signal that is about twice or three times the round-trip frequency, i.e., ∼7.78 GHz and ∼11.67 GHz, respectively. THz emission spectra and corresponding beat-notes are plotted in Figures 4.5.6(a) and 4.5.6(b) under the conditions of second-order and third-order harmonic injection. Similar lasing bandwidth broadening is observed, while the "lobes" in the spectral maps appear to indicate an FSR increased to $2f_{rt}$ and $3f_{rt}$ compared to that in the case of fundamental injection — likely in a harmonic comb

state. At the same time, the second and third-order electrical beat-notes clearly demonstrate beat-note pulling and locking phenomena to the injected RF signal, with locking bandwidths estimated around 3.5 MHz and $\leq$4.3 MHz — the locking bandwidth in the case of third-order harmonic injection may be overestimated because the third harmonic beat-note signal is too weak in comparison with the injected RF signal and is close to the noise floor.

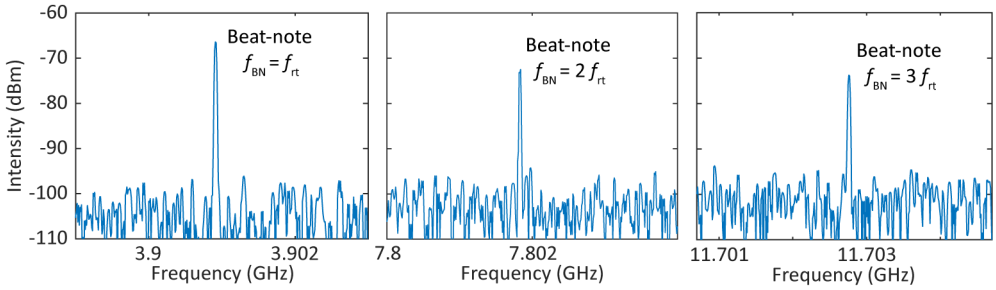

Figure 4.5.5: Free-running beat-notes at the cavity round-trip frequency and its harmonics are detectable in the RF-improved device.

On the other hand, Figures 4.5.6 and 4.5.7(b-j) present high-resolution FTIR spectra obtained at different RF injection frequencies. When the RF injection frequency is tuned around the second and third harmonics of the beat-note frequency, a conversion between the dense spectrum (where FSR is one round-trip frequency) and the harmonic spectrum (where FSR is equal to multiple round-trip frequencies) is observed. For instance, FSR at $1f_{rt}$ is reached at f_{RF} = 7779.9 MHz in Figure 4.5.6(c), where second-order harmonic injection is used, and is converted to $2f_{rt}$ at higher injection frequencies (d-h). The maximum lasing bandwidth is around 210 GHz, and there are around 24 detectable lasing modes. The spectra obtained under third-order harmonic injection are shown in Figure 4.5.7. Plots (b-c) display dense spectra with an FSR of $1f_{rt}$, whereas (e-f) depicts an intermediate in between the dense and harmonic spectra. It is transformed to a pure harmonic spectrum with an FSR of $3f_{rt}$ in (h-j), where the maximum lasing bandwidth is around 170 GHz with an estimated 14 modes.

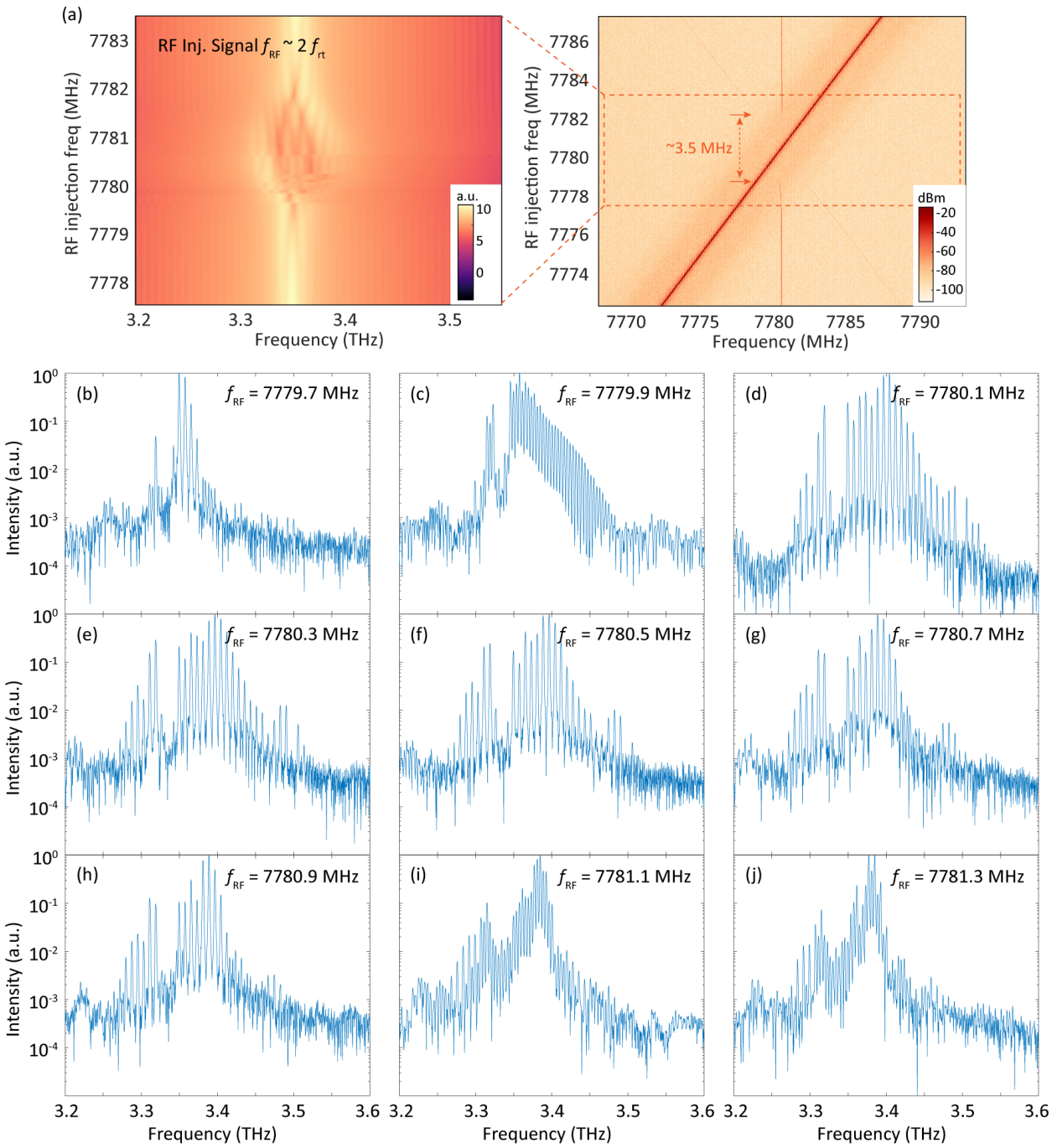

Figure 4.5.6: Second-order harmonic injection. (a) Log scale lasing spectra and corresponding beat-notes collected under second-order harmonic injection, i.e., $f_{RF} \approx 2f_{rt}$. The red dashed box indicates the beat-notes collected in the same RF injection frequency range as the lasing spectra. (b-j) High-resolution FTIR spectra collected at various RF injection frequencies. Lasing modes separation of $2f_{rt}$ is observed in (d-h).

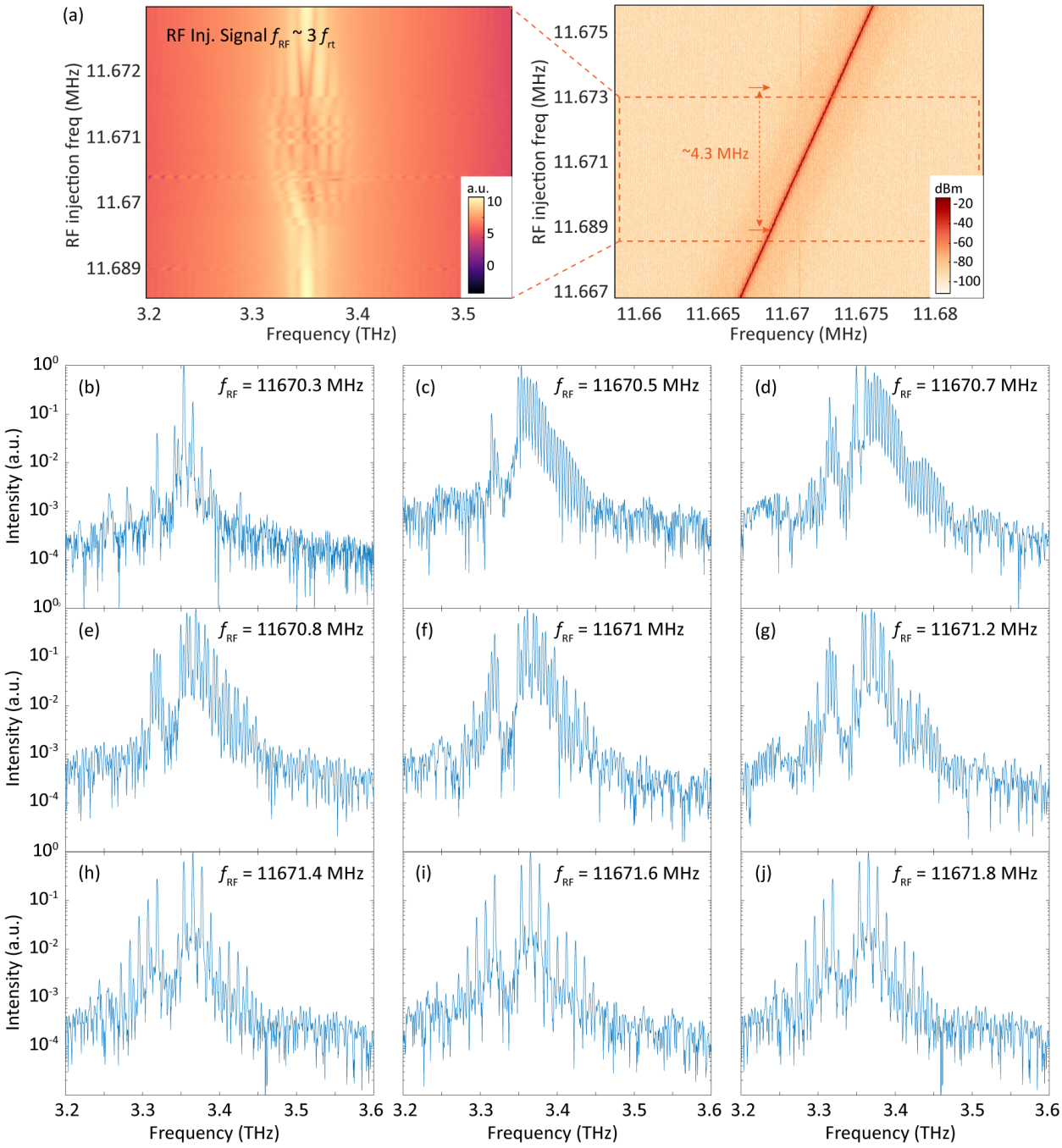

Figure 4.5.7: Third-order harmonic injection. (a) Log scale lasing spectra and corresponding beat-notes collected under third-order harmonic injection, i.e., $f_{RF} \approx 3f_{rt}$. The red dashed box indicates the beat-notes collected in the same RF injection frequency range as the lasing spectra. (b-j) High-resolution FTIR spectra collected at various RF injection frequencies. Lasing modes separation of $3f_{rt}$ is observed in (h-j).

Sub-harmonic injection

The inherently strong nonlinearity that arises in the QC-device allows an RF signal injected at the sub-harmonic frequency to lock its beat-note, which we refer to as sub-harmonic injection. Three phases illustrating this method are shown in Figure 4.5.8. First, an RF signal f_{RF} at a frequency of about $\frac{1}{2}f_{rt}$ ~1.95 GHz is input into a spectrum analyzer and is not sent into the QC-device. Consequently, Figure 4.5.8(a) displays a clean RF spectrum, and any harmonic signals resulting from the nonlinearity of the RF instruments need to be removed using an RF filter. Second, a harmonic signal of the injected RF signal is created at a frequency of about $1f_{rt}$ due to the nonlinearity of the QC-device when the sub-harmonic RF signal is fed into it. As seen in Figure 4.5.8(b), this occurs even in the absence of electrical bias and lasing activity. Third, the electrically biased device produces an intermodal beat-note signal at precisely $1f_{rt}$. It is recorded by the spectrum analyzer in addition to the

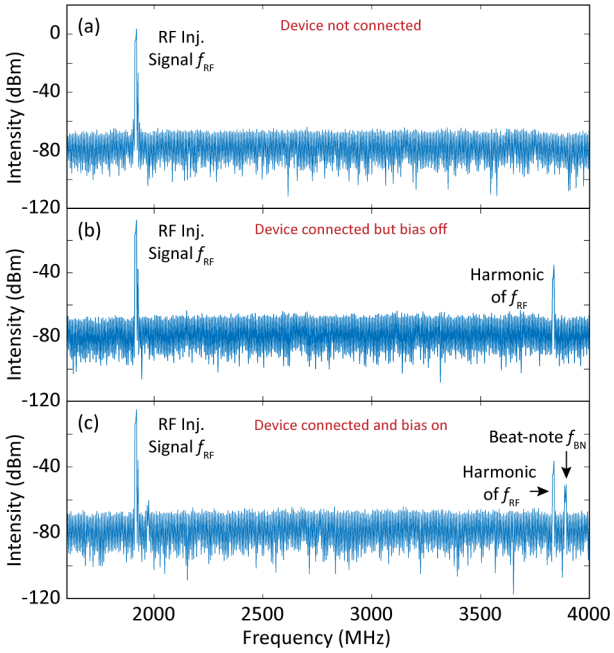

Figure 4.5.8: Illustration of sub-harmonic injection locking method. (a) An RF signal at $\sim \frac{1}{2}f_{rt}$ is input into the spectrum analyzer which is not sent into the QC-device. (b) The RF signal is fed into the QC-device which is turned off. A harmonic signal at $\sim 1f_{rt}$ is generated due to the strong nonlinearity of the QC-device. (c) As the device is turned on, a beat-note signal at exactly $1f_{rt}$ is observed and can be locked to the harmonic signal.

harmonic signal of f_{RF} and can be locked to the latter (Figure 4.5.8(c)).

The collected lasing and beat-note spectral maps as well as high-resolution FTIR spectra are collected as the RF injection signal is swept around half of f_{rt} in Figure 4.5.9 and one-third of f_{rt} in Figure 4.5.10. When comparing sub-harmonic injection to fundamental injection, much narrower lasing bandwidths and locking ranges are observed. For example, under $\frac{1}{2}$-harmonic injection, an estimated locking range of ~1 MHz is obtained, with a maxi-

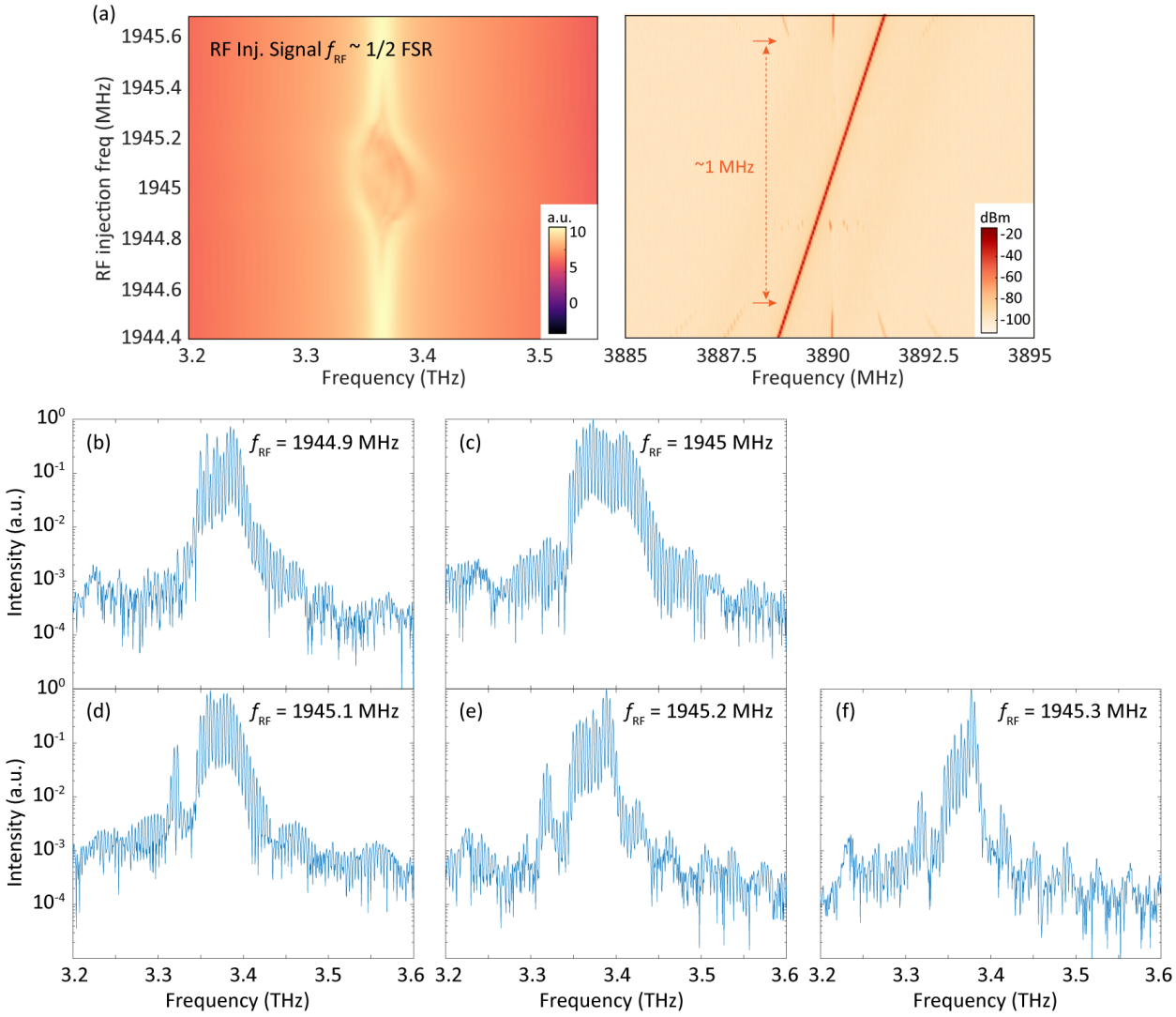

Figure 4.5.9: $\frac{1}{2}$-harmonic injection. (a) Log scale lasing spectra and corresponding beat-notes collected at $\frac{1}{2}$-harmonic injection, i.e., $f_{RF} \approx \frac{1}{2} f_{rt}$. (b-f) High-resolution FTIR spectra collected at various RF injection frequencies with lasing modes separation of $1 f_{rt}$.

mum lasing bandwidth of approximately 110 GHz; under $\frac{1}{3}$-harmonic injection, an estimated locking range of ∼13 kHz is obtained, with a maximum lasing bandwidth of approximately 50 GHz. This could be the result of an additional nonlinear process leading to lower RF modulation efficiency. It should be noticed that the spacing between each two lasing modes is $1f_{rt}$, meaning that dense spectra are produced under sub-harmonic injection. This strategy is thought to be helpful in certain circumstances, such as when a short cavity length of ∼10 mm generates an equivalent round-trip frequency up to 15 GHz, resulting in extremely strong RF losses and low RF injection efficiency for fundamental injection.

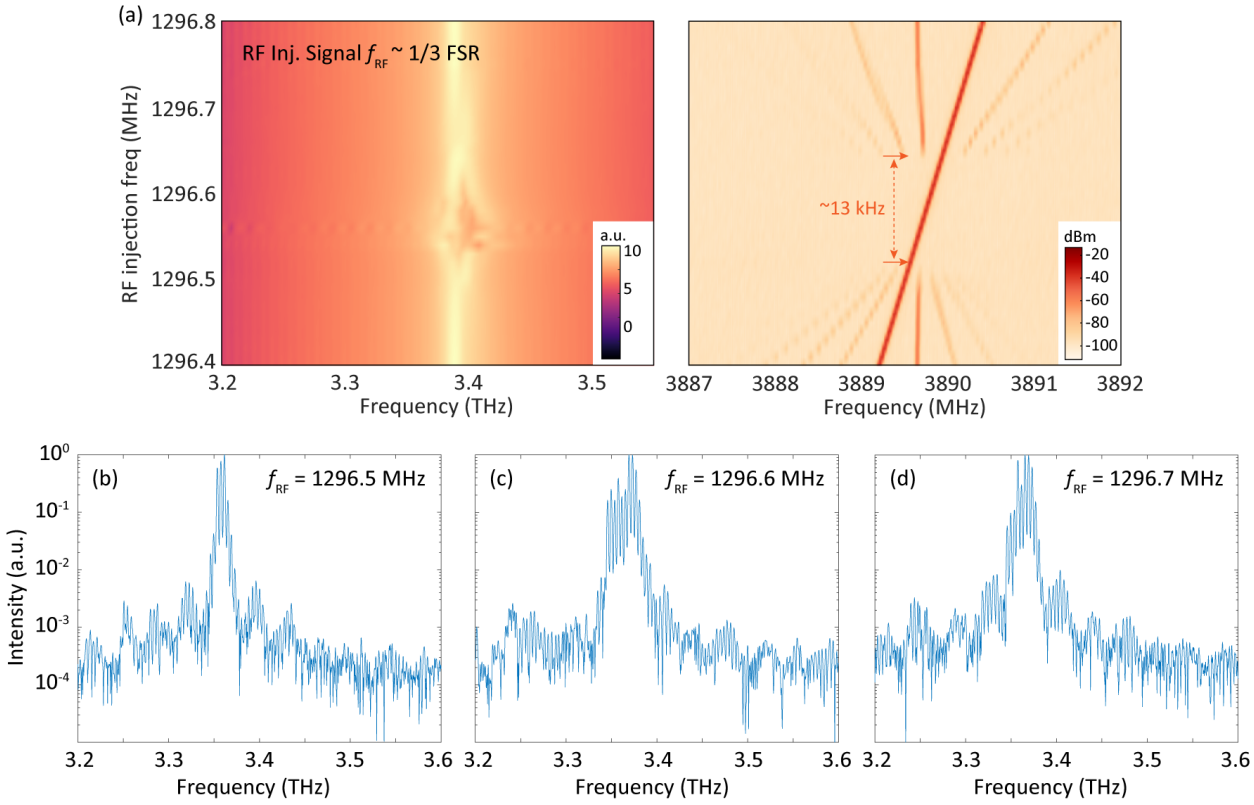

Figure 4.5.10: $\frac{1}{3}$-harmonic injection. (a) Log scale lasing spectra and corresponding beatnotes collected at $\frac{1}{3}$-harmonic injection, i.e., $f_{RF} \approx \frac{1}{3} f_{rt}$. (b-d) High-resolution FTIR spectra collected at various RF injection frequencies with lasing modes separation of $1f_{rt}$.

4.6 Reflectance compensation in the OAP-focusing QC-VECSEL

The technique introduced in Chapter 2 was also applied in an OAP-focusing QC-VECSEL. Restricted by the dimension of optical components, the minimum achievable external cavity length in the OAP-focusing cavity with an OAP mirror focal length of 12.7 mm is ~25 mm. In that case, we are not able to match each longitudinal mode with the output coupler reflectance oscillation. As a result, an external cavity length of ~30 mm and a silicon output coupler with a thickness of 3 mm are selected, where $L_c \approx 3 \times n_{Si} L_{OC}$. This encourages the formation of a harmonic spectrum by letting one of the three cavity longitudinal modes align with the output coupler reflectance peaks.

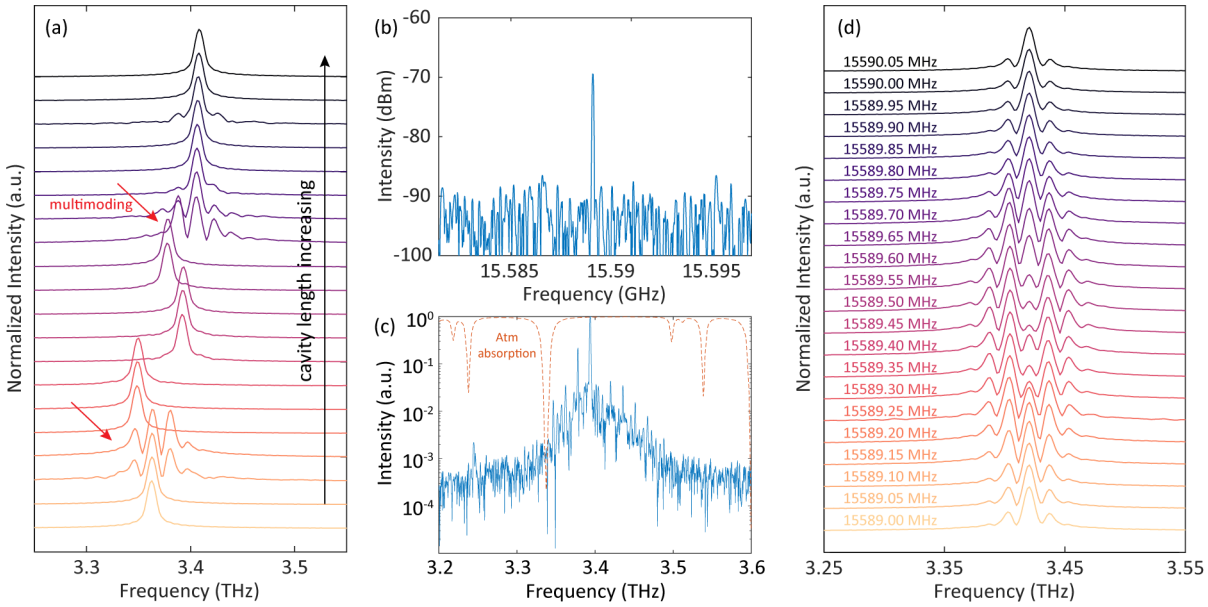

Figure 4.6.1: (a) Free-running spectra collected by Nicolet FTIR at various cavity lengths. Spectra showing multimode operation are highlighted by red arrows. (b) The corresponding free-running beat-note at the third-order harmonic frequency. (c) High-resolution FTIR spectrum indicating the generation of a harmonic spectrum with at least 9 lasing modes separated by $3f_{rt}$. (d) Lasing spectral broadening under 18 dBm RF modulation with RF injection frequency tuning around $3f_{rt}$.

The QC-VECSEL applied in experiments is made of QC-device VA1204-SR, which allows for CW biasing, and a 3 mm-thick silicon output coupler with metallic pattern P10-A4. The

output coupler was fixed on a piezoelectric stage for cavity length tuning around L_c ~30 mm. The experimental spectra collected using Nicolet FTIR are plotted in Figure 4.6.1(a) at stepping cavity lengths. It is noticed that at specific cavity lengths (pointed out by red arrows), the lasing spectrum is converted from a single lasing mode to multiple lasing modes, similar to the phenomenon demonstrated in Chapter 2. The spacing between each lasing mode is now three times the cavity round-trip frequency with a third-order harmonic beat-note generated around 15.59 GHz (Figure 4.6.1(b)). A high-resolution FTIR spectrum is plotted in Figure 4.6.1(c) which indicates the generation of a harmonic spectrum with at least 9 numbers of free-running lasing modes. Besides that, we applied RF modulation to the same device at a specific cavity length that allows multimode operation. The device produces three free-running lasing modes in the absence of RF modulation; lasing bandwidth broadening is encouraged by RF modulation at an RF power of 18 dBm and a modulation frequency close to $3f_{rt}$ (Figure 4.6.1(d)). The number of lasing modes is very slightly increased from 3 to ~7, suggesting that the RF-induced bandwidth broadening is not very significant. The possible reason may be a low RF injection efficiency at a high RF frequency of ~15.6 GHz.

This initial experimental realization is significant in terms of its ability to trigger free-running multimode operation under CW operation. The observation of a single-peak, narrowband beat-note signal acts as a starting point for further research on spontaneous frequency comb generation in a THz QC-VECSEL. It can also act as an effective method to trigger harmonic combs by choosing an output coupler with a specific thickness. According to the theoretical model described in Chapter 2.3, fundamental reflectance compensation, where $L_c \approx n_r L_{OC}$, appears to be more effective and can trigger more free-running lasing modes in a wider spectral range. For this purpose, a thicker silicon substrate will be needed, e.g., it should be 1 cm-thick for an external cavity length of ~30 mm, or the external cavity length should be made smaller using a smaller-sized OAP with reduced focal length.

Chapter 5

Fourier-Transform Infrared Spectrometers: instrumentation and data processing

5.1 Introduction

FTIRs are the most commonly used infrared spectrometers in scientific and industrial applications for measuring the optical absorbance or transmittance of various samples. Its key component is a two-beam interferometer originally designed by Michelson in 1891, named the Michelson interferometer. The sketch of the Michelson interferometer is plotted in Figure 5.1.1. An ideal 50-50 beam splitter (BS) splits the input beam of radiation into two paths. The two beams are then reflected by a fixed and movable mirror, respectively, and eventually recombined at the detector. Their optical path difference (i.e., retardation) is therefore determined by the travel distance of the movable mirror. For different optical path differences, two beams will either constructively or destructively interfere and exhibit an intensity variation at the detector. The instantaneous intensity as a function of time delay

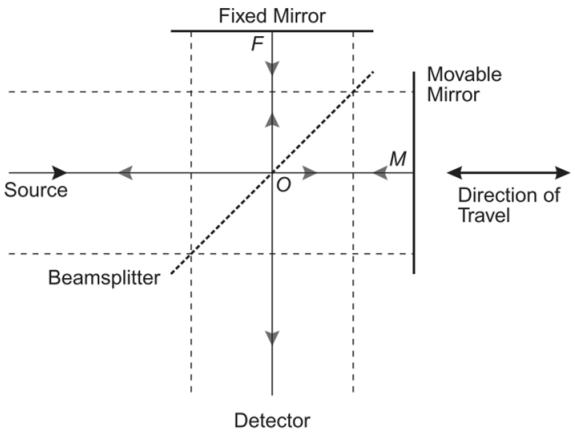

Figure 5.1.1: Sketch of the Michelson interferometer. Figure taken from Ref. [177]

τ caused by the path difference between two beams is given as:

$$S(t,\tau) = \frac{1}{2}(E(t)+E(t-\tau))^2 = \frac{1}{2}\sum_{n,m} E(\omega_n)E(\omega_m)e^{i(\omega_n-\omega_m)t}(1+e^{-i(\omega_n-\omega_m)\tau}+2e^{i\omega_n\tau}), \quad (5.1.1)$$

where the beams are expressed as a superposition of modes radiating at a frequency of ω_n, i.e., $E(t) = \sum_n E(\omega_n)e^{i\omega_n t}$. The actual signal that is recorded at the detector in FTIR is a time integral of the instantaneous signal; due to the typically slow response speed of the detectors used, the only component that survives is when $\omega_n = \omega_m$ and Eq. 5.1.1 is simplified to:

$$S_0(\tau) = \sum_n \langle |E(\omega_n)|^2 \rangle (1 + e^{i\omega_n\tau}). \quad (5.1.2)$$

$S_0(\tau)$ is defined as the time integral of the instantaneous signal $S(t,\tau)$. It contains two terms: a non-interferometric DC term that can be eliminated because of its wavelength independence, and an interferometric AC term originating from light interference between two beams with different paths. Only the AC term contains the information needed for spectral analysis, whose expression is:

$$S_0(\tau) = \sum_n \langle |E(\omega_n)|^2 \rangle e^{i\omega_n\tau}, \quad (5.1.3)$$

It is also known as the interferogram (IFG).

Fourier Transform (FT) is applied to Eq. 5.1.3, transferring the term $e^{i\omega_n\tau}$ into a δ-function:

$$\mathscr{F}(S_0(\tau)) = \sum_n \langle |E(\omega_n)|^2 \rangle \delta(\omega - \omega_n). \tag{5.1.4}$$

$\mathscr{F}(S_0(\tau))$ contains all the spectral information, i.e., the radiation frequencies ω_n and relative intensity of each frequency $\langle |E(\omega_n)|^2 \rangle$, and is called an intensity spectrum. Conclusively, for monochromatic radiation, the collected IFG displays a simple sinusoidal oscillation, and FT extracts a single radiating frequency as $\delta(\omega - \omega_0)$ in the intensity spectrum. If there are several radiation sources at various frequencies, the collected IFG will be a superposition of multiple sinusoidal oscillations, with the strength of each oscillation being determined by the radiation intensity at each frequency. After FT, the spectral information can be extracted and displayed in the intensity spectrum.

For the generalization to continuous frequency distribution, we replace the summation in Eqs. 5.1.3 and 5.1.4 with an integral over frequency to obtain the basic FT-series for FTIR [168], [177]:

$$S_0(\tau) = \int_{-\infty}^{\infty} B_0(v) e^{i2\pi\nu\tau} d\omega \tag{5.1.5}$$

$$B_0(\nu) = \int_{-\infty}^{\infty} S_0(\tau) e^{-i2\pi\nu\tau} d\tau, \tag{5.1.6}$$

where $B_0(\nu)$ is the intensity spectrum of corresponding IFG $S_0(\tau)$. It should be noted that the collected IFG is purely real, which means that its FT should contain all spectral information on the positive frequency domain. This provides the possibility to construct any intensity spectrum by collecting IFGs from the 'zero-path-difference (ZPD)' point to infinity. Specifically, ZPD denotes the position of $\tau = 0$, where the movable mirror has the same distance to the BS as the fixed mirror. For monochromatic radiation, it is not significant; however, if there exist multiple radiation at various frequencies, a center-burst

will be produced at ZPD due to constructive interference of all the radiation (see Figure 5.2.1).

The study of FTIR in this chapter includes mainly two parts: 1) Interferometer buildup and collection of IFG; 2) appropriate data processing to convert the IFG into a high-quality spectrum. We will go into more detail about these two parts in combination with the actual FTIRs used. In Section 5.2, we will talk about data processing techniques for better spectral analysis based on the IFGs collected using a commercial relative low-resolution Nicolet 8700; in Section 5.3, we share our experience on building an FTIR with sub-GHz frequency resolution and provide some details on instrumentation and sampling.

5.2 Spectral analysis

5.2.1 Discrete Fourier Transform and nominal resolution

In the previous section, we made the assumption that IFG is a continuous function of τ with infinite extension. However, in the real case, IFG is sampled discretely as

$$\tau_n = n \cdot \Delta\tau, n = 0, 1, 2, ...N, \tag{5.2.1}$$

where $\Delta\tau$ is the sampled time delay spacing; its length is determined by the maximum traveling distance of the movable mirror d_m, i.e., $\Delta_{IFG} = N\Delta\tau = \frac{2d_m}{c}$. Therefore, Discrete Fourier Transform (DFT) is required, and the sampled IFG results in a sampled spectrum where

$$\nu_k = k \cdot \Delta\nu, k = 0, 1, 2, ...N. \tag{5.2.2}$$

Considering we have a doublet with a frequency separation of $\Delta\nu = \nu_1 - \nu_2$, each frequency generates a sinusoidal wave in the IFG that becomes out of phase away from the ZPD point and back in phase after a time delay of $\Delta\nu^{-1}$. To spectrally distinguish this doublet, the

length of IFG has to be long enough for the two waves to become in phase for at least the first time after ZPD, which means that $\Delta_{IFG} = \Delta\nu^{-1}$. The frequency resolution is therefore limited by the length of the IFG, i.e., $\Delta\nu = \frac{1}{\Delta_{IFG}}$, which is often referred to as the nominal resolution. It should be pointed out that, as we stated in the previous section, the DFT of IFG ranging from $\tau = -\Delta_{IFG}$ to $\tau = 0$ contains the same spectral information as that of IFG from $\tau = 0$ to $\tau = \Delta_{IFG}$. Therefore, instead of double-sided IFGs, which require double mirror traveling distance but yield the same frequency resolution, modern FTIRs record long single-side asymmetric IFGs with a very short double-side part in the beginning for phase correction.

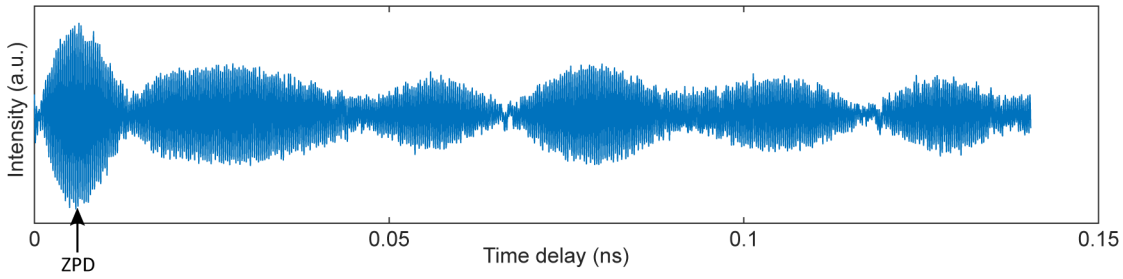

Figure 5.2.1: Using a Nicolet 8700 FTIR, an interferogram was recorded in an RF injection-locked QC-device at an RF power of 20 dBm. The corresponding lasing spectrum was presented in Figure 4.1.4(c). ZPD point is labeled where a center-burst shows up.

An example IFG collected using our Nicolet 8700 FTIR is given in Figure 5.2.1, where the ZPD point is labeled at the beginning of the IFG. It was collected in the case discussed in Section 4.1 when the QC-device was RF modulated to induce a broad lasing spectrum; the corresponding lasing spectrum was presented in Figure 4.1.4(c). Due to the limited mirror traveling distance, the resolution of Nicolet FTIR is 7.5 GHz. It is not enough to resolve the spectrum with a frequency separation of 4.8 GHz generated by this device. As a result, the sinusoidal waves originating from each lasing mode fail to come back in phase to produce another center-burst in the IFG. This, unfortunately, prevents us from doing further frequency comb analysis as described in Ref. [52]. In Ref. [52], the author introduced a useful technique to confirm the comb state by comparing the symmetry and periodicity of the measured IFG envelope; for precisely equidistant modes, the IFG should repeat itself

exactly after each time delay of f_{BN}^{-1}. Conversely, if the modes are not equally spaced, there will be a noticeable asymmetry during one IFG period because the beatings from each mode pair will become out of phase as the time delay increases. This method, therefore, requires the length of IFG to be at least $\Delta_{IFG} = f_{BN}^{-1}$.

5.2.2 Spectral leakage and apodization

The finite length of IFG leads to an unwanted effect called spectral leakage, where DFT interprets the real IFG as an infinite periodic signal truncated by a Boxcar/rectangular window with the same length as the IFG, i.e., $S_{real}(\tau) = S_0(\tau) \cdot T_{boxcar}(\tau)$. The FT of the product of two functions is therefore the convolution of the FT of each function, where the FT of the boxcar function is a Sinc function and is referred to as the instrumental line shape (ILS):

$$\mathscr{F}(T_{boxcar}(\tau)) = \Delta_{IFG} sinc(\pi\nu\Delta_{IFG}) \tag{5.2.3}$$

The ILS then convolves each signal frequency component, producing side modes in the resulting intensity spectrum $B_0(\nu)$. As depicted in Figure 5.2.2 taken from Ref. [168], we assume that there is only a single-frequency signal (green arrow). It generates a Sinc function line shape due to convolution (green dashed curve). It should be noted that the ILS in Eq. 5.2.3 has nodes at frequencies of $\frac{k}{\Delta_{IFG}}, k = 0, 1, 2, ...N$, which is exactly the DFT sampling frequencies v_k in Eq. 5.2.2. In general cases, the signal frequency does not coincide with the DFT sampling frequencies (grey arrows), which causes the single-frequency signal to leak into other frequencies in the resulting spectrum (red lines). If more than one signal is present, the DFT-derived final intensity spectrum will consist of the sum of all the signals with Sinc-lineshapes that are mapped to the sampling frequencies. This phenomenon is, therefore, called spectral leakage.

A standard method to mitigate the effects of spectral leakage and change the ILS function is through apodization. The functions to apodize the IFG are called window functions.

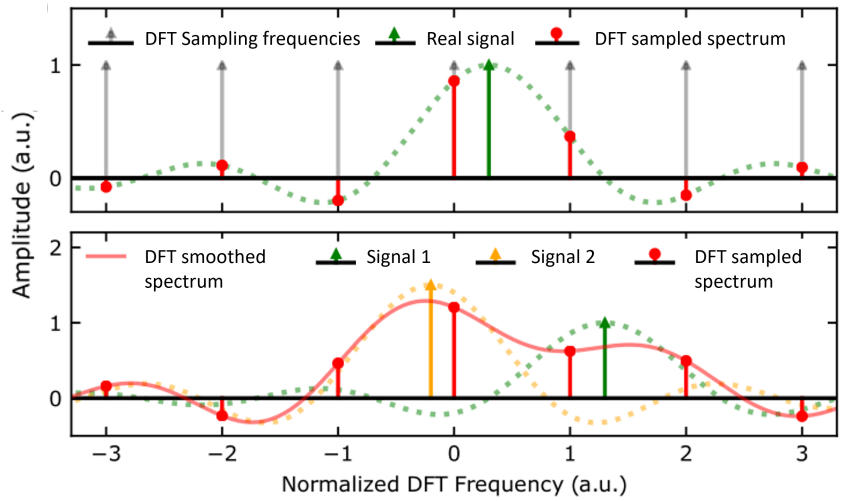

Figure 5.2.2: Illustration of spectral leakage due to convolution of the measured spectrum (green) with an ILS function (green dotted curve), which is mapped to DFT sampling frequencies (red). Figure modified from Ref. [168].

Some of the examples are the boxcar, triangular, Blackman, or Hanning window. They are all designed to reduce spectral leakage into the side lobes. However, side lobe suppression always comes with main lobe broadening; therefore, an appropriate choice of window function depends on the exact target of spectral analysis. Specifically, our Nicolet FTIR uses an asymmetric Happ-Genzel function for apodization. The Happ-Genzel function is centered at the ZPD point, while the interferogram before the ZPD point is apodized with a ramp function from 0 to 1, as plotted in Figure 5.2.3(a) in blue. The frequency response of such an asymmetric window function is plotted in 5.2.3(b) in blue. It shows that the main lobe has a 3-dB bandwidth of 8.3 GHz, which is slightly higher than the nominal resolution of 7.5 GHz, and a 20-dB bandwidth increased to 41.3 GHz with significant spectral leakage. By applying such a window function to the example IFG shown in Figure 5.2.1, we obtained a corresponding intensity spectrum after performing DFT. It is plotted on top of the frequency response of the asymmetric window function (which is frequency-shifted to match one of the lasing peaks) in Figure 5.2.4(a). The broad "shoulders" of the spectrum are then clearly seen to be artifacts originating from the ILS of the chosen window function rather than unresolved real lasing modes.

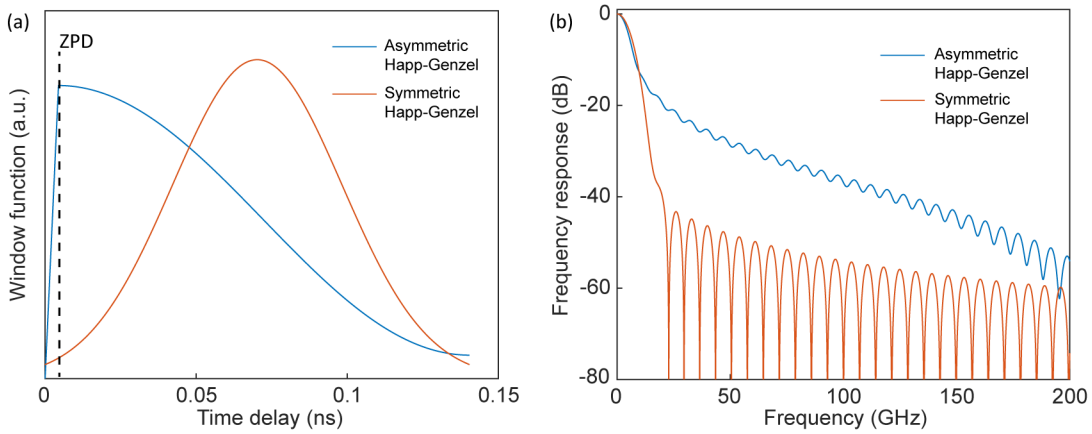

Figure 5.2.3: (a) Asymmetric (blue) and symmetric (red) Happ-Genzel window functions and (b) corresponding frequency responses. The length of the window functions matches that of the IFG in Figure 5.2.1, where the ZPD point is labeled in the asymmetric window function.

The artificial spectrum "shoulders" leads to confusion in determining the actual lasing modes; for example, if there exists a mode with an intensity 20 dB lower than its adjacent mode, it may not be properly resolved. To solve this problem, we reprocess the same interferogram by applying a symmetric Happ-Genzel window function. The symmetric window function and its frequency response are plotted in Figure 5.2.3 in red in comparison with the asymmetric ones. Its frequency response indicates a slightly higher 3-dB bandwidth of 9.2 GHz, but the 20-dB bandwidth is reduced to 23.9 GHz as a trade-off. The corresponding

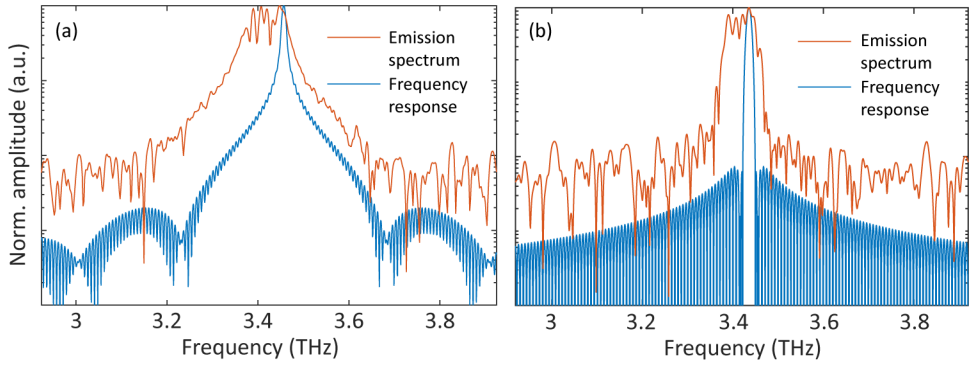

Figure 5.2.4: DFT of the IFG in Figure 5.2.1 applying asymmetric (a) and symmetric (b) Happ-Genzel window functions (red). The frequency response of each window function used is plotted on top of the intensity spectra for comparison, whose peak is centered at one of the lasing peaks (blue).

intensity spectrum is plotted in Figure 5.2.4(b) with a well-defined lasing bandwidth, which gets rid of the effect of artificial side modes. However, it should be noted that the symmetric window function cuts off a portion of the interferogram as the center-burst with the highest signal strength is located near the beginning of the IFG, where the window function has a small value of about 0. In some situations, this can result in spectral information loss and a poor signal-to-noise ratio, particularly if only one strong center-burst is collected in the finite IFG length. For a better illustration, we apply DFT to the IFG in Figure 5.2.1 with different lengths of the front part being cut off, i.e., the IFGs used in DFT begin at different locations with respect to the ZPD point (Figure 5.2.5(a)). The same boxcar window function is applied to get rid of the effect of apodization. The corresponding emission spectra are plotted in Figure 5.2.5(b), which indicates that the cutoff of IFG center-burst not only results in worse frequency resolution but also causes mode loss and narrows the actual spectrum bandwidth. This means that there might be more lasing modes than those shown in the spectrum in Figure 5.2.4(b) using the symmetric window function.

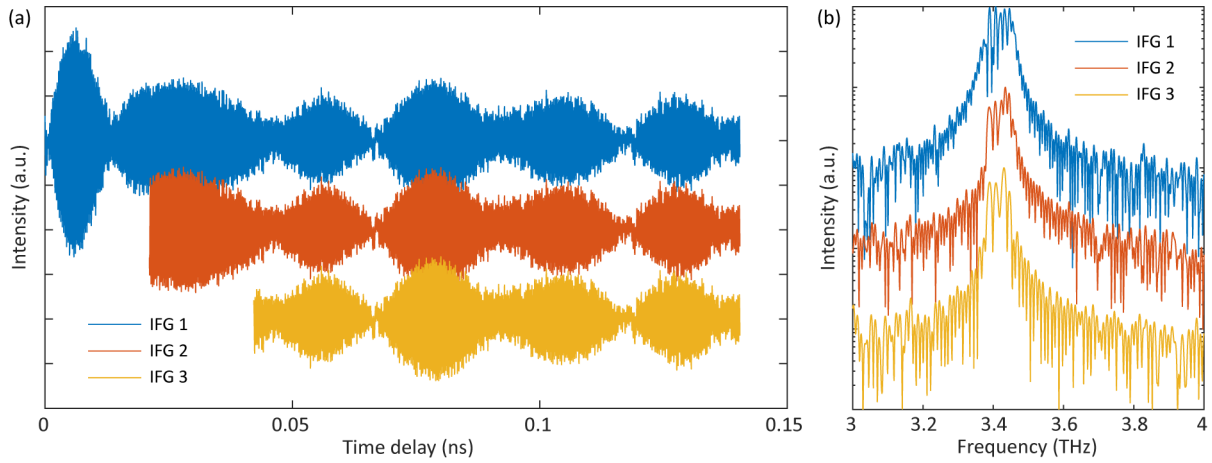

Figure 5.2.5: (a) IFGs with different cutoffs. IFG 1 (blue): full IFG as Figure 5.2.1; IFG 2 (red): the first 10000 sampling points being cut off; IFG 3 (yellow): the first 20000 sampling points being cut off. The corresponding intensity spectra are plotted in (b), which indicates that a higher cutoff of IFG leads to narrower spectrum bandwidth (Offset for clarity).

Considering the limitations of both symmetric and asymmetric window functions, the best IFG processing approach will be explored in the next section, in which the asymmetric

window function is used in conjunction with a specific phase correction method. Phase correction takes the real component of the asymmetric window function's frequency response rather than its absolute value, enabling better frequency resolution and efficient spectral leakage suppression [168].

5.2.3 Phase correction

In Eqs. 5.1.5 and 5.1.6, we consider the ideal case when the collected IFGs are real and even functions, i.e., they are symmetric with respect to the ZPD point. However, in real measurements, multiple effects can cause asymmetry in the collected IFGs, which results in complex intensity spectra according to the symmetry properties of FT: *If $f(t)$ is real and even, $\mathscr{F}(f(t))$ is purely real and even; If $f(t)$ is real and odd, $\mathscr{F}(f(t))$ is purely imaginary and odd.* The complex spectrum $B(\nu)$ has an expression of:

$$B(\nu) = Re(B(\nu)) + i * Im(B(\nu)) = B_0(\nu)e^{i\theta_{tot}} = \int_{-\infty}^{\infty} S(\tau)e^{-i2\pi\nu\tau}d\tau, \tag{5.2.4}$$

where $S(\tau)$ is the collected asymmettic IFG and $B_0(\nu)$ is the purely real true spectrum. The imaginary component of the complex spectra can also be represented as a frequency-dependent phase term θ_{tot}, which can be considered as a contribution from different components according to [177], [178]:

$$\theta_{tot}(\nu) = \theta_{DC} + \theta_l(\nu) + \theta_{NL}(\nu) + \theta_{ram}. \tag{5.2.5}$$

1) The DC component θ_{DC} is due to sources such as inverting amplifiers and high-pass filters in the detector readout electronics. 2) Linear phase error $\theta_l(\nu)$ arises from the sampling effect, where the exact ZPD is not sampled but the sampling point is before the ZPD by a value of ϵ. The wrong assumption of ZPD results in a delay shift of the whole IFG as $\theta_l(\nu) = 2\pi\nu\epsilon$. 3) The nonlinear phase component, $\theta_{NL}(\nu)$, may come from nonlinear electronic signal processing or optical components such as a dispersive beam splitter or

optical filter. 4) Random phase error θ_{ram} accounts for the effects of noise during IFG collection, e.g., optical and electrical noise of the detector, as well as mechanical vibration in optical delay measurement.

Phase correction is the process of retrieving the true spectrum $B_0(\nu)$ from the complex output $B(\nu)$ of the FT. The most straightforward method is taking the absolute value of $B(\nu)$, i.e., $|B(\nu)| = \sqrt{Re(B(\nu))^2 + Im(B(\nu))}$ as we did in Section 5.2.2, which is often referred to as the power spectrum. However, this method accounts for the noise in both real and imaginary components and, in fact, doubles the noise with the true spectrum $B_0(\nu)$. A proper phase correction method includes the extraction of the phase error function $\theta_{tot}(\nu)$ according to Eq. 5.2.4:

$$\theta_{tot}(\nu) = arctan(\frac{Im(B(\nu))}{Re(B(\nu))}). \tag{5.2.6}$$

In practice, the phase error is a slowly varying function of frequency. Therefore, we don't necessarily need a full double-side IFG to calculate a high resolution $\theta_{tot}(\nu)$; instead, it can be adequately resolved and corrected based on a very short double-side part of the single-side IFG collected by modern FTIRs.

With the knowledge of $\theta_{tot}(\nu)$, there are mainly two commonly used methods for phase correction, which are known as Forman method and Mertz method [179], [180]. The Forman method converts the multiplication in the frequency domain into convolution in the time domain. By convoluting the collected asymmetric IFG with the FT of the phase error term, a phase-corrected, symmetric IFG $S_0(\tau)$ is obtained as:

$$B_0(\nu) = B(\nu)e^{-i\theta_{tot}} \Rightarrow S_0(\tau) = S(\tau) * \mathscr{F}(e^{-i\theta_{tot}}), \tag{5.2.7}$$

The Mertz method, on the other hand, does not involve convolution. As a result, it is less computational and is more commonly used in modern FTIRs. According to Eq. 5.2.4, the

true spectrum, which is purely real, has a simple expression of:

$$B_0(v) = B(v)e^{-i\theta_{tot}(v)} = Re(B(v))cos(\theta_{tot}(v)) + Im(B(v)sin(\theta_{tot}(v))). \tag{5.2.8}$$

Detailed steps for phase correction implementation can be found, for example, in [177], [181], [182]. It should be pointed out that an asymmetric window function is applied to the single-side IFG in the Mertz method, where the short double-sided part of the interferogram is apodized with a ramp function from 0 to 1. The ramp function has a value of 1/2 at the ZPD, which is different from the asymmetric window function in Figure 5.2.3. The effect of the ramp function can be understood by decomposing it into a boxcar function with a value of 1/2 and a ramp across the ZPD. Due to the symmetry properties of FT, the even boxcar function contributes only to the real part of FT; its value of 1/2 avoids counting the double-side part twice (the same double-side part is used twice for phase error calculation and DFT of the whole IFG). The odd ramp function, on the other hand, will not contribute to the final spectrum, which is purely real; its purpose is to suppress spectral leakage.

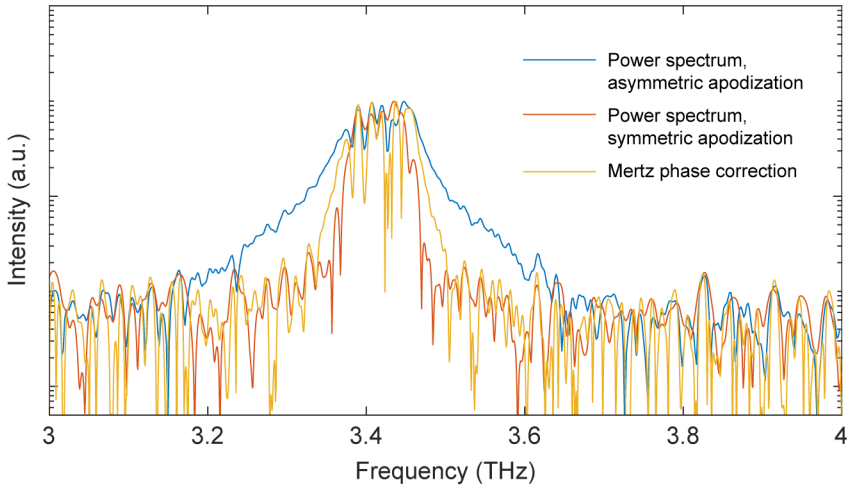

Figure 5.2.6: Comparison of the phase-corrected spectrum (yellow) with uncorrected spectra using asymmetric (blue) and symmetric (red) apodization. The phase-corrected spectrum is the same one as that presented in Figure 4.1.4(c) in Section 4.1.

We apply phase correction to the example IFG in Figure 5.2.1 based on the Mertz method.

Figure 5.2.6 compares the phase-corrected spectrum (yellow curve) with uncorrected ones. The blue curve shows the same spectrum as that in Figure 5.2.4(a) apodizing using an asymmetric Happ-Genzel function, and the red curve is the same as Figure 5.2.4(b) using a symmetric Happ-Genzel function. It becomes obvious that the closely spaced lasing modes are better resolved in the phase-corrected spectrum. By taking the real component of the asymmetric window function, spectral leakage is effectively suppressed. At the same time, no IFG center-burst is cut off, which preserves all the spectral information and allows us to assess the exact lasing bandwidth more confidently. Better IFG processing results hold as long as phase correction works. However, it should be noted that meaningful phase information exists where the signal is present and everywhere else, or where the signal has a low intensity, the phase is actually random and relies on interpolation to give a value. If phase error is not properly retrieved or interpolated, the phase correction method may result in failure. For example, when a laser source with a limited bandwidth is used, a very short double-sided part of the IFG will produce a low-frequency resolution phase error. The phase error in this case may not be adequately mapped in the narrow lasing bandwidth, which could lead to worse spectral leakage after applying phase correction.

5.2.4 Sub-nominal resolution with frequency comb sources

We noted in Section 5.2.2 that the observed signal is convolved with an ILS function due to the truncation of optical path length, which causes spectral leakage when it is mapped at discrete DFT sampling frequencies (Figure 5.2.2). However, in a special case where all the signal frequencies now overlap with the DFT sampling frequencies, the ILS of each signal now has zero crossings at DFT sampling frequencies and will not produce side modes. Spectral leakage is eliminated in this case, as illustrated in Figure 5.2.7 (red curve). This situation can be realized using frequency comb sources in combination with certain DFT sampling procedures.

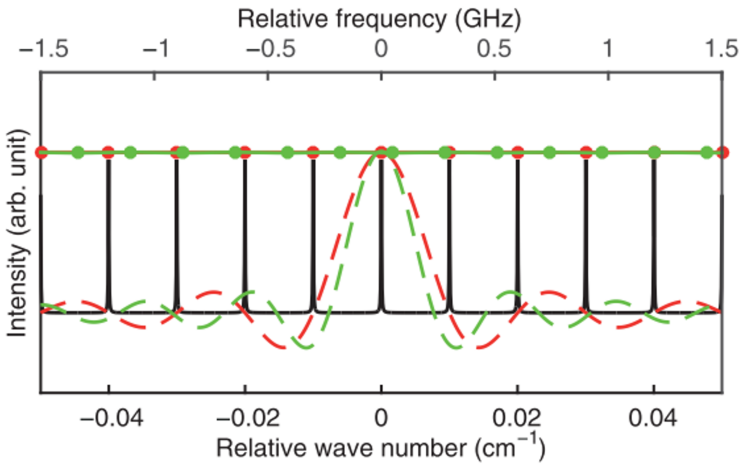

Figure 5.2.7: Illustration of spectral leakage of a frequency comb source. Green dots represent the DFT sampling frequencies in the case when they are not aligned with the comb lines and therefore generate spectrum leakage. A special case exists when the zero-crossings of the ILS of one comb line (red dashed curve) are at the positions of the neighboring comb lines, leaving them unaffected. Spectral leakage is eliminated in this case. Figure taken from Ref. [183].

As mentioned in Chapter 1, the frequency comb has a simple mathematical expression as $f_n = f_{ceo} + n \times f_{rep}$, where f_n is the frequency of the comb line with an index of n. Considering a simplified situation where $f_{ceo} = 0$, it is clear that when the length of collected IFG matches $1/f_{rep}$, i.e., spacing of DFT sampling frequencies is equivalent to comb repetition rate as $\Delta\nu = \frac{1}{\Delta_{max}} = f_{rep}$, each comb line naturally aligns with the DFT sampling frequency, giving an ILS-free spectrum after DFT. By zero-padding the IFG, one can precisely control the DFT sampling frequencies. However, it should be noted that in practice, the IFG is typically sampled at intervals corresponding to a simple fraction of the reference laser wavelength λ_{ref} (for example, the He-Ne laser is commonly used as a reference and will be covered in more detail in the next section). This results in a discrete number of DFT sampling frequency spacings as $\Delta\nu = \frac{1}{\Delta_{max}} = \frac{qc}{\lambda_{ref} N}$, where $\frac{\lambda_{ref}}{q}$ is the step size of moving mirror displacement and N is the total sampling number. On the other hand, the repetition rate of a frequency comb can be any continuous number. This indicates the existence of a small but unavoidable mismatch between f_{rep} and $\Delta\nu$, which leads to imperfection in eliminating the spectral leakage. Fortunately, given the extremely high number of sampling

points (10^6 in [184], for example), this mismatch is negligible. It can also be reduced by zero-padding the length of the IFG to a higher integer number of $1/f_{rep}$; additionally, it can be corrected to arbitrary precision through Fourier interpolation, as noted in Ref. [185].

The f_{ceo} of the comb typically has a nonzero value. In this case, the entire IFG should be multiplied by a factor of $e^{-2\pi i f_{ceo} t}$ in order to shift the corresponding spectrum in the frequency domain by f_{ceo} and match the positions of comb lines to sampling frequencies. This technique therefore requires a precise knowledge of f_{ceo} of the comb. While f_{rep} can be extracted precisely from the electrical beat-note of the device using a spectrum analyzer, f_{ceo} is traditionally measured through f-to-2f interferometry, which requires an octave-spanning source and becomes impractical for many cases. In Refs. [168], [185], another effective method has been introduced to estimate the value of f_{ceo} based on the phase shift in the collected IFG. It is known that the IFG of a frequency comb shows a center-burst at ZPD where all the comb lines constructively interfere, and several satellite center-bursts are separated by multiple integers of time delay $T_r = 1/f_{rep}$. The first satellite center-burst can be expressed as:

$$S_0(\tau + T_r) = \sum_n \langle |E(\omega_n)|^2 \rangle e^{i\omega_n(\tau + T_r)}, \tag{5.2.9}$$

where $\omega_n = \omega_{ceo} + n \times \omega_{rep}$. It is noted that while $e^{i\omega_{rep} T_r} = 1$, periodicity is not preserved in the IFG due to the existence of comb offset frequency — there is a relative phase shift $\Delta\phi$ in the satellite center-burst compared with the first center-burst at ZPD as:

$$\Delta\phi = Arg(\frac{\hat{S}_0(\tau + T_r)}{\hat{S}_0(\tau)}) = \omega_{ceo} T_r + \omega_{rep} T_r = \omega_{ceo} T_r + 2\pi. \tag{5.2.10}$$

Hilbert transformation has been applied to the real IFG $S_0(\tau)$ in Eq. 5.2.10 as follows:

$$\hat{S}_0(\tau) = S_0(\tau) + i\mathscr{H} S_0(\tau). \tag{5.2.11}$$

Benefited by the precise knowledge of T_r i.e., f_{rep}, and the accuracy of the reference laser

wavelength used for optical path difference measurement, the value of f_{ceo} can be directly extracted from the IFG containing at least one satellite center-burst.

Frequency comb-based spectrometers are free of the influence of spectral leakage that limits conventional FTIR spectroscopy. For a given optical path length, it allows a frequency resolution that is greater than the FTIR nominal resolution. For example, MHz-resolution spectra have been achieved using frequency comb-based FTIR with a millimeter optical path length, i.e., GHz-nominal resolution. This technique has been applied to resolve high-precision molecule absorption features using stabilized frequency comb sources [183], [185]. Additionally, this data treatment technique can be used to distinguish frequency comb from multi-mode operation. Spectral leakage will be largely eliminated if the laser source is a frequency comb; however, the same data treatment will result in higher spectral leakage if the lasing modes are not exactly equidistantly spaced [168].

5.3 Home-built high-resolution FTIR

5.3.1 Martin-Puplett Interferometer

The experimental setup of a home-built high-resolution FTIR is illustrated in Figure 5.3.1, where an ultralong delay line stage (Newport DL325) up to 325 mm is applied to achieve a nominal frequency resolution of 500 MHz. A wire-grid polarizer oriented at 45° is used as the THz BS. It consists of a regular array of parallel free-standing metallic wires, which are placed in a plane perpendicular to the incident beam. Electromagnetic wave with a polarization parallel to the wires induces the free movement of electrons along the length of the wires, and is almost completely reflected with an extra π phase shift as the metal wire array, in this case, behaves like a typical metal surface. On the contrary, electromagnetic wave with a polarization perpendicular to the wires is able to transmit through the polarizer, as the electrons cannot be excited very far across the width of the wire grids, which is typically in

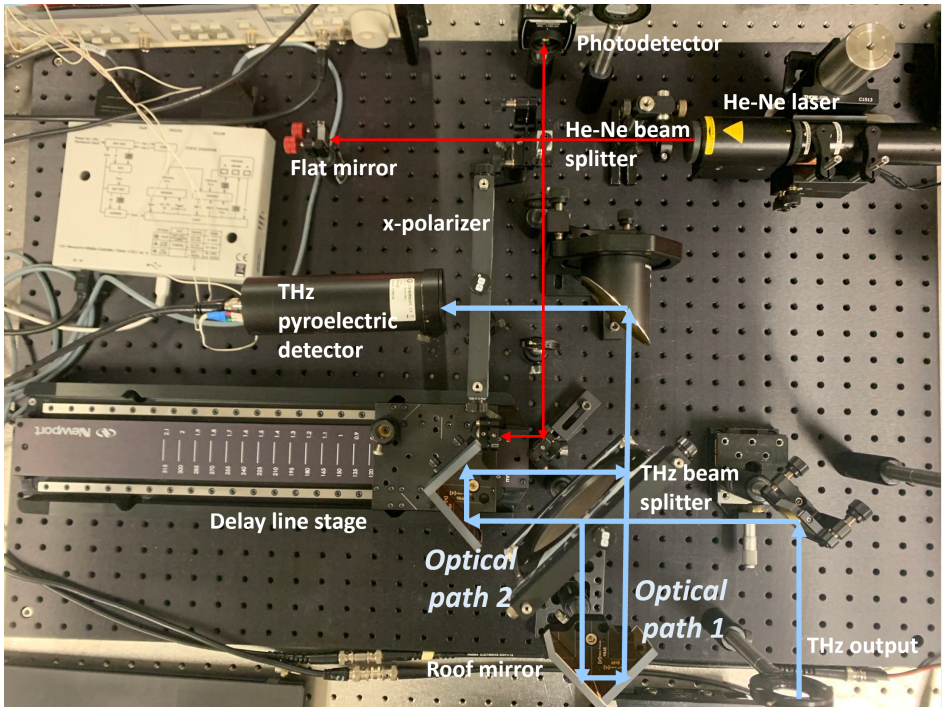

Figure 5.3.1: Experimental setup of the home-built high-resolution FTIR, including a THz interferometer (blue) and a He-Ne interferometer (red).

the micron range. Therefore, for the wire-grid polarizer oriented at a direction of $(\vec{\boldsymbol{x}} + \vec{\boldsymbol{y}})$, where $\vec{\boldsymbol{x}}$ is the horizontal direction and $\vec{\boldsymbol{y}}$ is vertical, THz wave incident from the QCL source with a horizontal or vertical polarization is split evenly into two components:

$$E_1(t) = -\frac{1}{\sqrt{2}} \sum_n E(\omega_n) e^{i\omega_n t} (\vec{\boldsymbol{x}} + \vec{\boldsymbol{y}}), E_2(t) = \frac{1}{\sqrt{2}} \sum_n E(\omega_n) e^{i\omega_n t} (\vec{\boldsymbol{x}} - \vec{\boldsymbol{y}}). \tag{5.3.1}$$

The incident THz wave is expressed as $E(t) = \sum_n E(\omega_n) e^{i\omega_n t}$. The reflected and transmitted THz waves $E_1(t)$ and $E_2(t)$ at the BS travel through optical paths 1 and 2, respectively. As they are reflected by the fixed and movable roof mirror, the incident field with a TE-polarization (electric field along the roof line, i.e., $\vec{\boldsymbol{y}}$ direction) will not change its polarization; the incident field with a TM-polarization will be reflected backward with opposite polarization. The expression of THz waves after reflection at the roof mirrors therefore

becomes:

$$E_1'(t) = \frac{1}{\sqrt{2}} \sum_n E(\omega_n) e^{i\omega_n t}(\vec{\boldsymbol{x}} - \vec{\boldsymbol{y}}), E_2'(t-\tau/2) = -\frac{1}{\sqrt{2}} \sum_n E(\omega_n) e^{i\omega_n (t-\tau/2))}(\vec{\boldsymbol{x}} + \vec{\boldsymbol{y}}), \quad (5.3.2)$$

where the time delay τ accounts for the optical path difference. These two THz waves then recombine at the wire-grid polarizer. $E_1(t)$ now has a polarization perpendicular to the wire-grid polarizer and will be transmitted; $E_2(t)$ has a polarization parallel to the wire-grid polarizer and will be reflected as:

$$E_1''(t) = \frac{1}{\sqrt{2}} \sum_n E(\omega_n) e^{i\omega_n t}(\vec{\boldsymbol{x}} - \vec{\boldsymbol{y}}), E_2''(t-\tau) = \frac{1}{\sqrt{2}} \sum_n E(\omega_n) e^{i\omega_n (t-\tau)}(\vec{\boldsymbol{x}} + \vec{\boldsymbol{y}}). \quad (5.3.3)$$

They have horizontal polarization and will not interfere with each other unless an extra polarizer is applied. That's the reason we have an $\vec{\boldsymbol{x}}$-polarized polarizer added before the THz pyroelectric detector. The instantaneous intensity of THz waves received by the detector is therefore:

$$S(t,\tau) = \frac{1}{2}(E_{1,\vec{\boldsymbol{x}}}''(t) + E_{2,\vec{\boldsymbol{x}}}''(t-\tau))^2 = \frac{1}{4} \sum_{n,m} E(\omega_n) E(\omega_m) e^{i(\omega_n - \omega_m)t}(1 + e^{-i(\omega_n - \omega_m)\tau} + 2e^{i\omega_n \tau}). \quad (5.3.4)$$

We retrieve the same expression as Eq. 5.1.1 in Section 5.1, with an extra factor of 1/2 as we lose half of THz intensity through the polarizers. This type of interferometer using wire-grid polarizers in combination with roof mirrors is named a Martin-Puplett interferometer. It should be noted that:

1. A Martin-Puplett interferometer requires the incident wave to have a horizontal or vertical polarization in order to evenly split the incident wave into two components, this condition is naturally satisfied in QC-VECSEL configuration. If the incident wave

is not evenly split, the intensity received by the detector will be modified as:

$$S(t,\tau) = \frac{1}{2}\frac{1}{\sqrt{x^2+1}}(E_1(t) + xE_2(t-\tau))^2, \tag{5.3.5}$$

where the intensity ratio between the reflected and transmitted portions is 1:x. In this case, an extra factor of $\frac{x}{\sqrt{x^2+1}}$ will enter the interferometric term in Eq. 5.1.3, which reduces the strength of both the interferogram and the resulting spectrum (Eq. 5.1.4). It is the same scenario if an uneven beam splitter is used in a conventional Michelson interferometer.

2. In reality, the wire-grid polarizer is not an ideal BS. Let us say the transmission is $T_\perp$ when the incident polarization is perpendicular to the wire grid polarizer; the transmission is $T_\parallel$ when the incident polarization is parallel to the wire grid polarizer. A parameter typically used to characterize a wire grid polarizer is the extinction ratio (ER), defined as $ER = \frac{T_\perp}{T_\parallel}$. In the case of a non-ideal wire-grid polarizer with $T_\perp < 1$ and $T_\parallel > 0$, an extra factor of $\Gamma \equiv T_\perp(1-T_\parallel) + T_\parallel(1-T_\perp)$ will enter the expression of $E_1''(t)$ and $E_2''(t-\tau)$ in Eq. 5.3.3. As a result, the interferometric term and the strength of the intensity spectrum will be reduced by a factor of Γ^2. Assuming a wire-grid polarizer with $T_\perp = 0.99$ and $T_\parallel = 0.01$, we have estimated values of $ER \approx 0.01$, $\Gamma^2 \approx 0.98$.

5.3.2 Interferogram sampling and data treatment

Precise values of the time delay or optical path difference are necessary for the correct extraction of the spectral information; these values are dependent upon the moving distance and speed of the delay line stage. Given the lack of a perfect motion stage that can move the mirror at a consistent and well-known speed, a more practical and reliable solution adopted in modern FTIRs would be to utilize a double-interferometer architecture — laser interferometer is constructed to facilitate the acquisition of a decent IR (THz) IFG. Its IFG

provides precise position data based on its well-defined operation frequency.

For this reason, we built a reference Michelson interferometer beside the THz interferometer (Figure 5.3.1). They share the same position information as their movable mirrors are fixed on a single delay line stage. Frequency-stabilized He-Ne laser (Newport, 25-STP-910) is used as the optical source, with an exact wavelength of λ_0=633 nm. To avoid optical feedback that may disturb frequency stabilization, an optical isolator is placed right after the He-Ne laser. The collected He-Ne IFG is ideally a cosine curve, as described in Ref. [177]:

$$I(\delta) = \frac{1}{2} I_0(\lambda_0)(1 + cos 2\pi \frac{\delta}{\lambda_0}), \tag{5.3.6}$$

where the optical path difference is related to twice the mirror displacement as $\delta = 2k_0\Delta d$. Therefore, the IFG repeats itself as the mirror moves a distance of $\Delta d = \frac{\lambda_0}{2}$. Assume a constant mirror speed of v_m, the IFG pattern is amplitude-modulated at a frequency of $f_{He-Ne} = \frac{\nu_m}{\Delta d}$. For example, for the mirror velocity of 1 mm/s used in our measurement, the IFG modulation frequency is $f_m = 32$ kHz.

The IFG modulation frequency sets the following parameters: 1) The photodetector used to capture He-Ne IFG should have a bandwidth over f_m, i.e., it should have enough responsivity to detect a fast oscillating signal. Otherwise, the collected IFG will have reduced intensity, or its pattern may be washed out. 2) The sampling rate is suggested to be at least two times larger than the modulation frequency in order to collect enough sampling points in a single period to better identify the cosine-shaped interference pattern. A lower sampling rate may result in inaccurate position information extraction. To obtain a sampling rate on the order of tens or hundreds of kilohertz, e.g., $f_{sam} = 200$ kHz in our case, the signal collected by the photodetector is later fed into a data acquisition hardware (DAQ). The DAQ we used (NI USB-6351) has a maximum sampling rate of 1.25 MS/s, and a USB port to communicate with the PC. It collects the He-Ne IFG and the THz IFG simultaneously. Both IFGs are then sampled at every peak, valley, or half-transition point of the cosine-shaped He-Ne IFG.

According to Eq. 5.3.6, the sampling points indicate a precise mirror displacement distance of $\lambda_0/4$. As a result, the THz IFG is guaranteed to be sampled with a constant displacement of the moving mirror, as illustrated in Figure 5.3.2.

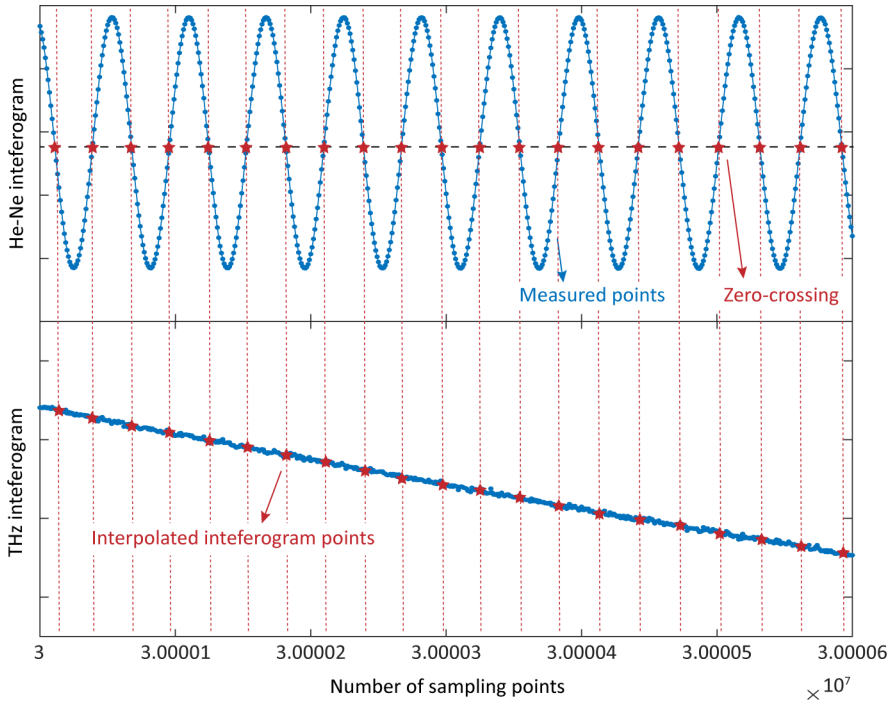

Figure 5.3.2: Synchronization of the collected He-Ne and THz IFGs. Mirror velocity is chosen as 1 mm/s and sampling rate as 200 kHz. Distances between sampling points (red dots) are exactly $\lambda_0/4$.

An example of resampled THz IFG is plotted in Figure 5.3.3(a) with respect to accurate values of time delay. It is collected in the same RF injection-locked QC-VECSEL as described in Section 4.1, i.e., the same QC-metasurface is applied in an OAP-focusing VECSEL cavity, and the injected RF power is 20 dBm with an injection frequency around the cavity round-trip frequency. Thanks to the ultralong delay line stage used, which has a length of 325 mm, the length of the collected IFG is $\Delta_{IFG} = \frac{2\times325}{c} \approx 2.16$ ns. It is equivalent to a nominal resolution of $\Delta\nu = \frac{1}{\Delta_{IFG}} \sim$500 MHz. In the IFG, multiple center-bursts are observed with a time interval of 0.28 ns. It indicates that the RF injection-locked QC-VECSEL operates in multiple lasing modes with an FSR around $\frac{1}{0.28e-9} \approx 3.52$ GHz. It is noted that as the mirror moves, the collected IFG shows decreasing strength; this might be the result of an

imperfect moving stage alignment.

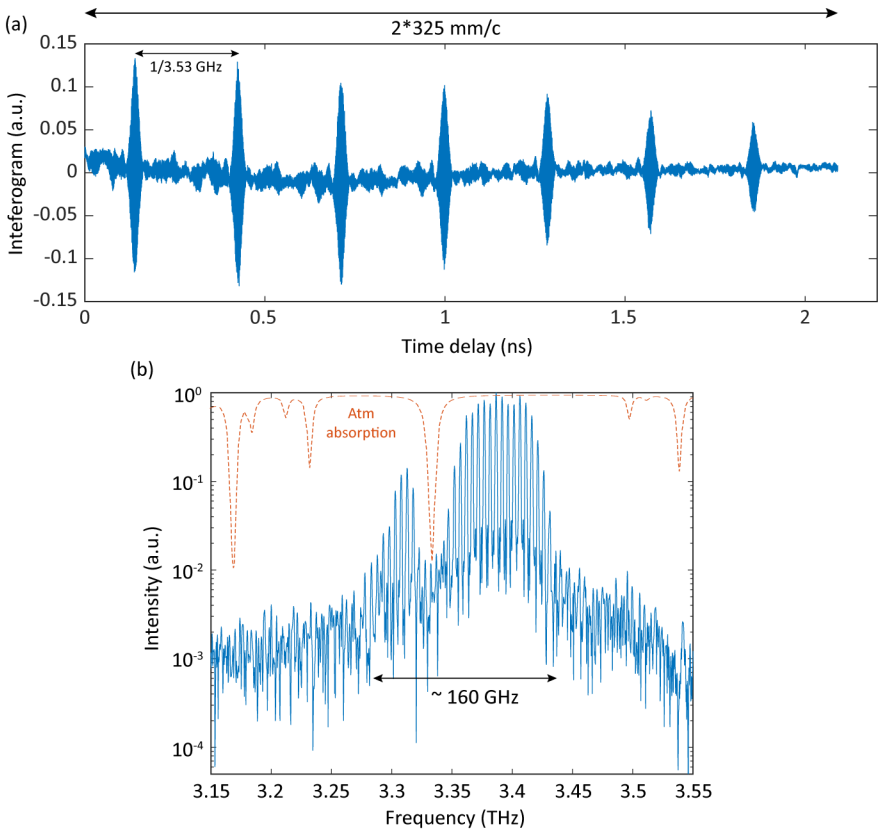

Figure 5.3.3: Resampled THz IFG (a) and corresponding spectrum (b) of an RF injection-locked QC-VECSEL. The QC-metasurface is the same as that used in Section 4.1; the applied RF modulation power is 20 dBm with an injection frequency close to the cavity round-trip frequency. Symmetric apodization is applied without phase correction to obtain the intensity spectrum.

A list of data treatment steps to convert the resampled IFG into a THz intensity spectrum includes:

1. A moving average window is applied to the THz IFG to smooth its fluctuation coming from detector noise;

2. The baseline of the THz IFG is corrected by subtracting its DC component;

3. Certain apodization is applied as elaborated in section 5.2.2;

4. (Optional) Phase correction is applied as elaborated in section 5.2.3;

5. Zero-padding is applied; DFT to obtain the intensity spectrum.

The resulting spectrum is plotted in Figure 5.3.3(b). Compared with what we have obtained using a commercial Nicolet FTIR with a frequency resolution of 7.5 GHz in Figure 4.1.4, the home-built high-resolution FTIR enables us to distinguish the exact lasing bandwidth and the number of lasing modes in an RF injection-locked system. It is considered to be the ideal tool for future studies of QC-VECSEL frequency combs. One way to further analyze the comb nature of our system is to use the technique described in Section 5.2.4; this can be thought of as a preliminary distinction between frequency comb and multimode operation. Moreover, this home-built FTIR is compatible with phase-sensitive measurements, where the slow THz pyroelectric detector is replaced with a fast THz detector. The fast THz detector has a bandwidth greater than the cavity round-trip frequency and is able to record the interference term between neighboring lasing modes that contain intermodal phase information. Because of its ability to analyze the phase coherence of each lasing mode and reconstruct the electric field distribution in the time domain, this setup — known as Shifted Wave Interference Fourier Transform Spectroscopy (SWIFTS) — is regarded as a standard method for analyzing QCL frequency combs.

Chapter 6

Conclusion and future work

6.1 Key experimental results

In this thesis, we have exploited the approaches towards frequency comb/active mode-locking in a novel metasurface-based VECSEL configuration of QCL, which is named THz QC-VECSEL. The research comprises several facets, with the primary experimental findings being enumerated here:

1. **QC-metasurface optimization**

   For applications of broadband frequency comb/narrow mode-locked pulses, the QC-metasurface of a QC-VECSEL has been optimized to satisfy all the following requirements: 1) broad amplification bandwidth; 2) low GDD; 3) high output power; 4) CW operation; 5) high RF modulation efficiency. For this reason, we introduced an optimal metasurface design based on double-patch arrays, where the coupled non-degenerate unit cells enable broad spectral response with low dispersion, while patch-based elements allow for low current draw and heat dissipation for CW biasing. Moreover, the whole metasurface is designed with a small dimension to reduce its parasitic capac-

itance; it is built in a well-designed PCB package with a 50 Ω transmission line for electrical connection and efficient RF signal transmission. The RF-improved device therefore enables efficient RF modulation and extraction up to 15 GHz.

2. **Intra-cryostat focusing VECSEL cavity design**

A novel V-shape intra-cryostat focusing VECSEL cavity design has been introduced to eliminate intra-cavity diffraction losses. This enables lasing with an external cavity length over 50 mm using small-sized metasurfaces — metasurface with a minimum bias diameter of 0.35 mm has been successfully demonstrated. Though smaller-sized metasurfaces suffer more from alignment difficulty, they extract less current and are favorable for CW operation. This focusing cavity design ensures good lasing performances, such as low lasing threshold, high output power, good temperature performance, and nearly Gaussian-shaped beam patterns, in contrast to previous demonstrations of plano-plano cavities with cavity lengths of hundreds of microns. Due to theoretically collimated output beams, it displays no significant degradation in lasing performances as the cavity length is tuned, e.g., in a range from 30 mm to 50 mm, as long as a satisfactory optical alignment is established.

3. **Multimode instability**

As mentioned, THz QC-VECSELs are naturally operating in a single-mode regime mainly due to a lack of SHB. Our two key approaches to encourage multimode functioning were as follows:

(a) *Vernier selection and reflectance compensation*

QC-VECSEL with a thick output coupler can be viewed as a cascaded Fabry-Perot cavity where the output coupler itself acts as one of the resonators that couples to the second resonator, i.e., the VECSEL cavity. At a specific combination of output coupler thickness and external cavity length, where $L_c \approx n_r L_{OC}$, these two

resonators have nearly aligned resonant modes where the lasing modes selected by Vernier effect experience similar reflection loss from the output coupler; the output coupler reflectance essentially compensates to the active metasurface reflectance, enabling multiple modes with nearly identical lasing thresholds to lase simultaneously.

This method was first applied in a plano-plano VECSEL cavity with a large-sized metasurface that can only support pulsed biasing. A maximum number of nine lasing modes spaced around 21 GHz has been demonstrated using a ∼2 mm-thick silicon output coupler. It can also be applied to OAP-focusing QC-VECSELs which allows for small-sized metasurfaces and CW operation. Free-running harmonic spectrum has been observed as a ∼3 mm-thick silicon output coupler is used in a ∼30 mm-long ($\approx 3 \times n_{Si} L_{OC}$) VECSEL cavity, along with the observation of a clear free-running beat-note signal. This method is considered promising for future studies of spontaneous frequency comb generation in THz QC-VECSELs and may be an effective method to promote harmonic combs. It is expected to produce a free-running dense spectrum with more lasing modes if a thicker silicon output coupler is available or the external cavity length is shortened to reach a fundamental condition where $L_c \approx n_{Si} L_{OC}$.

(b) *RF injection locking*

We experimentally demonstrated the transition from one or a few lasing modes to a broadband lasing spectrum under strong RF modulation, as the modulation frequency is tuned close to the cavity round-trip frequency. A typical lasing bandwidth of 100–300 GHz can be achieved with an RF power of 20 dBm.

4. **Experimental characterization**

For a more thorough analysis of the frequency comb/mode-locking phenomena, ide-

ally, phase-sensitive measurements are ideally needed to access the phase information of each lasing mode or reconstruct the intensity profile in the time domain, which is currently unavailable in our lab. Two main methods applied in this thesis to characterize the experimental results are 1) electrical beat-note extraction, which is considered an effective method to characterize RF injection locking; 2) FTIR spectroscopy. We built up a high-resolution FTIR with a sub-GHz nominal resolution. It is well-suited for the characterization of our RF injection-locked QC-VECSELs, as FSR are typically over 3 GHz.

6.2 First demonstration of RF injection locking in THz-QC-VECSELs

The successful demonstration of RF injection locking in THz QC-VECSELs is considered the most important achievement towards further realization of frequency comb/active mode-locking. It is possible that frequency combs and THz pulses may already exist in our RF injection-locked system, but further characterization is required for confirmation. Compared with previous demonstrations in RF injection-locked ridge-waveguide and ring QCLs, our experimental results share some similarities:

- Under weak RF modulation, beat-note pulling and locking to the injected RF signal is observed with a well-defined locking bandwidth increasing as the square root of the RF injection power, according to Adler's equation.

- Under strong RF modulation, lasing bandwidth broadening is observed as the RF injection frequency is tuned close to the cavity round-trip frequency; beat-note pulling effect is not observable while the lasing bandwidth deviates from Adler's equation towards higher values.

- In the case of applying a short external cavity length and effectively ultra-strong RF

modulation, beat-note spectra with side peaks and pedestals are observed within the locking bandwidth.

Additionally, novel experimental phenomena in RF injection-locked THz QC-VECSELs are reported as follows:

- THz QC-VECSEL configuration provides great degrees of freedom, where the experimental phenomena and RF injection-locked laser states are affected by multiple impacting factors, e.g., QC-metasurface design, external cavity length (round-trip time), and optical feedback. Among those, the effects of optical feedback have been elaborated. It is noticed that extra lasing modes are excited with the observation of free-running beat-note under certain conditions of optical feedback; it also plays an important role in determining the injection locking bandwidth and lasing spectrum in RF injection-locked QC-VECSELs. Experimental results are discussed in terms of optical feedback length (phase), strength, and angle; in particular, the impact of tilted optical feedback should be emphasized because it appears to be essential for the formation of multiple lasing modes.

- Harmonic injection and sub-harmonic injection is demonstrated as the RF injection frequency is tuned around $2f_{rt}/3f_{rt}$ (harmonic) and $\frac{1}{2}f_{rt}/\frac{1}{3}f_{rt}$ (sub-harmonic). Harmonic injection induces harmonic spectra with lasing modes spaced at multiple round-trip frequencies; sub-harmonic injection enables RF modulation at a frequency fractionally smaller than the cavity round-trip frequency and may be useful in cases when the round-trip frequency is not accessible.

6.3 Towards mode-locked THz QC-VECSELs

Despite a number of high-performance demonstrations, the studies of frequency comb/mode-locking in THz QC-VECSELs are still in their early stages. Immediate future work aimed at

further experimental characterization and potential research directions includes, but is not limited to:

1. **Further characterization based on the home-built high-resolution FTIR**

   On one hand, the ability of FTIR to pre-evaluate the comb nature of our laser system has not been fully exploited. Appropriate data treatment is needed to verify the equidistant spacing of our RF injection-locked QC-VECSELs, which allows us to immediately distinguish multimode operation from potential comb operation. On the other hand, the home-built FTIR is compatible with phase-sensitive and temporal profile measurements as the slow THz pyroelectric detector is switched to a fast THz detector with bandwidth over comb repetition frequency. This setup, known as SWIFTS, is considered as a standard tool for assessing the coherence and temporal profile of QCL frequency combs.

2. **Dispersion engineering for spontaneous frequency comb formation**

   The effect of cavity dispersion has been widely studied in THz QCL frequency combs, as it has been demonstrated that a certain amount of dispersion promotes the generation of spontaneous frequency combs in ridge-waveguide and ring QCLs. This may also apply to THz QC-VECSELs, and more efforts should be put into dispersion engineering, which mainly includes two parts:

   - Engineering the GDD of QC-metasurface. It is noticed that coupled-cavity metasurface design allows lower GDD than basic single-element metasurface, while their GDD profiles exhibit opposite directions. A potential dispersion compensation can be achieved by combining a single-element metasurface with a coupled-cavity one. In this case, a more complicated VECSEL cavity design is required for an extra dispersion compensation element to be introduced into the external cavity.

- Selection of the output coupler. Dispersion coming from the output coupler is comparable to that from the metasurface and may be applied to compensate for the latter. Output coupler dispersion is mainly determined by its thickness, i.e., FP oscillations in the thick substrate, and is partially affected by the metallic mesh pattern. The structure of our QC-VECSEL in combination with a thick output coupler is similar to the geometry of the Gires-Tournois interferometer (GTI), where dispersion compensation may be achieved at a specific choice of output coupler thickness.

  On the other hand, by using an ultrathin output coupler, we successfully obtained a nearly flat frequency response and experimentally saw free-running multimode operation. Although we consider parylene membrane output couplers to be mechanically unstable, especially at cryogenic temperatures, SOI wafers — whose thick silicon substrate can be etched to leave an incredibly thin membrane — are thought to be a better choice.

3. **Passive mode-locking using fast saturable absorbers**

   We did some initial simulation on a metasurface-based saturable absorber mirror, where intersubband transitions allow for fast saturable absorption; the metasurface provides strong optical confinement, which lowers the effective saturation intensity to a level comparable to the intra-cavity circulating intensity in QC-VESCELs. Such a saturable absorber element will be integrated into the external VECSEL cavity with an adjustable cavity round-trip time to investigate possible passive mode-locking. Additionally, more work will go into the QCL active region design to obtain a longer gain recovery time.

4. **Laser master equation in THz QC-VECSELs**

   A laser master equation that could theoretically analyze the underlying physics of THz

QC-VECSELs in the free-running and RF injection-locked cases is needed. Maxwell-Bloch equation has been demonstrated successfully in describing laser dynamics and predicting frequency comb behaviors in ridge-waveguide and ring QCLs. It is anticipated that further application of the Maxwell-Bloch equation to QC-VECSELs would improve our understanding of the experimental phenomena; appropriate modeling of light-matter interaction in the active metasurface is necessary.

Appendix A

Information of the QC-devices and output couplers

A.1 Design parameters of the QC-metasurfaces

Device label	VA1035-TM_{03}	VB0739-SR	VA1035-DP	VA1204-SR
Ridge width	32.5 μm	12.2 μm	16 μm/12 μm	11.8 μm
Period	65 μm	41.7 μm	36 μm/48 μm	41.7 μm
Bias diameter	2.4 mm	0.4 mm	0.35 mm	0.35 mm
Dimension	5×5 mm^2	1.5×1.5 mm^2	1×1 mm^2	0.6×1 mm^2
Designed resonance frequency	3.75 THz	3.3 THz	∼3.8 THz	3.4 THz
Bias operation	Pulsed	CW	CW	CW
RF optimization	No	No	No	Yes
Position in the thesis	Chapter 2	Chapter 3 and Chapter 4.1-4.4.1	Chapter 4.4.2	Chapter 4.5-4.6

Table A.1: A table summarizing the design parameters of the QC-metasurfaces used in the thesis.

A.2 Data of the QC-active region

The QC-active region with a wafer number of VB0739 is based on the hybrid bound-to-continuum/resonant-phonon design scheme, first described in Ref. [186]. The layer sequence for one module consists of alternating layers of GaAs/$Al_{0.15}Ga_{0.85}As$ with the following thicknesses: 10.3/**1.7**/10.7/**3.7**/8.8/**3.7**/<u>17.2</u>/**5.1** nm. The barrier layers are in bold and the central 8.8 nm of the underlined well is Si-doped at $5 \times 10^{16}\,cm^{-3}$. 163 repeated modules are grown 10 μm thick via molecular beam epitaxy. The characterization of metal-metal waveguide QC-laser based on this wafer can be found in the supplementary material in Ref. [187].

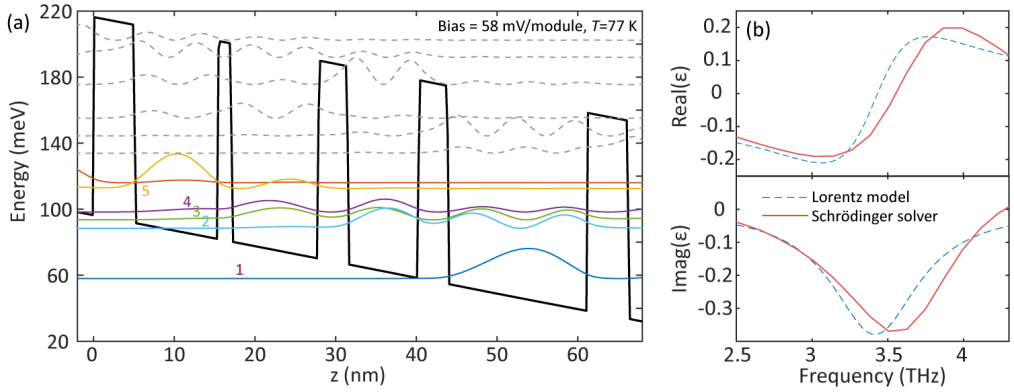

Figure A.2.1: (a) Conduction band diagram of the active region at the bias of 58 mV/module. (b) The real and imaginary parts of the permittivity of the active region simulated using the Schrödinger-Poisson solver (red solid curves) and fitting based on the Lorentz model (blue dashed curves).

We simulated the band diagram for one module of the active region using a self-consistent Schrödinger-Poisson solver at the bias providing maximum gain (Figure A.2.1(a)) and obtained its permittivity along the growth direction (Figure A.2.1(b)). The dominant intersubband transition occurs between the upper lasing state 5 and the lower lasing state 4 at a frequency of ν_{34}= 3.4 THz with oscillator strength of $f_{54} = 0.427$, where the population inversion takes up 25% of the total doping concentration. A good qualitative fitting of the permittivity is obtained by considering only the $5 \rightarrow 4$ transition using a Lorentz oscillator

model (Figure A.2.1(b), dashed lines):

$$\epsilon_z(\omega) = \epsilon_{core} + \frac{N_{ISB}e^2}{m * L_{mod}} \frac{f_{54}}{\omega^2 - \omega_{54}^2 + i\omega\gamma}; \tag{A.2.1}$$

where N_{ISB} is the population inversion sheet density per module, ϵ_{core} is the semiconductor permittivity excluding free carrier contributions, $m*$ is the GaAs electron effective mass, L_{mod} is the length of one module of the active region and γ is the damping term which is set as $2\pi \times 700\,\text{GHz}$ for best fit. The resonance frequency offset between the Lorentz model and Schrödinger simulation results can be explained by uncertainties in growth thicknesses and compositions of the QC-material.

The QC-active regions with wafer numbers VA1035 and VA1204 are regrowths of wafer VB0739.

A.3 Thin quartz output coupler

The typical output coupler in a THz QC-VECSEL comprises an inductive Ti/Au mesh evaporated on a 100 μm-thick double-side-polished z-cut quartz substrate. The mesh pattern determines the overall transmittance magnitude. The pattern with 10 μm period and 4 μm wide lines (labeled as P10-A4) provides a relative low transmittance of around 0.5% at a target frequency of 3.4 THz. The pattern with 13 μm period and 3 μm wide lines (labeled as P13-A3) provides ~5.4% transmittance at 3.4 THz; the one with 15 μm period and 2.5 μm wide lines (labeled as P15-A2.5) provides ~13.2% transmittance at 3.4 THz

Figure A.3.1 plots the experimental transmittance of these three output couplers measured using Nicolet FTIR with a liquid helium-cooled bolometer as the detector. Spikes visible on the transmittance curves are artifacts of fluctuations in residual water vapor between the signal and reference FTIR scans. Oscillatory behavior is related to standing waves within the quartz substrate

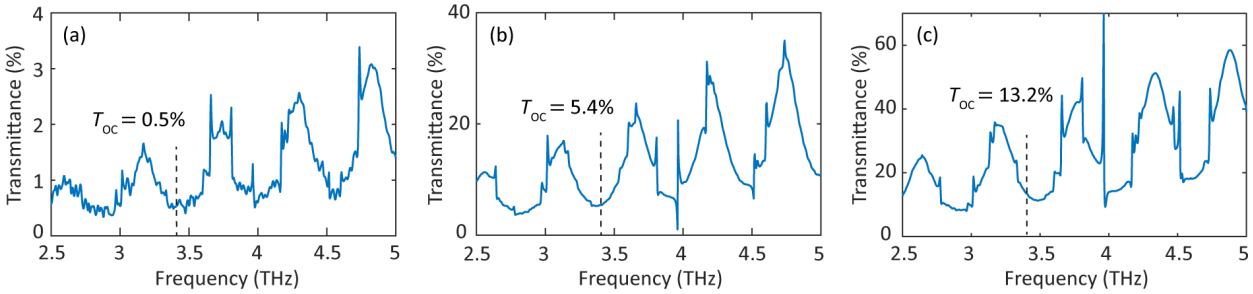

Figure A.3.1: Experimental transmittance of the output couplers (a) P10-A4, (b) P13-A3 and (c) P15-A2.5 collected with an FTIR at a resolution of 7.5 GHz and a liquid helium-cooled bolometer.

A.4 Anti-reflective coated silicon output coupler

Anti-reflective (AR) coating has been applied to silicon-based output couplers in order to remove FP oscillations in the output coupler substrate. The most basic AR coating is based on "quarter wavelength impedance matching". It is composed of a single thin layer of low THz loss material and its refractive index is the square root of the substrate's refractive index. The coating thickness is one-quarter of the wavelength designed for the

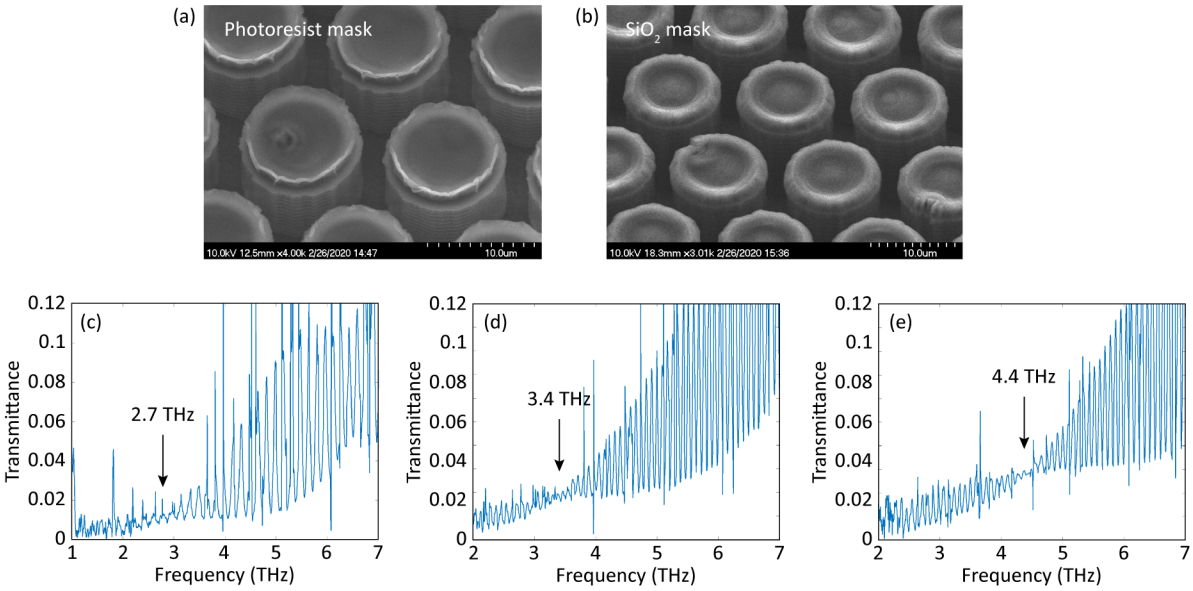

Figure A.4.1: (a-b) SEM figures of the silicon pillars. Photoresist and SiO_2 were used as masks during dry etching, respectively. (c-e) Experimental transmittance of the output couplers with silicon pillar AR coating designed at different target frequencies. The metallic pattern is P10-A4, and the silicon substrate thickness is 500 μm.

substrate. This method could effectively provide zero reflectance at the target wavelength while decreasing reflectance for wavelengths in a broad band around the center.

We fabricated the AR quarter-wavelength coating on silicon substrate by etching an array of subwavelength micro-scale pillars. The target wavelength of the pillar layer is determined by the etching depth, while its effective refractive index is controlled by the fill factor, where $n_{eff} \approx \sqrt{n_{Si}}$. It was fabricated through photolithography followed by FDRIE dry etching. Figure A.4.1(a-b) displays the SEM figures of silicon pillars using photoresist and SiO_2 as etch masks; this suggests that a SiO_2 mask functions more effectively to guarantee vertical etch walls. Multiple etch depths were selected for AR coatings at various target frequencies. After that, the silicon pillar layer was protected by a thick photoresist and then flipped over for metallic patterning. The metallic pattern chosen is P10-A4. Figure A.4.1(c-e) shows the experimental transmittance of some of the AR-coated output couplers. They were collected using Nicolet FTIR with a liquid helium-cooled bolometer.

Appendix B

Alignment procedures of the OAP-focusing VECSELs

A well-aligned OAP-focusing VECSEL is necessary for the perfect elimination of the intra-cavity diffraction loss, which allows for a low lasing threshold and high output power. Below is a list of the steps involved in alignment:

1. The QC-metasurface is mounted at the center of the chip carrier. First, two auxiliary lines are drawn on the chip carrier for alignment (Figure B.0.1(a)). The bias circle of the QC-metasurface is positioned at the cross-section of the two auxiliary lines by

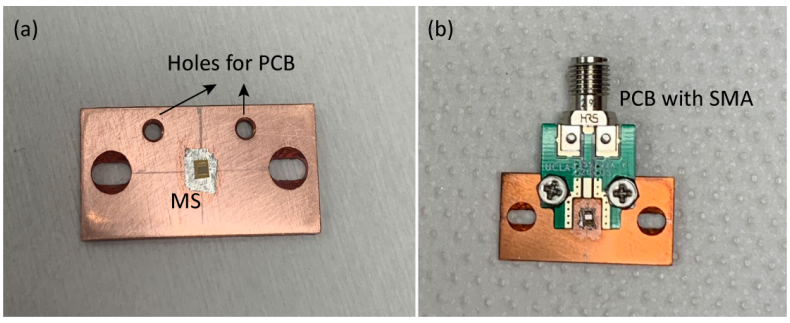

Figure B.0.1: (a-b) Pictures of the QC-device. (a) The QC-metasurface is aligned at the center of the chip carrier. (b) After the chip is indium-bonded on the chip carrier, a well-designed PCB is fixed on the chip carrier and wire-bonded to the QC-metasurface.

gently pushing the sidewalls of the QC-chip with a tweezer. A microscope can help tell whether it is centered before indium bonding is performed. After that, a well-designed PCB is screwed onto the chip carrier and wire-bonded to the QC-metasurface for an RF-efficient electrical connection, as illustrated in Figure B.0.1(b). The edge of the PCB has a SMA connector screwed into it.

2. The chip carrier is fixed to a CNC-machined OAP-focusing cavity mount, to which a half-inch focal length OAP mirror has been attached. A He-Ne laser is used to aid in the following alignment steps.

3. First, the He-Ne laser is illuminating a flat mirror positioned right above the OAP mirror, as shown in Figure B.0.2(a). The flat mirror could be made of a tiny piece of silicon that has been coated with a metal layer and is supposed to be perpendicular to the optical axis of the OAP mirror. If the incident He-Ne beam is reflected by the flat mirror back to its output port, it is therefore parallel to the OAP mirror's optical axis.

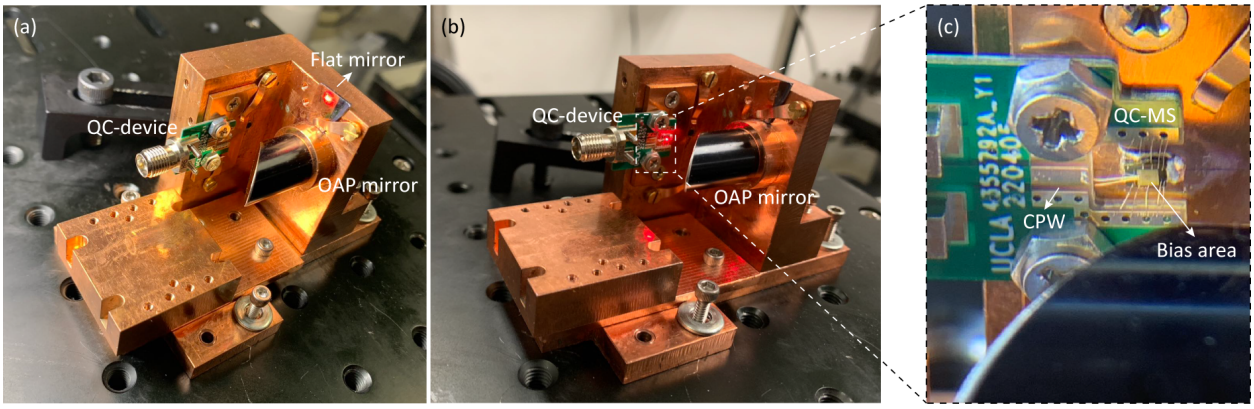

Figure B.0.2: (a) The He-Ne laser is first illuminating a flat mirror to ensure it is parallel to the OAP mirror's optical axis. (b) The He-Ne laser (or the mount) is then moved in the z-direction to ensure parallel illumination onto the center of the OAP mirror. The QC-device is centered at the focus point of the He-Ne beam. (c) The boundary of the bias area can be observed with the help of a lighted magnifier.

4. The He-Ne laser (or the mount) is then moved in the z-direction to ensure parallel

illumination onto the center of the OAP mirror. The OAP mirror concentrates the He-Ne beam onto the QC-metasurface (see Figure B.0.2(b)). The key alignment step is to ensure that the bias area center of the device is aligned at the OAP mirror's focus point — that is, the He-Ne beam is focused at the center of the bias area. We utilize a magnifier with light to help us locate the bias area; the bias area is visible due to the boundary of the insulating SiO_2 layer, as shown in Figure B.0.2(c). Based on the author's experience, if we look at the device from a specific angle and have light shining on it obliquely, we can see the boundary more clearly. It is easier to see the bias area of ridge-based metasurfaces instead of patch-based metasurfaces due to different SiO_2 patterns.

Upon identifying the bias area, we ensure that the He-Ne beam is focused at its center. The difficulty of this step depends on how well the QC-chip was mounted in the chip carrier's center. Since the QC-chip is rarely exactly in the center, we will need to slightly unscrew the screws holding the chip carrier to the OAP-focusing cavity mount, so we could slightly move the chip carrier to overlap the bias area and the focused He-Ne beam. By using an additional pair of clips to firmly fasten the chip carrier to the

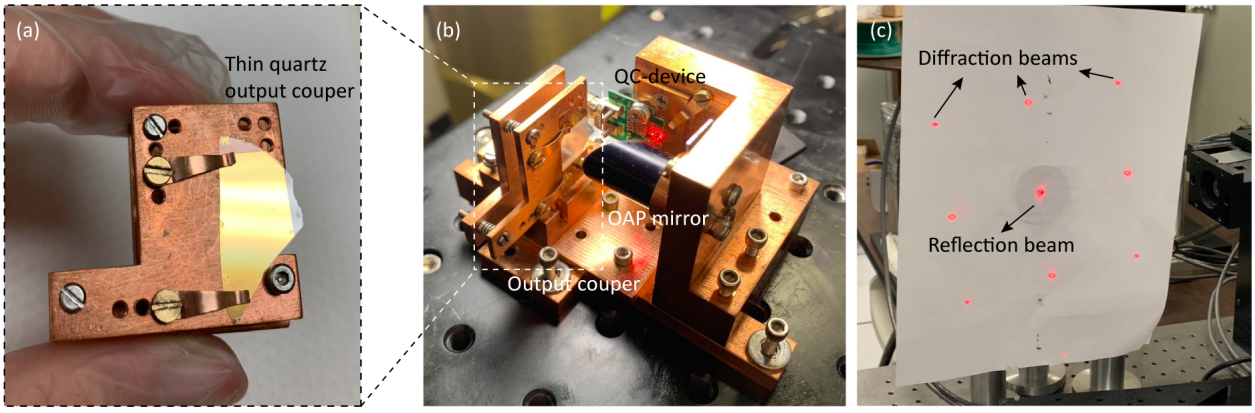

Figure B.0.3: (a) The output coupler made of a thin quartz substrate deposited with metallic mesh. It is clipped on a mount with adjustable tilted angle. (b) The output coupler mount is screwed onto the OAP-focusing cavity mount and is tuned to be perpendicular to the He-Ne beam. (c) The He-Ne beam reflected by the output coupler exhibits an array of diffraction patterns. The 0th order of reflection is guaranteed to return to the output port.

mount, effective heat dissipation of the QC-device is ensured.

5. Aligning the output coupler comes next after aligning the QC-device. As seen in Figure B.0.3(a), the output coupler is clipped onto an output coupler mount, whose tilted angle is adjusted using three pairs of springs and screws. The output coupler mount is then screwed onto the OAP-focusing cavity mount so that the He-Ne laser illuminates the output coupler (Figure B.0.3(b)). As seen in Figure B.0.3(c), the He-Ne beam reflected by the quartz output coupler exhibits an array of diffraction patterns because of the micro-scale metallic mesh that was deposited on the output coupler substrate. We then tune the three screws on the output coupler mount, i.e., tune its tilted angle, to make sure the 0th order of the diffraction pattern is reflected back to the output port. If the output coupler is made of silicon, which is opaque, there will be only a single reflection beam (0th order). As a result, we guarantee that the output coupler is perpendicular to the He-Ne beam and thus the optical axis of the OAP mirror.

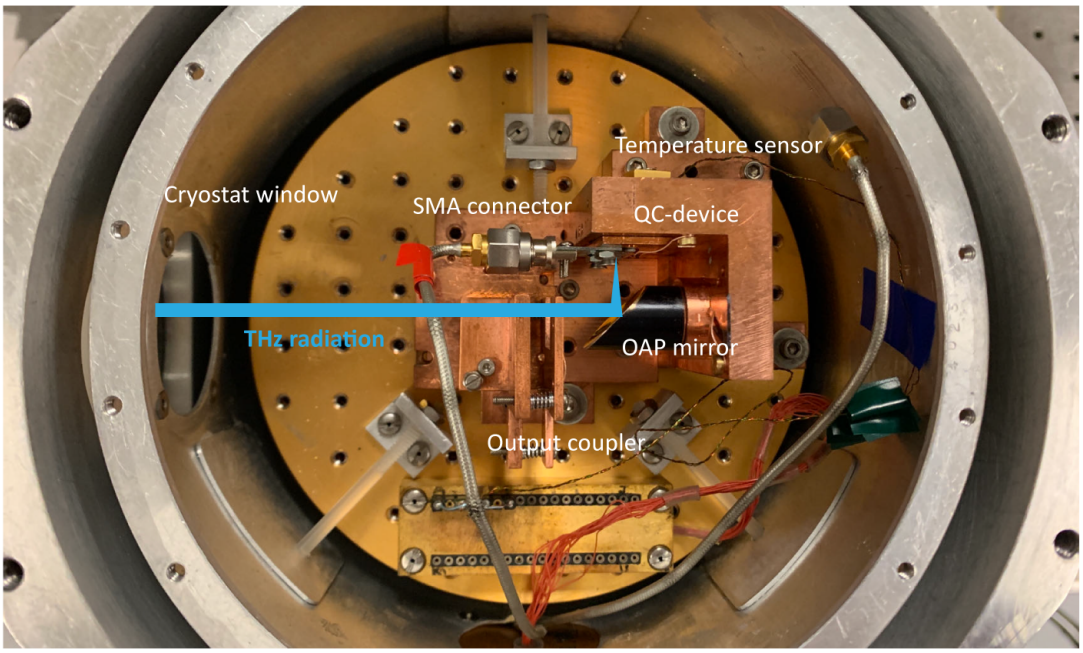

Figure B.0.4: Picture of a well-aligned OAP-focusing QC-VECSEL in the cryostat.

6. The entire mount, which is carefully aligned, is then placed inside the cryostat and screwed to its cold stage, as illustrated in Figure B.0.4. For accurate temperature monitoring, a temperature sensor is fastened directly on the mount. The SMA semi-rigid cable is connected to the SMA connector on the QC device; caution is required to prevent the device's position from shifting. Alignment of the OAP-focusing QC-VECSEL is preserved following cooldown within the liquid-nitrogen cooled vacuum cryostat, which ensures good lasing performances.

Bibliography

[1] P. H. Siegel, "Terahertz technology," *IEEE Transactions on Microwave Theory and Techniques*, vol. 50, no. 3, pp. 910–928, 2002.

[2] M. Tonouchi, "Cutting-edge terahertz technology," *Nature photonics*, pp. 97–105, 2007.

[3] K. Delfanazari, R. A. Klemm, H. J. Joyce, D. A. Ritchie, and K. Kadowaki, "Integrated, Portable, Tunable, and Coherent Terahertz Sources and Sensitive Detectors Based on Layered Superconductors," *Proceedings of the IEEE*, vol. 108, no. 5, pp. 721–734, 2020.

[4] A. Khalid, G. M. Dunn, R. F. Macpherson, S. Thoms, D. Macintyre, C. Li, M. J. Steer, V. Papageorgiou, I. G. Thayne, M. Kuball, C. H. Oxley, M. Montes Bajo, A. Stephen, J. Glover, and D. R. Cumming, "Terahertz oscillations in an In0.53Ga0.47As submicron planar Gunn diode," *Journal of Applied Physics*, vol. 115, no. 11, p. 114 502, 2014.

[5] E. Wasige, K. H. Alharbi, A. Al-Khalidi, J. Wang, A. Khalid, G. C. Rodrigues, and J. Figueiredo, "Resonant tunnelling diode terahertz sources for broadband wireless communications," *Terahertz, RF, Millimeter, and Submillimeter-Wave Technology and Applications X*, vol. 10103, 101031J, 2017.

[6] T. Zimmer, J. Bock, F. Buchali, *et al.*, "SiGe HBTs and BiCMOS Technology for Present and Future Millimeter-Wave Systems," *IEEE Journal of Microwaves*, vol. 1, no. 1, pp. 288–298, 2021.

[7] T. Maekawa, H. Kanaya, S. Suzuki, and M. Asada, "Oscillation up to 1.92 THz in resonant tunneling diode by reduced conduction loss," *Applied Physics Express*, vol. 9, no. 2, p. 024 101, 2016.

[8] R. A. Hadi, Y. Zhao, Y. Li, Y. Du, C. Curwen, M. K. Lo, B. S. Williams, and M. C. Chang, "Multi-spectral terahertz interferometric imaging based on a monolithic retroactive silicon chip," *2017 IEEE International Conference on Microwaves, Antennas, Communications and Electronic Systems, COMCAS 2017*, 2017.

[9] S. Thomas, S. Razavian, W. Sun, B. F. Motlagh, A. D. Kim, Y. Wu, B. S. Williams, and A. Babakhani, "A 0.4-4 THz p-i-n Diode Frequency Multiplier in 90-nm SiGe BiCMOS," *IEEE Journal of Solid-State Circuits*, vol. 58, no. 9, pp. 2407–2420, 2023.

[10] J. Neu and C. A. Schmuttenmaer, "Tutorial: An introduction to terahertz time domain spectroscopy (THz-TDS)," *Journal of Applied Physics*, vol. 124, p. 231 101, 2018.

[11] M.-H. Mammez, Z. Buchanan, O. Pirali, M.-A. Martin-Drumel, J. Turut, G. Ducournau, S. Eliet, F. Hindle, S. Barbieri, P. Roy, G. Mouret, and J.-F. Lampin, "Optically Pumped Terahertz Molecular Laser: Gain Factor and Validation up to 5.5 THz," *Advanced Photonics Research*, vol. 3, no. 4, p. 2 100 263, 2022.

[12] A. Amirzhan, P. Chevalier, J. Rowlette, H. T. Stinson, M. Pushkarsky, T. Day, H. O. Everitt, and F. Capasso, "A quantum cascade laser-pumped molecular laser tunable over 1 THz," *APL Photonics*, vol. 7, no. 1, p. 016 107, 2022.

[13] P. Tan, J. Huang, K. F. Liu, Y. Q. Xiong, and M. W. Fan, "Terahertz radiation sources based on free electron lasers and their applications," *Science China Information Sciences*, vol. 55, no. 1, pp. 1–15, 2012.

[14] S. Komiyama, "Far-infrared emission from population-inverted hot-carrier system in p-Ge," *Physical Review Letters*, vol. 48, no. 4, pp. 271–274, 1982.

[15] R. Kohler, A. Tredicucci, F. Beltram, H. E. Beere, E. H. Linfield, A. G. Davies, D. A. Ritchie, R. C. Iotti, and F. Rossi, "Terahertz semiconductor-heterostructure laser," English, *Nature*, vol. 417, no. 6885, pp. 156–159, 2002.

[16] B. S. Williams, S. Kumar, Q. Hu, and J. L. Reno, "High-power terahertz quantum-cascade lasers," *Electronics letters*, vol. 42, no. 2, pp. 89–91, 2006.

[17] L. H. Li, L. Chen, J. R. Freeman, M. Salih, P. Dean, A. G. Davies, and E. H. Linfield, "Multi-Watt high-power THz frequency quantum cascade lasers," *Electronics Letters*, vol. 53, no. 12, pp. 799–800, 2017.

[18] C. Walther, M. Fischer, G. Scalari, R. Terazzi, N. Hoyler, and J. Faist, "Quantum cascade lasers operating from 1.2 to 1.6 THz," *Applied Physics Letters*, vol. 91, p. 131 122, 2007.

[19] L. Li, I. Kundu, P. Dean, E. H. Linfield, and A. G. Davies, "High-power GaAs/AlGaAs quantum cascade lasers with emission in the frequency range 4.7–5.6 THz," no. September, pp. 7–9, 2016.

[20] S. Kumar, B. S. Williams, Q. Hu, and J. L. Reno, "1.9 THz quantum-cascade lasers with one-well injector," *Applied Physics Letters*, vol. 88, no. 12, pp. 12–14, 2006.

[21] G. Scalari, C. Walther, M. Fischer, R. Terazzi, H. Beere, D. Ritchie, and J. Faist, "THz and sub-THz quantum cascade lasers," *Laser and Photonics Reviews*, vol. 3, no. 1-2, pp. 45–66, 2009.

[22] S. Miho, T. T. Lin, and H. Hirayama, "1.9 THz selective injection design quantum cascade laser operating at extreme higher temperature above the kBT line," *Physica Status Solidi C*, vol. 10, no. 11, pp. 1448–1451, 2013.

[23] S. Kumar, C. W. I. Chan, Q. Hu, and J. L. Reno, "A 1.8-THz quantum cascade laser operating significantly above the temperature of hw /kB," *Nature Physics*, vol. 7, no. 2, pp. 166–171, 2011.

[24] A. Khalatpour, M. C. Tam, S. J. Addamane, J. Reno, Z. Wasilewski, and Q. Hu, "Enhanced operating temperature in terahertz quantum cascade lasers based on direct phonon depopulation," *Applied Physics Letters*, vol. 122, no. 16, p. 161 101, 2023.

[25] B. S. Williams, "Terahertz quantum-cascade lasers," *Nature Photonics*, vol. 1, no. 9, pp. 517–525, 2007.

[26] J. Faist, M. Beck, T. Aellen, and E. Gini, "Quantum-cascade lasers based on a bound-to-continuum transition," *Applied Physics Letters*, vol. 78, no. 2, pp. 147–149, 2001.

[27] B. S. Williams, H. Callebaut, S. Kumar, Q. Hu, and J. L. Reno, "3.4-THz quantum cascade laser based on longitudinal-optical-phonon scattering for depopulation," *Applied Physics Letters*, vol. 82, no. 7, pp. 1015–1017, 2003.

[28] B. S. Williams, S. Kumar, H. Callebaut, Q. Hu, and J. L. Reno, "Terahertz quantum-cascade laser at λ 100 μm using metal waveguide for mode confinement," *Applied Physics Letters*, vol. 83, no. 11, pp. 2124–2126, 2003.

[29] A. Khalatpour, A. K. Paulsen, C. Deimert, Z. R. Wasilewski, and Q. Hu, "High-power portable terahertz laser systems," *Nature Photonics*, vol. 15, pp. 16–20, 2021.

[30] E. E. Orlova, J. N. Hovenier, T. O. Klaassen, I. Kašalynas, A. J. Adam, J. R. Gao, T. M. Klapwijk, B. S. Williams, S. Kumar, Q. Hu, and J. L. Reno, "Antenna model for wire lasers," *Physical Review Letters*, vol. 96, no. 17, p. 173 904, 2006.

[31] L. Xu, C. A. Curwen, P. W. Hon, Q. S. Chen, T. Itoh, and B. S. Williams, "Metasurface external cavity laser," *Applied Physics Letters*, vol. 107, no. 22, p. 221 105, 2015.

[32] T. Udem, J. Reichert, R. Holzwarth, and T. W. Hänsch, "Absolute optical frequency measurement of the cesium D1 line with a mode-locked laser," *Physical Review Letters*, vol. 82, no. 18, pp. 3568–3571, 1999.

[33] T. Udem, J. Reichert, R. Holzwarth, and T. W. Hänsch, "Accurate measurement of large optical frequency differences with a mode-locked laser," *Optics Letters*, vol. 24, no. 13, p. 881, 1999.

[34] T. Udem, R. Holzwarth, and T. W. Hänsch, "Optical frequency metrology," *Nature*, vol. 416, no. 6877, pp. 233–237, 2002.

[35] R. Paiella, F. Capasso, C. Gmachl, H. Y. Hwang, D. L. Sivco, A. L. Hutchinson, A. Y. Cho, and H. C. Liu, "Monolithic active mode locking of quantum cascade lasers," *Applied Physics Letters*, vol. 77, no. 2, pp. 169–171, 2000.

[36] H. Choi, L. Diehl, Z. K. Wu, M. Giovannini, J. Faist, F. Capasso, and T. B. Norris, "Gain recovery dynamics and photon-driven transport in quantum cascade lasers," *Physical Review Letters*, vol. 100, no. 16, p. 167 401, 2008.

[37] D. R. Bacon, J. R. Freeman, R. A. Mohandas, L. Li, E. H. Linfield, A. G. Davies, and P. Dean, "Gain recovery time in a terahertz quantum cascade laser," *Applied Physics Letters*, vol. 108, no. 8, p. 081 104, 2016.

[38] T. J. Kippenberg, R. Holzwarth, and S. A. Diddams, "Microresonator-Based Optical Frequency Combs," vol. 332, no. April, pp. 555–560, 2011.

[39] J. Haas and B. Mizaikoff, "Advances in Mid-Infrared Spectroscopy for Chemical Analysis," *Annual Review of Analytical Chemistry*, vol. 9, no. July, pp. 45–68, 2016.

[40] D. Burghoff, T.-Y. Kao, N. Han, C. W. I. Chan, X. Cai, Y. Yang, D. J. Hayton, J.-R. Gao, J. L. Reno, and Q. Hu, "Terahertz laser frequency combs," *Nature Photonics*, vol. 8, no. 6, pp. 462–467, 2014.

[41] G. Villares, S. Riedi, J. Wolf, D. Kazakov, M. J. Süess, P. Jouy, M. Beck, and J. Faist, "Dispersion engineering of quantum cascade laser frequency combs," *Optica*, vol. 3, no. 3, p. 252, 2016.

[42] F. Wang, H. Nong, T. Fobbe, V. Pistore, S. Houver, S. Markmann, N. Jukam, M. Amanti, C. Sirtori, S. Moumdji, R. Colombelli, L. Li, E. Linfield, G. Davies, J. Mangeney, J. Tignon, and S. Dhillon, "Short Terahertz Pulse Generation from a Dispersion Compensated Modelocked Semiconductor Laser," *Laser and Photonics Reviews*, vol. 11, no. 4, p. 1 700 013, 2017.

[43] A. Hugi, G. Villares, S. Blaser, H. C. Liu, and J. Faist, "Mid-infrared frequency comb based on a quantum cascade laser," *Nature*, vol. 492, no. 7428, pp. 229–233, 2012.

[44] M. Rösch, G. Scalari, M. Beck, and J. Faist, "Octave-spanning semiconductor laser," *Nature Photonics*, vol. 9, no. 1, pp. 42–47, 2014.

[45] M. Wienold, B. Röben, L. Schrottke, and H. T. Grahn, "Evidence for frequency comb emission from a Fabry-Pérot terahertz quantum-cascade laser," *Optics Express*, vol. 22, no. 25, p. 30 410, 2014.

[46] J. B. Khurgin, Y. Dikmelik, A. Hugi, and J. Faist, "Coherent frequency combs produced by self frequency modulation in quantum cascade lasers," *Applied Physics Letters*, vol. 104, no. 8, p. 081 118, 2014.

[47] G. Villares and J. Faist, "Quantum cascade laser combs: effects of modulation and dispersion," *Optics Express*, vol. 23, no. 2, p. 1651, 2015.

[48] M. Singleton, P. Jouy, M. Beck, and J. Faist, "Evidence of linear chirp in mid-infrared quantum cascade lasers," *Optica*, vol. 5, no. 8, p. 948, 2018.

[49] N. Opačak and B. Schwarz, "Theory of Frequency-Modulated Combs in Lasers with Spatial Hole Burning, Dispersion, and Kerr Nonlinearity," *Physical Review Letters*, vol. 123, no. 24, p. 243 902, 2019.

[50] D. Kazakov, M. Piccardo, Y. Wang, P. Chevalier, T. S. Mansuripur, F. Xie, C.-e. Zah, K. Lascola, A. Belyanin, and F. Capasso, "Self-starting harmonic frequency comb generation in a quantum cascade laser," *Nature Photonics*, vol. 11, no. 12, pp. 789–792, 2017.

[51] A. Forrer, M. Franckié, D. Stark, T. Olariu, M. Beck, J. Faist, and G. Scalari, "Photon-Driven Broadband Emission and Frequency Comb RF Injection Locking in THz Quantum Cascade Lasers," *ACS Photonics*, vol. 7, no. 3, pp. 784–791, 2020.

[52] A. Forrer, Y. Wang, M. Beck, A. Belyanin, J. Faist, and G. Scalari, "Self-starting harmonic comb emission in THz quantum cascade lasers," *Applied Physics Letters*, vol. 118, no. 13, p. 131 112, 2021.

[53] M. Piccardo, P. Chevalier, T. S. Mansuripur, D. Kazakov, Y. Wang, N. A. Rubin, L. Meadowcroft, A. Belyanin, and F. Capasso, "The harmonic state of quantum cascade lasers: origin, control, and prospective applications [Invited]," *Optics Express*, vol. 26, no. 8, p. 9464, 2018.

[54] T. S. Mansuripur, C. Vernet, P. Chevalier, G. Aoust, B. Schwarz, F. Xie, C. Caneau, K. Lascola, C. E. Zah, D. P. Caffey, T. Day, L. J. Missaggia, M. K. Connors, C. A. Wang, A. Belyanin, and F. Capasso, "Single-mode instability in standing-wave lasers: The quantum cascade laser as a self-pumped parametric oscillator," *Physical Review A*, vol. 94, no. 6, p. 063 807, 2016.

[55] Y. Wang and A. Belyanin, "Harmonic frequency combs in quantum cascade lasers: Time-domain and frequency-domain theory," *Physical Review A*, vol. 102, no. 1, p. 13 519, 2020.

[56] M. Piccardo, P. Chevalier, S. Anand, Y. Wang, D. Kazakov, E. A. Mejia, F. Xie, K. Lascola, A. Belyanin, and F. Capasso, "Widely tunable harmonic frequency comb in a quantum cascade laser," *Applied Physics Letters*, vol. 113, no. 3, p. 031 104, 2018.

[57] F. Wang, V. Pistore, M. Riesch, H. Nong, P. B. Vigneron, R. Colombelli, O. Parillaud, J. Mangeney, J. Tignon, C. Jirauschek, and S. S. Dhillon, "Ultrafast response of harmonic modelocked THz lasers," *Light: Science and Applications*, vol. 9, no. 1, p. 51, 2020.

[58] N. Henry, D. Burghoff, Q. Hu, and J. B. Khurgin, "Temporal characteristics of quantum cascade laser frequency modulated combs in long wave infrared and THz regions," *Optics Express*, vol. 26, no. 11, p. 14 201, 2018.

[59] H. Risken and K. Nummedal, "Self - Pulsing in Lasers," *Journal of Applied Physics*, vol. 39, no. 10, pp. 4662–4672, 1968.

[60] R. Graham and H. Haken, "Quantum theory of light propagation in a fluctuating laser-active medium," *Zeitschrift für Physik*, vol. 213, no. 5, pp. 420–450, 1968.

[61] M. Piccardo, B. Schwarz, D. Kazakov, M. Beiser, N. Opačak, Y. Wang, S. Jha, J. Hillbrand, M. Tamagnone, W. T. Chen, A. Y. Zhu, L. L. Columbo, A. Belyanin, and F. Capasso, "Frequency combs induced by phase turbulence," *Nature*, vol. 582, no. 7812, pp. 360–364, 2020.

[62] N. Opačak, S. D. Cin, J. Hillbrand, and B. Schwarz, "Frequency Comb Generation by Bloch Gain Induced Giant Kerr Nonlinearity," *Physical Review Letters*, vol. 127, no. 9, p. 093 902, 2021.

[63] B. Meng, M. Singleton, M. Shahmohammadi, F. Kapsalidis, R. Wang, M. Beck, and J. Faist, "Mid-infrared frequency comb from a ring quantum cascade laser," *Optica*, vol. 7, no. 2, p. 162, 2020.

[64] M. Jaidl, N. Opačak, M. A. Kainz, S. Schönhuber, D. Theiner, B. Limbacher, M. Beiser, M. Giparakis, A. M. Andrews, G. Strasser, B. Schwarz, J. Darmo, and K. Unterrainer, "Comb operation in terahertz quantum cascade ring lasers," *Optica*, vol. 8, no. 6, p. 780, 2021.

[65] B. Meng, M. Singleton, J. Hillbrand, M. Franckié, M. Beck, and J. Faist, "Dissipative Kerr solitons in semiconductor ring lasers," *Nature Photonics*, vol. 16, p. 142, 2021.

[66] L. Columbo, M. Piccardo, F. Prati, L. A. Lugiato, M. Brambilla, A. Gatti, C. Silvestri, M. Gioannini, N. Opačak, B. Schwarz, and F. Capasso, "Unifying Frequency Combs in Active and Passive Cavities: Temporal Solitons in Externally Driven Ring Lasers," *Physical Review Letters*, vol. 126, no. 17, p. 173 903, 2021.

[67] T. Herr, V. Brasch, J. D. Jost, C. Y. Wang, N. M. Kondratiev, M. L. Gorodetsky, and T. J. Kippenberg, "Temporal solitons in optical microresonators," *Nature Photonics*, vol. 8, no. 2, pp. 145–152, 2014.

[68] T. J. Kippenberg, A. L. Gaeta, M. Lipson, and M. L. Gorodetsky, "Dissipative Kerr solitons in optical microresonators," *Science*, vol. 361, p. 567, 2018.

[69] Y. Yang, "Terahertz Laser Frequency Combs: Devices and Applications," *PhD Thesis*, 2017.

[70] P. Marin-Palomo, J. N. Kemal, M. Karpov, A. Kordts, J. Pfeifle, M. H. Pfeiffer, P. Trocha, S. Wolf, V. Brasch, M. H. Anderson, R. Rosenberger, K. Vijayan, W. Freude, T. J. Kippenberg, and C. Koos, "Microresonator-based solitons for massively parallel coherent optical communications," *Nature*, vol. 546, no. 7657, pp. 274–279, 2017.

[71] P. Trocha, M. Karpov, D. Ganin, M. H. Pfeiffer, A. Kordts, S. Wolf, J. Krockenberger, P. Marin-Palomo, C. Weimann, S. Randel, W. Freude, T. J. Kippenberg, and C. Koos, "Ultrafast optical ranging using microresonator soliton frequency combs," *Science*, vol. 359, no. 6378, pp. 887–891, 2018.

[72] M. G. Suh and K. J. Vahala, "Soliton microcomb range measurement," *Science*, vol. 359, no. 6378, pp. 884–887, 2018.

[73] D. T. Spencer, S. H. Lee, D. Y. Oh, M.-G. Suh, K. Y. Yang, and K. Vahala, "An optical-frequency synthesizer using integrated photonics," *Nature*, vol. 557, no. 7703, pp. 81–85, 2018.

[74] P. Micheletti, U. Senica, A. Forrer, S. Cibella, G. Torrioli, M. Frankié, M. Beck, J. Faist, and G. Scalari, "Terahertz optical solitons from dispersion-compensated antenna-coupled planarized ring quantum cascade lasers," *Science advances*, vol. 9, no. 24, eadf9426, 2023.

[75] S. Barbieri, W. Maineult, S. S. Dhillon, C. Sirtori, J. Alton, N. Breuil, H. E. Beere, and D. A. Ritchie, "13 GHz direct modulation of terahertz quantum cascade lasers," *Applied Physics Letters*, vol. 91, no. 14, p. 143 510, 2007.

[76] P. Gellie, S. Barbieri, J. F. Lampin, P. Filloux, C. Manquest, C. Sirtori, I. Sagnes, S. P. Khanna, E. H. Linfield, H. E. Beere, and D. A. Ritchie, "Injection-locking of terahertz quantum cascade lasers up to 35GHz via RF amplitude modulation," *IRMMW-THz 2010 - 35th International Conference on Infrared, Millimeter, and Terahertz Waves, Conference Guide*, vol. 18, no. 20, pp. 20 799–20 816, 2010.

[77] H. Li, P. Laffaille, D. Gacemi, M. Apfel, C. Sirtori, J. Leonardon, G. Santarelli, M. Rösch, G. Scalari, M. Beck, J. Faist, W. Hänsel, R. Holzwarth, and S. Barbieri, "Dynamics of ultra-broadband terahertz quantum cascade lasers for comb operation," *Optics Express*, vol. 23, no. 26, p. 33 270, 2015.

[78] A. Forrer, L. Bosco, M. Beck, J. Faist, and G. Scalari, "RF injection of THz QCL combs at 80 K emitting over 700 GHz spectral bandwidth," *Photonics*, vol. 7, no. 1, p. 9, 2020.

[79] F. Kapsalidis, B. Schneider, M. Singleton, M. Bertrand, E. Gini, M. Beck, and J. Faist, "Mid-infrared quantum cascade laser frequency combs with a microstrip-like line waveguide geometry," *Applied Physics Letters*, vol. 118, p. 071 101, 2021.

[80] E. Rodriguez, A. Mottaghizadeh, D. Gacemi, M. Jeannin, Z. Asghari, A. Vasanelli, Y. Todorov, Q. J. Wang, and C. Sirtori, "Tunability of the Free-Spectral Range by Microwave Injection into a Mid-Infrared Quantum Cascade Laser," *Laser and Photonics Reviews*, vol. 14, no. 5, p. 1 900 389, 2020.

[81] B. Schneider, F. Kapsalidis, M. Bertrand, M. Singleton, J. Hillbrand, M. Beck, and J. Faist, "Controlling Quantum Cascade Laser Optical Frequency Combs through Microwave Injection," *Laser and Photonics Reviews*, vol. 15, no. 12, p. 2 100 242, 2021.

[82] J. Hillbrand, D. Auth, M. Piccardo, N. Opačak, E. Gornik, G. Strasser, F. Capasso, S. Breuer, and B. Schwarz, "In-Phase and Anti-Phase Synchronization in a Laser Frequency Comb," *Physical Review Letters*, vol. 124, no. 2, p. 023 901, 2020.

[83] J. Hillbrand, N. Opačak, M. Piccardo, H. Schneider, G. Strasser, F. Capasso, and B. Schwarz, "Mode-locked short pulses from an 8 μm wavelength semiconductor laser," *Nature Communications*, vol. 11, no. 1, p. 5788, 2020.

[84] S. Barbieri, M. Ravaro, P. Gellie, G. Santarelli, C. Manquest, C. Sirtori, S. P. Khanna, E. H. Linfield, and A. G. Davies, "Coherent sampling of active mode-locked terahertz quantum cascade lasers and frequency synthesis," *Nature Photonics*, vol. 5, no. 5, pp. 306–313, 2011.

[85] A. Mottaghizadeh, D. Gacemi, P. Laffaille, H. Li, M. Amanti, C. Sirtori, G. Santarelli, W. Hänsel, R. Holzwart, L. H. Li, E. H. Linfield, and S. Barbieri, "5-Ps-Long Terahertz Pulses From an Active-Mode-Locked Quantum Cascade Laser," *Optica*, vol. 4, no. 1, p. 168, 2017.

[86] U. Senica, A. Forrer, T. Olariu, P. Micheletti, S. Cibella, G. Torrioli, M. Beck, J. Faist, and G. Scalari, "Planarized THz quantum cascade lasers for broadband coherent photonics," *Light: Science and Applications*, vol. 11, no. 1, p. 347, 2022.

[87] D. Bachmann, M. Rosch, G. Scalari, M. J. Suess, M. Beck, J. Faist, K. Unterrainer, and J. Darmo, "Short pulse generation and mode control of broadband terahertz quantum cascade lasers," *International Conference on Infrared, Millimeter, and Terahertz Waves, IRMMW-THz*, vol. 2016-Novem, no. 10, pp. 18–25, 2016.

[88] J. Maysonnave, K. Maussang, J. R. Freeman, N. Jukam, J. Madéo, P. Cavalié, R. Rungsawang, S. Khanna, E. Linfield, A. Davies, H. Beere, D. Ritchie, S. Dhillon, and J. Tignon, "Mode-locking of a terahertz laser by direct phase synchronization," *Optics Express*, vol. 20, no. 19, p. 20 855, 2012.

[89] D. Oustinov, N. Jukam, R. Rungsawang, J. Madéo, S. Barbieri, P. Filloux, C. Sirtori, X. Marcadet, J. Tignon, and S. Dhillon, "Phase seeding of a terahertz quantum cascade laser," *Nature Communications*, vol. 1, p. 69, 2010.

[90] R. P. Green, A. Tredicucci, N. Q. Vinh, B. Murdin, C. Pidgeon, H. E. Beere, and D. A. Ritchie, "Gain recovery dynamics of a terahertz quantum cascade laser," *Physical Review B*, vol. 80, no. 7, p. 075 303, 2009.

[91] C. G. Derntl, G. Scalari, D. Bachmann, M. Beck, J. Faist, K. Unterrainer, and J. Darmo, "Gain dynamics in a heterogeneous terahertz quantum cascade laser," *Applied Physics Letters*, vol. 113, p. 181 102, 2018.

[92] P. Tzenov, I. Babushkin, R. Arkhipov, M. Arkhipov, N. Rosanov, U. Morgner, and C. Jirauschek, "Passive and hybrid mode locking in multi-section terahertz quantum cascade lasers," *New Journal of Physics*, vol. 20, no. 5, p. 053 055, 2018.

[93] E. Riccardi, V. Pistore, S. Kang, L. Seitner, A. De Vetter, C. Jirauschek, J. Mangeney, L. Li, A. G. Davies, E. H. Linfield, A. C. Ferrari, S. S. Dhillon, and M. S. Vitiello, "Short pulse generation from a graphene-coupled passively mode-locked terahertz laser," *Nature Photonics*, vol. 17, pp. 607–614, 2023.

[94] G. B. Rieker, F. R. Giorgetta, W. C. Swann, I. Coddington, L. C. Sinclair, C. L. Cromer, E. Baumann, A. M. Zolot, and N. R. Newbury, "Open-path dual-comb spectroscopy of greenhouse gases," *CLEO: Science and Innovations, CLEO_SI 2013*, 2013.

[95] A. Cuisset, F. Hindle, G. Mouret, R. Bocquet, J. Bruckhuisen, J. Decker, A. Pienkina, C. Bray, É. Fertein, and V. Boudon, "Terahertz rotational spectroscopy of greenhouse

gases using long interaction path-lengths," *Applied Sciences (Switzerland)*, vol. 11, no. 3, p. 1229, 2021.

[96] H. Zhong, A. Redo-Sanchez, and X.-C. Zhang, "Identification and classification of chemicals using terahertz reflective spectroscopic focal-plane imaging system," *Optics Express*, vol. 14, no. 20, p. 9130, 2006.

[97] E. Baumann, F. R. Giorgetta, W. C. Swann, A. M. Zolot, I. Coddington, and N. R. Newbury, "Spectroscopy of the methane ν 3 band with an accurate midinfrared coherent dual-comb spectrometer," *Physical Review A*, vol. 84, p. 062 513, 2011.

[98] L. Yang, T. Guo, X. Zhang, S. Cao, and X. Ding, "Toxic chemical compound detection by terahertz spectroscopy: A review," *Reviews in Analytical Chemistry*, vol. 37, no. 3, p. 20 170 021, 2018.

[99] C. Kulesa, "Terahertz spectroscopy for astronomy: From comets to cosmology," *IEEE Transactions on Terahertz Science and Technology*, vol. 1, no. 1, pp. 232–240, 2011.

[100] I. Coddington, N. Ewbury, and W. Swann, "Dual-comb spectroscopy," *Optica*, vol. 3, no. 4, p. 414, 2016.

[101] G. Villares, J. Wolf, D. Kazakov, M. J. Süess, A. Hugi, M. Beck, and J. Faist, "On-chip dual-comb based on quantum cascade laser frequency combs," *Applied Physics Letters*, vol. 107, no. 25, p. 251 104, 2015.

[102] G. Villares, A. Hugi, S. Blaser, and J. Faist, "Dual-comb spectroscopy based on quantum-cascade-laser frequency combs," *Nature Communications*, vol. 5, p. 5192, 2014.

[103] Y. Yang, D. Burghoff, D. J. Hayton, J.-R. Gao, J. L. Reno, and Q. Hu, "Terahertz multiheterodyne spectroscopy using laser frequency combs," *Optica*, vol. 3, no. 5, p. 499, 2016.

[104] D. Burghoff, Y. Yang, and Q. Hu, "Computational multiheterodyne spectroscopy," *Science Advances*, vol. 2, no. 11, p. 1 601 227, 2016.

[105] M. Rösch, G. Scalari, G. Villares, L. Bosco, M. Beck, and J. Faist, "On-chip, self-detected terahertz dual-comb source," *Applied Physics Letters*, vol. 108, no. 17, p. 171 104, 2016.

[106] Y. Zhao, Z. Li, K. Zhou, X. Liao, W. Guan, W. Wan, S. Yang, J. C. Cao, D. Xu, S. Barbieri, and H. Li, "Active Stabilization of Terahertz Semiconductor Dual-Comb Laser Sources Employing a Phase Locking Technique," *Laser and Photonics Reviews*, vol. 15, no. 4, p. 2 000 498, 2021.

[107] Z. Li, W. Wan, K. Zhou, X. Liao, S. Yang, Z. Fu, J. C. Cao, and H. Li, "On-Chip Dual-Comb Source Based on Terahertz Quantum Cascade Lasers under Microwave Double Injection," *Physical Review Applied*, vol. 12, no. 4, p. 044 068, 2019.

[108] Y. Sun, M. Y. Sy, Y.-X. J. Wang, A. T. Ahuja, Y.-T. Zhang, and E. Pickwell-MacPherson, "A promising diagnostic method: Terahertz pulsed imaging and spectroscopy," *World Journal of Radiology*, vol. 3, no. 3, p. 55, 2011.

[109] M. Yahyapour, A. Jahn, K. Dutzi, T. Puppe, P. Leisching, B. Schmauss, N. Vieweg, and A. Deninger, "Fastest thickness measurements with a Terahertz time-domain system based on electronically controlled optical sampling," *Applied Sciences*, vol. 9, no. 7, p. 1283, 2019.

[110] M. Naftaly, N. Vieweg, and A. Deninger, "Industrial applications of terahertz sensing: State of play," *Sensors*, vol. 19, p. 4203, 2019.

[111] T. Yasui, T. Yasuda, K. I. Sawanaka, and T. Araki, "Terahertz paintmeter for non-contact monitoring of thickness and drying progress in paint film," *Applied Optics*, vol. 44, no. 32, pp. 6849–6856, 2005.

[112] J. White, G. Fichter, A. Chernovsky, D. Zimdars, J. F. Whitaker, D. Das, and T. M. Pollock, "Time-domain terahertz mapping of thickness and degradation of aircraft turbine blade thermal barrier coatings," *2008 Conference on Lasers and Electro-*

Optics and 2008 Conference on Quantum Electronics and Laser Science, pp. 1–2, 2008.

[113] X. Zhang, Q. Guo, T. Chang, and H. L. Cui, "Broadband stepped-frequency modulated continuous terahertz wave tomography for non-destructive inspection of polymer materials," *Polymer Testing*, vol. 76, no. April, pp. 455–463, 2019.

[114] M. Haaser, K. C. Gordon, C. J. Strachan, and T. Rades, "Terahertz pulsed imaging as an advanced characterisation tool for film coatings - A review," *International Journal of Pharmaceutics*, vol. 457, no. 2, pp. 510–520, 2013.

[115] T. Ervasti, P. Silfsten, J. Ketolainen, and K. E. Peiponen, "A study on the resolution of a terahertz spectrometer for the assessment of the porosity of pharmaceutical tablets," *Applied Spectroscopy*, vol. 66, no. 3, pp. 319–323, 2012.

[116] S. Shi, S. Yuan, J. Zhou, and P. Jiang, "Terahertz technology and its applications in head and neck diseases," *iScience*, vol. 26, no. 7, p. 107 060, 2023.

[117] D. M. Mittleman, S. Hunsche, L. Boivin, and M. C. Nuss, "T-ray tomography," vol. 22, no. 12, pp. 904–906, 1997.

[118] V. P. Wallace, E. MacPherson, J. A. Zeitler, and C. Reid, "Three-dimensional imaging of optically opaque materials using nonionizing terahertz radiation," *Journal of the Optical Society of America A*, vol. 25, no. 12, p. 3120, 2008.

[119] E. Pickwell, B. E. Cole, A. J. Fitzgerald, M. Pepper, and V. P. Wallace, "In vivo study of human skin using pulsed terahertz radiation," *Physics in Medicine and Biology*, vol. 49, no. 9, pp. 1595–1607, 2004.

[120] E. Pickwell, V. P. Wallace, B. E. Cole, S. Ali, C. Longbottom, R. J. Lynch, and M. Pepper, "Using terahertz pulsed imaging to measure enamel demineralisation in teeth," *IRMMW-THz 2006 - 31st International Conference on Infrared and Millimeter Waves and 14th International Conference on Terahertz Electronics*, vol. 83, p. 578, 2006.

[121] S. Y. Huang, E. Macpherson, and Y. T. Zhang, "A feasibility study of burn wound depth assessment using terahertz pulsed imaging," *Proceedings of the 4th IEEE-EMBS International Summer School and Symposium on Medical Devices and Biosensors, ISSS-MDBS 2007*, pp. 132–135, 2007.

[122] L. Xu, C. A. Curwen, D. Chen, J. L. Reno, T. Itoh, and B. S. Williams, "Terahertz metasurface quantum-cascade VECSELs: Theory and performance," *IEEE Journal of Selected Topics in Quantum Electronics*, vol. 23, no. 6, p. 1 200 512, 2017.

[123] L. Xu, D. Chen, T. Itoh, J. L. Reno, and B. S. Williams, "Focusing metasurface quantum-cascade laser with a near diffraction-limited beam," *Opt. Express*, vol. 24, no. 21, pp. 24 117–24 128, 2016.

[124] L. Xu, D. Chen, C. A. Curwen, M. Memarian, J. L. Reno, T. Itoh, and B. S. Williams, "Metasurface quantum-cascade laser with electrically switchable polarization," *Optica*, vol. 4, no. 4, p. 468, 2017.

[125] C. A. Curwen, J. L. Reno, and B. S. Williams, "Terahertz quantum cascade VECSEL with watt-level output power," *Applied Physics Letters*, vol. 113, p. 011 104, 2018.

[126] C. A. Curwen, J. L. Reno, and B. S. Williams, "Broadband metasurface design for terahertz quantum-cascade VECSEL," *Electronics Letters*, vol. 56, no. 23, pp. 1264–1267, 2020.

[127] C. A. Curwen, J. L. Reno, and B. S. Williams, "Terahertz quantum-cascade patch-antenna VECSEL with low power dissipation," *Applied Physics Letters*, vol. 116, p. 241 103, 2020.

[128] E. Morag, S. Li, A. Kim, S. Addamane, and B. Williams, "THz quantum-cascade VECSELs based upon disordered metasurfaces," *SPIE Photonics West*, 2023.

[129] S. Kalchmair, R. Blanchard, T. S. Mansuripur, G. M. De Naurois, L. Diehl, C. Pfluegl, M. F. Witinski, F. Capasso, and M. Loncar, "Sampled grating quantum cascade lasers

with high tuning stability," *2015 Conference on Lasers and Electro-Optics (CLEO), San Jose, CA, USA*, 2015.

[130] I. Kundu, P. Dean, A. Valavanis, J. R. Freeman, M. C. Rosamond, L. Li, Y. Han, E. H. Linfield, and A. G. Davies, "Continuous Frequency Tuning with near Constant Output Power in Coupled Y-Branched Terahertz Quantum Cascade Lasers with Photonic Lattice," *ACS Photonics*, vol. 5, no. 7, pp. 2912–2920, 2018.

[131] I. Kundu, J. R. Freeman, P. Dean, L. Li, E. H. Linfield, and A. G. Davies, "Wide-band Electrically Controlled Vernier Frequency Tunable Terahertz Quantum Cascade Laser," *ACS Photonics*, vol. 7, no. 3, pp. 765–773, 2020.

[132] Q. Qin, J. L. Reno, and Q. Hu, "MEMS-based tunable terahertz wire-laser over 330 GHz," *Optics Letters*, vol. 36, no. 5, p. 692, 2011.

[133] C. A. Curwen, J. L. Reno, and B. S. Williams, "Broadband continuous single-mode tuning of a short-cavity quantum-cascade VECSEL," *Nature Photonics*, vol. 13, no. 12, pp. 855–859, 2019.

[134] A. D. Kim, C. A. Curwen, Y. Wu, J. L. Reno, S. J. Addamane, and B. S. Williams, "Wavelength scaling of widely-tunable terahertz quantum-cascade metasurface lasers," *IEEE Journal of Microwaves*, vol. 3, no. 1, pp. 305–318, 2023.

[135] D. Turčinková, G. Scalari, F. Castellano, M. I. Amanti, M. Beck, and J. Faist, "Ultra-broadband heterogeneous quantum cascade laser emitting from 2.2 to 3.2 THz," *Applied Physics Letters*, vol. 99, no. 19, p. 191 104, 2011.

[136] Y. Wu, S. Addamane, J. L. Reno, and B. S. Williams, "Multi-mode lasing in terahertz metasurface quantum-cascade VECSELs," *Applied Physics Letters*, vol. 119, no. 11, p. 111 103, 2021.

[137] N. Laman and D. Grischkowsky, "Terahertz conductivity of thin metal films," *Applied Physics Letters*, vol. 93, no. 5, p. 051 105, 2008.

[138] A. Gordon, C. Y. Wang, L. Diehl, F. X. Kärtner, A. Belyanin, D. Bour, S. Corzine, G. Höfler, H. C. Liu, H. Schneider, T. Maier, M. Troccoli, J. Faist, and F. Capasso, "Multimode regimes in quantum cascade lasers: From coherent instabilities to spatial hole burning," *Physical Review A*, vol. 77, no. 5, p. 053 804, 2008.

[139] J. Dai, J. Zhang, W. Zhang, and D. Grischkowsky, "Terahertz time-domain spectroscopy characterization of the far-infrared absorption and index of refraction of high-resistivity, float-zone silicon," *Journal of the Optical Society of America B*, vol. 21, no. 7, p. 1379, 2004.

[140] D. T. Reid, C. M. Heyl, R. R. Thomson, P. P. Vasil, and H. Ian, "Optically pumped VECSELs : review of technology and progress," *Journal of Physics D: Applied Physics*, vol. 50, p. 383 001, 2017.

[141] Y. Wu, C. Curwen, J. L. Reno, and B. Williams, "Continuous Wave Operation of Terahertz Metasurface Quantum-cascade VECSEL with a Long Intra-cryostat Cavity," *Applied Physics Letters*, vol. 121, p. 191 106, 2022.

[142] Y. Shen, A. D. Kim, M. Shahili, C. A. Curwen, S. Addamane, J. L. Reno, and B. S. Williams, "THz time-domain characterization of amplifying quantum-cascade metasurface," *Applied Physics Letters*, vol. 119, no. 18, p. 181 108, 2021.

[143] Y. Wu, Y. Shen, S. Addamane, J. L. Reno, and B. S. Williams, "Tunable quantum-cascade VECSEL operating at 1.9 THz," *Optics Express*, vol. 29, no. 21, p. 34 695, 2021.

[144] A. A. Danylov, A. R. Light, J. Waldman, N. R. Erickson, X. Qian, and W. D. Goodhue, "2.32 THz quantum cascade laser frequency-locked to the harmonic of a microwave synthesizer source," *Optics Express*, vol. 20, no. 25, p. 27 908, 2012.

[145] A. Barkan, F. K. Tittel, D. M. Mittleman, R. Dengler, P. H. Siegel, G. Scalari, L. Ajili, J. Faist, H. E. Beere, E. H. Linfield, A. G. Davies, and D. A. Ritchie, "Linewidth and

tuning characteristics of terahertz quantum cascade lasers," *Optics Letters*, vol. 29, no. 6, p. 575, 2004.

[146] P. Khosropanah, A. Baryshev, W. Zhang, W. Jellema, J. N. Hovenier, J. R. Gao, T. M. Klapwijk, D. G. Paveliev, B. S. Williams, S. Kumar, Q. Hu, J. L. Reno, B. Klein, and J. L. Hesler, "Phase locking of a 2.7 THz quantum cascade laser to a microwave reference," *Optics Letters*, vol. 34, no. 19, p. 2958, 2009.

[147] D. Rabanus, U. U. Graf, M. Philipp, O. Ricken, J. Stutzki, B. Vowinkel, M. C. Wiedner, C. Walther, M. Fischer, and J. Faist, "Phase locking of a 1.5 Terahertz quantum cascade laser and use as a local oscillator in a heterodyne HEB receiver," *Optics Express*, vol. 17, no. 3, p. 1159, 2009.

[148] C. A. Curwen, J. H. Kawamura, D. J. Hayton, S. J. Addamane, J. L. Reno, B. S. Williams, and B. S. Karasik, "Phase locking of a THz QC-VECSEL to a microwave reference," *IEEE Transactions on Terahertz Science and Technology*, vol. 13, no. 5, pp. 448–453, 2023.

[149] D. Corzo, G. Tostado-Blázquez, and D. Baran, "Flexible Electronics: Status, Challenges and Opportunities," *Frontiers in Electronics*, vol. 1, p. 594 003, 2020.

[150] X. Liu, S. MacNaughton, D. B. Shrekenhamer, H. Tao, S. Selvarasah, A. Totachawattana, R. D. Averitt, M. R. Dokmeci, S. Sonkusale, and W. J. Padilla, "Metamaterials on parylene thin film substrates: Design, fabrication, and characterization at terahertz frequency," *Applied Physics Letters*, vol. 96, no. 1, p. 011 906, 2010.

[151] I. E. Khodasevych, C. M. Shah, S. Sriram, M. Bhaskaran, W. Withayachumnankul, B. S. Ung, H. Lin, W. S. Rowe, D. Abbott, and A. Mitchell, "Elastomeric silicone substrates for terahertz fishnet metamaterials," *Applied Physics Letters*, vol. 100, no. 6, p. 061 101, 2012.

[152] I. M. Pryce, K. Aydin, Y. A. Kelaita, R. M. Briggs, and H. A. Atwater, "Highly strained compliant optical metamaterials with large frequency tunability," *Nano Letters*, vol. 10, no. 10, pp. 4222–4227, 2010.

[153] W. Liu, Y. Shen, G. Xiao, X. She, J. Wang, and C. Jin, "Mechanically tunable sub-10 nm metal gap by stretching PDMS substrate," *Nanotechnology*, vol. 28, no. 7, p. 075 301, 2017.

[154] J. Wang, H. Tian, S. Li, G. Wang, Y. Wang, L. Li, and Z. Zhou, "Dual-band terahertz switch with stretchable Bloch-mode metasurface," *New Journal of Physics*, vol. 22, no. 11, p. 113 008, 2020.

[155] M. Choi, S. H. Lee, Y. Kim, S. B. Kang, J. Shin, M. H. Kwak, K. Y. Kang, Y. H. Lee, N. Park, and B. Min, "A terahertz metamaterial with unnaturally high refractive index," *Nature*, vol. 470, no. 7334, pp. 369–373, 2011.

[156] H. Tao, C. M. Bingham, A. C. Strikwerda, D. Pilon, D. Shrekenhamer, N. I. Landy, K. Fan, X. Zhang, W. J. Padilla, and R. D. Averitt, "Highly flexible wide angle of incidence terahertz metamaterial absorber: Design, fabrication, and characterization," *Physical Review B - Condensed Matter and Materials Physics*, vol. 78, no. 24, 241103(R), 2008.

[157] J. S. Schalch, K. Post, G. Duan, X. Zhao, Y. D. Kim, J. Hone, M. M. Fogler, X. Zhang, D. N. Basov, and R. D. Averitt, "Strong Metasurface–Josephson Plasma Resonance Coupling in Superconducting La2xSrxCuO4," *Advanced Optical Materials*, vol. 7, no. 21, p. 1 900 712, 2019.

[158] A. Forrer, M. Franckié, D. Stark, T. Olariu, M. Beck, J. Faist, and G. Scalari, "Photon-Driven Broadband Emission and Frequency Comb RF Injection Locking in THz Quantum Cascade Lasers," *ACS Photonics*, vol. 7, no. 3, pp. 784–791, 2020.

[159] Y. Wu, C. A. Curwen, J. L. Reno, and B. S. Williams, "RF injection locking of THz metasurface quantum-cascade-VECSEL," *Laser & Photonics Reviews*, vol. 2023, p. 2 300 007, 2023.

[160] X. Qi, K. Bertling, T. Taimre, Y. L. Lim, T. Gillespie, P. Dean, L. H. Li, E. H. Linfield, A. G. Davies, D. Indjin, and A. D. Rakić, "Terahertz imaging with self-pulsations in quantum cascade lasers under optical feedback," *APL Photonics*, vol. 6, no. 9, p. 091 301, 2021.

[161] X.-G. Wang and C. Wang, "Non-linear dynamics modeling of quantum cascade lasers with tilted optical feedback," *Proc. SPIE 12141, Semiconductor Lasers and Laser Dynamics X, 121410A*, 2022.

[162] P. Gellie, S. Barbieri, J. F. Lampin, P. Filloux, C. Manquest, C. Sirtori, I. Sagnes, S. P. Khanna, E. H. Linfield, H. E. Beere, and D. A. Ritchie, "Injection-locking of terahertz quantum cascade lasers up to 35GHz via RF amplitude modulation," *Optics Express*, vol. 18, no. 20, pp. 20 799–20 816, 2010.

[163] M. R. St-Jean, M. I. Amanti, A. Bernard, A. Calvar, A. Bismuto, E. Gini, M. Beck, J. Faist, H.C.Liu, and Carlo Sirtori, "Injection locking of mid-infrared quantum cascade laser at 14 GHz, by direct microwave modulation," *Laser & Photonics Reviews*, vol. 8, no. 3, pp. 443–449, 2014.

[164] B. Schneider, F. Kapsalidis, M. Bertrand, M. Singleton, J. Hillbrand, M. Beck, and J. Faist, "Controlling Quantum Cascade Laser Optical Frequency Combs through Microwave Injection," *Laser and Photonics Reviews*, vol. 15, no. 12, p. 2 100 242, 2021.

[165] Y. Wang and A. Belyanin, "Active mode-locking of mid-infrared quantum cascade lasers with short gain recovery time," *Optics Express*, vol. 23, no. 4, p. 4173, 2015.

[166] L. Gu, W. J. Wan, Y. H. Zhu, Z. L. Fu, H. Li, and J. C. Cao, "High frequency modulation and injection locking of terahertz quantum cascade lasers," *Journal of Optics (United Kingdom)*, vol. 19, no. 6, p. 065 706, 2017.

[167] B. Hinkov, A. Hugi, M. Beck, and J. Faist, "Rf-modulation of mid-infrared distributed feedback quantum cascade lasers," *Optics Express*, vol. 24, no. 4, p. 3294, 2016.

[168] A. Forrer, "RF Control and Coherence Spectroscopy of THz Quantum Cascade Laser Frequency Combs," *PhD thesis*, 2022.

[169] C. C. Teng, J. Westberg, and G. Wysocki, "Gapless tuning of quantum cascade laser frequency combs with external cavity optical feedback," *Optics Letters*, vol. 48, no. 2, p. 363, 2023.

[170] X. Liao, X. Wang, K. Zhou, W. Guan, Z. Li, X. Ma, C. Wang, J. C. Cao, C. Wang, and H. Li, "Terahertz quantum cascade laser frequency combs with optical feedback," *Optics Express*, vol. 30, no. 20, p. 35 937, 2022.

[171] D. S. Seo, J. D. Park, J. G. Mcinerney, and M. Osinski, "Multiple Feedback Effects in Asymmetric External Cavity Semiconductor Lasers," *IEEE Journal of Quantum Electronics*, vol. 25, no. 11, pp. 2229–2238, 1989.

[172] X. G. Wang, B. B. Zhao, Y. Deng, V. Kovanis, and C. Wang, "Nonlinear dynamics of a quantum cascade laser with tilted optical feedback," *Physical Review A*, vol. 103, no. 2, p. 23 528, 2021.

[173] B. Zhao, Y. Peng, X. Wang, and C. Wang, "Modulation characteristics of period-one oscillations in quantum cascade lasers," *Applied Sciences*, vol. 11, p. 11 730, 2021.

[174] B. B. Zhao, X. G. Wang, and C. Wang, "Low-Frequency Oscillations in Quantum Cascade Lasers with Tilted Optical Feedback," *IEEE Journal of Selected Topics in Quantum Electronics*, vol. 28, no. 1, p. 1 800 207, 2022.

[175] J. D. Park, D. S. Seo, and J. G. Mcinerney, "Self-Pulsations in Strongly Coupled Asymmetric External Cavity Semiconductor Lasers," *IEEE Journal of Quantum Electronics*, vol. 26, no. 8, pp. 1353–1362, 1990.

[176] C. Silvestri, X. Qi, T. Taimre, and A. D. Rakić, "Frequency combs and optical feedback in Quantum Cascade Lasers: a unifying theoretical framework," *arXiv:2305.04454v1 [physics.optics]*, 2023.

[177] P. R. Griffiths and J. A. De Haseth, *Fourier Transform Infrared Spectrometry*. 2007, A JOHN WILEY & SONS, INC., PUBLICATION.

[178] L. D. Spencer, "Spectral characterization of the Herscher SPIRE photometer," *Master thesis*, 2005.

[179] L. Mertz, "Auxiliary computation for Fourier spectrometry," *Infrared Physics*, vol. 7, no. 1, pp. 17–23, 1967.

[180] M. L. Forman, W. H. Steel, and G. A. Vanasse, "Correction of Asymmetric Interferograms Obtained in Fourier Spectroscopy*," *Journal of the Optical Society of America*, vol. 56, no. 1, p. 59, 1966.

[181] M. Waves, "Correction of phase errors in fourier spectroscopy," *International Journal of Infrared and Millimeter Waves*, vol. 4, no. 2, pp. 273–298, 1983.

[182] D. E. Armstrong, "Mathematical Formulation used by MATLAB Code to Convert FTIR Interferograms to Calibrated Spectra," *LA-UR 16-XXXXX*, 2016.

[183] P. Maslowski, K. F. Lee, A. C. Johansson, A. Khodabakhsh, G. Kowzan, L. Rutkowski, A. A. Mills, C. Mohr, J. Jiang, M. E. Fermann, and A. Foltynowicz, "Surpassing the path-limited resolution of Fourier-transform spectrometry with frequency combs," *Physical Review A*, vol. 93, no. 2, 021802(R), 2016.

[184] L. Rutkowski, P. Masłowski, A. C. Johansson, A. Khodabakhsh, and A. Foltynowicz, "Optical frequency comb Fourier transform spectroscopy with sub-nominal resolution and precision beyond the Voigt profile," *Journal of Quantitative Spectroscopy and Radiative Transfer*, vol. 204, pp. 63–73, 2018.

[185] L. A. Sterczewski and M. Bagheri, "Sub-nominal resolution Fourier transform spectrometry with chip-based combs," *arXiv:2303.13074v1 [physics.optics]*, 2023.

[186] M. I. Amanti, G. Scalari, R. Terazzi, M. Fischer, M. Beck, J. Faist, A. Rudra, P. Gallo, and E. Kapon, "Bound-to-continuum terahertz quantum cascade laser with a single-quantum-well phonon extraction/injection stage," *New Journal of Physics*, vol. 11, p. 125 022, 2009.

[187] L. Xu, C. A. Curwen, J. L. Reno, and B. S. Williams, "High performance terahertz metasurface quantum-cascade VECSEL with an intra-cryostat cavity," *Applied Physics Letters*, vol. 111, no. 10, p. 101 101, 2017.